Studying the surface structure and chemical nature of foul release coatings in operation.

Thomas Sexton

Submitted for the degree of
Doctor of Philosophy

The University Of Sheffield.

Department of Physics and Astronomy
The University of Sheffield
2021

Declaration of Originality

I the author, confirm that the work described in this thesis was undertaken at the The University of Sheffield between September 2017 and December 2021 under the supervision of Dr Andrew J. Parnell and Professor Richard A.L. Jones , with additional support from representatives of Akzo Nobel. I confirm that the thesis is my own work except except where data was acquired with the assistance of colleagues in which case my contribution and the contribution of other authors is explicitly stated. I confirm appropriate credit has been given within this thesis where reference is made to the work of others. This work has not been submitted in part or in whole for any other degree at this or nay other institution.

Thomas Sexton (December 2021)

Abstract

The objective of this thesis is the study of the foul release properties of short chain amphiphilic triblock copolymers Perfluoropolyether Polyethylene Oxide (PFPE-PEO) incorporated into Polydimethylsiloxane (PDMS) coatings , with a particular interest in the surface structural and chemical properties of such coatings in water. To this end thin films incorporating both materials were produced suitable for neutron analysis. Challenges associated with the development of these model systems such as autophobic dewetting from substrate were explored using SIMS analysis. Successful development of model systems allowed in fluid surface analysis to be performed using neutron reflectivity and atomic force microscopy, this determined that PDMS/PFPE-PEO coatings undergo surface reconstruction in water with a $\approx$ 3nm monolayer of PFPE-PEO wetting the PDMS water interface via hydrophobic interactions between the PFPE block and the PDMS surface. In this monolayer the PEO groups in the amphiphile are solvated and render the surface hydrophilic whilst also changing the surface mechanical properties. Bioadhesion on these model surfaces was assessed in real time using QCM and neutron reflectivity and post situ using AFM which demonstrated a significant reduction in protein adsorption of at least 75% compared to PDMS controls, with some experiments detecting negligible protein adsorption on PFPE-PEO/PDMS surfaces these studies also verified the hydrophobic nature of protein adsorption on PDMS surfaces. The nature of the foul resistance of this interface was postulated to be the result of strong hydrogen bonds between the surface wand local water molecules inducing a hydration barrier to adhesion. Finally, the diffusion of PFPE-PEO amphiphiles was studied using water contact angles to monitor diffusive time lags finding a diffusion coefficient of $3.55\pm0\ 0.24 \times 10^{-12}\mathrm{m}^2\mathrm{s}^{-1}$, this was corroborated by ion milling XPS depth profiles of PDMS diffusion samples which also revealed evidence of surface enrichments of PFPE-PEO amphiphiles in PDMS coatings.

Acknowledgements

I would like to thank my supervisors Richard Jones and Andrew Parnell for their guidance and advice throughout this project, particularly the efforts they made during the covid pandemic to maintain regular contact and their efforts to help reopen the labs and facilitate my research in extremely challenging circumstances.
I would like to also thank former/current post docs in our group; Michael Weir for his positive attitude and practical support early in the project teaching thin film preparation techniques and Stephanie Burg whose advice and assistance with data analysis techniques and python applications was extremely helpful and has encouraged me to continue to develop this skillset.
Debbie Hammond's assistance with surface analysis techniques SIMS and XPS was absolutely invaluable to chapters 3 and 6, without which we would have far less evidence for our conclusions about the autophobic dewetting effects or the nature of diffusion. I thank her for her work and her patience with my frequent revisions to planned experiments.
I would like to than Raveen Tank for her assistance acquiring the liquid AFM images used in chapter 4, her willingness to perform these measurements in the last few days of her research contract before moving to a new position was greatly appreciated. In the difficult circumstances of December 2020 many would not have made the effort but this work greatly added to my research.
I would like to thank all the beamline scientists who assisted the neutron reflectivity performed for this thesis particularly Alexei Klechikov who made every effort to make challenging experiment successful, Phillip Gutfreund whose support on D17 was exemplary and Samantha Micculla whose diligence in communicating and willingness to cooperate with planning was hugely appreciated and ensured my protein adsorption experiment could be successfully performed remotely, with all desired data acquired in the allotted single day.
I would like to thank Akzo Nobel, specifically Dr Simon Welsh my industrial liaison, for their assistance in providing materials and technical information and bringing this problem to the physics department and investing in me as a researcher.

I would also like to thank my fellow PhD students in particular Tom Catley who helped with a beamline experiment and provided contacts to AFM research labs and Rachel Kilbride who has been a consistent presence throughout the project , providing advice and support and shown a willingness to share resources and skills that has helped me overcome many technical challenges.
I would like to thank my parents for the ongoing support throughout this project and my friends Sarah, Lydia, Joanna, Harry and Nick who have offered a sympathetic ear during periods of frustration.

Contents

Chapter 1

Introduction

1.1 Biofouling overview:

Biofouling is a remarkably broad category describing mechanisms by which surfaces are subject to the adhesion, colonisation and development of biological material such as algaes, plaques bioslimes and even macro matter like mussels and barnacles[1]. For many biological species, large invertebrates or unicellular bacteria, the migration and attachment of organisms onto novel surfaces are vital mechanism for the propagation and expansion into new environments. The evolutionary process has produced an incredibly diverse collection of organisms optimised for effective attachment to a wide variety of surface types and surface chemistries.

This ubiquitous phenomenon is not simply a curiosity but can prove highly undesirable in many industrial environments and as such there is significant commercial and scientific interest in understanding, controlling or eliminating biofouling.

Biofouling is of particular concern to the medical industry which has championed much contemporary research into biofouling owing to the demand for medical devices that can resist unwanted biofouling. Classic examples of biofouling in medicine include the risk of bacterial fouling of contact lenses causing Keratitis [2] or the failure of catheters due to thrombosis as blood platelets, fibrin and red blood cells adhere and aggregate to the catheter walls causing an occlusion of the tube and rendering the catheter inoperable[3]. Significant bacterial adhesion on a medical implant inserted into the body can represent a serious infection risk,[4][5] given that biofilms are known to be particularly resistant to to

antibiotic treatments[6] this can cause a very acute medical problems. Utilising anti fouling or foul resistant materials in biomedical implants can mitigate these biofouling risks, prolonging the life of implants, reducing the need for repeated medical interventions and increasing patient confidence.

The civil water industry also wrestles with the problem of biofouling in the vast and diverse water pipe infrastructure it must maintain. With drinking water kept at near optimal temperatures for many bacterial and bioslimes, they represent an extremely hospitable environment for many biological species leading to significant biofouling of pipes. If this build up is not controlled it can lead to large masses of bioslime building up which may break off into the water supply in significant quantities contaminating drinking water. These biofilms can also contribute to the erosion of metal pipe infrastructure which in turn can lead to oxide leeching into drinking water leading to discolouration events and customer discontent [7]. Biofouling is also a hindrance to novel desalination reverse osmosis membranes for extracting fresh water from sea water, biofilms forming on these membranes has been described as an 'Achilles heel' for these membranes[8] with biofouling and biological organic fouling matter responsible for large declines in water flux through the nonporous membranes and an increase in the salt content of the resultant fresh water. Mitigating these problems may be key to ensuring the viability of these technologies and hence, global water security. Although seemingly a chronic problem in water management there is a growing industrial interest in understanding the mechanisms and developing methods of monitoring the problem [9] in order to manage and minimise the burden on the water supply.

Biofouling is a multifaceted problem which can be very environment specific; biofouling species can have distinct modes of adhesion, surfaces that effectively mitigate against one organism may be vulnerable to another organism's adhesion strategy so surfaces in environments with diverse biofouling populations can be very hard to design to remain unspoilt.

1.2 Marine biofouling

The primary focus of this thesis is foul release coatings for marine applications, considering novel polymeric amphiphiles which can improve foul release coatings as favoured foul resistance strategies over more invasive biocidal coatings.

The fouling of ships submerged hull by sea organisms has been perennial problem since the dawn of sea faring cultures, with the accrued mass of barnacles, weeds and slimes affecting a ship's profile in the water increasing drag and

ultimately leading to the degradation of the hull. An early modern solution to the problem was adopted by the British navy in the 18th century who employed copper sheathing on their ship's underside which proved to be a highly effective biocide [10] preventing the growth and development of algaes Molluscs and bacterial slimes on the hull surface [11]. Although highly effective this copper based method fell out of favour as naval architecture and ship building replaced wood hulled ships with iron and steel it was found the combination of copper and salt water had a particularly corrosive electrolytic effect on iron hulls [12].

Whilst copper fell out of favour the demand for foul resistant ships remained as the hindrance caused by significant biofouling can severe; Surface bioslimes can significantly increase fluid drag whilst hard fouling matter like mussels and barnacles with shells cause the ship profile to become much rougher with a 75% hull coverage with shells resulting in a 85% increase in skin friction forces exerted on the ship as it transits through the water [13]. This in turn markedly increases fuel consumption by between 30-50%[14], studies by the US Navy suggest biofouling associated maintenance for the entire fleet costs $400-540m annually, as such, the costs of implementing foul resistance strategies are comfortably justified by the prospective savings in fuel consumption and biofouling related maintenance. The emissions profile of the marine shipping industry is significant, representing 18-30% of all global NO_x emissions [15] and ≈2-3% of all greenhouse emissions[16] therefore foul resistance technologies which help minimise shipping fuel consumption will have a positive environmental impact.

1.3 Marine biofouling composition

Marine biofouling an be broken down into three main categories[17]:

1. Microfouling matter: Usually considered the initial phase of all biofouling, Micro-fouling begins with the adhesion of single celled organisms often bacteria or in the marine context unicellular algae's such as diatoms. When these unicellular organisms arrive at a surface part of the adhesion process involves the treatment of the surface with. a conditioning film of organic biomolecules such as proteins[18]; this seems to play a key role in bacterial adhesion. Once several bacteria have attached to a surface they form a cohesive biofilm by excreting a coating of Extracellular Polymeric Substances (EPS)[1] onto the surface binding the unicellular organisms to each other and the surface. These EPS substances make up over 50% of the organic matter in biofilms and are principally composed of polysaccharides, proteins lipids and extracellular DNA [19]. Biofilm slimes are very complex organic

structures aiding the growth, stability and coordination of a bacterial colony (gene transfer and quorum sensing). Biofilm slimes particularly caused by marine diatoms are some of the most persistent and challenging forms of biofouling.

2. Macro-fouling soft matter: Weeds, algaes, corals sponges and other soft invertebrates.
3. Macro-fouling hard matter: Larger invertebrates with shells such as barnacles and mussels.

Macro-fouling is often preceded by the development of micro fouling biofilm slimes upon which larger species can more easily adhere, this sequential development of biofouling suggests that limiting the more diverse and more persistent microfilming effects is essential for controlling surface biofouling.

1.4 Anti biofouling approaches: biocidal coatings

Much like biocidal copper many coatings have been developed embracing the biocidal design approach of incorporating an antimicrobial agent into a coating that will either harm and kill any adhering organisms or is steadily released from the hull surface increasing the biotoxicity of the aquatic environment in close proximity to the ship, killing unicellular organisms before they manage to attach to the surface and thus inhibiting micro fouling.

By the early 1970s the marine industry had embraced biocidal coatings based on tri-butyl-tin (TBT) compounds, figure 1.1 shows the structure.

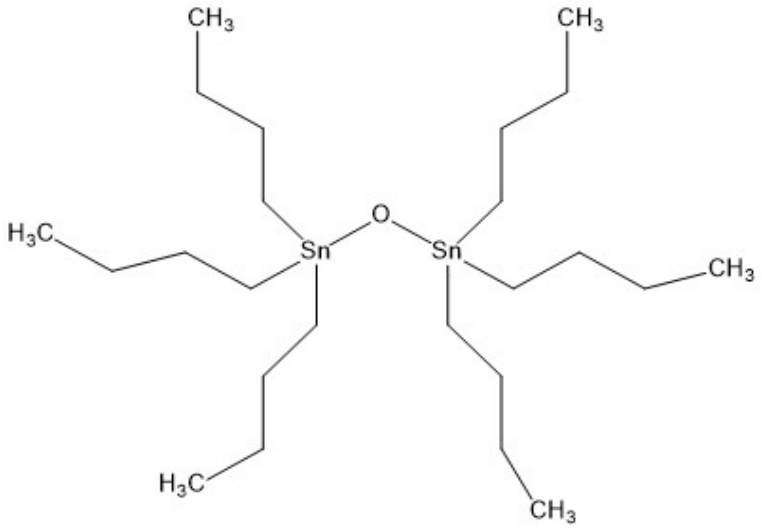

Figure 1.1: Tri-Butyl-Tin.

Coatings based around TBT compounds formed a global majority of foul resistant paint coatings used by the industry until the end of the 20^{th} century [20] proving to be extremely effective. By incorporating biocidal TBT compounds into a self polishing copolymer matrix coating, it was possible to achieve a constant emission of biocide into the surroundings over the course of the coating lifetime via the steady ablation of the copolymer coating over time which also kept the coating smooth [13].

However, the potency of TBT proved to be having a hazardous effect on the wider marine ecology, with the emission of this compound being implicated in the abnormal growth of oysters and imposex phenomena amongst dog whelk sea snails. Consequently, TBT has been banned from use in the marine paints industry [21].

Although alternative biocidal coatings have been developed the greater regulatory scrutiny of marine biocide pollution has spurred greater research and development of Foul Release coatings to limit biofouling. These coatings work from the principle of minimising adhesion and the strength of adhesion between biomolecules and the surface, with the objective of controlling biofouling by ensuring organisms cannot achieve secure attachments to the ship and will be periodically removed by hydrodynamic shear forces.Foul release coatings also benefit from greater applicability with potential applications in biomedical devices where biocidal approaches would be inappropriate.

1.5 Physics of bio-adhesion and characteristics of good foul-release materials

In order to develop foul release coatings general design principles have to be developed and an understanding of the properties of weakly adhesive coatings have to be established. One of the earliest and most influential studies of bioadhesion to surfaces was performed by Baier who investigated the quantity of blood plasma that adhered to a series of chemical surfaces, which was then associated to the material surface energy. A simple hypothesis would predict that decreasing surface energy of a material would result in less overall adhesion as low energy surfaces are already highly stable. This means it may be difficult to form strong interfacial bonds between the surface and the adhering matter as this bond is less likely to be energetically favoured. However, the Baier curve as shown in figure 1.2 demonstrated a more complex relationship between bioadhesion and surface energy with bioadhesion reaching a minima for materials with a surface energy of $\gamma_C = 0.25 mJcm^{-2}$ whilst several fluorinated materials lower surface energies saw greater amounts of platelet adhesion.

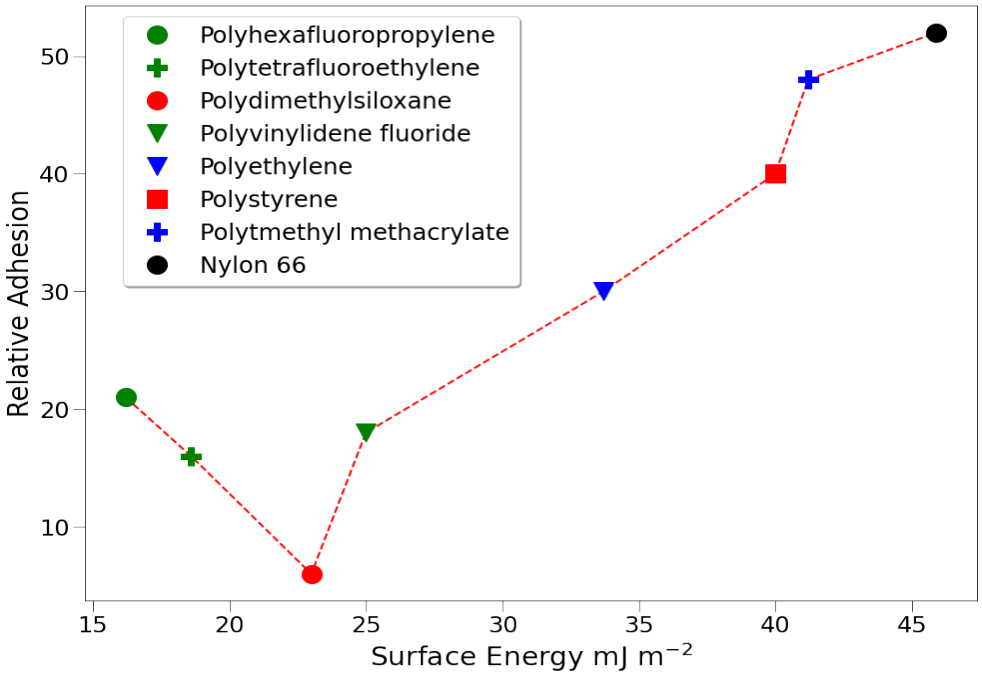

Figure 1.2: The Baier curve[22] reproduced using data from[23] showing the relationship between a material's surface tension and bio-adhesion.

By considering also the elastic modulus of the material a clearer relationship between material properties and biaodhesion could be achieved. It has been shown that the elastic modulus of the material is important to foul release behaviour as this dictates the mechanical fracture performance with an empirical relationship being developed

$$R_{Adh} \propto (E\gamma_c)^{0.5} \tag{1.1}$$

This relationship could characterise fouling performances of many simple surface materials.

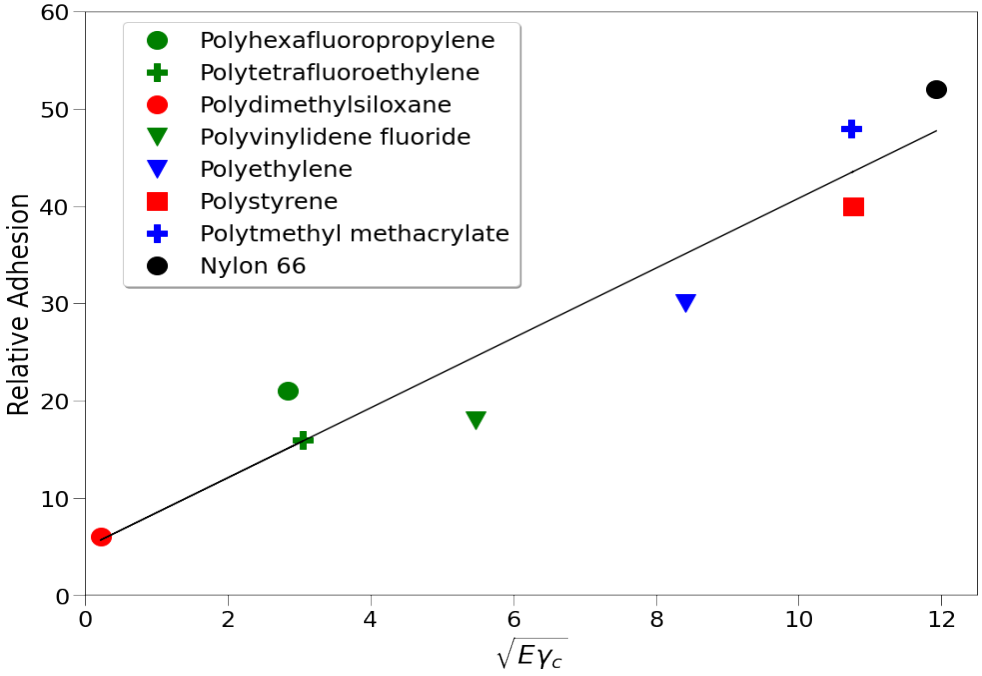

Figure 1.3: Relative adhesion as a function of the square root of the product of the material surface energy and elastic modulus showing a clear linear relationship relationship, plotted using data from[23].

Although the relationship shown in figure 1.3 does not represent a theoretically derived relationship, Brady et al found that the the quantity $(E\gamma_c)^{0.5}$ correlated with relative adhesion to a greater extent than either surface energy and or the elastic modulus of the material individually[23]. Elastic modulus is thought to be particularly important for the removal of adhered material as a lower elastic moduli reduces the critical fracture force necessary to mechanically detach objects adhered to an elastomeric surface.

1.5.1 PDMS

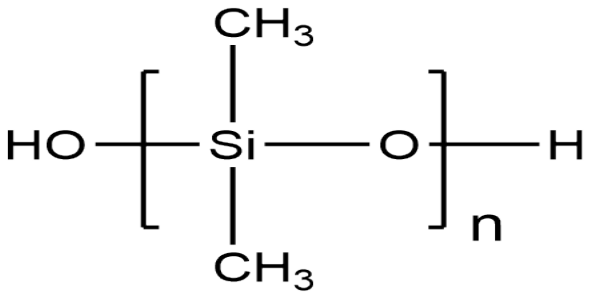

Figure 1.4: PDMS, Hydroxy terminated.

PDMS (structure shown in figure 1.4) has been used as the bulk coating platform for many foul release coatings owing to its combined advantages of low surface energy $\gamma_C = 23mJm^{-2}$ and low elastic modulus $E\ 2 - 3MPa$[24] demonstrating its soft rubbery properties. With room temperature well above the PDMS glass transition the polymer is typically a viscous fluid, which can be crosslinked by chemically reacting chains together to form a a flexible, potentially self healing[25] rubbery network. As a polymer with numerous industrial applications it benefits from being well characterised and inexpensive. PDMS has demonstrated itself to be an effective foul release material for hard macro foulants with experiments studying the removal of both organic barnacles and synthetic pseudo barnacles made of epoxy resins showing that the adhesion strength of these hard foulants on PDMS surface was low [26] and in fact, incorporating PDMS silicone into higher energy epoxy coatings reduced the strength of adhesion of pseudo barnacles on these surfaces[27]. PDMS does struggle however against micro-fouling species, having been found to be vulnerable to protein adsorption as proteins can adhere to the PDMS via hydrophobic interactions in an irreversible process which can aid the adhesion of bacteria on the surface[28]. Specifically in the marine context diatom slimes have been shown to adhere effectively on PDMS coatings [29]. Because this vulnerability to protein fouling is a function of its interfacial tension with water; its hydrophobicity, researchers have considered incorporating additives into bulk PDMS coatings which segregate to the solid/liquid interface in order to minimise hydrophobic adsorption effects but still maintain the favourable bulk mechanical properties of PDMS.

This microfouling on PDMS coatings highlights another paradox of biofouling on surfaces; although there is evidence to support the use of low surface energy materials as effective foul release coatings such as the Baier curve seen in figure 1.2, low surface energy materials such as fluoropolymers and PDMS silicones are

usually hydrophobic, having a high interfacial tension with water. These hydrophobic materials are vulnerable to protein adsorption via hydrophobic interactions in which the protein denatures, forming a strong bond with the surface which is usually irreversible. Finlay et al investigated the adhesion of microfouling diatoms on a series of self assembled monolayers terminated with either CH_3 and OH groups. Tuning the balance of these hydrophobic methyl groups and hydrophilic hydroxy groups, created series of surfaces of varying hydrophobicity as inferred from contact angle measurements. Finlay et al determined that the most hydrophobic surfaces (Contact angle $\approx 92°$) saw the highest overall adhesion of diatoms, more than ten times the most hydrophilic monolayer (contact angle $\approx 20°$)[30] . However, upon subjecting the surfaces to a shear tress of 56Pa for 5 minutes the hydrophobic surfaces saw the highest rates of diatom removal of 90% and the most hydrophilic surfaces saw the least removal of algae 25%. Similar observations were made by Callow et al investigating the attachment of algal zoospores [31].

The higher biofouling resistance of more hydrophilic surfaces resulted in a further revision of the Baier curve; some materials with higher surface energies closer to that of water i.e. greater than $60 mJm^{-2}$ showed lower bioadhesion, a notable example being Polyethylene glycol (PEG)

1.5.2 PEG

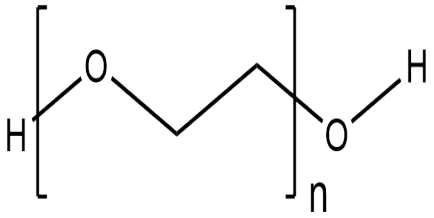

Figure 1.5: PEG

Polyethylene glycol/oxide (PEG/PEO, see figure 1.5 for structure) is a polymer that is generally regarded as biocompatible, has a high surface tension of 43.5 mJm^{-2} , is very hydrophilic and yet has been shown consistently to resist protein adsorption and cell adhesion. Polyethylene surfaces treated with a surface grafted coating of PEG saw radically reduced blood platelet adhesion[32].

The precise cause of PEG protein and cellular resistance is still a matter of debate but the most established theory was postulated by Andrade and De Gennes [33] who argued that PEG chains at water interfaces are highly solvated

and swollen with water molecules. In order for protein molecules to bond to the surface these water molecules have to be forced out of the PEG layer which is thermodynamically unfavourable, the resistance to PEG dehydration leads to a steric repulsion effect for adhering proteins and result in PEG surfaces being highly bioinert. They predict that this protein resistance will increase with both increasing PEG chain length and increasing surface density of PEG chains. This has been somewhat corroborated by experiments of protein adsorption on grafted PEG layers, which observed optimal protein resistance for grafting layer density in which the area per PEG molecule is smaller than the dimensions of the adhering protein molecule[34]. However, some questions regarding the protein resistance of PEG surfaces remain unsolved; PEG protein interactions appear to be weakly attractive and for a given grafting density increasing chain length enables greater protein penetration of the brush. Neutron reflectivity studies of Protein adsorption on tether PEG brush surfaces show limited tertiary protein adsorption on these PEG treated surfaces; with proteins entering the brush and adhering not to the top of the PEG surface or the interior of the chain but at the tethered substrate of the PEG surface[35][36].

PEG presents a very interesting material for the field of biofouling, however the material lacks many of the mechanical properties necessary in a coating and many of the preparation techniques such as grafting are not appropriate for many applications. Instead, PEG is incorporated into many as an amphiphilic block copolymer additive in order to achieve PEG solid/liquid interfaces whilst maintaining optimal bulk properties in a foul release coating.

1.5.3 Advanced amphiphilic coatings

Attempts to incorporate hydrophilic PEG into foul release coatings have employed amphiphilic molecules with both hydrophobic and hydrophilic components. One notable example is Pluronic, (See figure 1.6) an amphiphilic triblock copolymer of PEG and polypropylene oxide, a hydrophobic block.

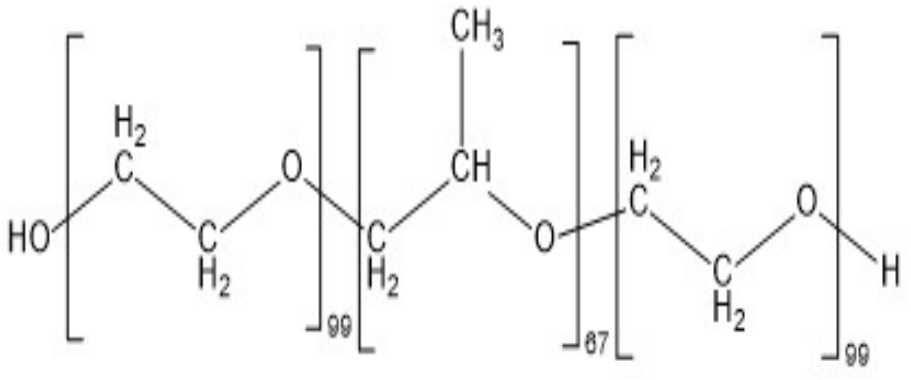

Figure 1.6: Pluronic

Pluronic molecules have proved to be highly effective foul release additives when incorporated in poly(ether sulfone) coatings where they have been shown to functionalise the solid-liquid interface and reduce bioadhesion by up to 90% [37].

A recent alternative approach by Oda et al incorporated both PEG and low surface energy hydrophobic fluoroalkyl groups into the same hyper branched polymer as twin branches in each terminal portion of the polymer. In air, the low energy fluoroalkyl groups drive the terminal branches to be enriched at the surface. When the surface is subject to water this alignment of the end branches at the surface allows for rapid and well ordered surface segregation of the PEG end branches at the solid/liquid interface [38].

Utilising fluorinated amphiphiles to help drive PEG to the surface of coatings is a strategy that was employed by the Segalman group using polypeptide chemistry to create polymers with well defined sequences of hydrophobic fluoroalkyl groups and hydrophilic ethylene glycol (PEG) groups [39] which showed just three fluoroalkyl groups close to the backbone of a long PEG chain is sufficient to help drive the segregation of the peptide group to the surface and increasing the foul release properties of the coating.

1.5.4 Perfluoropolyether Polyethylene Oxide PFPE-PEO

PFPE-PEO triblock copolymers are amphiphilic polymers which appear to be good prospects as additives for foul release coatings.

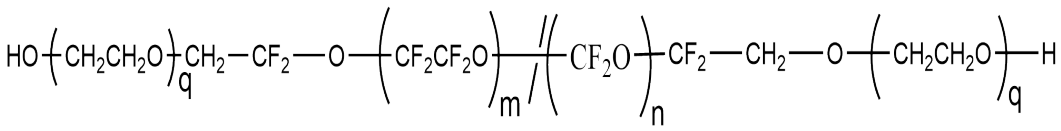

Figure 1.7: PFPE-PEO

PFPEs are amphiphilic copolymers that are liquid at room temperature. As can be seen from their structure in figure 1.7, they contain blocks of hydrophobic fluorinated groups CF_2CF_2O and CF_2O and bookended by two termination blocks of polyethylene oxide (interchangeable term for polyethylene oxide PEG) hydrophilic groups CH_2CH_2O. These two chemical blocks are quite incompatible with wide angle x ray scattering studies showing ready micro-phase separation of bulk liquid PFPE-PEO into domains of PEG and PFPE upon heating[40] with a calculated interaction parameter of $\chi = 2 - 2.5$.This could prove advantageous for strong self assembly behaviour at interfaces where one block in the amphiphile is more energetically favoured than the other eg. PEG at the solid liquid interface.

Elastomers formed of PFPE-PEO by crosslinking methacrylate terminated variants of the molecule have shown promising foul release properties [41, 42]. In a study by Molena et al protein fouling was assessed for PFPE-PEO elastomers using a fluorescent BSA protein monitoring both the initial protein adhesion and subsequent removal of adhered matter elastomer coatings incorporating PFPE-PEG block copolymers showed 80% less adhesion when compared to PMMA and PDMS surfaces. Advancing and receding contact angles for PFPE-PEG elastomers showed evidence of contact angle hysteresis when compared with pure PFPE crosslinked films implying the surface becomes more hydrophilic over time when exposed to water, potentially due to surface reconstruction as PEG blocs segregate to the solid liquid interface.

This recent research suggests that PFPE-PEO has great potential as a foul release material, their adoption in the industry may be inhibited by the comparative cost of these material compared to more conventional polymer coatings such as PDMS. Rather than homogenous elastomer coatings it may be possible to use these amphiphiles as additives to bulk elastomer coatings; the low surface energy of these fluorine based molecules should drive a surface enrichment of the block copolymer in most materials [43], thus incorporating the amphiphile into a coating at even small concentrations should result in a effective surface segregation of PFPE-PEO [44].

A PFPE-PEO amphiphile of particular interest is Fluorolink E10/6 which is

a perfluoropolyether sourced from Solvay.This amphiphile is a viscous liquid at room temperature. With reference to figure 1.7, the structure of the molecule is. as follows; the central perfluoropolyether section is made of two blocks; tetrafluoroethylene oxide with m=5 repeat units and difluoromethylene oxide with n=4 repeat units. The molecular weight is listed as M_w=2000. The PEO blocks have an average chain length of q=4.5, such that and average molecule has a total of 9 PEO units distributed across both end blocks of the amphiphile. In this Thesis we explore the incorporation of this PFPE-PEO amphiphile into PDMS cross-linked coatings to determine its performance as an additive to this established foul release material. We will study the compatibility of the two materials, the surface activity of PFPE-PEO within PDMS, use in situ techniques to determine the nature of the solid liquid interface of these composite coatings in water and assess the foul release performance of these coatings compared to base PDMS with the objective of identifying key material properties or interaction effects that may contribute to foul release coating performance.

Chapter 2

Summary of key techniques

2.1 Introduction

This PhD utilised a broad range of analytical techniques in order to analyse various aspects of model foul release coatings, for example radically different techniques were required to examine interfacial behaviour in air to water, or to measure bulk diffusion properties or the bioadhesive response. A summary of the key techniques utilised in the project now follows.

2.2 Ellipsometry

Ellipsometry is a relatively simple non invasive optical spectroscopy technique for determining the thickness and optical properties of very thin layers of angstroms to micrometers. A beam of optical light with defined polarisation state is incident on the sample surface, the reflection of this optical beam from the surface is collected and analysed and the change in the polarisation of light upon reflection from the surface is determined, this change allows us to determine information about the reflecting surface, such as optical constants (n and k, the refractive and complex refractive indices and the thin film thickness).

For spectroscopic ellipsometry the polarised light is projected onto the flat surface of the sample as an ellipse which has oscillating components parallel to the surface plane and parallel to the sample surface normal referred to as the 's' and 'p' waves. These waves have a difference between these two oscillating components, δ and an amplitude Ψ which are known as the ellipsometric angles. The light beam

itself is incident on the sample at a fixed and defined angle of incidence ϕ. The reflected beam is also projected from the plane of incidence of the sample at an angle ϕ.

The reflectance of the p-waves and s-waves from the sample surface are measured and can be related to δ and Ψ as

$$\frac{r_p}{r_s} = tan(\Psi)exp(i\delta) \tag{2.1}$$

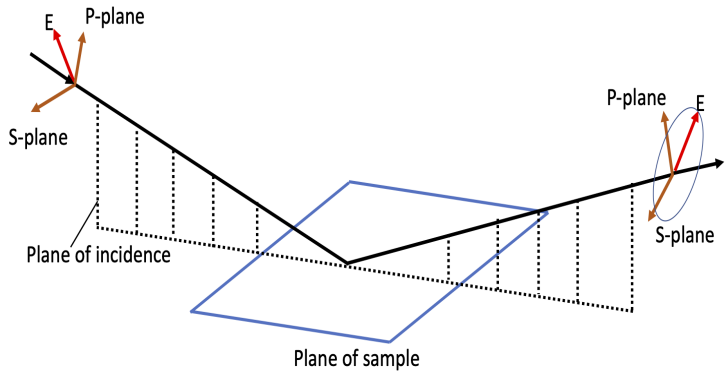

Figure 2.1: Geometry of a typical ellipsometry experiment.

This complex ratio gives the changes in polarisation of light due to the probed sample as depicted in figure 2.1, from this ratio ψ and δ can be inferred. The reflectance of the 'p' and 's' waves are also dictated by the physical properties of the reflecting medium and the optical properties of the sample. For a reflecting sample composed of a single homogenous layer r_s and r_p can be determined using Fresnel's law[45].

$$r_p = \frac{N_s \cos(\phi_0) - N_0 cos(\phi_t)}{N_s \cos(\phi_0) + N_0 cos(\phi_t)} \tag{2.2a}$$

$$r_s = \frac{N_0 \cos(\phi_0) - N_s cos(\phi_t)}{N_0 \cos(\phi_0) + N_s cos(\phi_t)} \tag{2.2b}$$

N_0 is the complex refractive index of the optical medium, typically this air or vacuum in which case this is N_0=1 and N_s is the complex index of refraction (n+ik, where n is the refractive index and k is the complex extinction coefficient) and ϕ_0 and ϕ_t are the incident angle and angle of the component transmitted into the sample respectively.

The incident angle for spectroscopic ellipsometry is kept close to the Brewster's angle for total internal reflection for which the reflected 'p' wave is zero

$$tan(\phi_B) = \frac{N_s}{N_0} \tag{2.3}$$

At this angle, the value Ψ is zero and for δ is a step function from zero to π at this angle. If we imagine there was a thin film intermediate layer with a different refractive index, the effect at the Brewster's angle becomes less sharp, Ψ no longer falls completely to zero and the step function in δ becomes smoother. The perturbation of the Brewster angle effect caused by even very thin layers makes ellipsometry a technique that is highly sensitive to the presence of thin films or absorbed layers on a well characterised optical substrate.

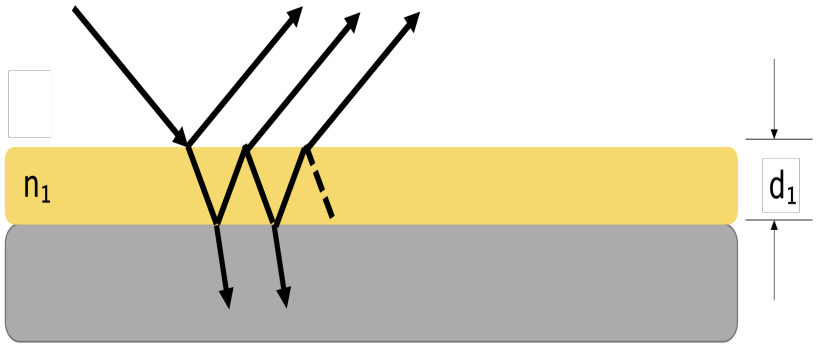

Figure 2.2: Reflection and transmission of light from a sample in air with a thin intermediate layer on top.

Looking again at equation 2.2 and considering the case in which a thin film of thickness d_1 and refractive index n_1 is present between the medium and the sample substrate s as illustrated in figure 2.2. We can consider that light will be reflected from both the top of the thin film and that light transmitted through the

film will then be reflected from the substrate interface, this transmission will be governed by a further set of Fresnel equations but the phase shift β in the overall reflected light as a result of the thin film can be defined as:[46]

$$\beta = 2\pi \left(\frac{d_1}{\lambda} \right) n_1 cos\theta_1 \tag{2.4}$$

where λ is the wavelength of light and θ_1 is transmission angle of light through the film. From this we can see that the phase shift of polarised light can be directly linked to the thickness and refractive index of the film as depicted in figure 2.2.

For modern spectroscopic ellipsometers a range of wavelengths 350nm $<$ λ $<$1000nm of visible are utilised polarised light is reflected off the sample of interest into a pinhole camera and the change in polarisation measured in the form of the ellipsometric angles ψ and δ are determined for each wavelength of light. Effective modelling of samples requires knowledge of the optical properties of the incoming medium (i.e air) and of the substrate, ideally a reflective material like silicon can be used. With the known parameters and information about the phase shift and reflectance from the ellipsometer a best fit for the thickness and optical constants of the thin layer can be obtained.

If the thin film is optically transparent i.e. k is zero throughout the measured optical range, then the thin film can be modelled using a Cauchy function[47] to find its refractive index as a function of λ:

$$n(\lambda) = A + \frac{B}{\lambda^2} + \frac{C}{\lambda^4} \tag{2.5}$$

Where the 3 terms A, B and C are just constants which are varied to find the best fit for the layer.

Ellipsometry is a powerful technique which utilises a phenomenon as simple and non invasive as polarised light to find the thicknesses of nanometer or even angstrom thick films using visible light to probe layers smaller than the optical diffraction limit. The sensitivity and rapidity of this technique which typically takes seconds per measurement allows for real time observations of minute changes in layer thickness or composition. This enabled researchers to find the glass transition temperature of thin sub 100nm polystyrene films by observing a discontinuity in the thermal expansivity of the polymer layer over a heating/cooling cycle[48][49]. It is possible to perform ellipsometry in any transparent media with known optical properties, ellispometric measurements have been conducted in air, water and solvent/solvent vapour and a variety of environmental conditions in the past it has been used to perform *in situ* measurements looking at the adsorption of protein

from solution onto silica [50] and the voltage dependent swelling behaviour of weak polybase brushes in water [51].

2.2.1 Experimental setup

For this project all ellipsometry measurements were conducted using a Woollam M2000V rotating compensator ellipsometer, this allows the ellipsometer to illuminate samples with light of periodically varying polarisation. The Woollam M2000V ellipsometer was set to a fixed incident angle of 70° and uses a 50W Halogen lamp capable of producing light of wavelengths 350-1000nm[52]. Reflected light is collected through a pinhole camera and into an analyser. The intensity of reflected light will vary depending on the polarisation which oscillates periodically due to the rotating compensator. The intensity of reflected light is measured using a silicon photodiode. The oscillation of the intensity of polarised light is determined and the phase shift from initial polarisation used to infer the ellipsometric angles Ψ and δ across the full wavelength spectrum. All data produced by the ellipsometer are fitted using the Woollam CompleteEase software, typically using Cauchy models for the thin film of interest and in built optical models [53] for known materials such as the silicon and silicon oxide substrates to build multi layered models of thin film samples on reflective substrates that could produce model Ψ and δ values that best fit the experimental data.

2.3 Atomic force microscopy

Atomic force microscopy (AFM) is a versatile non invasive technique for examining surface topography and morphology at extremely small, molecular length scales. AFM's operate on a principle similar to a scanning tunnelling microscope but does not require the sample to be conductive or to be coated with a conducting layer. In scanning tunnelling microscopy a cantilever with a sharp tip, usually fabricated from Nickel, is brought into the vicinity of a surface of interest. The tip is scanned across the surface to build up a picture line by line in a manner similar to profilometry but with far higher spatial resolution. With tunnelling microscopy the information about the surface comes from a tunnelling current between the tip and the surface, [54]. In the case of Atomic Force Microscopy, there is no tunnelling current between the probe and the surface and tips are typically fabricated from silicon or silicon nitride. Instead, the force between the surface and the cantilever tip is measured, providing information about the surface topography and material response(viscoelasticity). Atomic force microscopy is capable of imaging samples

with extremely high resolution far blow the optical diffraction limit, because of the nature of the technique maximum sensitivity is dictated by the tip quality but typically a lateral sensitivity of 10nm and a depth sensitivity of 0.1nm can be achieved [55] with more advanced, shaper tips achieving even higher resolution. Atomic Force microscopy has two main modes which operate slightly differently; contact and tapping modes.

2.3.1 Contact mode

In contact mode the tip is rastered across the surface whilst a laser is focused on the cantilever tip with the reflected beam sensed by a position sensitive detector. As the tip crosses the surface, variation in the height of the surface topography will cause changes in the forces between the tip and the surface forcing the cantilever to deflect to an extent dictated by its spring constant k as per Hooke's law. Changes in the cantilever deflection will be detected by the laser and position sensitive detector, a feedback system will then adjust the deflection to maintain a preset value for the cantilever loading force. These changes in deflection and feedback response are used to interpret changes in surface height and build a topographic image of the sample surface[56][57]. A general setup is illustrated in figure 2.3.

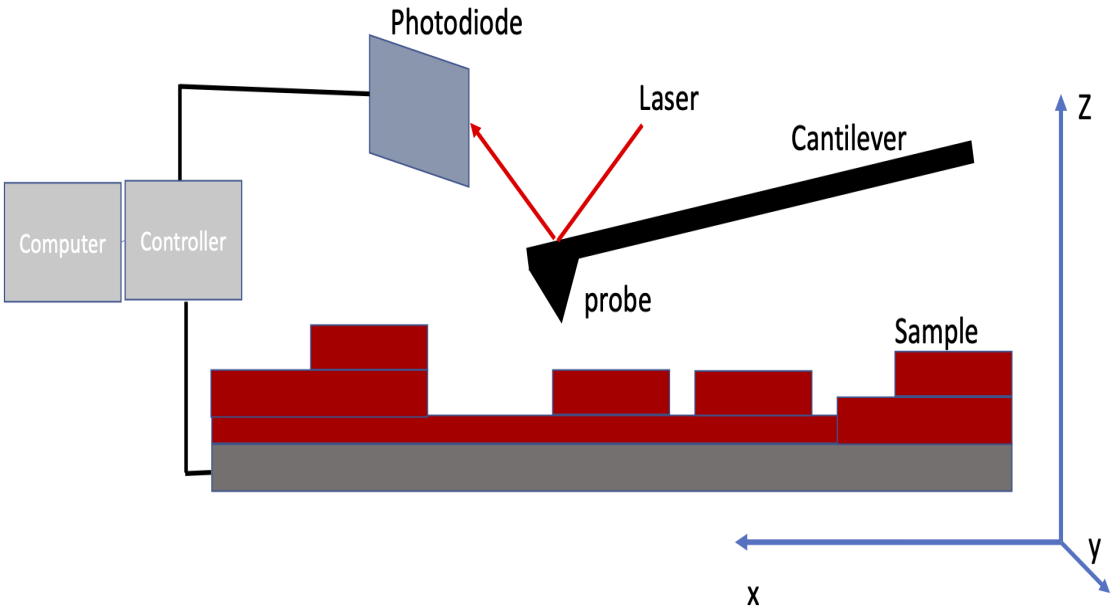

Figure 2.3: Atomic Force Microscope setup

2.3.2 Tapping mode

In tapping mode the cantilever is driven by a piezoelectric crystal resonant frequency (300-350 kHz) near the probed surface so the tip strikes or 'taps' the surface during each oscillation, the amplitude of these oscillations is sufficiently energetic to prevent short range Van der Waals interactions with the surface sticking the tip to the surface upon contact. The laser deflection detection signal monitors the root mean square of the amplitude cantilever oscillations, as the cantilever taps the surface and scans across the the surface as topography varies through peaks and troughs the rms amplitude of the tip oscillations will be perturbed to lesser and greater extents by intermittent surface collisions and a feedback system detects this amplitude shift. An amplitude set-point can be selected which in conjunction with the feedback system will adjust the height of the tip from the surface in order to maintain the desired set-point rms oscillation amplitude. Because the frequency of oscillation is so high this process occurs within fractions of a second at each sampled point. Through this method of height adjustment a topographic image of the surface is developed [58] from changes in the amplitude of oscillation.

Tapping has certain advantages over contact mode. With contact mode the tip is exerting a variable contact force on the surface in contact and as the cantilever rasters laterally across the surface the tip also applies a shear force to the surface. This can result in distortion of the samples made of soft and weakly bound material being eroded by the cantilever [59][60]. Stick-slip effects between the tip and sample features can also cause distortions or artefacts in the resulting images. Contact mode also exerts more stress on cantilever tips meaning they tend to wear down faster. As the tip is only in intermittent contact with the surface in tapping mode the shear stresses and tip sticking effects are minimised therefore reducing tip induced surface deformations[61].

Both these modes can be used to image sample in ambient air conditions without the need for ultra vacuum required for electron microscopy techniques that attain similar resolutions, atomic force microscopy also has the advantage of being capable of operating in liquid [62] allowing for the direct surface characterisation of many liquid processes like the examination of live bacteria cell walls[63] or the real time visualisation of the stimuli response of a pH sensitive brush in situ [64]

2.3.3 Force curve analysis

AFM, in contact mode or tapping mode depends on the displacement of the cantilever due to forces between the tip and the surface. A detailed analysis of the distance of the tip from the surface and the deflection of the cantilever can yield a force distance curve providing information about surface tip interaction forces and the mechanical properties of the surface. During force distance curve acquisition in simple contact mode the piezo drives the z distance of the tip to the surface, with variations in the cantilever deflection collected simultaneously. Tapping mode for force distance curve acquisition performs similarly but instead the cantilever deflection is measured using the rms amplitude perturbation as the tip approaches the surface. Combining force curves with the conventional topography mapping mode a 'force volume map' can be compiled for an area by sampling the force distance curves at selected points as the tip is rastered across the surface in the same manner as the height information is collected.[65]. A recent innovation in force volume mapping is the 'Quantitative imaging' mode developed by Bruker this uses an advanced control system to raster the tip almost as fast as in a typical tapping measurement but ensures that the tip is stationary in the x-y plane during a force indentation measurement[66], this permits the rapid acquisition of force distance curves for every pixel of an AFM image creating rapid, high resolution force volume maps.[67]

Force curves can be obtained in fluid, this removes a problem often found with ambient air force displacement curves in which a surface layer of absorbed water vapour will often disrupt and dominate the true surface tip interactions[68]. Atomic force microscopy has some advantages over other methods of surface force measurement such as the surface force apparatus because it can be performed on the nanoscale with lateral sensitivity of as little a 10nm and requires far smaller forces. With reference to figure 2.4, we should consider precisely how AFM force distance curves measure interactions with the surface; the true interaction force is given by the cantilever deflection δ_c and the spring constant K of the cantilever as per Hooke's law

$$f = -K\delta_c \tag{2.6}$$

However, during the measurement, the distance controlled is not the true sample to tip but rather Z the distance of the sample from the cantilever rest position which is modulated to observe the change in the force on the cantilever as the tip moves towards and then presses into the surface. The sample tip distance cannot be directly measured as it will be altered by both displacement of the cantilever and deformation of the sample surface.[69]

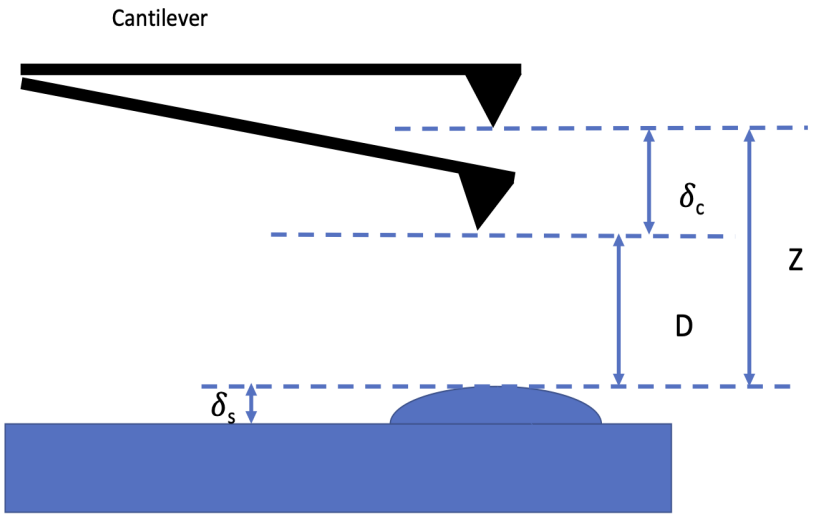

Figure 2.4: Sample tip system in a force distance curve curve measurement, true surface tip distance D differs from piezo height Z due to tip and sample displacements.

A range of important factors can be derived from the force distance curve considering both the approach and retraction components. Tip attraction and the surface adhesion are related to the hysteresis between the loading and unloading force curves and the mechanical properties of the sample such as stiffness and the elastic modulus.The ideal ideal force distance curve and the relevant quantities that can be determined from force distance curves are illustrated in figure 2.5.

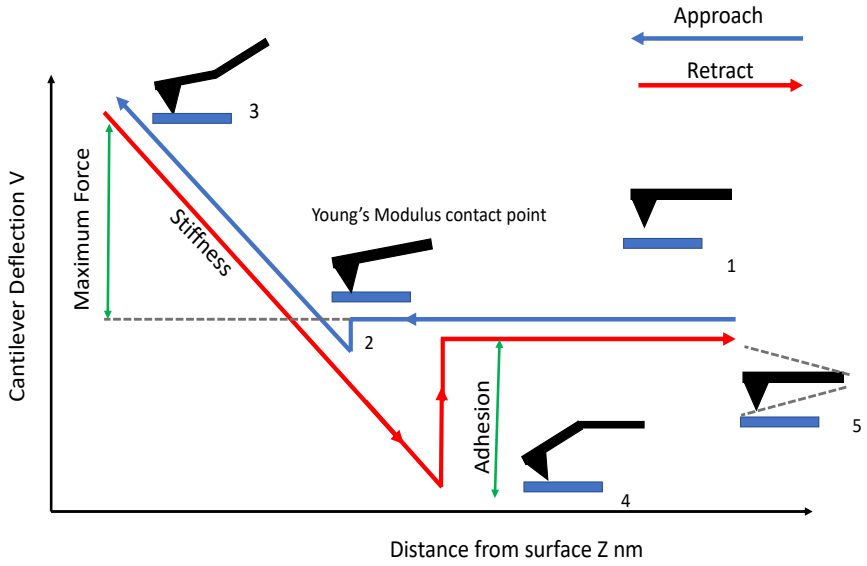

Figure 2.5: Ideal Force displacement curve.

This kind of mechanical analysis can be achieved with AFM but it requires an understanding of the tip geometry and the contact area between the sample and the tip which must be modelled , the earliest and most common model being the Hertz Sneddon model.[70].

The Hertz model is based on the interaction of spheres model, its application to surface tip forces requires a series of somewhat unphysical assumptions; the surface is modelled as a sphere with a radius of infinite curvature, whilst the tip is represented by a finite sphere. The model also assumes interactions are elastic with no adhesion and that the sample is considered rigid and much stiffer than the tip. This last assumption would render the model incapable of determining the elastic modulus of the surface but is corrected in the Sneddon analysis[71] which accounts for the elastic surface deformations, using the unloading force curve the reduced elastic modulus E_r is calculated using the following equation[72]:

$$E_r = \frac{\sqrt{\pi} S}{2\sqrt{A}} \tag{2.7}$$

Where S is the stiffness given by the gradient of the linear unloading curve. A is the contact area of the tip. The area of contact A can be determined using tip calibrations on well characterised surfaces with similar mechanical properties.

Although clearly flawed in it's assumptions, this model has shown itself to be quite effective at modelling the mechanical properties of flat low adhesion surfaces using small indentations. Adhesion values from a curve can be determined independently of the elastic modulus using the area of hysteresis. Hertz Sneddon models have been used successfully to probe the mechanical properties of cells[73].

2.3.4 Experimental apparatus

All in air topographical measurements were acquired using a Bruker Dimension 3100 in tapping mode with TESPA-V2 cantilevers of spring constant 37Nm^{-1} . All standard topographical images were processed using Nanoscope software and analysed with freely available gwyddion software[74]. Some liquid measurements were attempted using the D3100s and an mltc cantilever. All liquid measurements and force distance curves were acquired using the JPK Nanowizard 3 in quantitative imaging mode. Force curves were analysed using the JPK data processing software (JPK DP).

2.4 Neutron reflectivity

Neutron reflectivity was used extensively throughout this project as it is an extremely powerful technique for the analysis of thin films and interfacial states and can be performed under more diverse environmental conditions than almost any other surface analysis technique. This technique is particularly applicable to soft polymeric materials composed of light elements and for the analysis of surfaces in fluids.

2.4.1 Scattering Theory

Whether scattering using x-ray photons or neutrons, the interaction between a scattering particle and a sample surface can be defined by the change in momentum of the scattered particle. The momentum transfer can be described by eq2.4.1

$$P = \hbar k_i - \hbar k_f = \hbar Q \tag{2.8}$$

Where k_i and k_f are the incident and final wave vectors of the scattering particle and $\hbar$ is Planck's Constant in the form $\hbar$=h/2π.

We will consider only the case of elastic scattering in which there is no transfer of energy between the particles, only momentum, in this situation the modulus of

the initial and final wavevectors are equal and the wavelength of the particle is constant as shown in figure 2.6.

$$| k_i | = | k_f | = \frac{2\pi}{\lambda} \tag{2.9}$$

If we consider specifically the neutron as a scatterer we arrive at eq2.10; a neutron incident on the sample will scatter off an atomic nucleus in the sample, the neutrons elastic momentum transfer, Q will be a function of the scattered angle θ. [75]

$$Q = \frac{4\pi sin\theta}{\lambda} \tag{2.10}$$

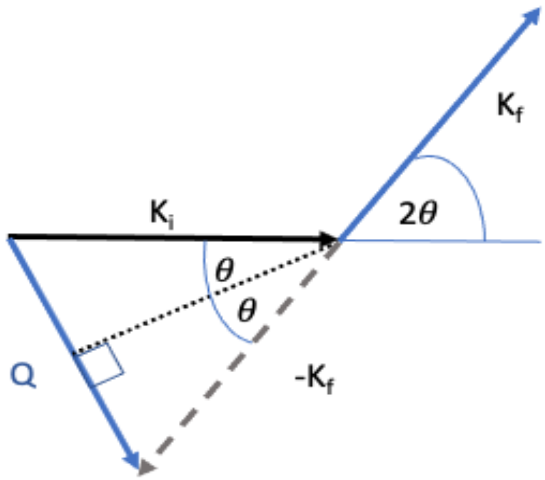

Figure 2.6: Vector diagram for elastic neutron scattering.

For neutrons with a specific wavelength we see that the scattered angle θ is the single variable dictating momentum transfer Q, we can imagine a function f(λ,θ) which determines the likelihood that neutrons of wavelength λ will be deflected in a given angular direction. Generally, for neutrons this function is insensitive to either the wavelength or angle i.e. all angles of deflection are equally as likely for all neutron wavelengths. So this function can be described by a constant.

$$f(\lambda, \theta) = -b \tag{2.11}$$

This constant b is known as the scattering length, this value is specific to the scattering atomic nuclei and will vary (sometimes significantly) between different

elemental isotopes, these values do not follow a simple relation with increasing atomic number. For nuclei with non zero quantum spin even this isotope will have more than one value of b.
Because some nuclei have these multiple scattering lengths the neutron scattering cross section of a nuclei is a summation of the square mean and variance of the scattering lengths, representing the coherent and incoherent scattering cross section

$$\sigma_{tot} = \sigma_{coh} + \sigma_{incoh} \tag{2.12a}$$
$$\sigma_{coh} = 4\pi\langle b\rangle^2 \tag{2.12b}$$
$$\sigma_{incoh} = 4\pi(\Delta b) \tag{2.12c}$$

For the experiments that we have conducted only the coherent scattering will contribute to the signal, the incoherent scattering will contribute to the background.

2.4.2 Neutron reflectivity at interfaces

For specular neutron reflectivity a beam of neutrons of known intensity, with wavelength λ is incident on a flat planar sample at some small grazing angle θ. The intensity of the neutron beam reflected at the same angle is measured and the reflectance is determined as a proportion of the incident beam.

$$R(Q) = \frac{Specular\ intensity\ of\ reflected\ scattering}{Intensity\ of\ incident\ neutron\ beam} \tag{2.13}$$

These measurements can be performed at a range of incident angles or using a range of neutron wavelengths rather than a monochromatic wavelength source which, as per equation 2.10, will vary the momentum transfer Q of the scattering event. From this data a reflectivity R(Q) curve as a function of momentum transfer can be produced. This reflectance curve can be related to the neutron scattering properties of the sample and used to discern key properties of the layer, such as the thickness and chemical composition. If we consider the reflectivity of the sample to be akin to a neutron refractive index [76]

$$n = 1 - \delta + i\alpha \tag{2.14}$$

The imaginary component relates to absorbance, which for most light elements is very low for neutrons and so can be neglected. δ is the significant quantity and can be defined as

$$\delta = \frac{\beta\lambda^2}{2\pi} \tag{2.15}$$

Where β is the scattering length density of the material. The scattering length density is a measure of the bulk scattering of material often composed of molecules of more than one element, this quantity can be used to predict or model the scattering behaviour of the material. The scattering length density can be calculated as:[75]

$$\beta = \frac{\rho N_A}{m} \sum_{K}^{j=1} \langle b \rangle \tag{2.16}$$

m is the mass of the molecule ρ is the molecule bulk density N_A is Avagadro's constant and the expression $\sum_K^{j=1}\langle b\rangle$ is the summation of the coherent scattering lengths of each elemental nuclei making up the material in question (for example in H_2O would be $2b_H + b_O$) Important features of neutron reflectivity that can be determined using this are fringe spacing and the critical edge. For a simple uniform 'substrate only' sample of reflectance n in air (n_0=1) the critical edge is given approximately by

$$\theta_c = \frac{n}{n_0} = n = \left(\frac{\lambda^2}{\pi}\beta\right)^2 \tag{2.17}$$

Using equations2.10 and 2.14 we can find this as a critical edge Q value

$$Q_c = 4\sqrt{\pi\beta} \tag{2.18}$$

For all Q values below Q_c the reflectance will be 1, however it should also be noted that in mediums other than air this can be different specifically mediums with a negative scattering length density such as water will have a neutron refractive index larger than n=1 and so there is no critical edge and the reflectance is never unity.

With an understanding of the scattering length density of a sample through its depth the reflectance can be related to depth through the following equation[77]

$$R(Q) \approx \frac{16\pi^2}{Q^4} \left| \int_{\infty}^{\infty} \frac{d\beta}{dz} e^{izQ} dz \right|^2 \tag{2.19}$$

In the case of a smooth single layer sample eg. pure silicon in air β=0 at z>0 and β_{sil} at z<0. If the sample is perfectly smooth the derivative of β with respect to z is a delta function around 0

$$\frac{d\beta}{dz} = -\beta_s \delta(z) \tag{2.20}$$

Integrating this according to equation 2.19 yields a relation to neutron reflectivity of

$$R(Q) \approx \frac{16\pi^2 \beta_s^2}{Q^4} \tag{2.21}$$

This is invalid for the low Q region close to the critical edge but at high Q reflectivity would be expected to reach this constant linear relation with respect to Q^4. Although, in reality an interface is almost never perfectly smooth and the surface roughness between interfaces is described by a gaussian σ_r, the large Q reflectivity is instead:

$$R(Q) \approx \frac{16\pi^2\beta_s^2}{Q^4} \times exp\left(-\sigma_r^2 Q^2\right) \tag{2.22}$$

So the more diffuse an interface the more the reflectivity will decay compared to its smooth ideal counterpart.

Going beyond a simple 1 layer case and considering additional layers of reflection we will see the effect of fringe spacing in reflectivity curves. A sample measured in air with a single smooth (discounting roughness) layer of scattering length density β_1 with a thickness L on a substrate β_s has a depth profile with two discontinuities

$$\beta(z) = \beta_s \ for \ Z < -L \tag{2.23a}$$
$$\beta(z) = \beta_1 \ for \ -L < z < 0 \tag{2.23b}$$
$$\beta(z) = 0 \ for \ z > 0 \tag{2.23c}$$

Here the gradient of $\frac{d\beta}{dz}$ is non zero at two points z=0 and z=-L and is described by a pair of delta functions[75]

$$\frac{d\beta}{dz} = (\beta_1 - \beta_s)\delta(z + L) - \beta_1\delta(z) \tag{2.24}$$

Integrating this expression across all space yields

$$\int_{\infty}^{\infty} \frac{d\beta}{dz} e^{izQ} dz = (\beta_1 - \beta_s)e^{iLQ} - \beta_1 \tag{2.25}$$

Inserting this into equation 2.19 and converting exponential expressions into cosines via trigonometric identities the reflectivity Q space relation is now described by [77]

$$R(Q) \approx \frac{16\pi^2\beta_s^2}{Q^4} \left[\beta_1^2 + (\beta_1 + \beta_s)^2 - 2\beta_1(\beta_1 - \beta_s)cos(LQ)\right] \tag{2.26}$$

Finally, by inspecting the cosine relationship between reflectivity and the thickness L of the intermediary layer 1 it is clear that there will be a sinusoidal variation in the reflectivity with Q, which will have the appearance of repeating fringes in

the reflectivity curve, known as Kiessig fringes. The period of this oscillation in reflectivity is related to the thickness of the sample layer L by the equation

$$\Delta Q = \frac{2\pi}{L} \tag{2.27}$$

Equations 2.27 and 2.26 demonstrate the kind of key information that can be derived from neutron reflectivity of samples with multiple layers. The fringe spacing can be invaluable for determining the thickness of a layer or observing the change in layer thickness subject to environmental conditions like thermal expansion due to temperature changes [78]. This fringe spacing also provides us with a critical understanding of the sensitivity and limitations of neutron reflectivity; the fringe spacing effect described is shown with respect to momentum transfer Q but for most neutron reflectivity experiments Q is measured in inverse Angstroms and depending on the neutron wavelengths or angle θ available at the particular reflectometer most measurements of reflectivity are collected over a Q range of $0.0002\mathring{A}^{-}1 < Q < 0.35\mathring{A}^{-}1$ converting to real space we can see this range is able to resolve fringes for layers as thin as a few nanometers making it ideal for the analysis of ultra thin polymer films [79]. However, we also see that there is a real limit in the thickness of layers that can be resolved with reflectivity as L increases ΔQ decreases so fringes will become smaller and smaller becoming impossible to resolve for most current instruments. Generally the total thickness of a sample for neutron reflectivity is limited to less than 400nm[80].

Looking again at equation 2.26 we can see that the amplitude of the Kiessig fringe oscillations is given by $2\beta_1(\beta 1 - \beta_s)$ therefore these oscillations become more pronounced the greater the scattering contrast between the two layers is.

With an understanding of the critical edge, Q^4 decay at large Q and fringe spacing relation to layer thickness it should now be clear how sensitive neutron reflectivity curves are to the SLD depth profile of the probed sample. Analysis of reflectivity curves enables the modelling of a layer by layer SLD depth profile for the sample that can provide invaluable information such as the presence of interface enrichment or the segregation of material components in a polymer blend[81][82]. The versatility of this technique is a real asset to interface and material analysis because the scattering neutrons are generally weakly interacting with light elements so measurements are usually non-destructive to samples and can be performed in a variety of fluid or vapour conditions.

Besides thickness, the other primary limitation of neutron reflectivity is the requirement for sufficient scattering contrast between materials of the scattering medium to observe clear reflectivity features. This can sometimes be a challenge when using polymers as many hydrocarbon based polymers have very similar scattering length densities, so differentiation between blends of polymers can

be challenging. When performing neutron experiments with water or with polymers, deuteration can be harnessed to create contrast; a hydrogen nucleus and the deuterium nucleus have radically different scattering lengths b_H=-3.74fm, b_D=6.67fm [83]. Methods of deuteration that replace hydrogen nuclei in the polymer chain with Deuterons can change the scattering length density. This will improve scattering contrast, allowing the differentiation of otherwise very similar chemical groups[84]. Water has an SLD β_{H_2O}=-0.55x$10^{-6}\mathring{A}^{-2}$ and D_2O β_{D_2O}=6.335x$10^{-6}\mathring{A}^{-2}$, because samples in H_2O will not have a critical edge, D_2O is the most common choice for liquid measurements. However, utilising both these liquids will allow for the acquisition of neutron scattering in liquid using multiple contrasts to aid fitting. Further, it is trivial to mix quantities of D_2O and H_2O to create a water mixture with intermediate scattering length density. This approach can be used to contrast match the water to specific materials in the sample such as the substrate, so there is no contrast between the substrate and medium at which point the reflectivity profile arises only from the interfacial layer allowing better characterisation of small surface adsorbing molecule like surfactants[85].

2.4.3 Neutrons: spallation and reactor sources

The primary limiting factor for neutron reflectivity is the need for a source of neutrons, this requires advanced infrastructure that is usually the preserve of national and international research centres with only a handful of universities having the capability to run neutron sources themselves. Neutrons are produced one of two ways via a reactor or a spallation source. Reactor sources use uranium to produce neutrons as a byproduct of nuclear fission. These sources produce neutrons at a constant flux which are thermalised by moderation (slowed down via collisions with a moderator often heavy water or graphite). Spallation sources operate by accelerating protons with electric fields to high energies in synchrotron rings before colliding them with a heavy element target. This collision causes neutrons and other subatomic particles to be ejected from nuclei in the target in a process called spallation. Because of the manner in which protons have to be accelerated and then discharged into the target, the resulting neutron flux is not constant in spallation sources but is instead pulsed.

2.4.4 Reflectometers; monochromatic and time of flight modes

Three reflectometers were used during this project D17 and SuperAdam at the ILL in France and OffSpec at the ISIS neutron source at the Rutherford Appleton

laboratory in the UK. The ILL is a reactor source whereas at ISIS neutrons are produced via spallation. Despite this both Offpsec and D17 can operate in time of flight mode. In this mode the wavelength of incident neutrons are determined via the time of flight from a common starting point to the detector(for D17 the wavelength range is $2\mathring{A} < \lambda < 27\mathring{A}$ and for OffSpec the range is $1.5\mathring{A} < \lambda < 14.5\mathring{A}$). This is simple to determine with a spallation source as neutron flux is already pulsed, the incident neutrons were all born at the same time when a packet of protons were fired at the neutron target. At D17 the flux is constant so neutrons have to be artificially pulsed using a series of choppers obstructing the neutron beam. The advantage of time of flight detection is that it allows the collection of reflectivity for a large range of Q values simultaneously, data point may have high uncertainty but it is possible to acquire an entire reflectivity curve in a minute or less allowing for the measurement of rapid kinetic processes[86].

For SuperAdam reflectivity is obtained by using a monochromatic neutron beam of constant wavelength ($5.21\mathring{A}$) and instead changing the angle of the detector θ to obtain values of reflectivity across the Q range. The control of angle means it is possible to achieve uniform high resolution in data points out to the highest Q values, a challenge for time of flight. However monochromatic sources cannot perform kinetic measurements as each R(Q) value is collected individually and the detector arm has to be physically moved from angle to angle to vary the Q value for which reflectivity is collected.

All reflectivity data was analysed using the GenX reflectivity software or the motofit plugin for igor pro wavemetrics software.

2.5 TOF-SIMS

Time of Flight Mass spectrometry (TOF-SIMS) is a surface analysis technique that can enable the identification and differentiation of elements, molecules or signature functional groups via mass spectroscopy. As illustrated in figure 2.7, this technique makes use of an ion beam which is incident on the sample surface. The primary ions of the incident beam have low energy typically in the 0.1-20 keV range and low penetration power interacting almost entirely with top 2-3 nm of the surface. When these charged ionic particles collide with the surface they will interact strongly and induce monatomic ions or charged molecular fragments to break off the sample as secondary ions [87]. The charged ions can have variable kinetic energy but these escaping charged fragments can be collected by an electric field and their mass spectrum determined by time of flight spectroscopy.

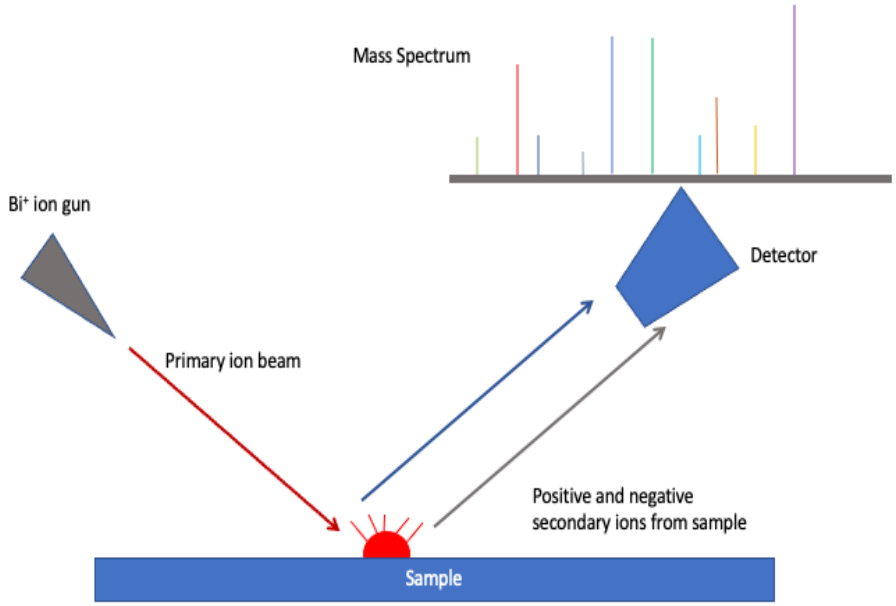

Figure 2.7: Schematic of a typical TOF-SIMS setup.

The intensity of secondary ions produced is given by the equation[88]:

$$I_s^x = I_p C_s S \gamma F \tag{2.28}$$

Where I_s^x is the current of secondary ions of a species, x I_p is the current of primary ions incident on the sample C_x is the concentration of the species x in the sample, S is the sputter ion yield of x, γ is the ionisation efficiency (the probability of species x forming charged ions under bombardment from primary ions) and F is a factor related to the transmission of the analysis system.

We can see that the current of secondary ions of this species will therefore be directly proportional to the concentration of species x in the probed sample, thus analysing this current can allow qualification of the surface concentration of various molecular species. Typically SIMS ion analysis is done using either a quadropole or a time of flight analyser as in TOF-SIMS. Quadrupoles are more limited in the ion mass range they can examine and the sensitivity at which they can distinguish different atomic masses[89]. In time of flight mass spectroscopy ion mass is determined by focussing secondary ions produced through a linear drift space of known length in which they are subject to a static electric field, in this field ions are subject to acceleration due to electrostatic attraction/repulsion.

The energy gained by the ion travelling through this field is proportional to the strength of the field and it's ionic charge $EZ = \frac{1}{2}mv^2$, this accelerating drift tube is setup such that the kinetic energy gained from the electric field dominate over the initial ions initial kinetic energy so ions of the same charge will leave the drift space with the same kinetic energy. Upon leaving the first drift space they enter a second, field-less drift space of known size at the end of which is a charge detector. The time for ions to cross this space is measured and the charge determined at the time ions are incident in the target. Having measured the charge of the incident ion its kinetic energy gained in the accelerating electric field can be calculated and knowing the time of flight in the second drift space, the mass of the ion can be determined as:

$$m = 2zU\frac{t^2}{d^2} \tag{2.29}$$

With mass m for the fragment found from equation 2.29, ionic charge z and accelerating electric field U, time of flight t and field-less drift tube length d.

With high time of flight spectrometry it is possible to identify a large range of mass fragments and with high sensitivity. With this form of ion induced fragment mass spectrometry specific species (molecules or elements) can be identified from high count mass fragments which correspond either with specific monatomic ions present in the sample (eg. surface fluorine or oxygen found in PDMS silicone would result in a series of secondary ions with mass 19u and 16u respectively) or with specific identifiable molecular fragments associated with the molecule or polymer. For example Polyethylene terephthalate (PET) SIMS spectra have been shown to have mass peaks at 193 u which is associated with the atomic mass of the polymer repeat unit [90] but SIMS spectra also show significant ion currents for identifiable sub fragments of the polymer as well, such as the benzene ring in the repeat unit yielding a peak at 77 u corresponding to $C_6H_5^+$. Consequently, SIMS is a powerful surface analysis technique capable of identifying different materials on a surface based on both the elemental composition at lower atomic masses and also from molecular structure, thus this technique is capable of differentiating materials even if they are made of the same elements, making SIMS highly complimentary to XPS surface analysis.

One particularly advantageous aspect of this ion beam technique is that the ionising beam can be focussed to a specific region rather than used to illuminate the entire sample. If the primary ions are incident on a small area then the resultant secondary ions will only originate from this localised region of the surface. By treating a larger probed surface in this way and rastering the primary ion beam across the scanned area, mass spectrometry from induced fragments can be found 'pixel by pixel' producing a 2-d intensity image mapping different key mass fragments with good resolution even at magnifications as low as 300x300μm . This

mass spectra imaging can enable the determination of the elemental or molecular composition of surface structures on a surface and the spatial distribution of different components of a composite surface. This has been used to great effect to probe heterogenous surfaces and their performance such as examining protein adsorption on a patterned polymer microassay [91] or using fingerprint residues such as surfactants to build to reconstruct a fingerprint on metal surfaces using mass spectrometry[92] [93]

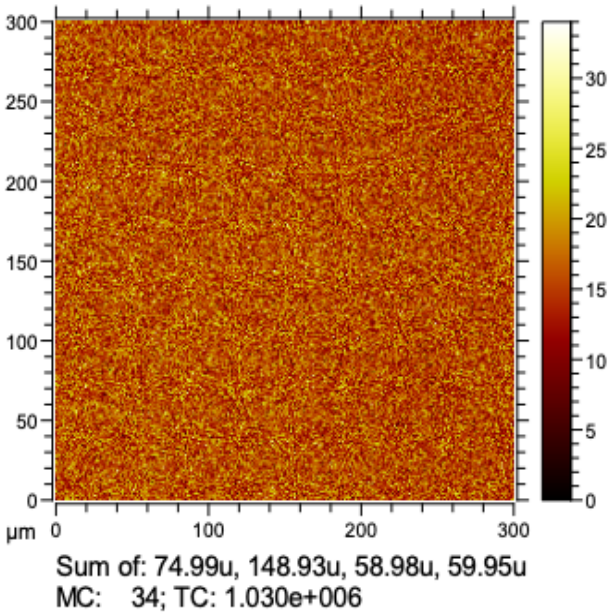

Figure 2.8: TOF-SIMS 300μm x 300μm image for a PDMS surface showing combined ion currents for PDMS associated mass fragments.

Figure 2.8 shows the measured SIMS distribution of PDMS mass fragments across a PDMS surface, perhaps unsurprisingly this distribution is very uniform but does illustrate the potential for mass spectra imaging for the identification of different molecular species on the surface as will be demonstrated in later chapters.

Because the TOF-SIMS method requires the direct measurement of charged ionic mass fragments the effective surface depth probed is quite small as secondary fragments produced at depth have poor penetrating power and are much less likely to escape the sample and reach the mass spectrometer, this limitation arguably

improves the utility of the technique for surface analysis as information from the bulk of the sample in the form of ions will not crowd out the surface signal. The surface limitation of this technique can be mitigated with the use of an ion milling source to perform depth profiling TOF-SIMS by physically etching away the top surface and performing SIMS measurements layer by layer to build up a profile[94]. Similarly the successful extraction of these fragments requires samples be probed under ultra high vacuum (UHV) conditions. Thus surfaces at liquid interfaces cannot be examined using this technique.

All images presented in this thesis were produced with the aid of the surface science analysis centre at the University of Sheffield using the TOF SIMS 5 system using a Bi cluster source to produce primary ions.

2.6 X-ray Photoelectron Spectroscopy

X-ray photoelectron Spectroscopy (XPS) is another surface sensitive analysis technique similar to TOF-SIMS but whereas SIMS can provide detailed image maps of the intensity of different mass fragments XPS can be used to determine the overall elemental composition and elemental concentration of a surface.

The principle of XPS relies on the photoelectric effect first theorised by Einstein [95]. When a photon of light is incident on atom, photoemission of an electron from an atomic orbit can occur provided the photon has high enough frequency ν and therefore sufficient energy given by hν, Planck's constant$\times$Frequency, to overcome the binding energy E_B of the electron. When this occurs the ejected electron will have a kinetic energy equivalent to the difference between the energy of the incident photon and the electron binding energy.

$$E_k = h\nu - E_B \tag{2.30}$$

In XPS, the surface of interest is exposed to incident X-rays of a fixed and known frequency ν. These are produced using a cathode to anode vacuum tube which accelerates electrons to high velocities before colliding with the metal target anode, when these high energy electrons collide with the metal atoms of the anode, they can induce inner shell ionisation, in which electrons are lost from inner electron energy levels of the atomic structure[96]. Electrons from a higher electron shell will then fall into this inner energy level vacancy, generating a photon with energy equivalent to the difference between the two electron states. Only some transitions are possible as the transitions between certain energy levels would violate quantum number conservation. When this inner ionisation occurs from the innermost energy level of the atom known as the 'k' shell and an electron collapses into this

vacancy from the second most inner most energy level defined as the 'l' shell, the resulting photons from this atomic ionisation are known as a kα photons. These kα events are typically high energy photons in the x-ray frequency range and are known as characteristic x-rays because the photo-emissions are characteristic of the target atom, with the generated x-rays having strictly defined frequency as a result of the strictly defined, quantised electron atomic energy levels. The metal used in the anode of the vacuum tube dictates the frequency and energy of the Kα x-ray photoemission with different metal anodes producing characteristic x-rays of differing energy. Although other transitions are also possible such as β transitions when electrons from the third electron shell fill the vacancy in the 'k' shell, the overall frequency of these inner ionisation events are low and the Kα x-ray photoemission is typically several times more intense than other possible emissions so the resulting x-ray beam can be treated as broadly monochromatic.

As depicted in figure 2.9 When these monochromatic x-rays are incident on the sample surface, photoelectrons are emitted from the surface and then detected, with the kinetic energy of emitted electrons analysed using electrostatics.

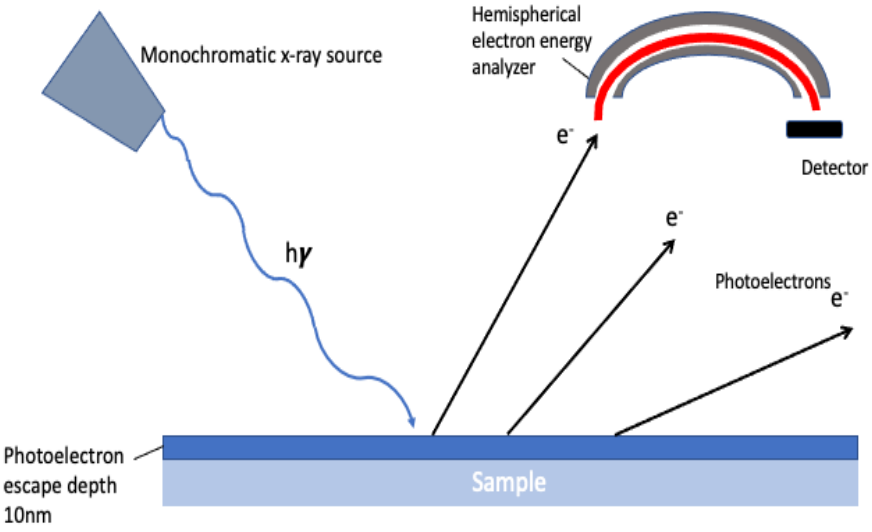

Figure 2.9: Schematic of typical XPS system.

With known incident x-ray and calculated electron energies it is quite sim-

ple to infer the original binding energy E_B of a photoelectron as per equation 2.30.

These binding energies are characteristic of the atomic core level transitions for individual elements allowing XPS to be utilised to detect the presence of different elements in the sample surface. Typically, photo emission of the outer electrons of the atom with low binding energies are not useful as these photoelectrons often have energies similar to the x-ray excitation energy and are hard to differentiate between elements. Instead, core level electron emissions from higher binding energy inner electrons produce well defined strong peaks that can be used as signatures for specific elements such as the Oxygen which is identified by its 1s innermost electron energy level with a binding energy of 543.1 eV in it's natural form.

2.6.1 XPS spectra

A typical XPS spectra contains a number of features which can be analysed to elucidate more information about the sample surface composition.

The first feature to be considered is the characteristic sample background, this results from scattering interactions between photoelectrons and the surrounding material as they escape the surface and reach the vacuum/detector, this can cause significant energy losses such that the calculated binding energy of these detected photoelectrons will be higher than the original energy core level transition which produced them[97]. If we imagine a typical XPS spectra comparing photoelectron counts per second against electron binding energy, the broad range of energies of these inelastically scattered photoelectrons will result in a 'saw tooth' like appearance with a larger background at the higher energy side of each core level peak than below this binding energy. This must be accounted for when fitting a baseline to determine peak intensities[98].

Core level peaks in XPS spectra are usually distinctive and strong but also broad and can contain additional information about a sample and it's atomic and molecular structure as well as simply demonstrating the presence of the element associated with the binding energy. For example a polymer like polymethyl methacrylate (PMMA) contains oxygen and carbon in different functional groups and bonding states and the atoms in these different chemical bonds have slightly different electron core binding energies, the O 1 binding energy for the C-O-C and C=O bounds being 533.5eV and 532.2eV respectively [99]. With a sufficiently sensitive electron analyser it is possible to detect and distinguish the contributions of both binding states to the XPS peak, in this way it is possible to identify the potential molecular confirmation of detected elements, or if the components of the

system are known distinguish clearly between elemental signals that correspond to the same atom in 2 or 3 different molecules such as silicon whose Si 2p core electron spectra can distinguish between silicon in PDMS silicone and silicon in it's base form.

Auger electrons are also produced during sample excitation and often feature in the XPS spectrum, although for the purposes of XPS analysis are generally discounted. Auger electron emission occurs as a result of secondary processes cause by photoelectron emission; if an electron is liberated from an inner core shell and ejected from the atom it leaves a vacancy or electron hole in the electron energy structure. Electrons in higher energy outer shell states then fall into this lower energy hole state, releasing energy characteristic of the difference between the quantised energy levels. This is often released via photoemission of an x-ray in a manner similar to the generation of the primary characteristic x-rays but in the Auger process this energy is instead transferred directly to another electron in the same energy level, this energy transfer is sometimes sufficient to liberate the electron producing Auger Electrons. Auger electrons will have kinetic energies determined by their binding energy and the energy transfer given by the initial and final energy levels of the relaxing electron. These factors are intrinsic to the specific atomic element and it's bonding state and wholly independent of the energy of incident x-rays. Electrons generated by the auger process can be detected alongside photoelectrons and form broad but much less intense, anomalous peaks in the XPS spectra. Although not useful fo XPS analysis by varying the x-ray wavelength it is possible to derive information from the Auger electron yield, for example as a method of X-ray absorption edge fine structure (NeXafs) spectroscopy, that can provide information about surface bonding states. Some more sophisticated synchrotron associated XPS spectrometers provide dual XPS/NeXafs capability[100].

XPS spectra can be quantified, taking the intensity of fitted spectra peaks for core level emissions for specific elements in order to determine the relative surface composition based on the preponderance of each element. For each given peak the number density of the element can be inferred from the measured intensity:

$$I(i) \propto \int_0^\infty N(i) exp\left(\frac{-\zeta}{\lambda \cos\theta}\right) d\zeta \tag{2.31}$$

with I(i) is the intensity of photoelectrons, N(i) is the number density of the element in the sample surface, λ is the electron mean free path and ζ is the path length of the photoelectrons taken before escaping the sample surface, with the angle θ being the angle at which photoelectrons are emitted relative to the normal of the surface. The proportionality is mediated by determinable factors such as

the analyser transmission function and the ionisation cross section for the atom and energy level. We can see from this equation that intensity falls exponentially as ζ increases, confirming the surface sensitive nature of this technique; electrons have limited penetrating power photoelectrons induced deeper into the surface than 10nm rarely escape the surface and are functionally undetectable using this method.

For typical XPS analysis a relative surface density of elements is determined by normalising the measured intensity for each element peak by a sensitivity factor for the given element and transition for the incident x-ray [101] comparing the normalised intensity yields a measure of surface atomic composition.

2.6.2 Limitations of XPS

An operational consideration for this technique is the risk of charge loading over long term x-ray exposure. For bulky insulating samples, x-ray photoelectron ionisation events can result in a build up of positively charged ions in the sample which are not neutralised. Consequently surface photoelectrons experience an electric surface potential as they leave the transit to the detector causing them to decelerate before they are analysed, this can cause the measured electron binding energies to be shifted to greater than their true values over time[102]. This can be mitigated for thin samples by coating the sample on a conducting substrate such as gold, to reduce charge buildup or in the case of bulkier samples by the employment of charge neutralisation devices which pump low energy electrons back into the sample to keep overall charge balanced[103].

One key limitation of XPS surface analysis is the inability of the technique to reliably detect either hydrogen or helium photoelectrons. Although helium is a noble gas which is rarely present in a solid surface unless specifically implanted, the insensitivity to hydrogen is a more severe limitation as hydrogen is present in many organic and polymeric materials that require surface analysis. This means all surface composition measurements represent the only the elemental ratios of the non hydrogen fraction of the surface. Two factors limit the detection of hydrogen in XPS; the comparatively small ionisation cross section for photoemission in hydrogen for typical XPS x-ray photon energies [104] meaning the likelihood and frequency of photoelectron emission is much lower for hydrogen atoms than for most elements. The other limiting factor is the lack of inner electron levels for hydrogen which possesses only one, valence band electron so the spectra of emissions that do occur will overlap with the spectra of valence photoelectrons from other elements making them very difficult to distinguish[105]. The scattering cross section for photoionisation is higher for hydrogen using lower energy ultraviolet

photoelectric spectroscopy. Further, it's recently been shown that XPS spectra could be obtained for gaseous hydrogen on a surface using very brilliant x-ray sources such as a synchrotron radiation source, where the significantly increased x-ray intensity increases the intensity of photoionisation events[106].

Finally, most lab top XPS systems require ultrahigh vacuum conditions in which to operate so surface response to environmental or interfacial conditions such as pressure, humidity or water adsorption cannot be directly measured in situ. This has changed somewhat with the rise of ambient pressure XPS systems. These instruments often require synchrotron x-ray sources but have been able to perform XPS studies at ambient pressure and humidity. AP-XPS even permits the use of thin water jets to coat sample surfaces, examining the adsorption of water onto selected self assembled monolayers[107] or thin film polymer surfaces[108]

2.6.3 XPS setup

All XPS measurements were performed with the assistance of the University of Sheffield's surface science analysis centre (SSAC) on the Kratos Axis Supra system using a monochromatic Al Kα x-ray source, this system is equipped with charge neutralisation system and an argon gas ion source that enables ion milling enabling layer by layer XPS depth profiling.

2.7 Quartz Crystal Microbalance with dissipation monitoring

Quartz Crystal Microbalance/with dissipation monitoring (QCM/QCM-D) is a very powerful technique for detecting very small changes in sensor mass or viscoelastic response in real time in range of conditions and sample environments; air gas or liquid.

Quartz is a crystalline form of silicon dioxide (silica) and a piezoelectric material meaning that when subjected to a voltage the crystal will deform, for piezoelectric materials the inverse is also true; when subject to pressure or deformation they produce an electric field. This phenomenon is seen in a variety of materials but is most common in crystals as it requires an ordered and orientated structure lacking in centro-symmetry. If a material is well ordered with large crystal domains with defined growth axes, the electrical dipoles of the molecules in the crystal structure are highly orientated. A deformation in the crystal structure caused by mechanical stress will cause a generalised reorientation of dipole moments between molecules

causing shifts in charge density and the generation of an electrical potential[109]. Using the 'converse' piezoelectric effect by applying a voltage to a piezoelectric crystal a change in the electric dipoles in the crystal structure will cause small but consistent changes to the material volume, with a well characterised crystal piezo it is possible to cause a defined and controlled deformation of the crystal corresponding to a known applied voltage.

If an alternating current is applied to a piezoelectric material like quartz it will induce periodic oscillations of known amplitude due to the periodic change in voltage. For QCM metal electrodes are deposited on both sides of thin discs of quartz crystal (typically in the form of a gold coating) which have been 'AT' cut along an axis offset 35° from the crystal z-axis[110]. This cut is selected as it determines the mode of crystal vibration and for quartz cut in this crystal orientation, induced oscillations occur in a shear mode through the thickness of the crystal, as shown in figure 2.10. These crystals have a fundamental vibrational mode for which the highest amplitude of oscillation can be achieved, an alternating current is applied to drive the crystal to this fundamental frequency f.

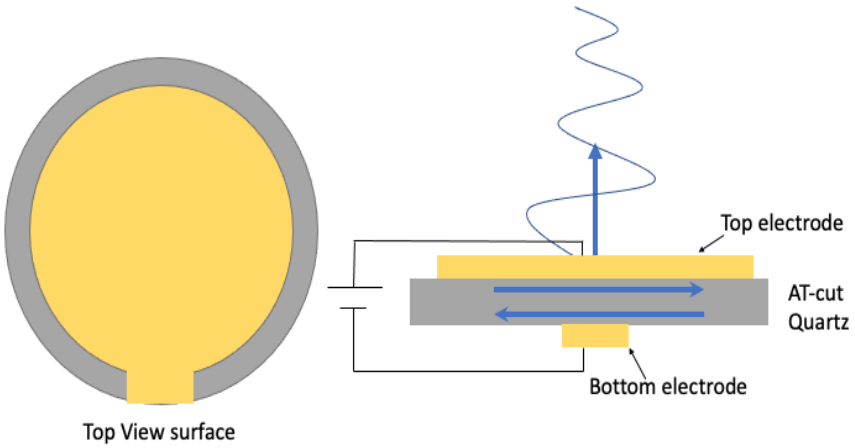

Figure 2.10: The Quartz crystal microbalance.

The fundamental frequency of oscillation is highly sensitive to changes in crystal mass and these small shifts in frequency can be used to determine small changes in crystal mass via a relation first identified by Sauerbrey[111]:

$$\frac{\Delta m}{A} = -\frac{\Delta f}{2nf_0^2}\sqrt{\rho_q \mu_q} \tag{2.32}$$

here the change in areal mass $\frac{\Delta m}{A}$ of the crystal depends on the fundamental frequency of the crystal f_0, the change in frequency Δ f, the mode of oscillation n(n=1,3,5...) and the density ρ_q and shear modulus μ_q of crystal cut quartz . For a typical AT cut quartz crystals several of these quantities are known; the density of quartz ρ_q= 2651 kg m$^-$3 and the shear modulus μ_q=2.95x10^{10}Nm^{-2} [112] for a crystal with a fundamental frequency f_0=5MHz this equation can be simplified to:

$$\frac{\Delta m}{A} = -\frac{C_{QCM}}{n}\Delta f \tag{2.33}$$

where the constant C_{QCM} is 17.7g cm^{-2}Hz^{-1} at f_0= 5MHz. This highly versatile equation has been used to sense the gas sorption of solvent vapour onto quartz sensors with nanogram sensitivity[113].

Although valuable, the Sauerbrey equation has limitations and is only valid in the following conditions:

- The adsorbed mass is evenly spread across the whole sensor surface,
- The adsorbed mass can be modelled as a rigid layer even under the oscillating shear of the crystal,
- The mass is far smaller than the overall mass of the QCM crystal,

The QCM technique can be used in liquids as well as in air [114] though the presence of liquid does have a damping effect on oscillations so the initial resonance frequency of the bare crystal will be different thus the resonance of the crystal in the liquid must be found before any mass uptake measurements can be performed, the frequency shift caused by a damping liquid of density ρ_{liq} and viscosity η_{liq} has been determined by Kanazawa as[115]:

$$\Delta f = -f_0^{\frac{3}{2}}\left(\frac{\eta_{liq}\rho_{liq}}{\pi \mu_q \rho_q}\right)^{\frac{1}{2}} \tag{2.34}$$

Typically, if the mechanics of interest occur in liquid such as protein adsorption from solution, the crystal resonance would be found first in liquid and then adsorbed masses could be related to further changes in frequency by the Sauerbrey equation. However, many adhered adhered layers in liquid like heavily hydrated polymer films [116] or polymer brushes demonstrate viscoelastic behaviour, their oscillations do not couple fully with those of the quartz crystal, failing to meet the conditions for which Sauerbrey analysis of the layer mass will be valid[117].

A valuable addition to the QCM system that can help identify viscoelastic films is dissipation monitoring (the D in QCM-D), dissipation represents the inverse of the Q factor of the oscillations; the loss of oscillation energy per cycle $E_{dissapated}$, normalised by the maximum energy stored at the resonant frequencyE_{stored}.[118]

$$D = \frac{1}{Q} = \frac{E_{dissapated}}{2\pi E_{stored}} \tag{2.35}$$

Dissipation losses are greater the more an adhered layer deforms during oscillation, so for rigid, Sauerbrey valid layers dissipation is small. But for softer, viscoelastic layers dissipation can increase quite significantly. Another indicator that QCM-D response is not in the Sauerbrey regime is if different crystal harmonic resonances n, yield radically different normalised frequency shifts; $\frac{\Delta f_n}{n}$ should be similar at each measured harmonic. For Sauerbrey films, the mass adsorbed should be derivable with equation 2.33 using any harmonic frequency so if the calculated mass for each overtone is not in strong agreement then the equation cannot be valid for the adhered film.

2.7.1 Modelling viscoelastic layers

Although for softer adhered layers the Sauerbrey model breaks down, alternative methods for modelling the mass of viscoelastic layers have been developed using the dissipation and frequency from shifts observed at multiple overtones.

A viscoelastic layer will have its own shear modulus distinct from the quartz crystal and will deform during oscillation. Viscoelasticity is a term that describes the behaviour of materials that have both viscous and elastic responses to an applied stress. Whilst an elastic material will have a Hookean linear strain deformation ϵ to an applied stress σ relative to its elastic modulus E. A viscous material like a liquid will deform continuously when a stress is applied with time dependent material strain related to the stress applied by the material viscosity η

$$\sigma = E\epsilon_{elastic} \tag{2.36a}$$

$$\sigma = \eta\frac{d\epsilon_{viscous}}{dt} \tag{2.36b}$$

Viscoelastic materials like polymers combine both these responses to stress exhibiting behaviours like creep, in which a material initially gives an elastic strain response to an applied constant stress but will then experience a further time dependent strain for as long as the stress applied. Models of viscoelasticity try to incorporate both the viscous and elastic together in a manner that best describes a material's response to stress, these models are often visualised in the standard

linear model a form of pseudo electric circuits composed of Hookean springs and dashpots; dampers used to measure viscous friction. These are used to represent different combinations viscous and elastic strain that represent the viscoelastic behaviour.

The model of interest for QCM-D is the Kelvin-voigt model of viscoelasticity shown in figure 2.11. The standard linear model depicts Kelvin-Voigt materials with a spring and a dashpot aligned in parallel such that the components experience the same strain and the overall stress is the summation of the stress experienced by both components.[119]

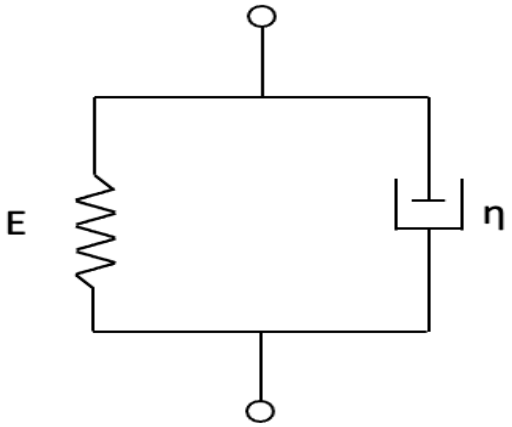

Figure 2.11: Standard Linear model for Voigt viscoelasticity.

$$\sigma = E\epsilon_{elastic} + \eta\frac{d\epsilon_{viscous}}{dt} \tag{2.37}$$

Using this viscoeleastic model Voinova et al were able to formulate a model for the QCM frequency response caused by viscoelastic layers by relating the change

in frequency to layer density, viscosity and thickness [120][121]:

$$\Delta f \propto \frac{1}{2\pi\rho_q h_q} h_L \rho_L f \left(1 + \frac{2h_L^2\chi}{3\delta^2(1+\chi^2)}\right) \tag{2.38a}$$

$$\Delta D \propto \frac{2h_L^3\rho_L f}{3\pi\rho_q h_q f_0} \frac{1}{\delta^2(1+\chi^2)} \tag{2.38b}$$

$$\chi = \frac{\mu}{2\pi\eta f} \tag{2.38c}$$

$$\delta = \sqrt{\frac{\eta}{\pi\rho_L f}} \tag{2.38d}$$

with ρ_q and ρ_L the density of quartz and the viscoelastic film layer respectively, h_q h_L the thickness of the quartz crystal and the film respectively, f is the measured frequency, f_0 is the natural resonant frequency of the crystal. χ is the ratio of the storage modulus(μ) and the loss modulus (η) of the layer and δ is the the viscous penetration depth. In the Voigt model of viscoelasticity the decay time of oscillations can be related to the shear rigidity and layer viscosity, the decay time can also be related to the dissipation of oscillations such that

$$\tau_L = \frac{\eta_L}{G_L} \tag{2.39a}$$

$$D = \frac{1}{\pi f \tau_L} \tag{2.39b}$$

Collecting frequency and dissipation data from several overtones it is possible to fit the Voigt model simultaneously and arrive at values for the 4 key variables, layer density, layer thickness, layer viscosity and layer shear modulus.

It should be noted that whilst powerful, this Voigt model also has limitations based on the thickness of the viscoelastic layer; when the thickness of the layer becomes greater than 25% of the wavelength of crystal oscillation, film resonance effects occur [122]. In the film resonance regime, an increase in mass results in an increase in the resonance frequency rather than a depression in frequency as seen in the Sauerbrey and viscoelastic regimes. This is effect generally unlikely to be a factor when considering biomolecule adhesion but must be taken into consideration when QCM is used to measure the rheological properties of viscoelastic films. For such measurements an ideal film is thick enough to be in the viscoelastic regime but not so thick as to cause film resonance[123].

2.7.2 Experimental setup

All QCM-D measurements were performed on a Biolin Scientific Qsense D300 QCM-D with a mass sensitivity of 1ngcm^{-}2 in air and 5 ngcm^{-}2 in water. Com-

patible with 5MHz AT cut Quartz crystals 14 mm in diameter, the instrument records frequency and dissipation simultaneously for the fundamental frequency and the 3rd,5th and 7th overtones. Biolin software Qtools was used to perform Voigt model fitting for viscoelastic layers. All QCM sensors were sourced either from Biolin scientific or from Open QCM.

2.8 Contact angle goniometry

Contact angle analysis is a comparatively simple but powerful surface analysis technique that can quickly yield information about the nature of surface energy and surface chemistry.
A contact angle measurement is performed on a surface of interest by placing a droplet of a known liquid, most commonly pure water, onto a flat surface and measuring angle formed between the liquid droplet and the surface. The contact angle a droplet makes with the surface is governed by 3 factors; the surface energy of the liquid γ_{LV}, the surface energy of the sample γ_{SV} and the solid/liquid interfacial tension γ_{SL} (often written as solid vapour/liquid vapour surface tension but in air this is close to the surface free energy of the material). The angle between a given solid and liquid phase will be finite and consistent in order to minimise the overall energy of the system.

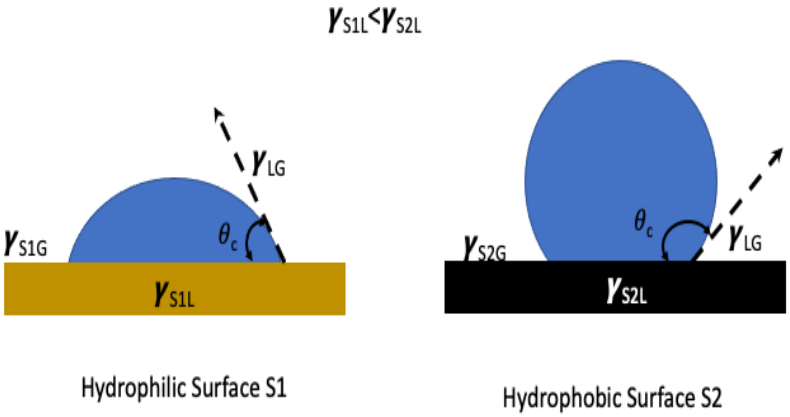

Figure 2.12: Water droplet on hydrophilic and Hydrophobic surfaces.

Consider a droplet of limited volume with a contact angle θ and a contact area A. If A is increased slightly ΔA (the droplet spreads further on the solid phase) there will also be a change in contact angle $\Delta\theta$ (if the droplet spreads the contact angle falls as the droplet thins into a liquid film across the surface). The change in Gibb's surface free energy ΔG^s is given by[124][125]:

$$\Delta G^s = \Delta A(\gamma_{SL} - \gamma_{SV}) + \Delta A\gamma_{LV}cos(\theta - \Delta\theta) \tag{2.40}$$

For equilibrium case

$$\lim_{\Delta A \to 0} \frac{\Delta G^s}{\Delta A} = 0 = \gamma_{SL} - \gamma_{SV} + \gamma_{LV}cos(\theta) \tag{2.41a}$$

$$\Rightarrow \gamma_{SL} = \gamma_{SV} - \gamma_{LV}cos(\theta) \tag{2.41b}$$

Known as the Young's-Dupré relation this represents a way of determining the interfacial tension value and can be very useful in identifying the hydrophobicity or hydrophilicity of a surface. This is illustrated in figure 2.12; for surface S1 the interfacial tension with water is low and the contact angle is $\theta < 90$, hence the surface is said to be hydrophilic and the droplet will spread more on the surface. For surface S2, the interfacial tension with water is higher, the contact angle $\theta > 90$ and the water droplet has a more spherical shape. Therefore this surface is considered hydrophobic. The work of adhesion W_{SL} to a surface can also be given by[126]:

$$W_{SL} = \gamma_{LV}(1 + cos\theta) \tag{2.42}$$

This is a particularly useful relation in cases where the surface energy of the solid phase γ_{SV} and interfacial tension γ_{SL} is unknown or variable. If we consider a more complex model of surface energy we can see additional information about a surface can be inferred from the contact of several liquids. Fowkes interpreted surface energy to be caused by both polar and dispersive, van der waals interactions such that a surfaces overall surface energy was a summation of these two components.[127]

$$\gamma = \gamma^P + \gamma^D \tag{2.43}$$

In a contact angle experiment the surface energy of both the liquid and the solid have dispersive and polar aspects, Fowkes determined that the contact angle is related to surface energy through the equation

$$\sqrt{\gamma_L^D \gamma_S^D} + \sqrt{\gamma_L^P \gamma_S^P} = \frac{\gamma_L(1 + cos\theta)}{2} \tag{2.44}$$

A similar relation was also determined independently by Owens-Wendt and Kaelble[128][129] but is functionally the same. We can see from equation 2.44 that using a non polar liquid (γ_L^P=0) such as hexadecane for a contact angle experiment eliminates the polar term and yields the dispersive surface energy of the solid phase from the contact angle

$$\gamma_S^D = \frac{\gamma_L(1 + cos\theta)^2}{4} \tag{2.45}$$

Performing a second droplet experiment with a polar liquid like water with known dispersive and polar surface energy 21.8 and 51 mNm^{-1} respectively [130], combined with the determined value for γ_S^D the polar surface energy for the solid phase can also be calculated from equation 2.44 and so the overall surface energy from the summation.
These methods allow for the measurement of the surface energy providing possible evidence for the surface enrichment of low surface energy components in mixtures, evidence of hydrophilic or hydrophobic surface chemistries and possible surface reconstruction to reduce the solid liquid interfacial tension.

2.8.1 Experimental setup

All contact angle measurements were performed using the Ossila contact angle Goniometer, with blue monochromatic light source and high resolution 1920x1080 pixel camera running at 20 frames per second. Contact angles were determined using the Ossila contact angle software based on an edge detection method.

Chapter 3

Development of blended thin film model systems; investigating the wetting and solution dynamics of PFPE-PEO in mixtures

3.1 Abstract

Thin film mixed blend coatings of PFPE-PEO and PDMS were developed using spin coating methods in order to create thin model systems of foul release coatings suitable for neutron reflectivity analysis.This process proved to be highly challenging with PFPE-PEO exhibiting exotic solution behaviour and forming aggregates when in mixed with PDMS. Films of PFPE-PEO or PFPE-PEO/PDMS mixtures also exhibited rapid detwetting on silicon substrates. This dewetting was determined to be caused by auto phobic phenomena resulting the from ultra low energy monolayers of PFPE-PEO forming on the silicon oxide layer. This was diagnosed using SIMS and a particular PFPE-PEO monolayer was characterised using ellipsometry, AFM and neutron reflectivity. A successful processes for producing thin film blends was developed, the importance of a high catalyst content and early crosslinking of initial film formation to prevent dewetting is demonstrated with a particular interest in the amino propyl terminated PDMS catalyst as an effective non hazardous catalyst for hydrolysis cross linking of PDMS. The importance of symmetrical substrates for spin coating thin film fabrication is also demonstrated from unsuccessful early neutron experiments, highlighting edge effects.

3.2 Author Contributions

All samples reported here were prepared by myself, all AFM and contact angle, ellipsometry and optical image data was acquired by myself. Prospect of autophobic dewetting property was considered with the assistance and consultation of Professor Richard Jones (University of Manchester, formerly UoS) and Dr Andrew Parnell (UoS). Alternative catalyst was found as a result of my literature research and verified by myself. Neutron reflectivity data for the PFPE-PEO monolayer on silicon was acquired on a beamline experiment conducted by Rachel Kilbride (doctoral student at the time of writing) who kindly agreed to examine my sample, I prepared the sample and performed the analysis and curve fitting. Neutron reflectivity experiments on SuperAdam at the ILL were performed with the assistance of Tom Catley(UoS)and Dr Andrew Parnell and with beam-line scientists Dr Alexei Klechikov and Dr Alexei Vorobiev. SIMS images were acquired by Dr Deborah Hammond (UoS) of the SSAC in the department of Chemistry of the University of Sheffield using samples I had prepared.

3.3 Introduction

As discussed in section 2.4.2 neutron reflectivity is an enormously powerful technique for interfacial and depth analysis of thin films. As one of the few techniques capable of probing the chemical state solid liquid interfaces of coatings in their natural environment, it is imperative that suitable model coatings be prepared so that successful neutron reflectivity experiments can be performed to ascertain the mode of foul resistance these coatings exhibit. However, most foul release coatings are produced with a significant thickness, for ease of application, optimal additive reservoir and good tear mechanics for the elastic pull off of macro foulers. The coating of interest is in its cured and finished form measured at 300μm thick, As previously established, this is far too thick for the resolution of neutron reflectivity which requires films less than 350-400nm thick. In order to produce model systems of this thickness spin coating was employed. This ubiquitous and simple technique is capable of producing thin uniform films down to the nanometer scale. Ideally, blends would be produced that would allow not just the examination of the solid liquid interface but also the distribution of PFPE-PEO in PDMS films. To this end an appropriate solvent or mixture of solvents must be found capable of containing PDMS and its cross-linker and quantities of PFPE-PEO in solution so it can be spun together into a single blended film. The solvent behaviour of PFPE-PEO was briefly investigated for the best candidate then its behaviour in a solution containing PDMS and cross-linker was also examined.

3.4 PFPE-PEO in solutions and mixed solutions

The safety data sheet for the PFPE-PEO Fluorolink E10/6, lists ketones and alcohols as the recommended solvents for PFPE-PEO. This presents something of a challenge for the preparation of blended solutions with PDMS as PDMS has poor solubility in most ketones and alcohols, dissolving instead in linear alkanes such as hexane and other non polar solvents like benzene and its derivatives. We investigate the solubility of PFPE-PEO in these solvents and the optimal solvents for producing PDMS/PFPE-PEO blends.

3.4.1 Methods and materials

The PFPE-PEO block copolymer used was Fluorolink E10/6 sourced from Solvay. Solvents n-hexane, acetone, tetrahydrofuran (THF), ethanol, methanol and acetyl acetone were all sourced from Sigma Aldrich. PDMS Sylgard 184 was sourced from Dow Corning. Solutions were made of PFPE-PEO in acetone, ethanol, methanol, THF and acetyl acetone to assess the solubility of PFPE-PEO. PDMS was dissolved in hexane and THF. Mixtures of PFPE-PEO and PDMS in THF and in hexane/acetone mixed solutions were made to assess the miscibility in solution.

3.4.2 Results

Investigating PFPE-PEO's solvent behaviour, some unusual solvent behaviour was observed; PFPE-PEO separates out of solution at low concentrations and dissolves more readily and fully at high concentration. This trend was found consistently for most solvents used and was first observed when solutions made in acetone with 1% by weight PFPE-PEO content became cloudy and opaque when moved or shaken as shown in figure 3.1. Initially, this was suspected to be the result of shear induced phase separation in which shear causes a solute to fall out of solution however on closer inspection it became clear that in the more dilute solutions where poor solvency was observed there were two phases in the solution suggesting that the PFPE-PEO does not mix at lower concentrations, this behaviour was apparent at comparatively high concentrations in some solvents. For example, at 7% and 20% by weight in solutions of acetyl-acetone PFPE-PEO appeared to separate into two phases but finally became miscible at 40% . This is somewhat counterintuitive given what we would generally expect a solute to dissolve at most low concentrations, the phase behaviour is not particularly well understood but it does create some concerns with regards to producing mixed coatings from solution;

the PFPE-PEO content in a blend must be some small fraction of the PDMS content to form an elastomer with this additive but if PFPE-PEO is only truly soluble at large 10%+ mass fractions of a solvent such as acetone this creates practical challenges for producing solutions with smaller PFPE-PEO:PDMS ratios as quite limited volumes of solution will have to be used.

(a) 2% PFPE-PEO in ethanol

(b) 2% PFPE-PEO in ethanol, shaken 10s.

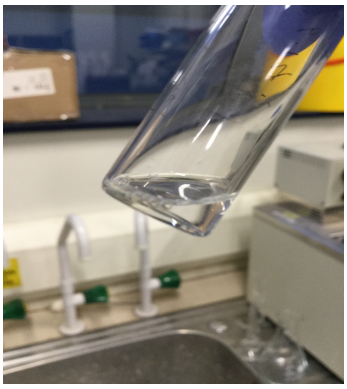

(c) 20% PFPE-PEO in ethanol, shaken 10s.

Figure 3.1: Solutions of PFPE-PEE in ethanol at 2% and 20%, low concentration solution shows some phase separation and forms a dispersion once shaken, high concentration solution remains clear even when subject to turbulence/shaking.

Table 3.1: Example solvents and mass fractions of PFPE-PEO.

Solvent	Mass fraction			
Acetone	0.1%: insoluble/	1%: insoluble/	5%: insoluble/	10%: soluble
Ethanol	1%: insoluble	2%: insoluble/	7%: insoluble	20%: soluble
Acetyl-acetone	7%: insoluble	20%: insoluble	40%: soluble	
Methanol	1%: insoluble	5%: soluble	20%:soluble	
THF	8%: soluble			
Hexane	insoluble			

The data assembled in table 3.1 suggested that of these potential solvents, THF initially showed promise as a carrier solvent because it is capable of dissolving PFPE-PEO at relatively small concentrations and crucially is capable of dissolving PDMS and cross-linkers as well. However, figure 3.2 shows that when PDMS and PFPE-PEO are mixed in THF aggregates rapidly form in solution; clear solutions

of either PDMS or PFPE-PEO in THF become cloudy once the other component is added. Attempts to spin coat mixed THF solutions failed resulting in radially distributed droplets on the surface rather than a true film.

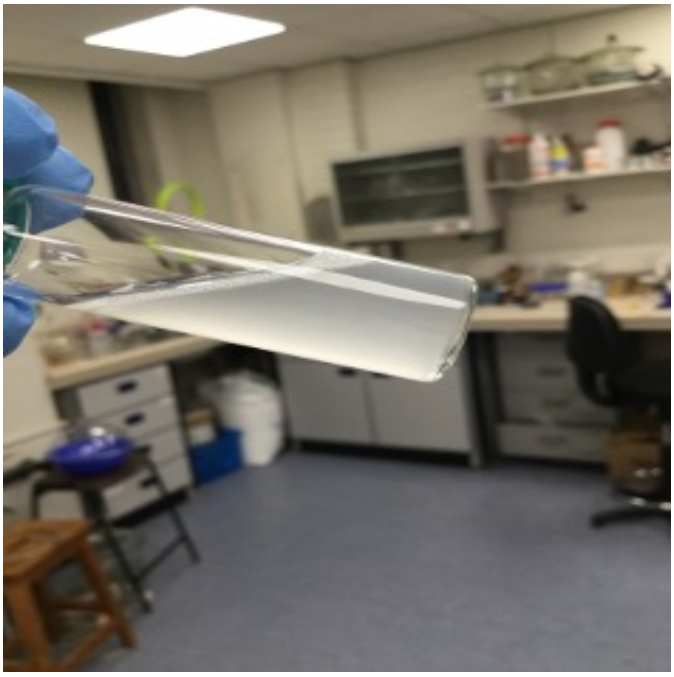

Figure 3.2: Aggregates forming in a a mixed solution of PDMS and PFPE-PEO in THF

Instead, it was decided that the best approach to making mixed films would be to use a combination of hexane and acetone, these solvents are individually solvents for PDMS and PFPE-PEO respectively and are themselves miscible with each other. With these mixed hexane/acetone solutions aggregates were less visible in solution. We selected this blend as the most promising solution combination to form thin film blends with minimal aggregation.

3.5 Comment on the limitations of using Sylgard 184 for spin coating thin films.

Sylgard 184 was initially used as a simple method of producing PDMS, coming in two components; a monomer A and the curing agent B which are mixed together

at a ratio of 10:1 and dissolved in the favoured solvent. This can be very simply assembled and cured at 65°C for 4 hours to crosslink. However, we find that this PDMS fails to produce quality thin films even without amphiphilic additives in the solution.

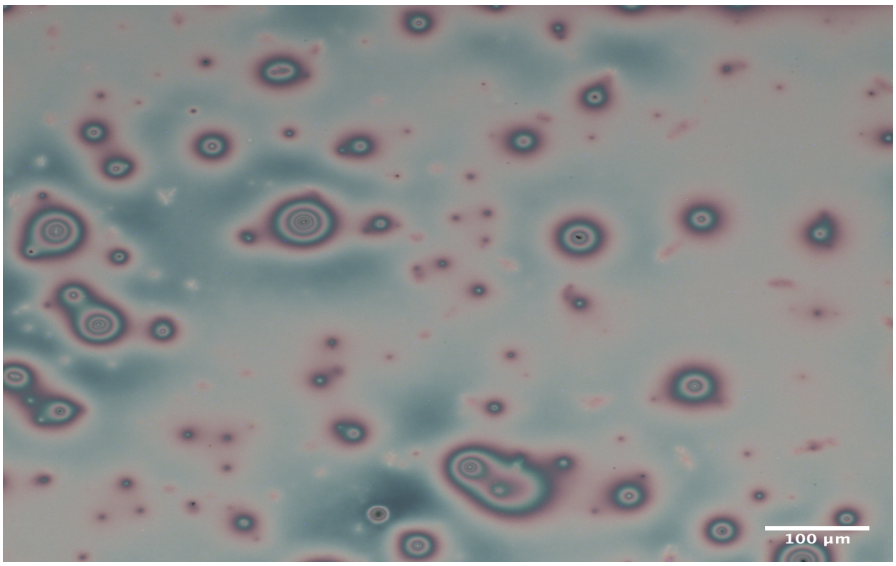

Figure 3.3: Micrograph image of a thin film of Sylgard PDMS spun from 6.87% in THF at 10x magnification.

Figure 3.3 shows how non-uniform spin coated films from Sylgard typically are; this level of roughness and the frequency of defects, even in this simple film is too high to reliably produce the smooth defect free thin films necessary for neutron reflectivity. Alternative PDMS chains using better defined higher purity analytical grade polymers and alternative curing mechanisms were needed. We consider instead hydroxyl terminated PDMS and sol gel cross-linking mechanisms. These are more pertinent to marine fouling coatings as these silicone based coatings are applied to large surface areas and have to be cured in ambient conditions. It is not viable to heat a large ship hull for thermally cured silicones such as Sylgard.

3.6 Hydroxy terminated PDMS cured with TES 40 and ATPDMS catalyst

3.6.1 Materials

The 3500Cst, 43500M_w Hydroxy terminated HT-PDMS was purchased from Sigma Aldrich. The cross linker employed was TES 40, an ethyl silicate, from Wacker Corporation. The catalyst used here was an amino propyl terminated oligomeric PDMS (ATPDMS) M_w=850 DMS A11 sourced from Gelest. TES 40 and catalyst is mixed with HT-PDMS at a ratio of 10% and 1%(w/w) respectively. All 3 components are dissolved together in an appropriate solvent usually n-hexane (sourced from Sigma Aldrich) and then spin coated onto a silicon wafer. Once the film was formed it was left to cure for 24 hours in ambient conditions (room temperature and humidity).

3.6.2 Curing and film behaviour

This OH terminated HT-PDMS cures via catalyst induced hydrolysis cross linking using moisture from the air. Typically, the most common catalyst for these hydrolysis reactions is an organotin catalyst such as dibutyltin-dilaurate. These catalysts were not employed for this project first and foremost because oraganotin catalysts are highly toxic[131] and the safety procedures around their use proved to be prohibitive. Further to this the environmental impact of the use of these catalysts is of increasing concern with high concentrations of these catalyst being found in rivers near industrial production[132], these chemicals are implicated in imposex phenomena in aquatic invertebrates much like tributyltin biocidal coatings[133]. As such, there is an additional incentive to find alternative catalysts in order to minimise the use of these organotin chemicals in aquatic environments.

TES 40 the cross-linker, is an ethyl silicate composed of an oligomeric combination of prehydrolyzed tetraethoxysilane monomers with an average formula of $Si(OC_2H_5)_{2.33}O_{0.835}$ [134]. A common alternative cross-linker for this sol gel reaction is tetraethyl orthosilicate TEOS which is available from a wider range of suppliers but is less favourable than TES 40 because curing times tend to be significantly longer with this cross-linker [134]. The faster curing times for TES 40 are invaluable when producing thin films from spin coating as defects in the film nucleate into holes over time, the faster the film gels, the quicker these dewetting processes can be arrested. Further, crosslinked PDMS using TES 40 has been

reported to have more favourable mechanical properties for reducing the strength of adhesion of pseudo barnacle macrofoulers [135].

The catalyst selected is a short chain PDMS with amine termination groups, as such it should be highly miscible with the bulk of the PDMS film. Amines have previously been reported as viable catalysts for hydrolysis cross linking but miscibility was often limited and curing times were generally longer than organotin equivalents [134]. ATPDMS has been shown as an effective catalyst for cross-linking PDMS with TEOS [136] with curing times reported in the region of 3-4 days.
Comparing the films shown in figures 3.3 and 3.4, we see that spin coated films formed from these components showed significantly higher film quality.

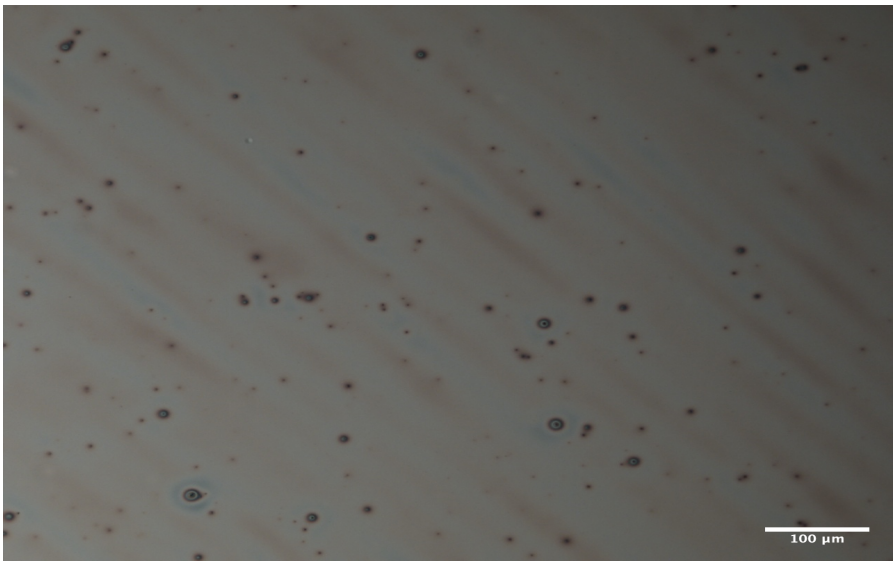

Figure 3.4: 10x magnification micrograph image of a cured, 214 nm thin film of PDMS, this was spun from a 4.5% by wt in n-hexane solution at 3000rpm.

Figure 3.5: 10x magnification micrograph image of a cured, 95 nm thin film of PDMS spun from 1% in from n-hexane at 3000rpm.

Considering figure 3.5 PDMS thin films from these materials produced much more uniform films with only minor defects even at sub 100nm thicknesses, showing a preferable mode of thin film formation than using Sylgard.

3.7 Comparison of TEOS and TES 40 cure

3.7.1 Methods

Thin films were also made using using TEOS via the same method spin coating from the same solvent with ATPDMS catalyst and PDMS. Bulk comparative tests were also performed by making elastomers of PDMS using both TES 40 and TEOS. To achieve this catalyst ATPDMS was combined with HT-PDMS at 0.375% by weight then dissolved in n-hexane at a solids content of 66% in hexane. This mixture was separated into 2 vials and weighed so the solids mass could be determined, TES 40 or TEOS were added to one of the mixtures at 10% of the weight of PDMS mass. Three, 1ml deposits of each of these TEOS and TES40 PDMS solutions were deposited into teflon pallets and left in a fume hood for 30 minutes to allow the hexane to evaporate leaving well mixed PDMS curing agent and catalyst solutes. The curing behaviour was monitored over the following week.

3.7.2 Observations

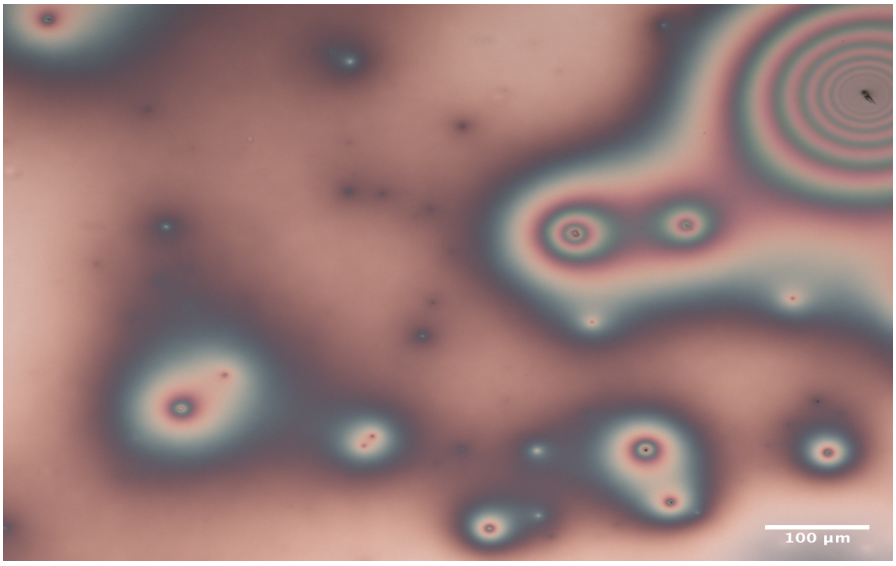

Figure 3.6: 10x magnification micrograph image of a PDMS film using TEOS at 10% w/w and 1% catalyst spun from 5% in from n-hexane at 3000rpm.

As can been seen in figure 3.6 the films formed formed using this crossslinker were visibly uneven. Even without the benefit of an optical microscope, crosslinking times were unacceptably long compared with TES 40 and we attribute this extended cure time for the uneven development of the film; the film remains liquid so holes in the film nucleate and result in either de-wetting or distortions in the film uniformity.

Bulk elastomers of PDMS also suggested much longer cure times for TEOS crosslinker. Even with as little as 0.375% catalyst elastomers with TES 40 noticeably thickened after 30 minutes and had become solid elastomers within 24 hours, whilst TEOS elastomers remained fluid over the same time period. TEOS crosslinked elastomers cured within 7 days.

3.8 Mixed PFPE-PEO PDMS thin films: dewetting effects

3.8.1 Method

Mixed solutions were formed by preparing the PDMS solution in hexane (Sylgard or HT-PDMS) crosslinker was added to the PDMS at ≈ 10% w/w and, in the case of HT-PDMS, catalyst is added at ≈1%. PFPE-PEO (Fluorolink E10/6, Solvay) was prepared in acetone then added to the hexane such that the weight ratio of PFPE-PEO to PDMS could be determined. The mixed hexane/acetone solution was the deposited on silicon via spin coating.

Specifically, presented here is a series of films formed from HT-PDMS at 4.5% in hexane with cross linker at 9.6% w/w of PDMS and the catalyst at a fraction of 1.6% w/w of PDMS. Films formed at 3000 rpm are compared with mixed solutions in which PFPE-PEO is added to the solution from an acetone solution at 25% such that the PFPE-PEO/HT-PDMS ratio in solution is 7%.
Further, we present films formed from this PDMS solution with PFPE-PEO concentration of 4% with a catalyst concentration of 1.6% and from a solution with more catalyst added so the catalyst concentration is 8%; the resultant films are discussed.

3.8.2 De-wetting films

When applying mixed films on silicon, it became apparent that there were far greater de-wetting effects when PFPE-PEO was incorporated into the film, as illustrated in figure 3.7. In some cases films appeared to spontaneously dewet from the surface of silicon entirely.

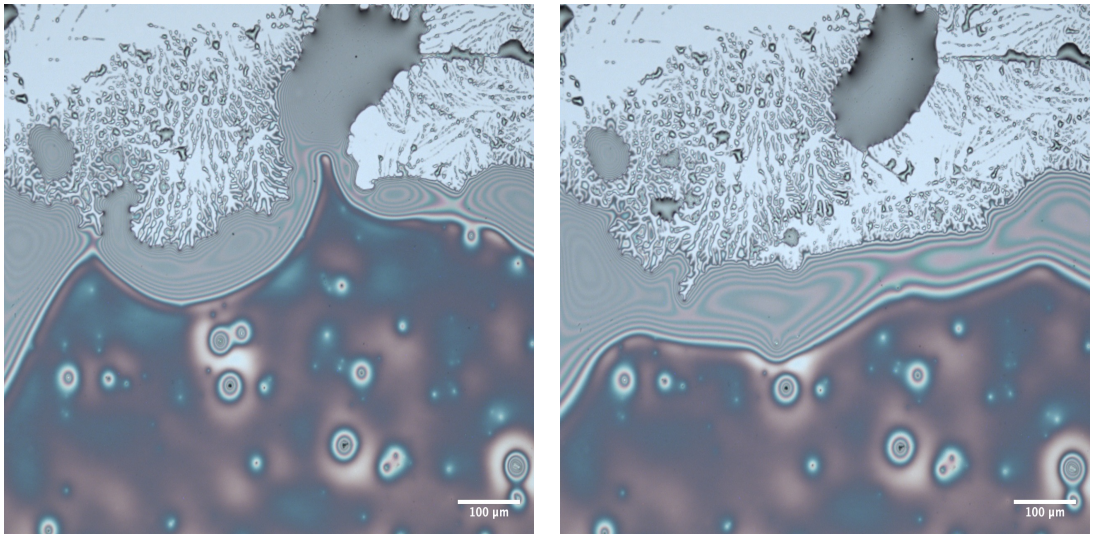

(a) Initial t=0 (b) t=300s

Figure 3.7: Sylgard based thin film with 2.5% PFPE-PEO de-wetting from edge over 5 minutes.

This problem was particularly acute with Sylgard based films but could also be seen when using HT-PDMS films. Notably, thin films of pure PFPE-PEO spin coated on silicon also de-wet spontaneously.

Comparing HT-PDMS based films in figure 3.8, we see the effect of high PFPE-PEO concentrations in the film on film stability.

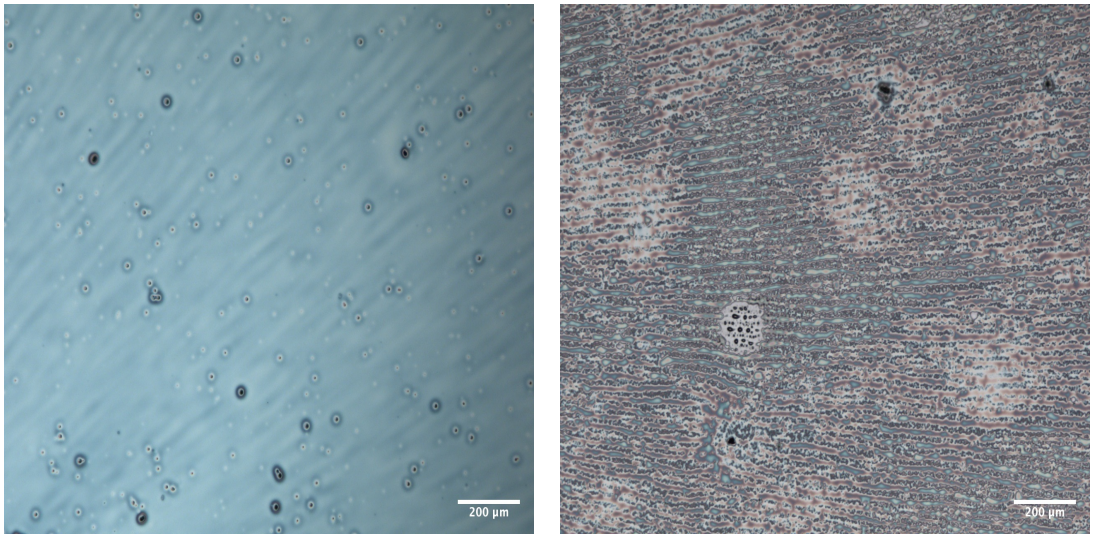

(a) Pure PDMS film (b) 7% PFPE-PEO

Figure 3.8: 5x magnification microscope images of PDMS films formed from 4.5%HT-PDMS films with 9.6% cross-linker and 1.6% catalyst.

In figure 3.9 we see the effect of increasing the concentration of ATPDMS catalyst on the stability of resultant PDMS/PFPE-PEO blend films.

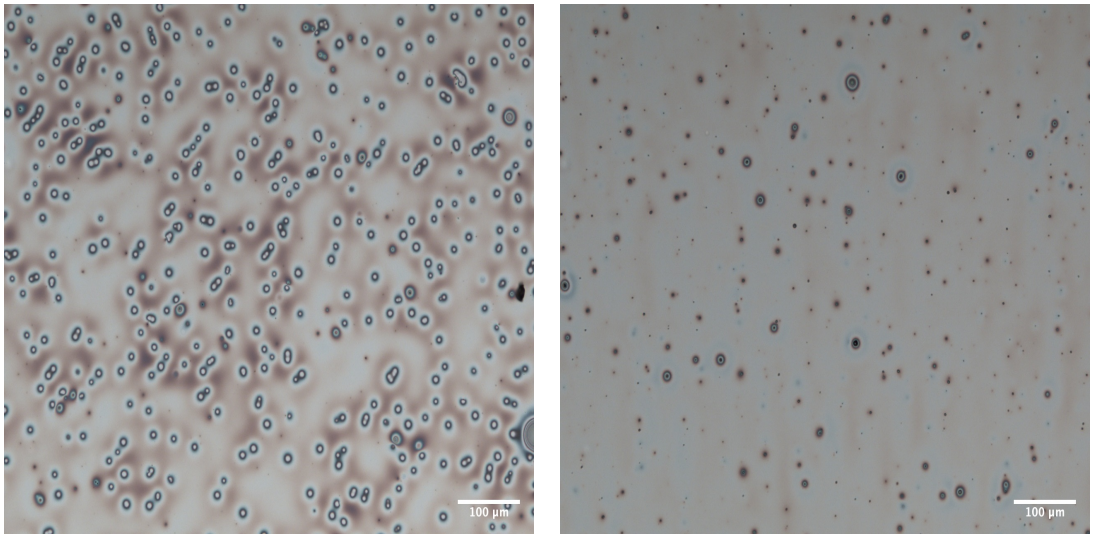

(a) Catalyst:1.6% (b) Catalyst:8%

Figure 3.9: 10x magnification microscope images of 4.2% PFPE-PEO/PDMS mixed blend solutions spun at 300rpm with varying w/w catalyst concentration in blend.

Clearly, high concentrations of PFPE-PEO cause more defects and radial streaks in the film. This is in part due to aggregation still forming in solutions even with mixed solvents; the film shown in 3.8b is not viable for any kind of spectroscopic analysis as it is not a cohesive film. Considering instead figure 3.9 a film with a lower PFPE-PEO concentration shows evidence of some spontaneous dewetting when smaller catalyst concentrations are employed; we see numerous pinhole defects in the film (the bright white spots in the film) that have grown enough to expose the silicon substrate underneath, observed over time, these de-wetting points do not ripen into larger holes. When compared with the film in figure 3.9b a potential explanation arises for why this dewetting does not progress; this film is far more uniform with only a few pinhole defects that have not grown enough to expose the substrate despite using the same concentration of PFPE-PEO.

From this we inferred that the catalyst plays a vital role in uniform film formation with these mixed PDMS/PFPE-PEO films; the presence to PFPE-PEO in the film is driving de-wetting but de-wetting can be prevented by crosslinkng of PDMS films as the polymer chains covalently bond together the molecular weight of the polymer is said to become effectively infinite hence the viscosity rises and chain motility is restricted as the film crosslinks and can no longer dewet in a fluid like manner. The hydrolysis cure of HT-PDMS is an ambient process in air, this must happen very early in the film formation, immediately at the onset film formation after solvent evaporation, we propose that with the higher catalyst concentration this process is rapid enough to limit the Ostwlad ripening of any pinholes in the film the film, as becomes too viscous for this process to occur.

Examining the films in figures 3.8 and 3.9 many of the defects are linearly distributed in a radial pattern, the continued formation of aggregates in these mixed solutions was considered one contributory factor to this phenomenon. In response to this filters were used to deposit the mixed solutions onto silicon before spin coating in order to remove any solid, large aggregates.

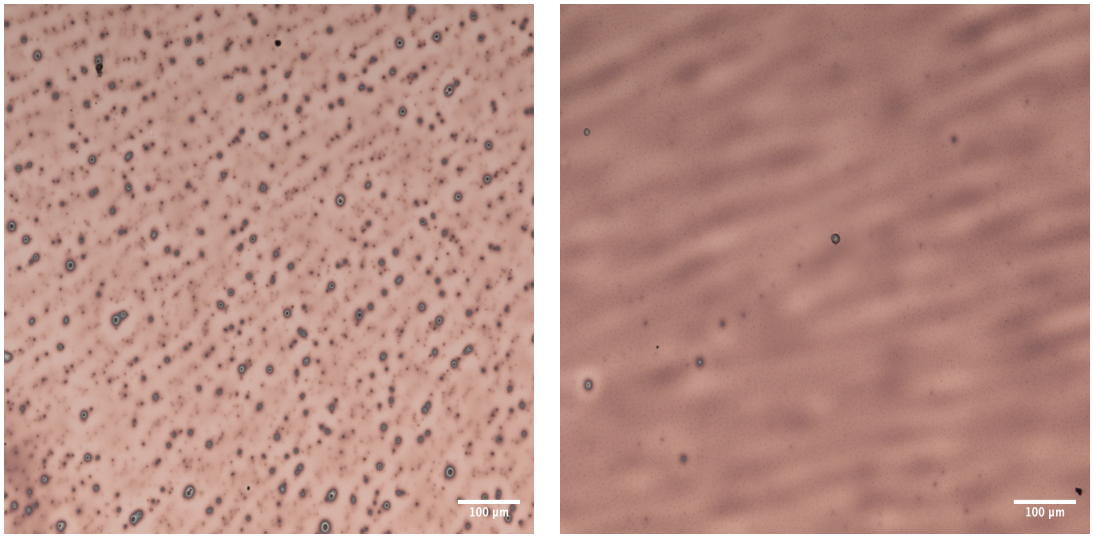

(a) Unfiltered (b) filtered

Figure 3.10: 10x magnification microscope images of films formed from 2.5% PFPE-PEO w/w to PDMS blend solutions in filtered and unfiltered form

Figure 3.10 shows that a marked improvement in film quality was achieved by using a 0.25μm filter when spin coating. This demonstrates the importance of removing aggregates from solution in order to minimise film defects. All further mixed solutions for thin films were produced using filtered solutions.

3.9 Importance of axisymmetric substrates for uniform NR quality thin films.

The first neutron reflectivity experiment using thin blend films in air and in water were prepared on rectangular substrates, this ultimately proved to be disastrous to the quality of films and the importance of axisymmetric or near axisymmetric substrates are necessary to produce thin films with good uniformity.

3.9.1 Methods and materials

Silicon substrates were sourced from Crystran. The substrates were cut from silicon of crystal orientation 100 cut to dimensions 15x50x80mm. All silicon substrates

were characterised with ellipsometry prior to film deposition to characterise the thickness of silicon oxide layer on each block.

Thin films were prepared by spin coating from solutions of n-hexane; HT-PDMS M_w=43500g/mol was dissolved in n-hexane (both sourced from Sigma Aldrich) then, TES 40 crosslinker (Wacker Chemical) and AT-PDMS catalyst (Gelest) were added to solution at 10% and 1% w/w$_{HT-PDMS}$ respectively. Solutions were deposited onto silicon substrates through filtered syringes with 0.25 μm pore sizes and then the spin coater was initiated for 60s. The spin coater employed was an Ossila brand vacuum-less coater using a chuck custom built to accommodate the substrates. Films formed on blocks were left in ambient conditions for 24 hours before inspection microscope images and ellipsometry measurements of the films were taken and both thickness and surface non uniformity were modelled using fitting functions for a cauchy film provided the complete ease software from J.A. Woolam.

Table 3.2: Ellipsometry determined film thickness and non-uniformity for fit for series of films formed on 50x80mm silicon substrates.

Sample	Measured Thickness nm	fitted non-uniformity %
Block 1	404.8	19.1
Block 4	408.7	20.85
Block 5	211.6	26.3
Block 6	192.93	27.14
Block 7	462.9	17.9
Block 8	373.4	24.3
Block 9	402.5	21.1
Block 10	512.5	20.8

Neutron reflectivity experiments were performed on the SUPERADAM reflectometer instrument at the ILL in Grenoble. This instrument uses a monochromatic source of neutrons of wavelength 5.21$\mathring{A}$ and a variable angle detector collecting reflectivity at each discrete Q value by varying detector scattering angle. Reflectivity was collected for Q-values up to 0.125$\mathring{A}^{-1}$. All samples including a silicon standard were measured initially in air before measuring in both D_2O and H_2O contrasts (with SLD's 6.335 and -0.55 $\times 106{-}2\mathring{A}^{-2}$ respectively). Solid/Liquid cells were obtained from the ILL custom built for silicon blocks of dimensions 50x80mm, machined from optically transparent Polycarbonate and using a PTFE(teflon) gasket[137]. The liquid volume contained by the solid liquid cell was 0.5ml. Con-

trasts were changed via the syringing of 20 times the cell volume through the cell to ensure good contrast exchange.
As the instrument utilised a scattering angle based system, resolution could be selected with high precision, with some samples measured at a resolution of 0.5% but most at 2.5%.

3.9.2 Results

Films formed on these rectangular substrates exhibited significant non uniformity despite repeated attempts using nine different blocks to improve film quality.

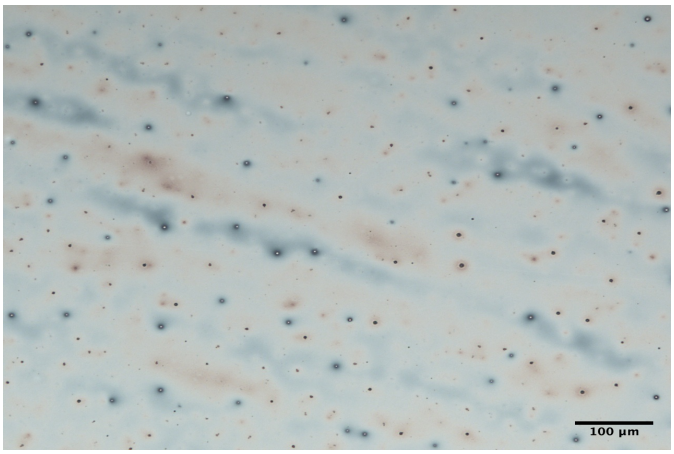

Figure 3.11: 10 x magnification micrograph image of block 6 blend PDMS/PFPE-PEO film with 2% PFPE-PEO by wt of PDMS.

We can see from figure 3.11 a significant radial colour variation, at these ≈10-400nm films the colour of thin spin coated films relates to interference scattering of optical light at a thin film boundary. The reflecting from a thin film and the light transmitting light through a thin film medium and reflecting at the second interface (in this case silicon) can constructively or destructively interfere when the film thickness is of the order of 1/2 or 1/4 respectively of a given wavelength of visible light. The loss of certain wavelengths of light from reflected white light gives the colourless transparent films the appearance of colour which relate to film thickness[138]. The changes in colour are quite significant rather than different shades of the same colour this therefore relates to a significant macro variation in the thickness of the film, summarised in table 3.2. Many of these films are

thicker than recommended for neutron reflectivity for which sub 400nm films are required. All of the films showed substantial thickness non uniformity according to the ellipsometry fit. Block 3 a silicon standard was measured to have an oxide layer of 1.97nm via ellipsometry. Characterising with neutron reflectivity in air a similar thickness was found see figure 3.12

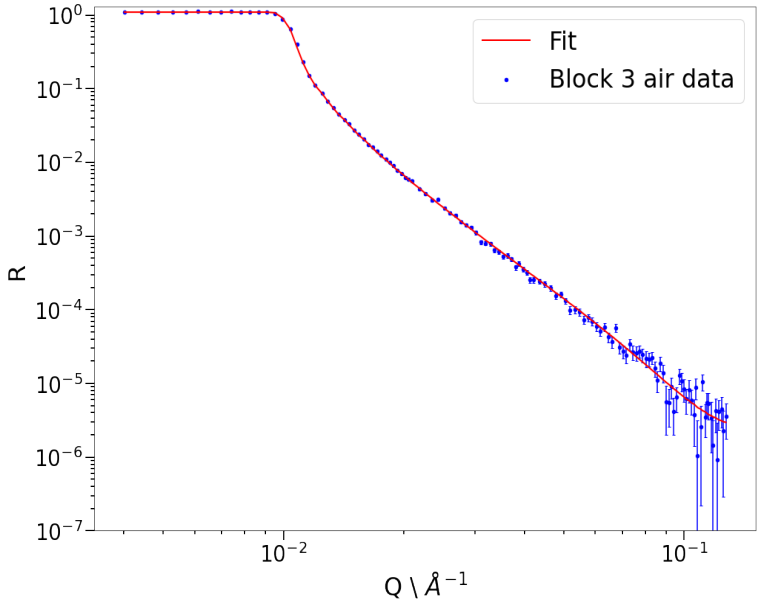

Figure 3.12: Neutron reflectivity fit for silicon oxide in air chi square fit 4.

For this fit a silicon oxide layer of 1.95nm was determined in good agreement with the ellipsometry measurement. Considering instead Block 6 a 193nm thick film with 2% PFPE-PEO content measuring this film in D_2O and H_2O.

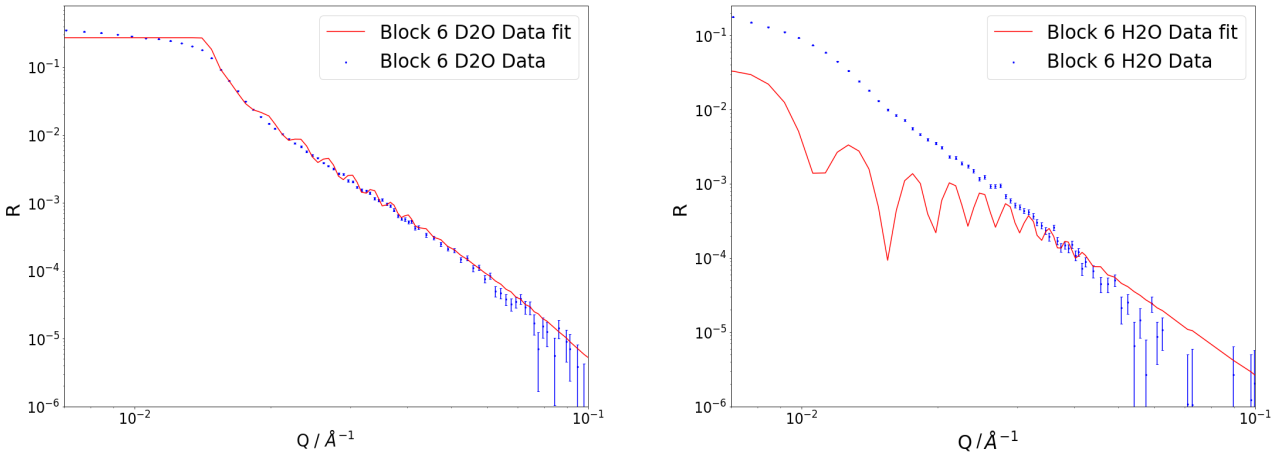

(a) Block 6 in D_2O with sim

(b) Block 6 in H_2O with sim

Figure 3.13: Neutron reflectivity for Block 6 193nm PDMS/2%PFPE-PEO blend in D_2O and H_2O fit with 8nm roughness.

Figure 3.13 presents the fits for Block 6 in both liquid contrasts (H_2O and D_2O) assuming 195nm sample thickness thickness with a roughness of 8nm. We can see the simulated fits are not representative of the neutron reflectivity data. PDMS has a small a SLD $0.0065\text{x}10^{-6}\mathring{A}^{-2}$ very close to air as such we do not expect large scattering contrast for the film in air so Kiessig fringes are not apparent but in liquid as the simulation demonstrates Kiessig Fringes should be clear and apparent. The absence of these features in the reflectivity from Block 6 makes it very difficult to accurately fit the sample. In H_2O the intensity is modelled for this contrast is radically lower than the value seen in the data, both contrasts were collected twice in this lower resolution mode and in a much higher resolution mode in an independent cycle of liquid contrasts with the same data sets present in both measurements it's unclear why this data would be so radically different from expectations in this contrast assuming successful and total contrast exchange. Attempting fits with much higher roughness removes the fringes from the fit but without clear identifiable features it was not possible to find plausible models that accurately capture the critical edge and achieve low error fits. χ^2 values for fits in figure 3.13 were over 100, far above the level of a quality fit ≈0-15. The reflectivity data shown for Block 6 in figure 3.13 is representative of the reflectivity data acquired from all measured films. No measured thin films showed clear features such as Kiessig fringes in any contrast and so no credible fits were obtained for these samples.

3.9.3 Summary

Although the SUPERADAM instrument and its associated beam-line scientists were very capable and could provide very high resolution reflectivity spectra the rough nature of the films resulted in very featureless reflectivity curves and an ultimately failed experiment. The relatively high thicknesses of the films was not intentional; similar concentrations of PDMS in solution had resulted in thinner films on smaller substrates. One possible explanation for this is the weight of the silicon Blocks totalling 140g, these were much heavier than the thin wafers that had been used to refine and test the formation of thin blend films.When using the Ossila spin coater with these blocks the coater took several seconds to accelerate this mass to the desired spin rate. Given the high evaporation rate of low boiling point hexane solutions much of the evaporation occurs within the first few seconds so the true spin rate over film formation may have been slower than programmed resulting in thicker than intended films. The primary difficulties associated with these films and their non-uniformity is attributed to the substrate shape and the volatility of the solutions. With rectangular substrates wave patterns form at the edges due to air foil at the edges of the substrate inducing faster drying at the corners, centrifugal forces will then drive fluid in the centre outwards resulting in more material build-up at the edges. This lead to films with a central circular region of one colour and edge sections which were of a different thickness and so these sections of the film were unusable for spectroscopic analysis[139]. For neutron reflectivity these regions were masked out in order to examine the more uniform central film. The radial waviness seen in figure 3.11 could be due to the Marangoni effects during film drying; here differences in surface cause the fluid to flow into regions of higher surface tension and deposited more material in those regions as the fluid evaporates resulting in non uniformities in the film [140], a high evaporation rate of the solvent has been shown to contribute to this effect but it is not clear why this would be so extreme for these substrates when prior films had developed in a much more uniform fashion.

It was concluded that preparing films on these substrates was very challenging, with very little benefit from the increased size of the rectangular substrates as the edge effects would mean a significant fraction of area around the edge of the substrate would not be uniform and would have to be masked out for the experiment. For the subsequent neutron reflectivity experiments, square or circular axisymmetric silicon substrates were used, producing far more uniform thin films even when using low boiling point solvent blends like hexane/acetone. On square substrates, as the example in figure 3.10b demonstrates, good quality films can be produced using these methods, the highly volatile nature of hexane and acetone may have contributed to surface waviness via Marangoni effects, these

solvents were still favoured because of their miscibility and similar boiling points: n-hexane 68°C, acetone 56°C.

3.10 Investigation of auto-phobic de-wetting of mixed PFPE-PEO PDMS films on silicon

The significantly increased propensity of PFPE-PEO mixed PDMS films to dewet on silicon substrates and the observed dewetting behaviour of bulk PFPE-PEO films on silicon gave rise to suspicions that the PFPE-PEO amphiphilic block copolymer was undergoing a process of spontaneous dewetting on surfaces known as autophobic de-wetting. This is a process in which the termination groups of the molecule bound very strongly to the oxide layer of silicon resulting in an ultra stable monolayer at the material substrate interface[141]. This is a process that is most common in materials with polar groups particularly polar end groups [142] that can bond to the polar oxide layer of silicon or other polar surfaces such as nitrogenated carbon [143] when considering the disjoining pressure Π on a film, that is the negative derivative of free energy with respect to thickness of a film [144] this can be defined as:

$$\Pi = \Pi_w + \Pi_e + \Pi_s \tag{3.1}$$

With Π_s the pressure component from van der Waals interactions between the substrate and the film, Π_e the pressure from electrostatic interactions between substrate and film and Π_s the pressure difference between molecules orientated in a film as opposed to their bulk liquid configuration. Because the derivative is negative and describes attractive interactions in the case of $\Pi > 0$ molecules are more stable in a film than in a liquid bulk and will not dewet. In this case where the monolayer has a lower energy than the bulk material the film disjoining pressure will be $\Pi < 0$ for film thicknesses above the monolayer thickness so the material will dewet off its grafted layer. This phenomenon was coined as autophobic dewetting as the film is dewetting from itself not the substrate[145]. Note in the diagram figure 3.14, this process process is partial; the stable monolayer will remain therefore evidence of autophobic dewetting could be found by detecting monolayers of PFPE-PEO on dewetted substrates.

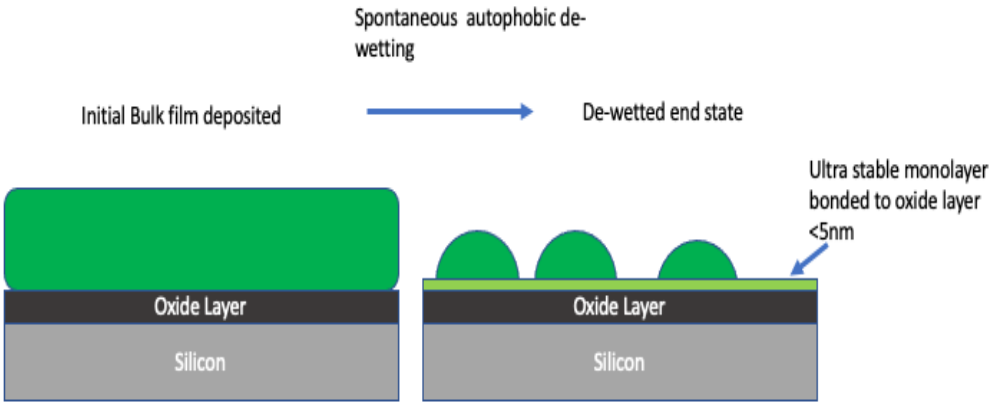

Figure 3.14: maybe autophobic dewetting diagram.

Several researchers have previously demonstrated autophobic dewetting phenomena for perfluoropolyethers such as OH terminated Fomblin Zdol[146],[147][148] and tetraol terminated z-tetraol[143].

Many molecules with polar terminal groups exhibit this behaviour of strong interactions with the substrate surface, in the case of PDMS experiments have observed droplets of PDMS on silicon spreading out of the droplet in a layer by layer molecular fashion[149][150]. But in the case of hydroxyl terminated PDMS this process appears to stop after a single layer has formed with thickness equivalent to the radius of gyration of the polymer chain [151][152]. Suggesting it is less energetically favourable for further polymer chains to spread on this Ht-PDMS-oxide monolayer.

Given that PFPE-PEO is a similar molecule with OH termination groups, incorporating the same non polar perfluoropolyether moitey as its central block, it is quite plausible that this molecule will exhibit the same, autophobic dewetting behaviour on polar surfaces. Experiments were conducted to verify this hypothesis and characterise bonded polymer monolayers on silicon substrates.

3.10.1 Methods

To diagnose auto-phobic dewetting of mixed blend films, a mixed PDMS Sylgard/PFPE-PEO film with high loading of 6% PFPE-PEO w/w was prepared in an ace-

tone/hexane solution and spun on a silicon wafer and then left to spontaneously dewet. The dewetted film was then analysed using an IONTOF 5 SIMS system with a Bi^{3+}*ioncluster* to determine the molecular and mass distribution across the surface. This SIMS analysis was performed with a particular focus on the presence of fluorine at 19 atomic mass units, Oxygen at 16 atomic mass units (present in both PDMS and PFPE-PEE as well as the silicon substrate). Mass fragments of 75, associated with the PDMS monomer and 25 which relates to the typical polymer mass fragment C_2H^- were also mapped.

The formation of stable bonded monolayers of PFPE-PEO on silicon was attempted by spin coating from dilute acetone dispersions on 5 inch silicon blocks. These blocks had been uv/ozone cleaned and the silicon oxide layer characterised with ellipsometry prior to deposition. PFPE-PEO was deposited from solutions of 0.008% in acetone then annealed for 1 hour at 120°C to bond the hydroxyl groups to the oxide[153] before rinsing in THF to remove unbound PFPE-PEO. This monolayer was then characterised with ellipsometry, atomic force microscopy and neutron reflectivity using the SURF time of flight reflectometer at the ISIS neutron source.
Further monolayers were produced using the same method from a broad range of PFPE-PEO solution concentrations on silicon wafers. Again, films were baked at 120°C and then rinsed in an appropriate solvent (ethanol, acetone or THF) before their thicknesses were characterised with elipsometry.

PDMS monolayers were also attempted using 3 different molecular weights of HT-PDMS 2800, 43500 and 4900 g/mol sourced from Sigma Aldrich. These PDMS monolayers were prepared by dissolving each in hexane at 3/5-4% w/w. Thin liquid PDMS film were formed by spin coating from solution on silicon substrates at 2000rpm. These films were left for 30 minutes at ambient temperature before heating to 120°C for 1 hour. Finally, the films were rinsed thoroughly in hexane for 10 minutes to remove the polymer not covalently bonded to the substrate. These films were then characterised with ellipsometry.

The contact angles of suspected PDMS and PFPE-PEO monolayers on silicon were measured with both deionised water and hexadecane, surface energy values were determined and compared with those for a bare silicon substrate and a simple PDMS thin film.

3.10.2 Autophobic dewetting results

Figure 3.15 depicts a spin coated Sylgard PDMS/6% PFPE-PEO blend dewetting on silicon within 30 minutes of film formation.

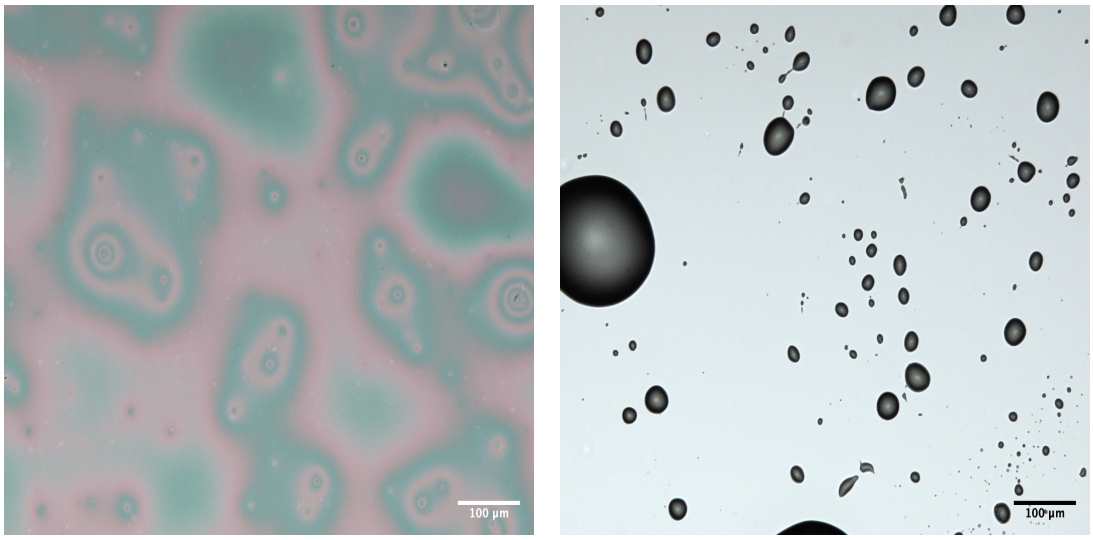

(a) Initial (b) Film 30 minutes later.

Figure 3.15: Optical 10x magnification micrographs of a 6% PFPE-PEO/PDMS blend film spin coated from 3.15a hexane which de-wetted within 30mins 3.15b.

Considering figure 3.15b we see that the film has formed a series of droplets on the surface, it appears that the silicon substrate has been exposed. However, SIMS analysis shown in figure 3.16 reveals that this is not the case.

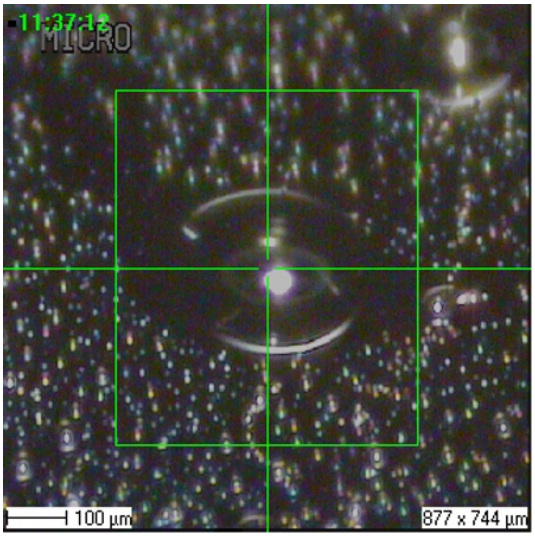

(a) Optical image: area of interest

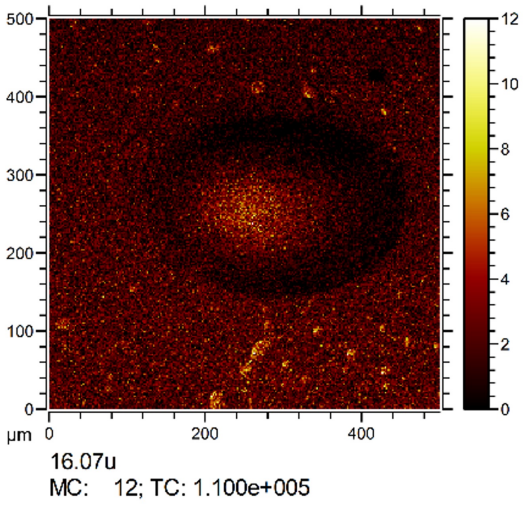

(b) 16 u mass fragments (Oxygen)

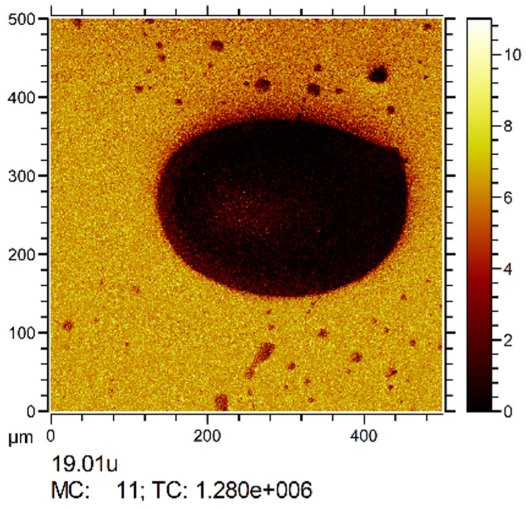

(c) 19 u mass fragments(Fluorine)

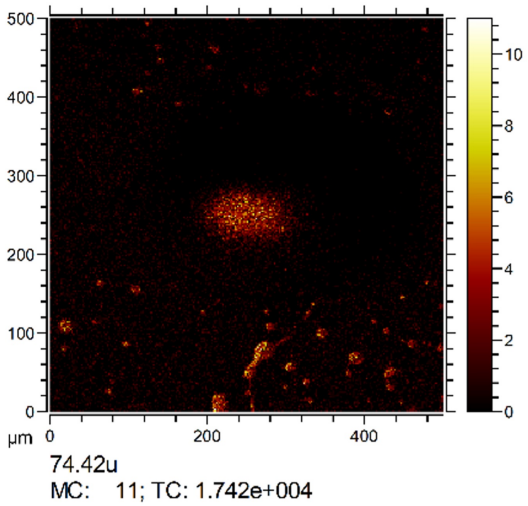

(d) 75 u mass fragments(PDMS)

Figure 3.16: ToF-SIMS negative ion analysis of dewetted 6%PFPE/PDMS mixed sample on silicon (atomic mass 28u).

From this first area it is already clear that the region not covered by droplets in figure 3.17c generates a strong SIMS signal for 19 u atomic mass fragments which corresponds to the atomic mass of the element fluorine. There is also some broad coverage of 16 u atomic mass fragments across the surface and the droplet suggesting Oxygenated species are present across the sample and the droplet. PDMS associated 74 u atomic mass fragments (figure 3.17d) are only strongly

present in the droplet formations.

Considering another area with smaller droplets we see very similar mass fragment distributions, as shown in figure 3.17:

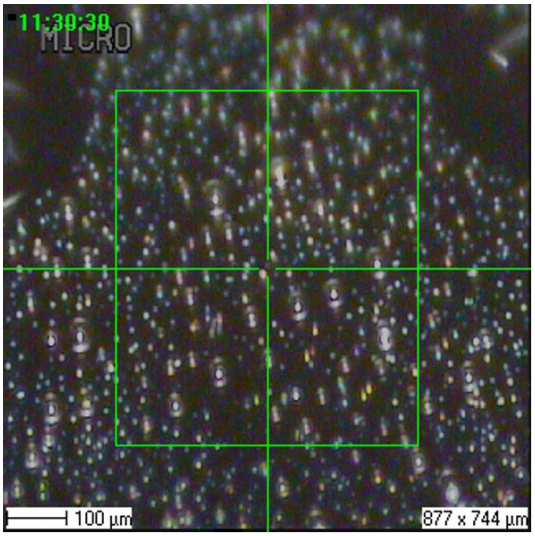

(a) Optical image: area of interest

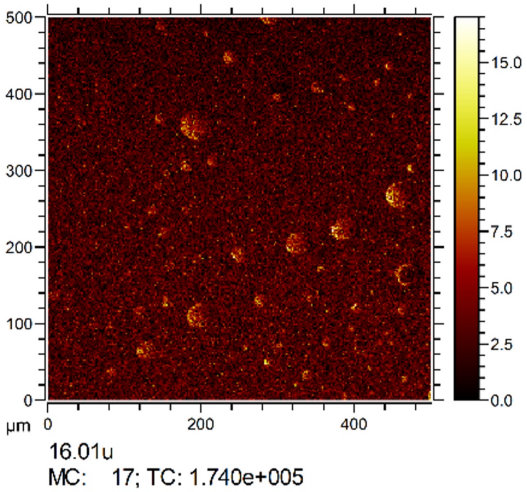

(b) 16 u mass fragments (Oxygen).

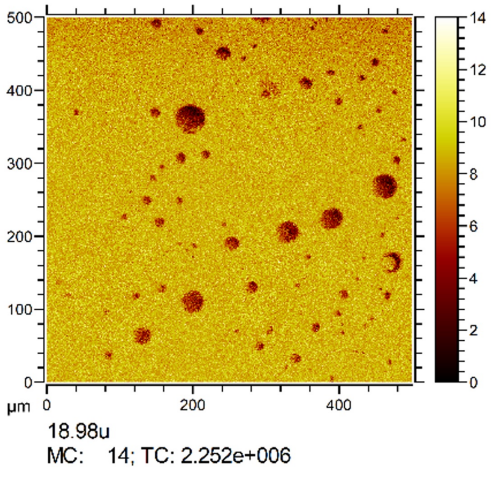

(c) 19 u mass fragments (Fluorine).

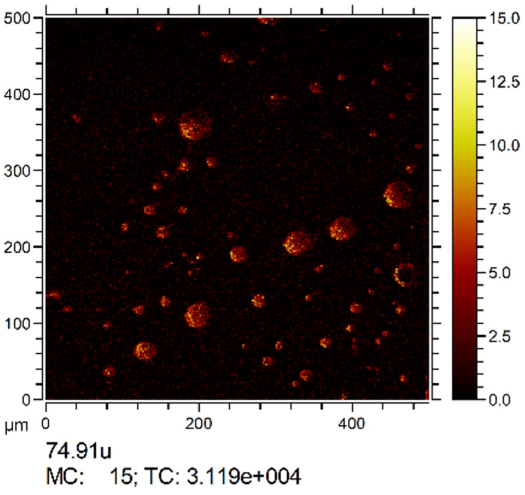

(d) 75 u mass fragments (PDMS).

Figure 3.17: ToF-SIMS negative ion analysis of a second area of a dewetted 6%PFPE/PDMS mixed sample on silicon.

Positively charged ion fragments were also examined, figure 3.18 shows a region of the dewetted film, focusing on the distribution of 31 u atomic mass

fragments which relates to CF+ ion fragments and 73 u mass fragments, the positive PDMS mass fragment equivalent to the 75 u PDMS negative ion fragment [154].

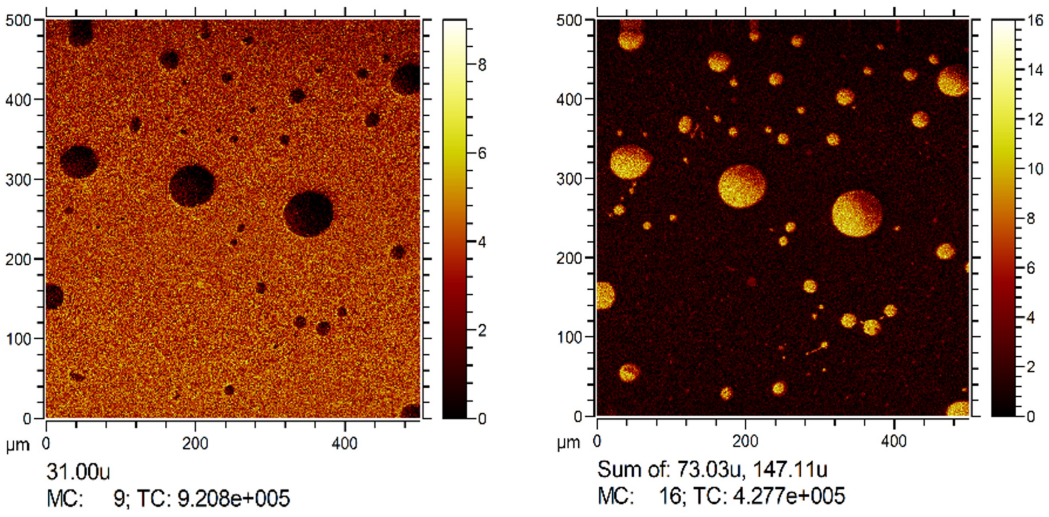

(a) 31 u CF+ (b) 73 u PDMS+

Figure 3.18: ToF-SIMS positive ion analysis of a second area of a dewetted 6%PFPE/PDMS mixed thin film sample on silicon

Comparing these ToF-SIMS images for both positive and negative ion species it is clear that the surface is largely covered in a fluorinated species and the dewetted blend has not in fact exposed the silicon substrate. Furthermore the droplet formations are largely composed of PDMS with a small amount of some fluorinated species.

Taking the entire image it's possible to find the total ion count collected across the image area for the selected mass fragments in both negative ion ToF SIMS images.

Table 3.3: ToF-SIMS mass fragment count from negative ion Tof-SIMS analysis

Fragment	16 O^-	25 C_2H^-	19 F^-	75 $PDMS^-$
Counts figure 3.16	113670	94836	2190168	17502
Counts figure 3.17	180980	185757	5945649	31399

Table 3.4: ToF-SIMS selected mass fragment ratios from negative ion Tof-SIMS analysis

Fragment ratio	F^-/C_2H^-	O^-/C_2H^-	$PDMS^-/F^-$	$O^-/PDMS^-$
Counts figure 3.16	23.09	1.2	0.01	6.49
Counts figure 3.17	32.01	0.97	0.01	5.76

The surface is fluorine rich to a far higher degree than it is PDMS rich despite the comparatively small quantities of PFPE-PEO in the initial film. This widespread detection of surface fluorine is consistent with the hypothesis of a spreading or bonded monolayer of PFPE-PEO that is stable on the silicon substrate and induces bulk film dewetting. The overall signal from the large droplet seen in figure 3.16 is quite poor. This may be due to the large size of the feature; 100's of micrometers in diameter. The incident ion beam is be incident on this droplet at an oblique angle to the curvature of the droplet so many secondary ions will be ejected at wide angles from the surface normal and so are less likely to be detected by the instrument mass spectrometer. This explanation is consistent with the observation that most intense measured mass fragments are detected from the centre of the droplet, where the droplet surface is most perpendicular to the incident ion beam. This may explain why there is a low rate of detection of any mass fragments from areas of the droplet.

The prepared monolayer was first characterised with AFM figure 3.19 before being analysed with for neutron reflectivity, which we present in both standard R vs Q and R vs RQ^4 form (figures 3.20 and 3.21). Figure 3.22, the resulting SLD model fit also showed strong evidence of some layer bonded to the silicon oxide.

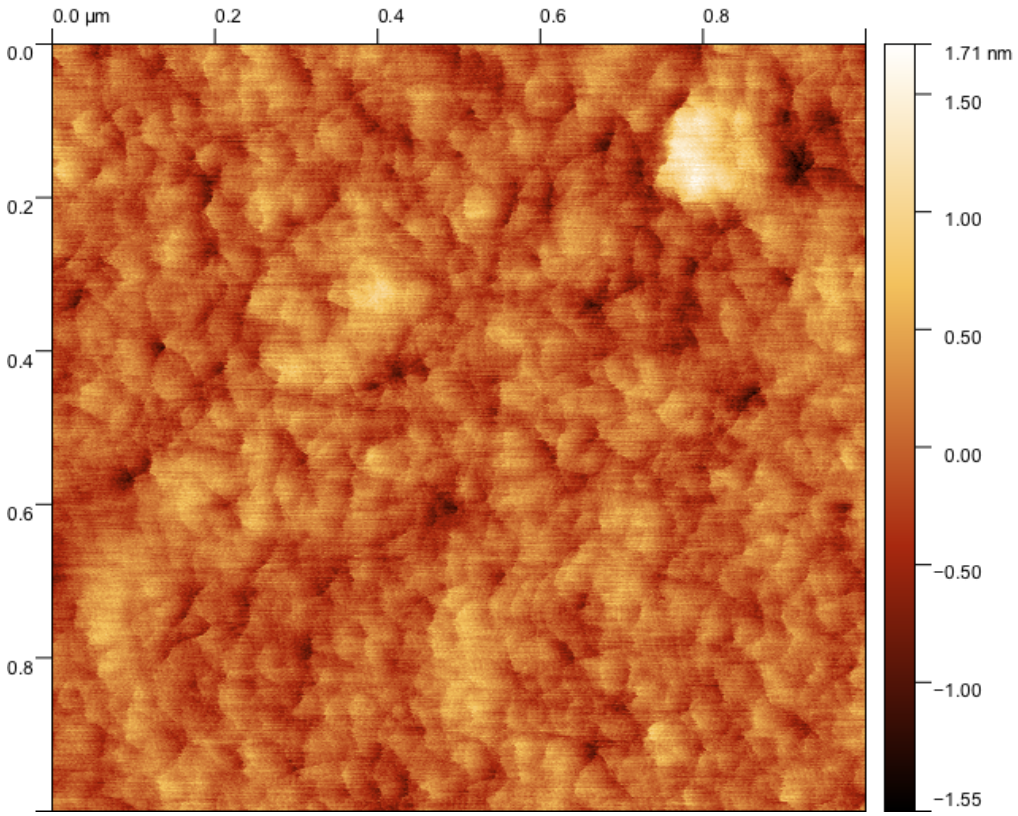

Figure 3.19: 1x1μm topographic tapping mode AFM height scan for bonded PFPE-PEO monolayer on silicon.

The monolayer was characterised using ellipsometry and neutron reflectivity, demonstrating the existence of a thin layer present on the silicon oxide layer.

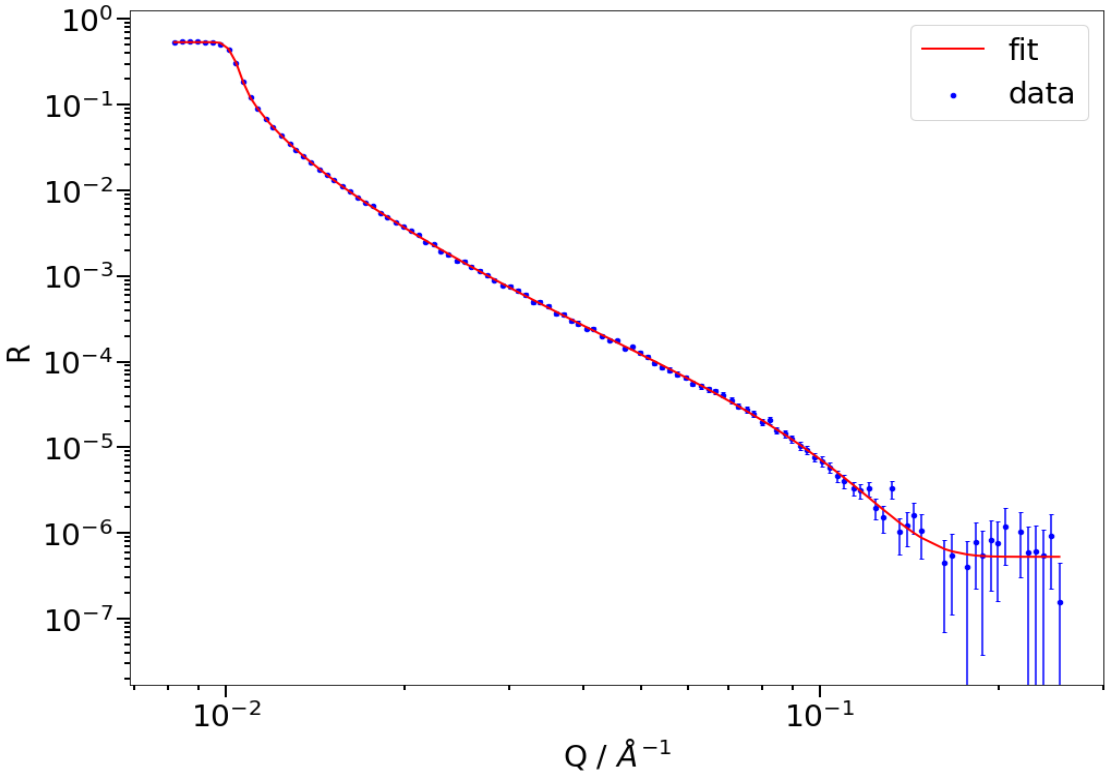

Figure 3.20: Neutron reflectivity in air fit curve for bonded monolayer of PFPE-PEO on silicon, data taken at SURF(ISIS UK).

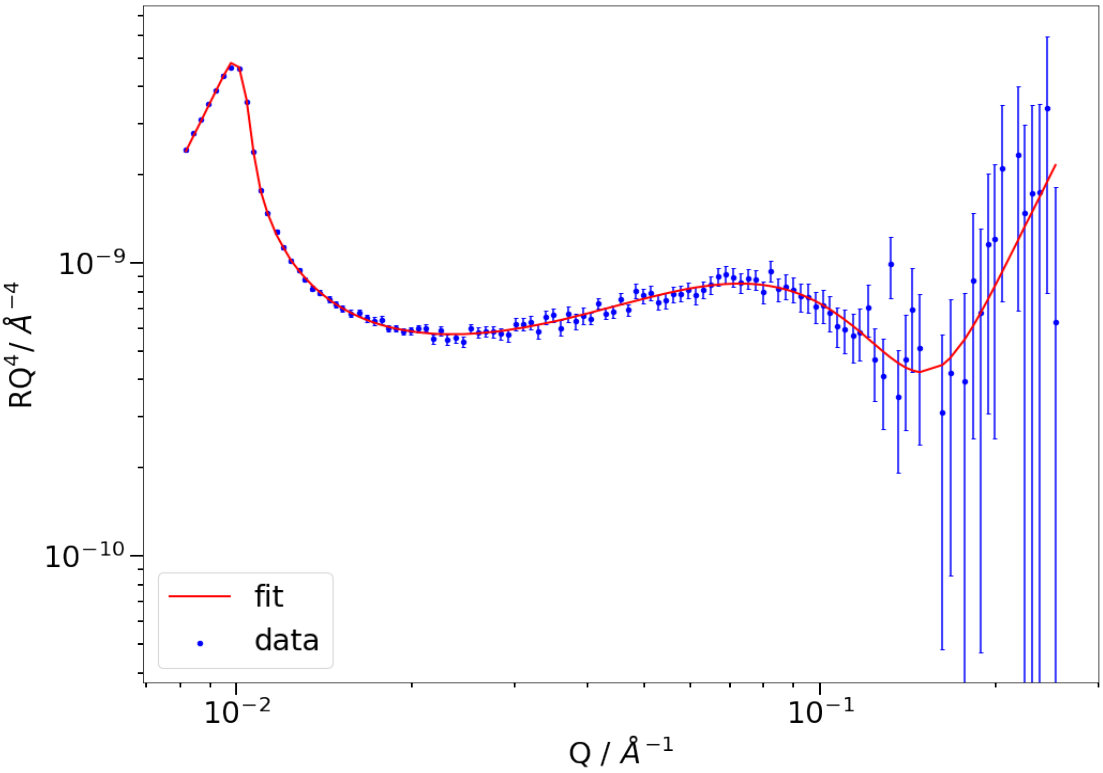

Figure 3.21: Neutron reflectivity curve and fit for the bonded monolayer in figure 3.20 in the RQ^4 form, data taken at SURF (ISIS UK)

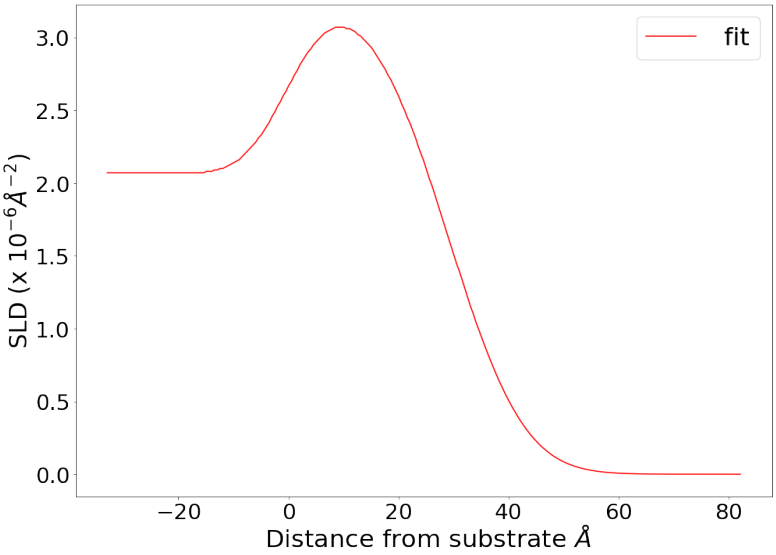

Figure 3.22: Scattering Length Density veritcal profile for fitted monolayer

Parameters for the PFPE-PEO monolayer on silicon determined by various techniques on silicon are summarised in table 3.5.

Table 3.5: Parameters found from ellipsometry, AFM and neutron reflectivity for a bonded monolayer on silicon.

	Ellispometry	AFM	Neutron reflectivity
Silicon oxide thickness (nm)	17.5		17.6
Monolayer Thickness (nm)	1.27		1.2± 0.03
Monolayer rms Roughness (nm)		1.2 ± 0.45	1.05± 0.05
Monolayer SLD (10^{-6} $\mathring{A}^{-2}$)			2.915± 0.01

For comparison with the modelled value of the SLD found from the neutron reflectivity shown in figure 3.20, the predicted SLD for Fluorolink E10/6 from calculation is $2.83\times10^{-6}\mathring{A}^{-2}$. Several other monolayers of FPFP-PEO on silicon were formed by depositing PFPE-PEO on silicon from various solutions, the thickness of the bonded monolayer in each case was measured with ellipsometry and summarised in table 3.6.

Table 3.6: Ellipsometry thickness for monolayers on silicon from a variety of solutions baked at 120°C and washed in solvent.

Monolayer	Ellipsometry Thickness (nm)
0.1% in acetone 2000rpm	0.97
0.008% in acetone 3000rpm	1.4
0.03 %in acetone 4000rpm	1.2
0.35 % in acetone dip coated	2.24±0.31
1.9 % in ethanol 2000rpm	2.78± 0.23

Wen considering the PDMS films on silicon, ellipsometry determined that a small layer of PDMS remained on the surface after baking and rinsing in solvent, the size of these monolayers for each molecular weight of PDMS is summarised in table 3.7.

Table 3.7: Ellipsometry thickness for PDMS monolayers of different molecular weights, spun from solution on silicon, and baked at 120°C and subsequently washed in Hexane.

PDMS molecular weight (g/mol)	Ellipsometry Thickness (nm)	Melt Mean radii of Gyration (nm)
M_w=26,000	5.80±0.63	4.51
M_w=43,500	8.60±0.37	5.84
M_w=49000	7.95±0.57	6.2

The water and hexadecane contact angle for several bonded monolayers of PFPE-PEO and PDMS on silicon was measured and the surface energy of the modified surface was determined, these results are presented in table 3.8 alongside a measurement of unmodified silicon for comparison.

Table 3.8: Contact Angles and calculated surface energy for a series of monolayers.

Material	water CA(°)	hexadecane CA(°)	Dispersion surface energy (mJm^{-2})	Polar surface energy (mJm^{-2})	Total surface energy (mJm^{-2})
Silicon wafer	73.2	35.2	22.4	33.6	55.9
PFPE-PEO 1.9 % in ethanol 2000rpm	76.8	70.4	12.1	34.0	46.1
PDMS vinyl terminated thin fim 60nm	116	15.2	26.2	0	26.8
PDMS M_w 26,000	104.6	38.6	21.5	5.3	26.2
PDMS M_w 43,500	106.7	41.3	20.8	4.3	25.1
PDMS M_w 49,000	102.6	41.3	20.8	5.9	26.7

3.10.3 Model systems: discussion

The fluorine functionalised silicon substrate demonstrated by figures 3.16,3.17 and 3.18 via SIMS analysis of de-wetted PDMS/PFPE-PEO blends is clear evidence of the auto-phobic dewetting effect occurring on these substrates. Ellipsometry measurements and neutron reflectivity also demonstrate the presence of a bonded layer on silicon after heating and extensive solvent washing which is consistent with the hypothesis that the PFPE-PEO monolayer at the silica interface forms a strongly bound layer that cannot easily be removed, and in this case we have seen that this monolayer destabilises any bulk layer spread on top resulting in the aforementioned autophobic dewetting.

The critical thickness of an autophobic dewetting substance is the maximum thickness at which the fluid can spread before dewetting occurs. We can consider this as the thickness for a complete monolayer above this thickness no more anchoring sites are available for the molecule. Monolayers below this critical thickness should also be stable on silicon but will not be a complete monolayer, this may well explain the discrepancy between the thickness values found for the monolayers formed in table 3.6 and the monolayer characterised in table 3.5; some of these monolayers were formed from very dilute solutions, which as previously discussed are of poor solubility and are dispersion like, so the characterised layers may be below the critical monolayer thickness. The monolayer from table 3.5 is well characterised with good agreement between parameter values found from ellipsometry

NR and AFM; the SLD found of 2.915 10^{-6} $\mathring{A}^{-2}$ is of interest, a calculation of the SLD of Fluorolink E10/6 from theory yields a value of $2.83\times10^{-6}\mathring{A}^{-2}$ so the values found from experiment are very close to the expected value.

The critical dewetting thickness has been related to the Radius of Gyration of autophobic molecules [153], the critical thickness and the capillary pressure of an autophobically dewetting monolayer of perfluoropolyether Zdol has previously been determined by dip coating successively thicker layers of the PFPE on silicon to observe the thickness of dewetting and using AFM to measure the height and radii of dewetting microdroplets R on a wetting monolayer [147] with capillary pressure P_c=-2γ/R where γ is the bulk surface tension. Such methods were not viable here because the poor solvency at low concentrations meant controlled ultra thin film deposition could not be performed reliably, nevertheless we have clearly demonstrated the autophobic dewetting properties of this PFPE-PEO copolymer. Identifying this phenomenon may be necessary for the application of wet PFPE-PEO containing coatings to the steel surface of marine ships. Autophobic dewetting of alcohols and Perfluoropolyether based molecules has been known to occur on stainless steels [142] [155]. If these PFPE-PEO based coatings are applied directly to ships they may fail to form a uniform coating on the applied surface due to these autophobic effects. Understanding and inhibiting this effect on the surface of application is essential to the formation of PFPE-PEO containing foul release coatings. We propose that autophobic dewetting can be prevented if the surface is first treated with a simple PDMS coating left to cure before the application of PFPE-PEO containing PDMS, this would prevent the formation of a monolayer of PFPE-PEO at the metal surface that could dewet the wet film before it has been able to cure.

It should be noted that for PFPE-PEO/PDMS blend films spin coated directly on silicon, this PFPE-PEO monolayer is not inhibited so the successful formation of thin blend films is due to the rapid crosslinking of the PDMS films induced by elevated catalyst content.

Experiments with hydroxy terminated PDMS corroborate prior reports of bonded monolayers forming on silica surfaces. These layers broadly increase in thickness with molecular weight/Radius of gyration (table 3.7) as one would expect if the bonded polymer chain grows longer. The mean radius of gyration was calculated using the formula R_g=0.27$(M_w)^{0.5}$, which was determined [156] and experimentally validated [157] for linear PDMS in melt form. It has been reported that PDMS melt films on silicon form an interfacial region somewhat larger than the melt radius of Gyration [158] which could indicate why the monolayer thicknesses were consistently larger than these radius values. X-ray reflectivity would be an excellent way of further characterising these very thin monolayers, as x rays

are particularly sensitive to ultra thin layers, complimentary information about layer thickness and X ray SLD can be determined, for simple in air measurements x ray reflectivity would be more appropriate than neutron reflectivity as data can be acquired much faster and sources are more readily available.

Considering table 3.8 we can see that these bonded monolayer have a profound effect on the hydrophobicity and surface energy of silicon wafers. All PDMS monolayers (with thicknesses as reported in table 3.7) have water contact angles and calculated surface energies that are essentially PDMS like despite being monolayers a few nanometers thickness. The silicon wafer surface energy values are experimentally determined and do not represent the true surface energy of a pure silicon surface but rather a combination of silicon and some oxide interface, the value found here is similar to the literature values of the surface energy determined using other P type 100 silicon wafers of 57.3mJm^{-2}[159]. The surface energy for the PFPE-PEO monolayer whilst lower than the silicon wafer is much higher than the surface energy found for PFPE-PEO from a pendant drop experiment of $\gamma_{PFPE-PEO}$=20.6mJm^{-2}. The PFPE-PEO monolayer on silicon should be chemically bonded to the surface after thermally annealing so we do not anticipate significant reconstruction of the monolayer in response to liquid, as the OH groups are anchored to the interface our model would have the PEO terminal groups of the molecule buried at the interface but and the PFPE backbone protruding from the interface, the high relatively hydrophilic contact angle measured for this surface is therefore surprising. A possible explanation is that this this was not a full monolayer of PFPE-PEO and the measured value was below that of the true critical thickness for a continuous film, so the measured surface energy involved some contribution from the silicon oxide layer.

3.11 Conclusion

Several challenges related to spin coating PFPE-PEO and developing thin film coatings have been identified and discussed such as autophobic dewetting on silicon, of poor solubility PFPE-PEO at low concentration and solution aggregation, protocols were developed to overcome these challenges. For further experiments blended thin films were made using blend solutions of n-hexane and acetone with TES 40 crosslinker and ATPDMS catalyst at concentrations of 2%w/w$_{HT-PDMS}$ filtered onto substrates to remove large aggregates and then spun on silicon. High catalyst content can prevent autophobic dewetting by encouraging rapid crosslinking. The TES 40 catalyst identified allowed hydrolysis crosslinking of PDMS in thin film form and bulk within 24 hours, this catalyst is highly miscible with the

PDMS and crosslinker offering an alternative curing route that is less environmentally hazardous and toxic than current industrial standard. Crucially, films produced using these methods were sufficiently uniform for neutron reflectivity analysis in air and in liquid.

Chapter 4

Surface reconstruction of PFPE-PEO oligomeric block copolymers on PDMS at the solid liquid interface

4.1 Abstract

The interface of blended PFPE-PEO/PDMS blend model coatings was investigated in air and water using contact angle goniometry and neutron reflectivity. AFM measurements indicate evidence of PFPE-PEO nano-droplets at the interface of blend thin films, this interface change was apparent with relatively small ratios of PFPE-PEO to PDMS although the relationship between surface quantities and bulk ratio was not clear. Despite the presence of surface PFPE-PEO in these blends, in situ neutron reflectivity measurements in air and in water show little evidence of surface reconstruction or a clear wetting layer of PFPE-PEO on the PDMS surface. Neutron reflectivity also shows unexpected structure in the PDMS films with or without PFPE-PEO which we attribute to silica forming as a curing by product and segregating to the buried interface as a diffuse layer. This inhibited the determination of a concentration profile of PFPE-PEO in blend film. XPS depth profiles indicate relatively small concentration of PFPE-PEO in blend samples which may be the cause poor surface reconstruction. Topcoats PFPE-PEO on PDMS were also investigated with SIMS AFM and neutron reflectivity. AFM and SIMS and ambient neutron reflectivity show PFPE-PEO dewets readily on PDMS in air with the interfacial tension determined via the contact angle of

nano-droplets as: $\underline{8.28 \text{mJm}^{-2}}$. Solid/Liquid reflectivity tests show that PFPE-PEO droplets form a partially wetting monolayer on the PDMS surface with a thickness of $\underline{30\mathring{A}}$ even at very small depositions. Larger more dense dewetting laters produced a hydrated lamella of PFPE-PEO on the surface 300nm thick. These observations were corroborated with QI liquid AFM imaging of surfaces showing reduced adhesion and elastic moduli on PDMS/PFPE-PEO topcoat surfaces compared to base PDMS and force curves from high deposition surfaces showing evidence for a thick lamella formation on the surface. We attribute this wetting behaviour to hydrophobic interactions between the the hydrophobic backbone of PFPE-PEO and the PDMS surface. A polybutadiene polyethylene glycol block copolymer was investigated for similar behaviour but proved not to exhibit this partial wetting phenomenon on PDMS . A design brief for similar amphiphiles capable of forming partial wetting layers for potential foul release applications is suggested.

4.2 Author Contributions

I prepared all samples and performed all in-air AFM, contact angle measurements and ellipsometry. I wrote all proposals for neutron experiments. Neutron reflectivity experiments at OFFSPEC at ISIS were performed by myself with the assistance of Rachel Kilbride(UoS), Dr Stephanie Burg (UoS) and beam-line scientists Dr Nina Steinke and Dr Jos Cooper. Neutron reflectivity experiments on D17 at the ILL were performed by myself with the assistance Dr Andrew Parnell(UoS), Dr Stephanie Burg and Rachel Kilbride with beam-line scientist Dr Phillip Gutfreund, all Specular fitting of reflectivity was performed by the author. Qi liquid AFM images were acquired by Dr Raveen Tank (University of Manchester, formerly UoS) at my request, using samples I had prepared. I performed all curve fitting and post process analysis of force curves associated with these Qi images was performed on JPK software. SIMS images and XPS surface and depth profiles were acquired by Dr Deborah Hammond(UoS) of the SSAC in the department of Chemistry of the University of Sheffield using samples I had prepared.

4.3 Introduction

When the surface of a substance is subject to a an interfacial change such as exposure to water or a change in environmental pH this can cause changes in the surface structure in order to minimise the interfacial tension with the new interface.

This phenomenon has been observed with even the simplest of interfaces such as uniform PDMS films in water; sum frequency generation experiments performed by Chen et al demonstrate that in air, the methyl side groups of the PDMS chains are segregated at the interface but in water the methyl group signal indicates a tilting of the functional groups towards the surface and in PDMS block copolymers with polystyrene methyl associated signals vanish in water with methyl groups now buried in the bulk and only polystyrene associated phenyl groups present at the surface [160]. This is driven by the unfavourable interactions between methyl groups and water.

Because PDMS is hydrophobic and has a high interfacial tension with water $\approx 49 \mathrm{mJm}^{-2}$ many additives can be placed in PDMS coatings that will be more favourable at a solid liquid interface resulting in surface reconstruction and effective segregation of the more hydrophilic species, this is extremely useful for foul release coatings in which amphiphilic additive can be incorporated into a bulk PDMS to improve the interfacial foul release properties. PDMS films terminated with biocidal quaternary ammonium salts successfully functionalised the solid liquid interface in water [161]. Simple block copolymers of PDMS and PEG mixed into PDMS films were found to segregate to the solid liquid interface from contact angle and neutron reflectivity experiments [162], the incorporation of PEG side chains into styrene ethylene butadiene styrene (SEBS) rubber results in a strong segregation of PEO at the solid liquid interface of the material changing the solid liquid interfacial properties and significantly improving the foul release properties of the rubber against diatom slimes [163]. The strong affinity of PEG to water drives its surface segregation and solvation in water, resulting in a solid liquid interface known to have effective resistance to biofouling, with particular improved resistance to protein fouling over hydrophobic rubber surfaces.

As amphiphiles with low overall surface energy and that contain terminal hydrophilic blocks which have low interfacial energy with water, PFPE-PEO's such as Fluorolink are likely candidates to use as additives to PDMS that could induce surface reconstruction at the solid liquid interface. Containing both a very hydrophobic PFPE central block and two hydrophilic PEO end blocks, we expect some surface enrichment of the amphiphile at the surface of mixed PDMS/PFPE-PEO coatings even in air but surface segregation in water will be driven by the PEO end blocks. In order to understand how these amphiphiles may add to the foul release properties of PDMS the precise solid liquid interface presented by these surfaces in water must be determined using in situ analysis techniques such as neutron reflectivity and liquid AFM to confirm surface segregation effects and determine the role each block in the amphiphile performs.

4.4 PDMS/PFPE-PEO blend surface analysis in air and liquid

Initially blend model thin films developed in the models chapter were considered for surface analysis and their response to liquid water. Having successfully produced stable thin films from blend solutions, it was necessary to consider what effect the presence of PFPE-PEO in the film had on surface chemistry and structure in air. Before considering surface reconstruction in water, evidence of surface enrichment of the amphiphile in air and changes to surface energy of blend thin films were investigated. This would give us insight into the quantities of PFE-PEO necessary to ensure effective surface presence. This was performed primarily with AFM to assess surface morphology and water contact angle goniometry using hexadecane and water to assess surface energy of thin films. Beyond just the surface presence, the general concentration profile of PFPE-PEO in blended films would be of interest to determine the extent of surface enrichment or the evidence of segregation of the amphiphile to the buried interface. Neutron reflectivity is an ideal technique for assessing this property of thin films as its sensitivity to the scattering length density of molecules ensures that concentration changes of PFPE-PEO in the PDMS film would affect the reflectivity spectra. In vacuum conditions another valuable technique for surface and depth analysis is XPS with ion etching depth profiling capability. Though less sensitive than neutron reflectivity and destructive to samples this technique allows us to identify PFPE-PEO specifically from the presence of fluorine in the otherwise fluorine free PDMS matrix. Having characterised blend surfaces neutron reflectivity was performed in liquid as the only techniques able to perform chemical analysis in aqueous conditions.

4.4.1 PDMS/PFPE-PEO blend surface analysis: Methods

4.4.1.1 Sample preparation for AFM analysis and surface energy measurements

PFPE-PEO/PDMS blend samples were prepared via the protocol outlined in the model systems chapter 3; HT-PDMS (3500 Cst, M_w=43500, Sigma Aldrich) was dissolved in Hexane (5-10%) and combined with TES 40 cross-linker (Wacker chemical) from Hexane solution (20% w/w) at a recorded ratio of 10-20% w/w HT-PDMS in hexane before the addition of ATPDMS catalyst (Gelest) from Hexane solution (8% w/w in n-Hexane) at 1-3% w/w HT-PDMS, PFPE-PEO(FLuprolink

E10/6, Solvay) dissolved in an acetone solution is then added to the solution at small w/w ratios to the HT-PDMS content of the solution (0.5-6%). Solutions would then be diluted further in Hexane to 1-3% w/w in Hexane before spin coating on silicon substrates from 0.25 μm PVDF filters.

Because the hydrolysis cure mechanism can occur in ambient conditions with water vapour, prepared solutions could not be kept and used over long terms before partial crosslinking occurred within hexane solution. This would render them too vicious for spin coating so solutions had to be remade regularly. Solutions were created by first forming solutions of polymer, crosslinker and initiator (eg. TES 40 in Hexane , HT-PDMS in Hexane ATPDMS in Hexane) and then combining fractions of each before spin coating. This kept the solutes dilute enough that crosslinking did not occur immediately upon contact between components. This made producing solutions of equal catalyst and crosslinker w/w % all but impossible across batch solutions. The crosslinker and catalyst content of solutions for each set of films was recorded in order to account for any significant discrepancies.

Films were produced and left to cure and then analysed with Tapping AFM in air using a Bruker Dimension 3100 system. Samples with PFPE-PEO content were compared with equivalent PDMS samples with same catalyst and crosslinking but without PFPE-PEO. Water droplet wetting behaviour of PFPE-PEO/PDMS blends were compared with PDMS films over time using the Ossila Goniometer.

A batch of films were prepared from a hexane solution of HT-PDMS with 11% w/w TES 40 crosslinker to HT-PDMS and 3.1% w/w catalyst to HT-PDMS. Films were produced by spin coating from fractions of this solution and then PFPE-PEO in acetone added to fractions of the solution to produce films with 0.95,2 and 5% PFPE-PEO w/w HT-PDMS, the contact angles for water and hexadecane were measured for the series of films in order to find the surface energy for films with increasing PFPE-PEO content.

4.4.1.2 OFFSPEC solid/air slid liquid neutron reflectivity measurements

Films were produced on 2 inch silicon circular wafers (Prolog Semicor) by spin coating. Samples are summarised in table 4.1. Some films were produced in pairs; one PDMS with a given crosslink and catalyst content and an equivalent PDMS/PFPE-PEO blend with a known PFPE-PEO content (eg. pair of samples OFFSPEC 1 10% x-linker, 1.8% catalyst and OFFSPEC 18 2.37% PFPE-PEO 10%

x-linker, 1.8% catalyst. And pair of samples OFFSPEC 11 18.6% x-linker 1.9% catalyst and OFFSPEC 8 2.2% PFPE-PEO w/w , 18.6% x-linker 1.9% catalyst). The crosslinking content was varied to determine this had any bearing on the film structure or distribution of PFPE-PEO. The oxide thickness on all wafers was determined prior to film deposition via ellipsometry and once cured, the film thicknesses were characterised using ellipsometry.

Table 4.1: List of OFFSPEC samples.

Sample	TES 40 (% w/w$_{PDMS}$)	ATPDMS (% w/w$_{PDMS}$)	PFPE-PEO (% w/w$_{PDMS}$)	Silicon oxide thickness (nm)	Film thickness (nm)
OFFSPEC 1	10.0	1.8	0	2.14	165
OFFSPEC 8	18.6	1.9	2.2	2.51	211
OFFSPEC 11	18.6	1.9	0	2.49	183
OFFSPEC 13	11.2	2.1	1.0	1.60	268

Neutron reflectivity was performed on the OFFSPEC Reflectometer at the ISIS Neutron Source in time of flight mode. Samples were measured first in air and then in liquid. All samples were measure at 2 angles 0.5 and 2° with measurements taking 105 minutes in air 80 minutes in D_2O and 120 minutes in H_2O. Figure 4.1 depicts the liquid cell used, which was of a custom ISIS design for 50mm diameter substrates. The sample is sandwiched between two silicon wafers with the interface of interest face down, a thin rubber gasket creates a seal between the sample and the inert silicon wafer which has two ports for the inlet and outlet of water connected to an HPLC pump for liquid exchange. The footprint in air was 1600mm^2, but in liquid this was reduced to 900mm^2 in order to avoid the neutron beam clipping the rubber gasket. Samples were measured in both H_2O and D_2O contrast, after each contrast exchange densiometry measurements were taken of the outgoing liquid to ensure good contrast exchange.

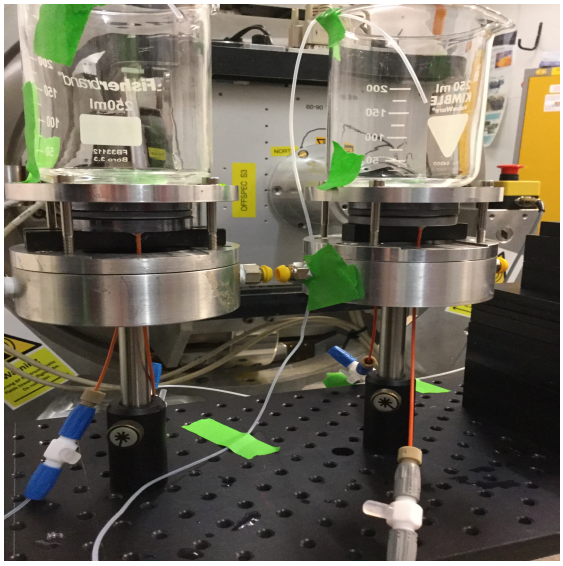

Figure 4.1: Sample in 50mm solid/liquid sample cell observe orange tubing under cell for liquid exchange.

Finally, after the experiment had been completed samples were examined with AFM and one sample OffSPEC 8, was selected for XPS surface and ion milling depth profiling. This process was carried out using the AXIS Supra XPS instrument with an argon gas cluster ion source in the SSAC following methods developed for the experiments described in Chapter 6, with an ion etch energy of 10keV and a crater diameter of 1.5mm. For each etch, the sample was subject to the ion source for 60s with the resultant etched depth per ion milling being $\approx$ 10nm of PDMS. Prior to the etch surface scans were performed collecting XPS spectra over 5 minutes at 2 points near the etch region.

4.4.2 PDMS/PFPE-PEO Surface morphology, wettability and surface energy.

Having produced thin films of PDMS and blends with PFPE-PEO surface topography at the micro-scale could be examined with AFM. Comparing surfaces with PFPE-PEO to equivalent pure PDMS films shows clear changes in the surface morphology:

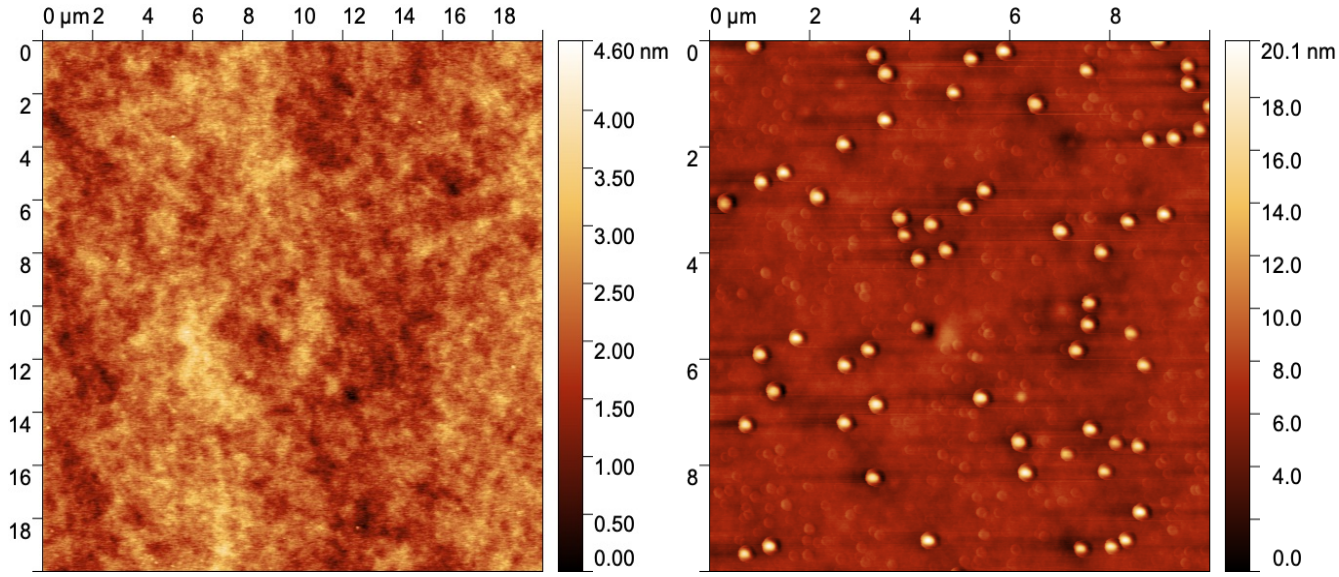

(a) PFPE-PEO free PDMS film 20x20μm

(b) PDMS film 1.16% PFPE-PEO w/w. 10x10μm

Figure 4.2: AFM height images for spin coated PDMS films with 10% cross-linker and 5% catalyst w/w$_{PDMS}$, showing the effect of incorporating 1.16% PFPE-PEO.

Here we can see from figure 4.2 that PDMS films figure 4.2a are quite smooth at a 20x20μm scale with an rms roughness of 0.463nm. In contrast, samples made from solutions with even as small a quantity of PFPE-PEO as 1.16% has radically different tropographical features with a significant amount of nanoscale droplet like features on the surface rms roughness values for the image figure 4.2b is 1.48nm. From this image using Otsu's grain analysis these droplets have a surface coverage of 2.6% with an average height of 12.6nm with an average are of 0.0351μm^2.

These features were observed on several similar samples from the same batch and also from other samples made with different quantities of PFPE-PEO:

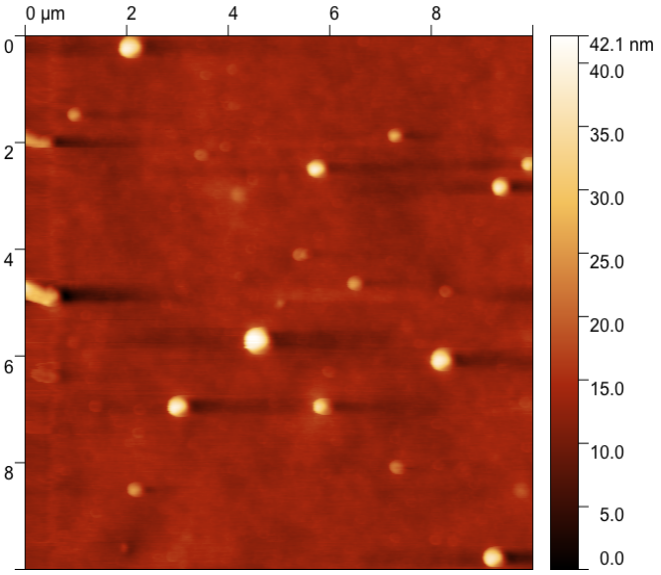

Figure 4.3: 10x10μm AFM height image of a thin film of PDMS with 14% crosslinker and 3.5% catalyst w/w and 3% PFPE-PEO.

Again we see nano-droplet like features in this image figure 4.3. Using grain analysis to identify the droplet features cover 1.22% of the projected surface with an average area of $0.755\mu m^2$ and the average peak height of the droplets was 27nm. The formation of these features on these blended surfaces could be interpreted as small droplets of PFPE-PEO segregating to the surface and forming the surface. These features were observed by selecting a region of each film at random when noting the surface density of these features at the micro-scale it is therefore likely that such nano-droplets are distributed across the entire surface. From these images alone it is not possible to clearly identify a relationship between PFPE-PEO content in blend and surface coverage but macro-scale surface measurements via tensiometry might yield clearer answers as the presence of PFPE-PEO should effect the interfacial tension experience by any micro-litre sized droplets on these surfaces.

However, analysis of the wetting behaviour of blend films and measured surface energy suggests the features observed in AFM have a limited effect on the bulk surface properties of the film.

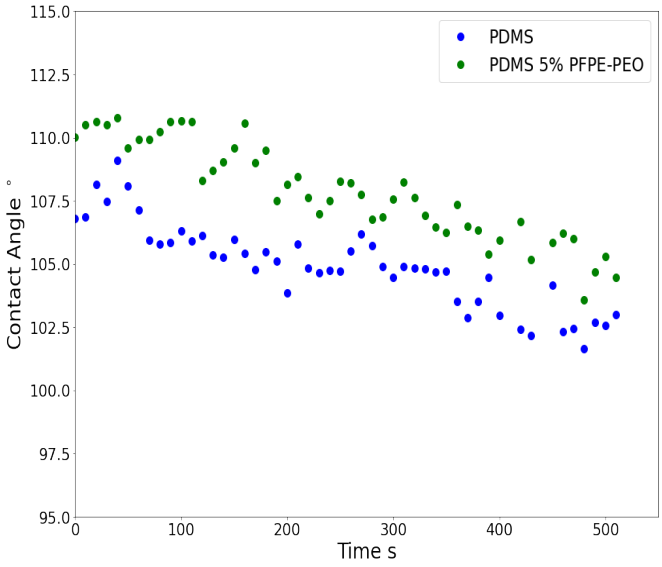

Figure 4.4: Liquid water contact angles for spin coated thin films of HT-PDMS with 11.5% crosslinker and 3.5% catalyst compared with an equivalent film with 5% PFPE-PEO in solution.

After more than 8 minutes sessile droplets of water on both surfaces in figure 4.4 are similar and despite being loaded with 5% w/w PFPE-PEO to PDMS in solution, the 5% blend thin film is neither noticeably more hydrophobic due to having a larger content of surface fluorine nor is there an observable wetting shift due to the hydrophilic PEO terminal blocks solvating in water. A series of films were tested with both water and hexadecane to determine associated contact angles from the first ten second of contact and hence the dispersive and polar surface energy, the results are summarised in table 4.2:

Table 4.2: hexadecane and water contact angles and surface energy components for a series of thin PDMS films spun from hexane solution with 11.5% w/w TES 40 crosslinker and 3.5% w/w PT-PDMS catalyst and increasing amounts of PFPE-PEO.

PFPE-PEO film content	water CA(°)	hexadecane CA(°)	Dispersion surface energy (mJm^{-2})	Polar surface energy (mJm^{-2})	Total surface energy (mJm^{-2})
0	110.9 ± 2.1	40.4±2.3	21.0	1.73	22.8
0.95	112.3 ±2.8	35.5 ±3.5	22.3	0.48	22.8
1.9	113.6 ± 4.3	38.5±2.5	21.5	0.161	21.7
5	113.9±1.0	40.8±3.3	20.9	0.225	21.2

The resultant contact angles form this blend series showed relatively little change between the surface energy of surfaces with PFPE-PEO content the polar component of surface energy for films appears to be slightly lower with the addition of PFPE-PEO but the uncertainty in contact angles derived from repeat measurements suggest all values are within a standard error of each other and there is not a significant observable difference in surface energy achieved by adding PFPE-PEO to blend thin films even if we can see evidence for nano-droplet like features on thin films formed this way.

4.4.3 OFFSPEC Results: neutron reflectivity on blend PDMS/PFPE-PEO thin films.

Further inspection of these PDMS/PFPE-PEO blends in air and in water was performed using neutron reflectivity at OFFSPEC. The first striking observation was that none of the films; PDMS or blend could be fit well as a single uniform layer in air as expected.

Presented below, figure 4.5 shows sample OFFSPEC 1 a PDMS sample with 10% TES 40 crosslinker and 1.8% ATPDMS catalyst w/w to HT-PDMS with an ellipsometry characterised silicon oxide layer of 2.13nm and a PDMS thickness of 165nm measured with neutrons in air.

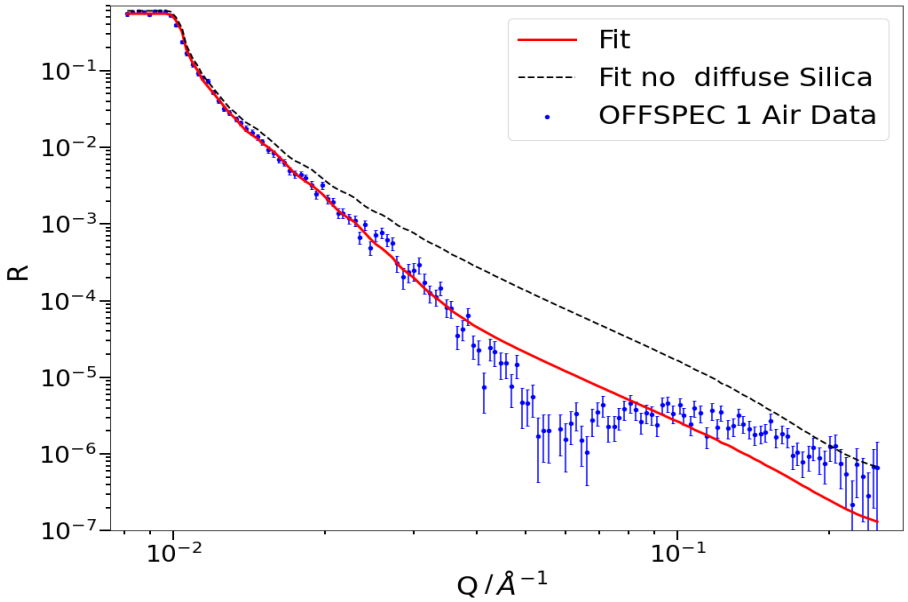

(a) Offspec NR in 1 air

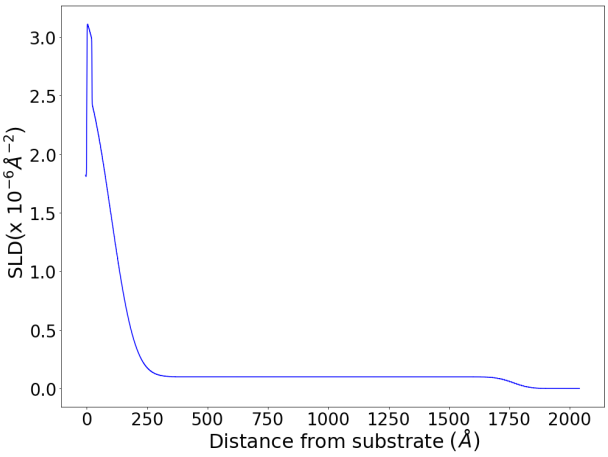

(b) sample 1 air SLD

Figure 4.5: Sample OFFSPEC 1 165 nm thin PDMS film (10% x-linker 1.8% catalyst w/w to HT-PDMS) neutron reflectivity in air.

The dashed line in figure 4.5a depicts a simulation for a single uniform layer of PDMS of 274 nm with a silicon Oxide layer of 2.13 nm. Such a fit badly missed all key features in the sample with a calculated normalised error for this fit of χ^2=707 demonstrating such a fit completely fails to accurately describe the neutron data, with PDMS being near transparent to neutrons in air such structure in the data

was surprising and shows there is some heterogeneity to the sample we were not expecting as this sample should not contain any additives besides crosslinker and catalyst.

HT-PDMS and the ATPDMS catalyst have a near zero SLD ($0.065\times10^{-6}\mathring{A}^{-}2$) as such neither should scatter neutrons in air significantly and neither would cause the structuring in the layer. The TES 40 crosslinker however is a polyethyl silicate which when crosslinking via hydrolysis produces 40% of it's weight in silica as a by product, this silica would have a similar SLD to that of the Oxide layer here modelled as $3.41\text{x}10^{-6}\mathring{A}^{-2}$. Previous studies of hydrolysis cured HT-PDMS with TES 40 crosslinker have shown a stratification of the ensuing silica by product after cure with higher concentrations of silica detected at the surface of bulk PDMS cured elastomers [136]. In this case they attribute the silica segregation to the slow penetration of water through the PDMS and the higher concentrations of similar ATPDMS at the air interface, with amine molecules known to migrate to air interfaces preferentially in many elastomers[164] causing an uneven distribution of catalyst, yielding uneven cross-linking and so a higher presence of silica by product in the elastomer at the surface.

Here we argue that a similar unequal distribution of the significant silica by product has occurred but at the substrate rather than the air interface. A higher SLD layer near the surface would render the whole thickness of the PDMS layer more visible in the neutron scattering data but we cannot see any Kiessig fringes that would be indicative of a 170nm film. Further, it is known that γ-aminopropyltriethoxysilane molecules can form hydrogen bonded monolayers on silica between amine groups and OH sites on silica or oxide surfaces [165], therefore we argue that during the process of film formation ATPDMS catalyst is preferentially distributed at the silicon oxide interface, perhaps forming a monolayer on the oxide and consequently the higher concentration of catalyst induces a greater crosslinking near the substrate and seeds more silica by product at the depth of the film leading to a diffuse layer near the substrate in which a higher concentration of high SLD silica generates structure in the film. We model this as a single diffuse layer between the bulk PDMS film and the silicon oxide layer fit to have a high roughness and an SLD between 0.065 and $3.41\text{x}10^{-6}\mathring{A}^{-2}$ (between volume fractions of total PDMS and total silica).

The fit depicted here with a red line achieves a χ^2 fit per point of 12.4 a significant improvement but still does not capture the feature around 0.6 $\mathring{A}^{-}1$ well. From the SLD profile 4.5b we can see the fit is consistent with the conceptual model of silica distribution; an enriched SLD layer forms that increases in SLD as it approaches the substrate indicating every increasing concentrations of silica as we approach the oxide layer.

Considering again the model of ATPDMS catalyst at the interface a model fit for the sample in air was developed with a very small layer with a PDMS like SLD of $0.065\times10^{-6}\mathring{A}^{-2}$ between the silicon oxide layer and the enriched silica layer of the PDMS film. This would be consistent with a scenario in which ATPDMS catalyst had formed a bonded monolayer on the silicon oxide layer across most or all of the silicon wafer.

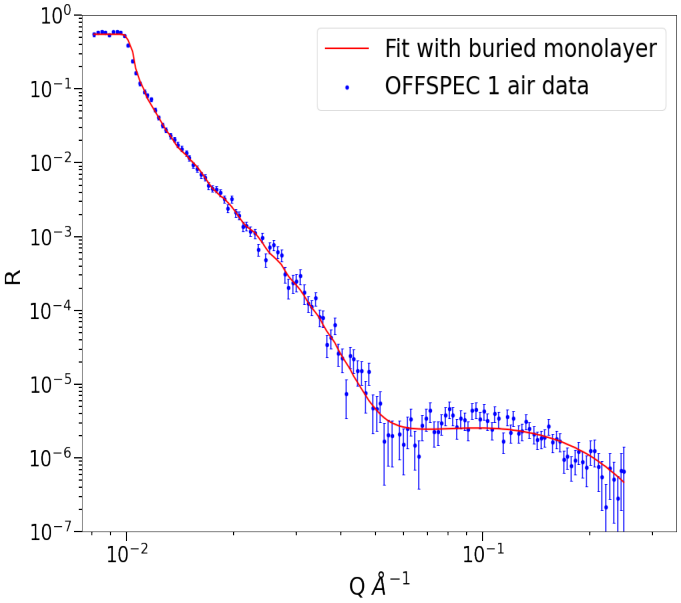

(a) OFFSPEC 1 in air with interfacial catalyst layer.

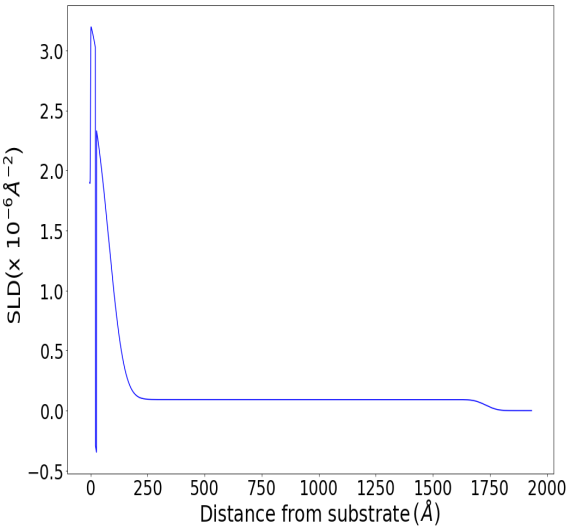

(b) OFFSPEC 1 SLD profile in air with interfacial catalyst layer.

Figure 4.6: Fitted neutron reflectivity for OFFSPEC 1 in air with an interfacial ATPDMS layer between silicon oxide and enriched silica layer of the PDMS.

The resultant fit in figure 4.6, is now noticeably improved with a χ^2 fit of 1.9. The thin layer on Oxide fits to a thickness of $4.95\mathring{A}$ not inconsistent with what we would expect from a small molecule like ATPDMS. The improvement in fitting lends weight to our argument but without specific evidence we would caution against assuming the presence of a monolayer of ATPDMS at the interface.

When observed in liquid contrasts both models with and without this ATPDMS layer are viable and can successfully provide at fit for the samples.

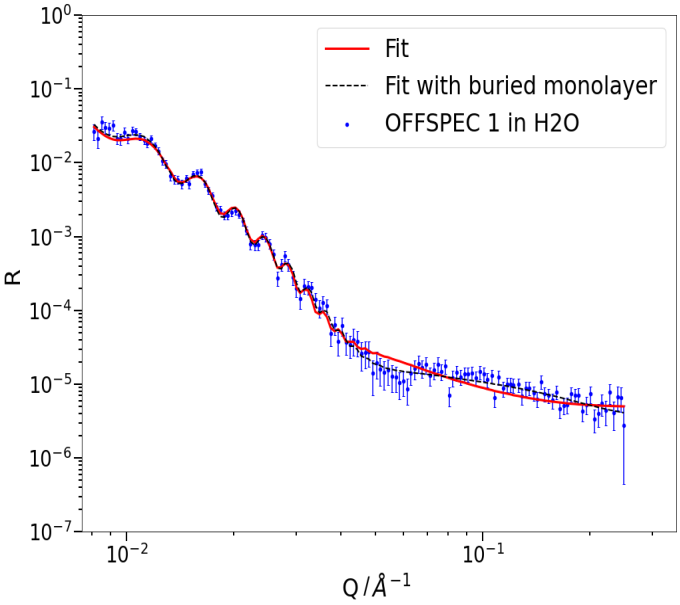

(a) OFFSPEC 1 H_2O

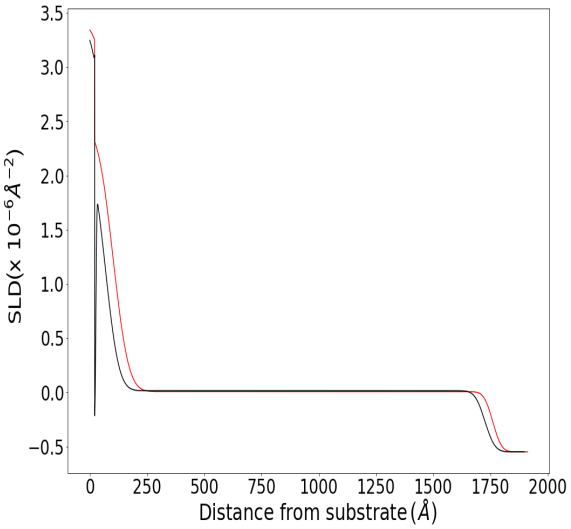

(b) OFFSPEC 1 SLD in H_2O

Figure 4.7: Fitted SLD for OFFSPEC thin film in H_2O

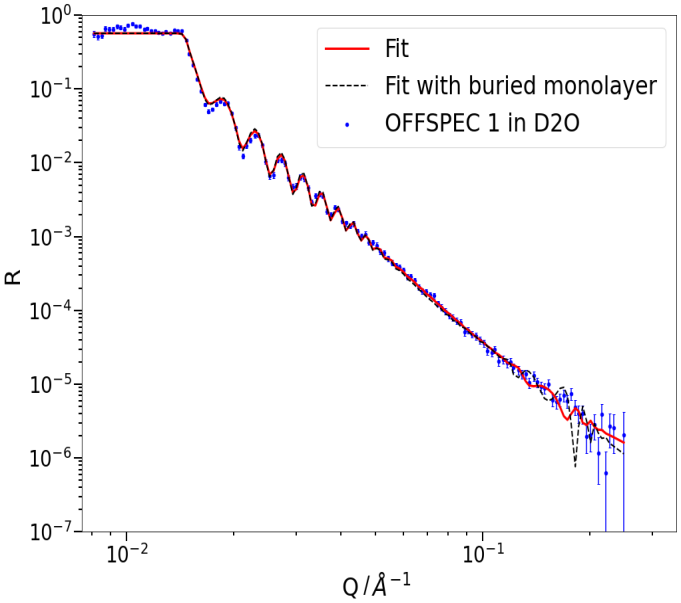

(a) OFFSPEC 1 D_2O

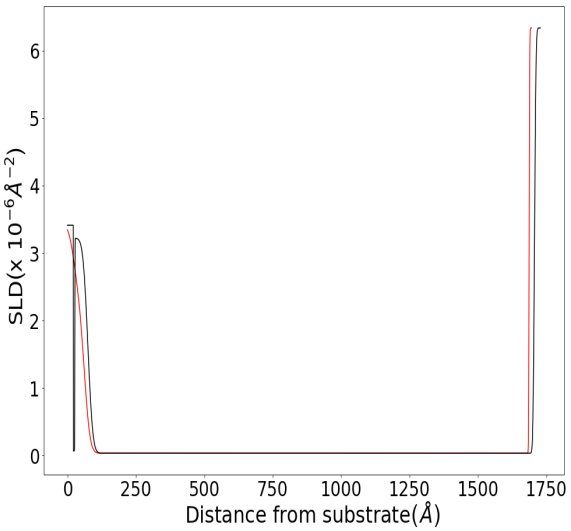

(b) OFFSPEC 1 SLD in D_2O modelled with and without ATPDMS monolayer at silicon interface

Figure 4.8: Fitted SLD for OFFSPEC 1 thin film in D_2O modelled with and without ATPDMS monolayer at silicon interface.

For figure 4.7 and figure 4.8 the χ^2 fits for both models were low; in H_2O χ^2=0.88 for the model without the interfacial ATPDMS layer and 0.82 with a small interfacial layer of ATPDMS. In D_2O fits achieved had errors of χ^2=3.13 and χ^2=3.61 for no ATPDMS and 5.4Å thin ATPDMS layer. Samples in liquid can fit far more readily to the simpler enriched layer PDMS layer model than in air, with the fits being generally insensitive to the presence of a thin monolayer of ATPDMS on the substrate. This is unsurprising given that the contrast difference between water/D_2O and PDMS is much greater than in air so scattering results from the whole sample whereas the bulk of the film is effectively transparent in air. Both contrasts fit to a diffuse layer of intermediate SLD indicative of silica in the film near the substrate. The precise form of this layer varied between the two contrasts, with the D_2O layer suggesting a higher SLD. The D_2O contrast was generally less sensitive to this layer; fits for a single uniform PDMS layer achieved a χ^2 of 3.8 although the fit line did not capture the higher Q Kiessig fringes as well. It is possible that some water uptake in the thin film occurs around domains of hydrophilic silica which could account for the differences in SLD for the enriched layer as an increased volume fraction of water in these regions would alter the SLD

up for D_2O an down for H_2O.

Having demonstrated the viability of fitting H_2O and D_2O neutron reflectivity for the PDMS films incorporating this ATPDMS monolayer we therefore argue that this layer is plausible and appears crucial for achieving lowest error fits for samples in air. However, as this layer is hypothesised and is not without precedent in literature it has not been demonstrated through alternative analysis of these films. As the primary interface of interest in these films is the solid/liquid interface between the film and water further fitting for neutron reflectivity samples in liquid will be modelled and presented without this ATPDMS monolayer to both simply the fit and demonstrate that the calculated depth profile for the film is not dependent on the assumption of a thin monolayer of ATPDMS functionalising the silicon oxide.

Considering a PDMS/PFPE-PEO blend sample in air OFFSPEC 13 a 270nm thin film with 11% x-linker 2.1% catalyst and 1% PFPE-PEO w/w to HT-PDMS. Similar features are observed upon fitting

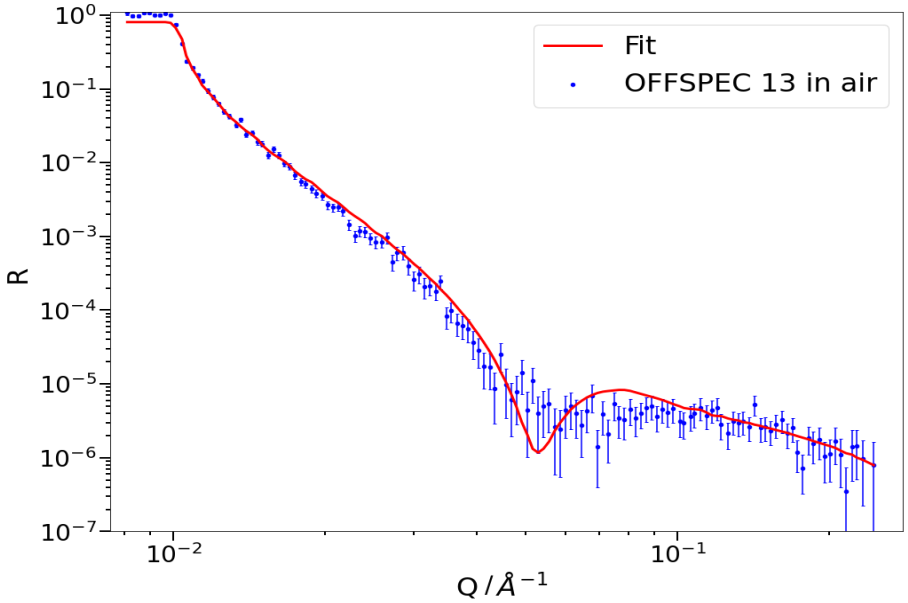

(a) Offspec NR in 13 air

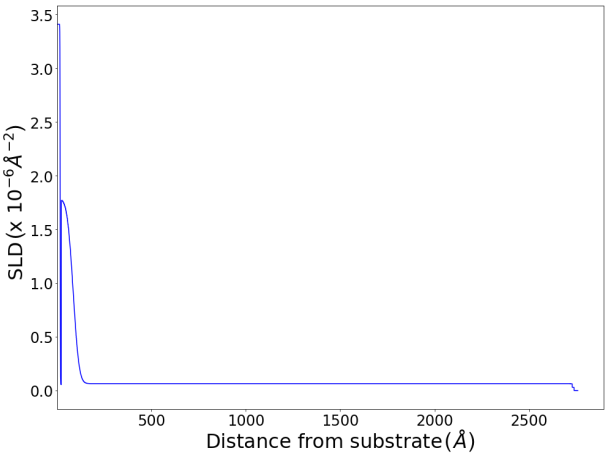

(b) sample 13 air SLD

Figure 4.9: Sample OFFSPEC 13 268 nm thin PDMS film (11% x-linker 2.1% catalyst and 1% PFPE-PEO w/w to HT-PDMS) neutron reflectivity in air. Fit assuming a thin monolayer of ATP-PDMS SLD 0.065x10^{-6}Å^{-2} and thickness 5.6Å on silicon oxide.

Assuming a monolayer of catalyst on the silicon substrate, figure 4.9 shows that an in air fit could be achieved of χ^2 4.41. Note that as this sample is a blend, it would be expected to have droplet like features associated with PFPE-

PEO at the surface (see figures4.2b). Despite this, there is no evidence of any interfacial layer that could be associated with PFPE-PEO at the surface. If a more scattering layer where present at the surface the Kiessig fringes associated with the full 270nm thickness of the sample would be apparent in air. The absence of any such layer suggests whatever interfacial enrichment in air is not uniform enough or concentrated enough to contribute to the specular scattering. Droplet like features are not dense enough to form an effective SLD layer on the surface. Because of the diffuse layer of silica in the film it is extremely difficult to discern any segregation of PFPE-PEO in the PDMS, without knowing the precise distribution of silica in the film it is not possible to model and differentiate higher SLD regions due to silica or PFPE-PEO.

Considering this layer in liquid we find sample with an SLD profile remarkably similar to PDMS OFFSPEC 1

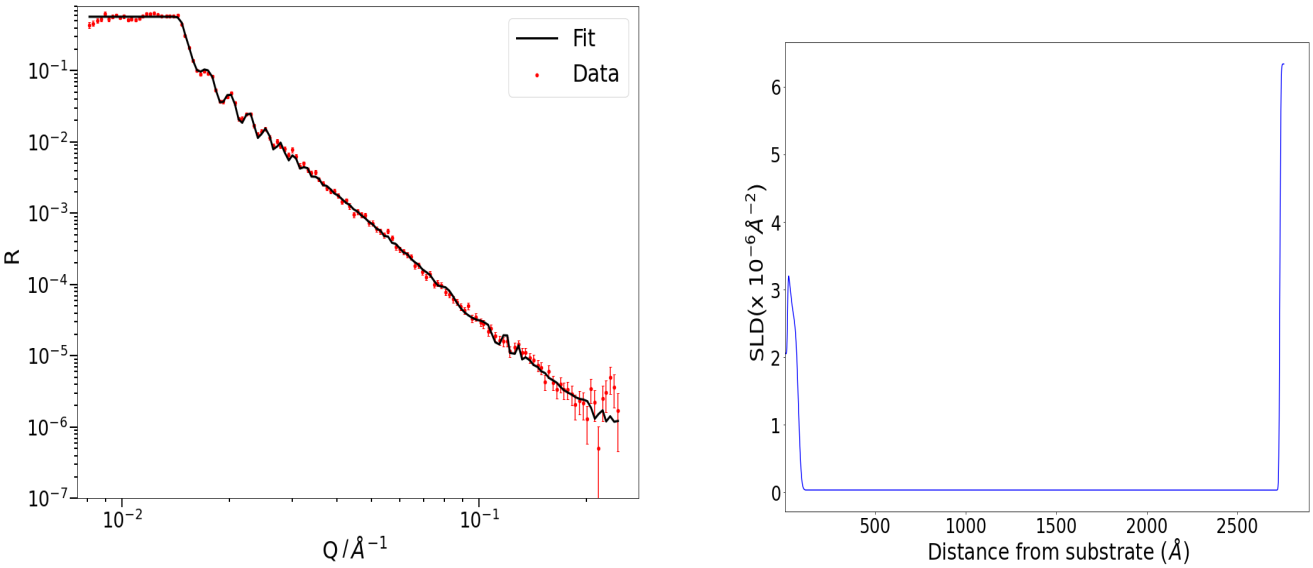

(a) OFFSPEC 13 in D_2O

(b) Fitted SLD in D_2O

Figure 4.10: Fitted SLD for OFFSPEC 13 thin film in D_2O

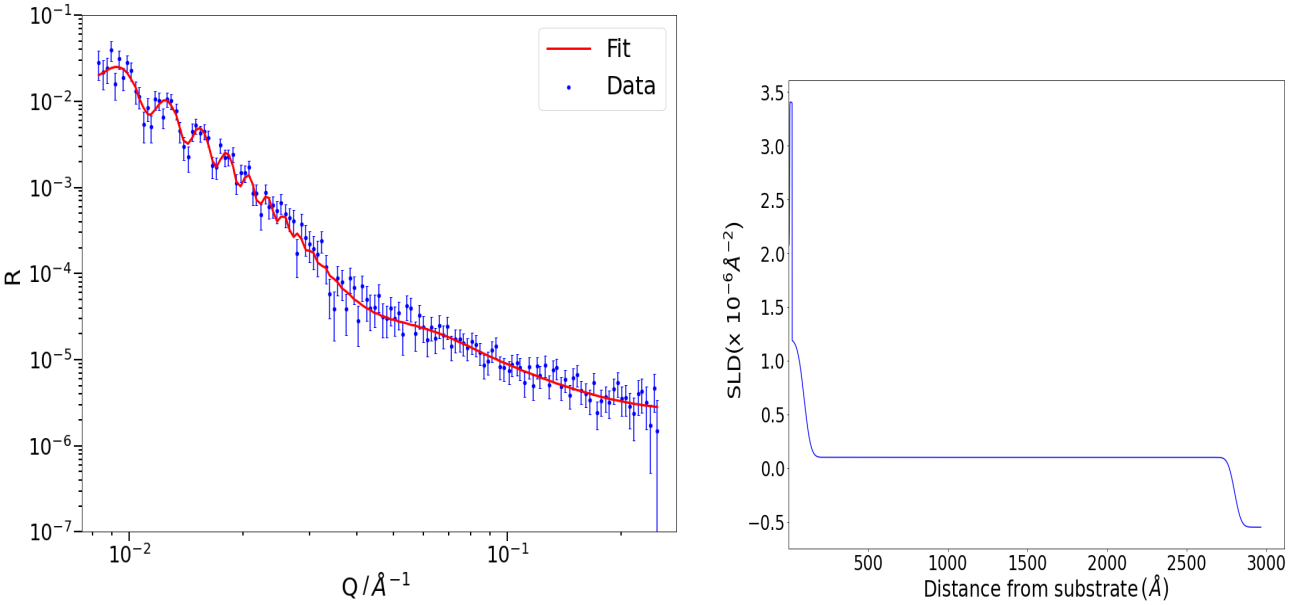

(a) OFFSPEC 13 H_2O (b) OFFSPEC 13 SLD in H_2O

Figure 4.11: Fitted SLD for OFFSPEC 13 thin film in H_2O

These simulations fit to the data in figures 4.10 and 4.11 yielded χ^2 of 1.15 and 0.738 for D_2O and H_2O respectively. The fit in D_2O was used to normalise R(Q) intensity for the fit in H_2O as both measurements were taken from the same instrument with the same sample alignment, with the water contrast exchanged i situ using an HPLC pump. Both fits found the layer thickness to be 265-275nm thick consistent with dry ellipsometry finding a value of 267.8± 2.50nm. Note that in both contrasts the modelled layer fit shown form the SLD profile figures 4.10b and 4.11 there is no evidence of an interfacial change at the solid liquid interface. Consistent with the long term contact angle measurement of wetting this implies that there is no surface reconstruction or interfacial ordering of PFPE-PEO in the PDMS/PFPE-POE blends at the solid liquid interface.

Further studies were performed on sample OFFPSEC 8 and OFFSPEC 11 these were samples produced from the same initial PDMS solution solution OFF-PEC 8 being produced from a fraction of this solution with added PFPE-PEO content such that the solution had a 2.2% PFPE-PEO content w/w to HT-PDMS as per Table4.1.

Modelling of NR spectra in D_2O and H_2O for both samples gain showed no evidence of surface change at the solid/liquid interface:

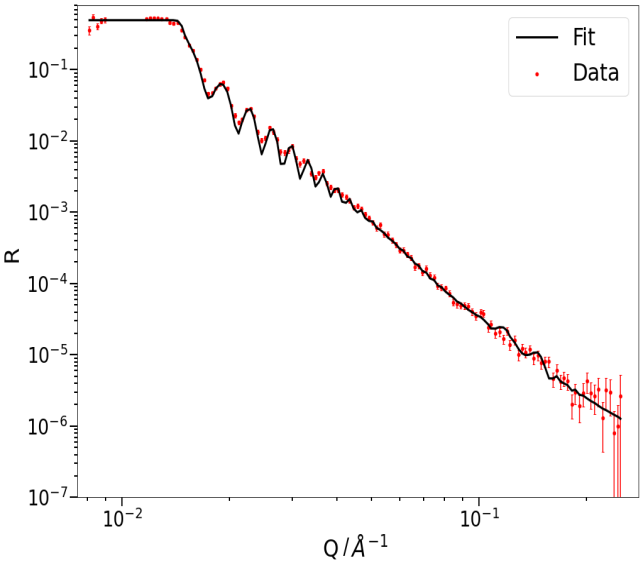

(a) OFFSPEC 11 in D_2O

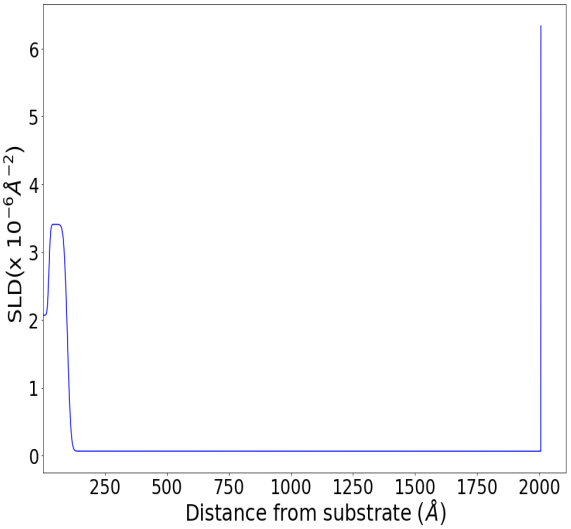

(b) Fitted SLD in D_2O

Figure 4.12: Fitted SLD for OFFSPEC 11 thin film in D_2O

The simulated fit in figure 4.12 was found to fit to data with an error of χ^2 fit of 3.02.

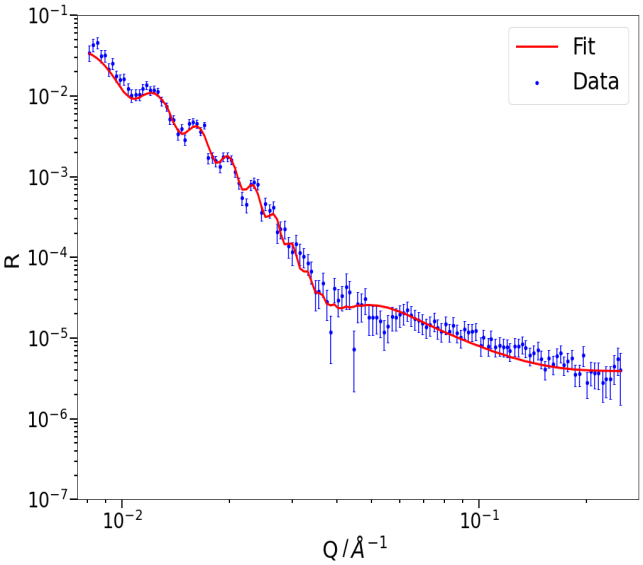

(a) OFFSPEC 11 in H_2O

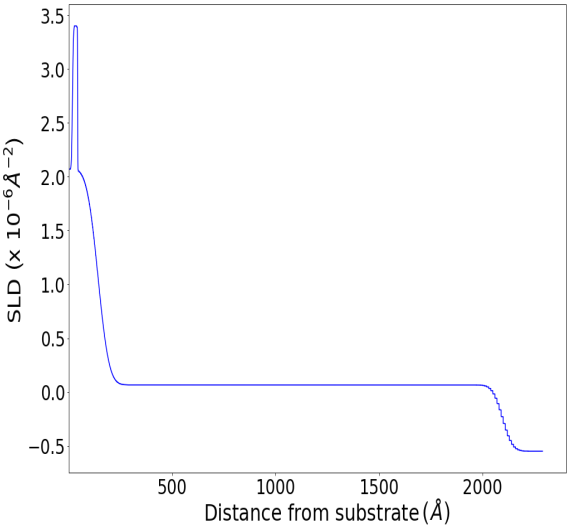

(b) Fitted SLD in H_2O

Figure 4.13: Fitted SLD for OFFSPEC 11 thin film in H_2O

The simulation in figure 4.13 was found to fit to data with an error of χ^2 fit of 3.02. χ^2 fit of 1.23.

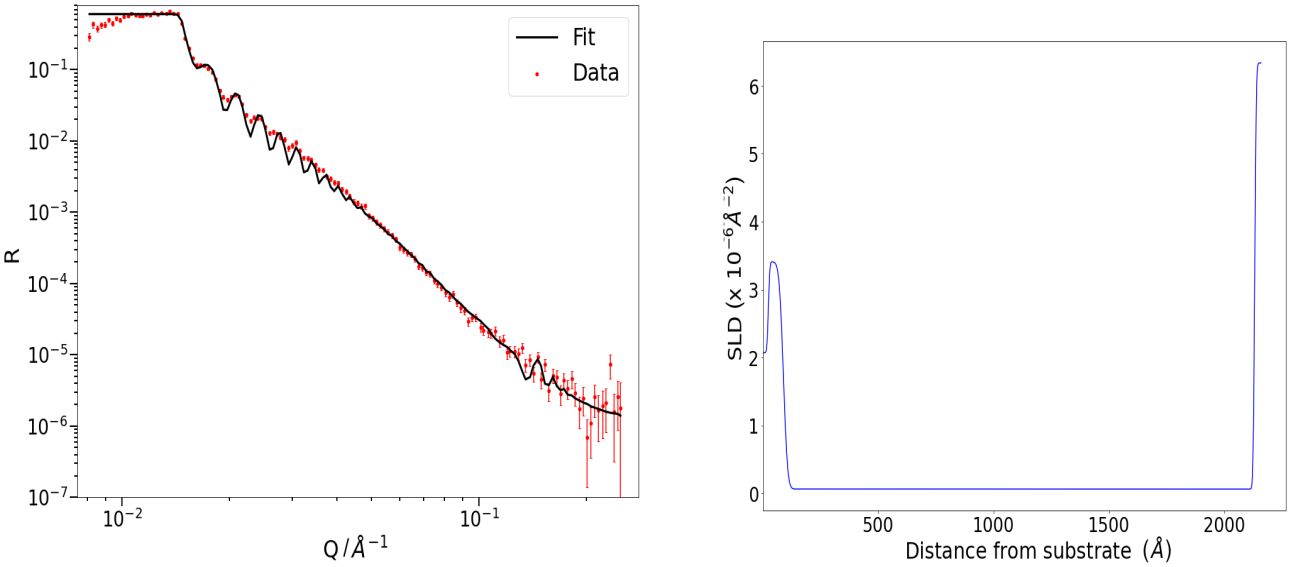

(a) OFFSPEC 8 in D_2O

(b) Fitted SLD in D_2O

Figure 4.14: Fitted SLD for OFFSPEC 8 thin film in D_2O

The simulated fit in figure 4.14 was found to fit to data with an error of χ^2 fit of 6.16 to an overall thickness of 208nm.

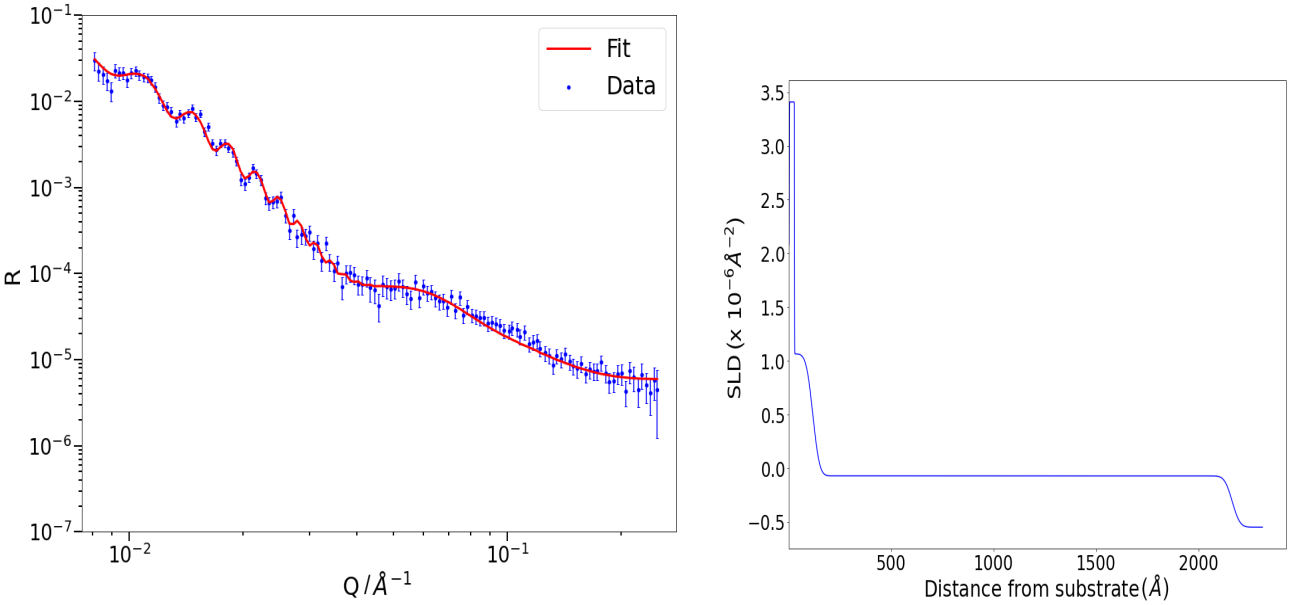

(a) OFFSPEC 8 H_2O (b) OFFSPEC 8 SLD in H_2O

Figure 4.15: Fitted SLD for OFFSPEC 8 thin film in H_2O

The simulated fit in figure 4.15 was found to fit to data with an error of χ^2 fit of 0.83 to an overall thickness of 212nm.

The model for both samples showed near identical structure in both structures with credible fits showing no evidence on an interfacial solid liquid layer of any kind. Hence we see from these solid liquid neutron experiments that surface reorganisation has not occurred on PDMS/PFPE-PEO blend thin film. With this result being counter to our hypothesis further analysis of these films were conducted post experiment using AFM to measure surface topography.

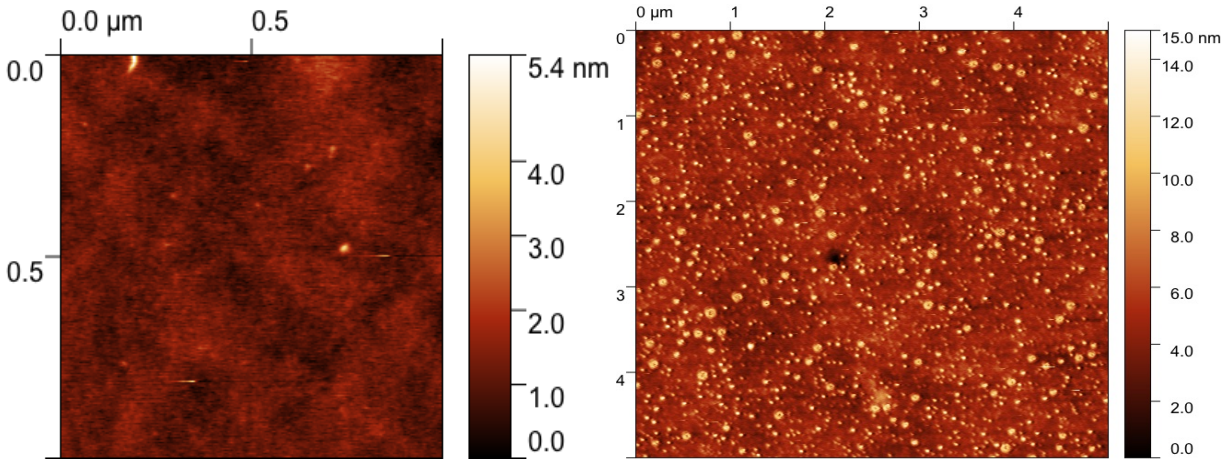

(a) OFFSPEC 1 (b) OFFSPEC 13

Figure 4.16: Post Experiment Height AFM images of OFFSPEC 1 and OFFSPEC 13.

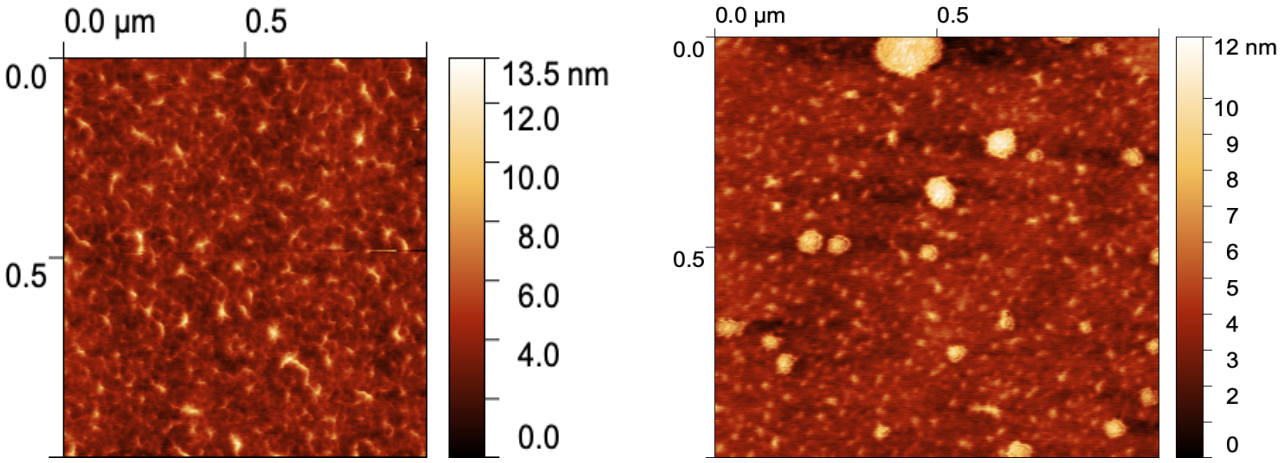

(a) OFFSPEC 11 1x1μm (b) OFFSPEC 8 1x1μm

Figure 4.17: Post experiment AFM height images for OFFSPEC 11 and OFFSPEC 8.

The AFM topography data figure 4.16 and 4.17 shows both similarities and contrasts between sample pairs. Firstly, addressing the PDMS base film OFFSPEC 1 and OFFSPEC 11 we find notable surface features; the 1x1μm image of OFFSPEC 11 figure 4.17a exhibits a mesh like structure on the surface of this simple PDMS film. This nonporous morphology is characteristic of PDMS successfully imaged at high resolution, with the mesh strands representing the distance

between crosslinking junction of chains of PDMS. Previous studies of PDMS surfaces have shown similar morphology with the structure becoming rougher and more prominent with increasing crosslinker concentrations [166] and typical mesh size on the order of nanometers to tens of nanometers. Although these studies used Sylgard PDMS and the crosslinking mechanism is different for the hydrolysis cure of HT-PDMS, in principle similar effects could occur with this PDMS as the degree of crosslinking increases as this morphology is due to the presence of molecular meshes in cross linked materials. This would explain the absence of similar morphology in the height image obtained for OFFSPEC 1 as the film has a lower crosslinker content (10% for OFFSPEC 1 and 18.6% for OFFSPEC 11) the lower crosslinking means there are more uncured, oligomeric PDMS chains in the film rendering the surface softer and more adhesive to the AFM cantilever tip, whilst the higher crosslinked film is more rigid and there are fewer uncured chains to stick to the cantilever and smear the image. Rms roughness values for OFFSPEC 1 and OFFSPEC 11 were 0.3nm and 1.08nm respectively.

Post experiment AFM corroborates expectations of droplet like formations on PDMS/PFPE-PEO blends (OFFPSEC 13 and OFFSPEC 8 figures 4.16b and 4.17b respectively) suggesting the presence of some amount of PFPE-PEO at the surface but the lack resulting surface activity in water is still surprising. With the diffuse silica crosslinking by product creating complicated neutron scattering profiles that obscure the presence of PFPE-PEO in the bulk of these blend films, XPS ion milling was used to determine the depth profile of fluorine and hence PFPE-PEO in OFFSPEC 8 a film spun from a solution with $\approx$ 2% PFPE-PEO solid content by mass.

This sample was selected as it was expected to have large enough fraction of PFPE-PEO to be detectable through the sample. OFFSPEC 8 has a solution composition of 2.2% PFPE-PEO w/w$_{PDMS}$, 18.6% TES 40 w/w$_{PDMS}$ and 1.9% ATPDMS w/w$_{PDMS}$, for the purposes of XPS this catalyst will be treated as PDMS as the nitrogen containing terminal groups are a small fraction of the molecule, meaning total PDMS mass is 101.9% of the HT-PDMS mass in solution. With a density of 1.73 g cm^{-3} for PFPE-PEO and 0.965 g cm^{-3} for PDMS and and a density 1.06g cm^{-3} for TES 40 we can find the volume fraction of PFPE-PEO from weight to be $\approx$ 1%. Based on the stoichiometry of Fluorolink PFPE-PEO described in section 1.5.4 fluorine is 36% of the non hydrogen elemental composition of this PFPE-PEO. Therefore we expect to detect from XPS an elemental composition of 0.36% fluorine in this blend sample.

Initial surface measurements of sample OFFSPEC 8 were performed prior to etching at two different points:

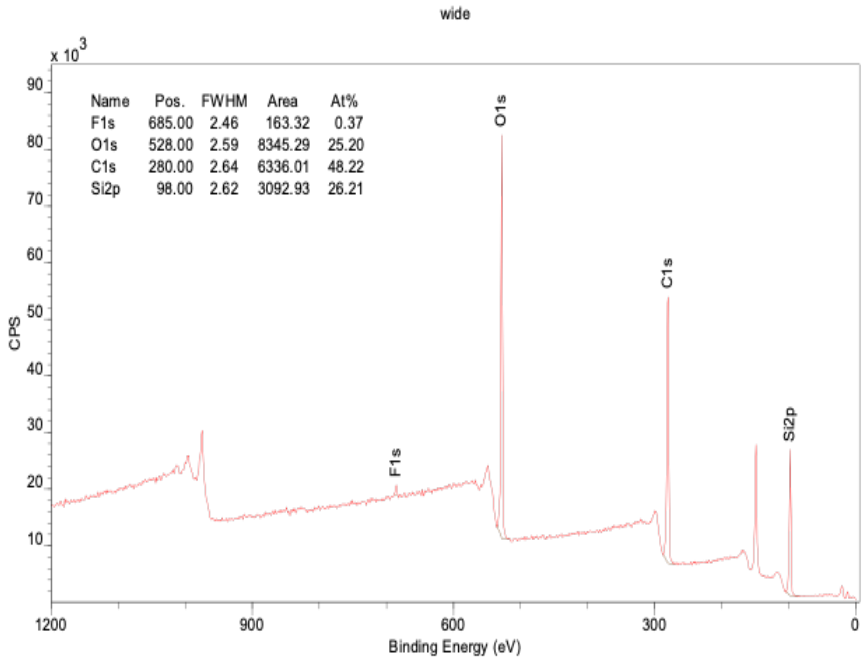

(a) 1st XPS surface spectrum for OFFSPEC 8.

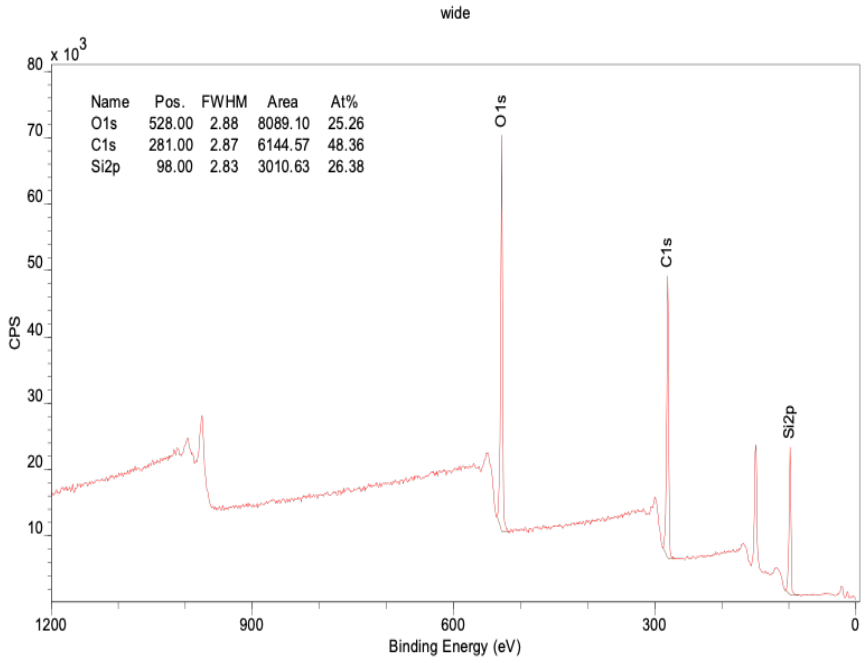

(b) 2nd XPS surface spectrum for OFFSPEC 8.

Figure 4.18: Pre and post experiment AFM images for Sample 2 PMS/PFPE-PEO (note sample suffered some surface abrasion during transit)

In this first XPS spectra figure 4.18a a small F1s signal is present which was determined to represent a 0.37% atomic surface composition. However, a second surface scan in a nearby region 4.18b finds no F1s signal above the detection limit of 0.1% atomic composition. This implies whilst PFPE-PEO is present at the surface it is at much lower concentrations than expected. Note also that ATPDMS catalyst was also not detected at the surface; nitrogen in the amino propyl groups would be represented by a N 1s peak at a binding energy $\approx$ 401eV [167] which is absent in both spectra.

Subsequently a depth profile was performed near the area scanned in figure 4.18a with XPS spectra taken after each etch of $\approx$ 10nm. With the sample having an ellipsometry measured thickness of 211nm a full depth profile of the sample could be etched effectively within a time frame $<$ 30 minutes. O1s Spectra attributable to oxygen in PDMS and oxygen in silicon oxide was monitored alongside F1s C1s and Si 2p spectra.

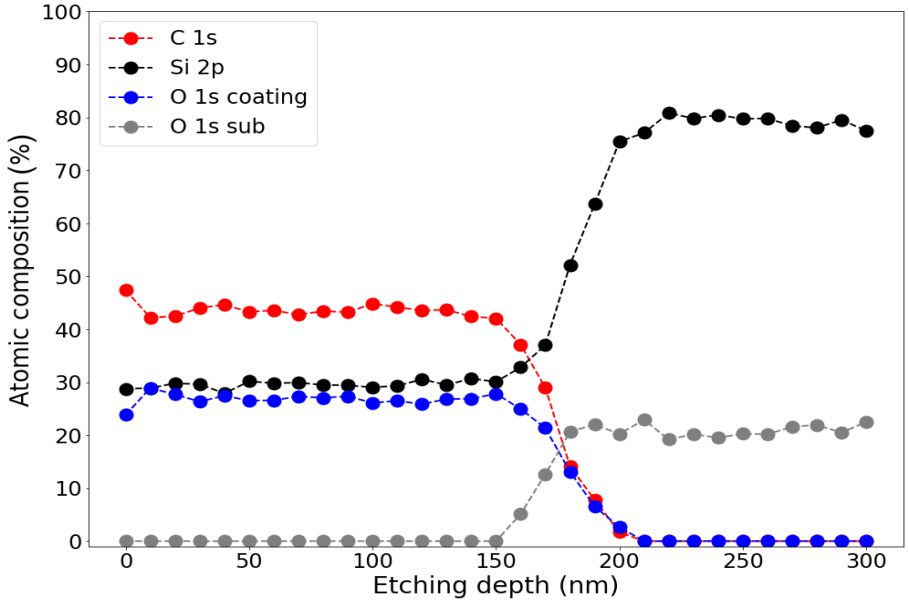

Figure 4.19: XPS atomic composition depth profile for sample OFFSPEC 8 with etch rate $\approx$ 10nm per 60s.

Upon etching, figure 4.19 shows no fluorine was detected across the entire sample depth. Fluorine was absent even at the surface, this can be explained by the higher signal to noise ratio at smaller area XPS scans used during ion etching.

The absence to fluorine suggests concentrations were below detection limits 0.1-0.2% and broadly uniform in distribution with some higher concentration at the surface where detection was achieved.

4.4.4 PDMS/PFPE-PEO blend samples in liquid discussion of Results

Although AFM and XPS spectra show some evidence for changes surface morphology and a minor surface enrichment of PFPE-PEO in PDMS blends, this proved to be very small with unreliable detection of fluorine via XPS and no apparent surface enrichment from in air neutron reflectivity. Water contact angle and in situ neutron reflectivity demonstrate no surface reconstruction in water and no interfacial layer of PFPE-PEO; surfaces appear unchanged.

When fitting blend neutron reflectivity samples in air samples were best fit with a small layer with a PDMS like SLD ($0.065\times10^{-6}\mathring{A}^{-2}$) which we hypothesise to be caused by hydrogen bonding of ATPDMS catalyst on silicon and a large diffuse (rough) layer with an intermediate SLD between 0 and 3.41 which we attribute to the silica by-product of TES 40 crosslinking of PDMS. As discussed, this has precedent in literature[136] but the presence of these wetting monolayers of catalyst has not been independently verified.

Depth profiling of sample OFFSPEC 8 formed from a solution with 2.2% PFPE-PEO solute content shows a far smaller overall content of PFPE-PEO in the sample than would be expected from the solution content. The mass fraction of Fluorolink PFPE-PEO in this sample resulted in a volume fraction of 1.02% so the expected elemental composition of fluorine in the sample was 0.36%. Even at the surface where an enrichment of the low surface energy PFPE-PEO may be enriched fluorine was inconsistently detected and the elemental composition of fluorine through the depth of the film was below detectable limits implying much smaller concentrations than expected. This provides some explanation for the lack of surface activity of PFPE-PEO in water; these attempted blend films of PDMS/PFPE-PEO do not result in the intended content of PFPE-PEO within the film. Therefore there may have an insufficient mass of the amphiphile within the coating for the expected surface reconstruction to occur. This disappointing result may be due to the aggregation effect observed in the models systems chapter, the filtering of solution necessary to produce defect free uniform thin films when spin coating may in fact be removing a significant fraction of PFPE-PEO from the solution in the form of these aggregates resulting a far smaller fraction in the final film. Surface effects such autophobic dewetting due to PFPE-PEO on silicon

at low catalyst concentrations observed in chapter 3 and nano-droplet topography seen in AFM images show PFPE-PEO has not been removed entirely from the films but the true concentrations are small and impossible to determine from the initial fractions prepared in solution. Given the challenges of producing these thin films that we have discussed previously, we consider the prospect of being able to produce sufficiently uniform and sufficiently thin sample films for neutron reflectivity that incorporate higher fractions of PFPE-PEO quite poor; aggregates are simply too large to form smooth films 200nm thick or less and filtering these aggregates leaves films with uncertain fractions of PFPE-PEO.

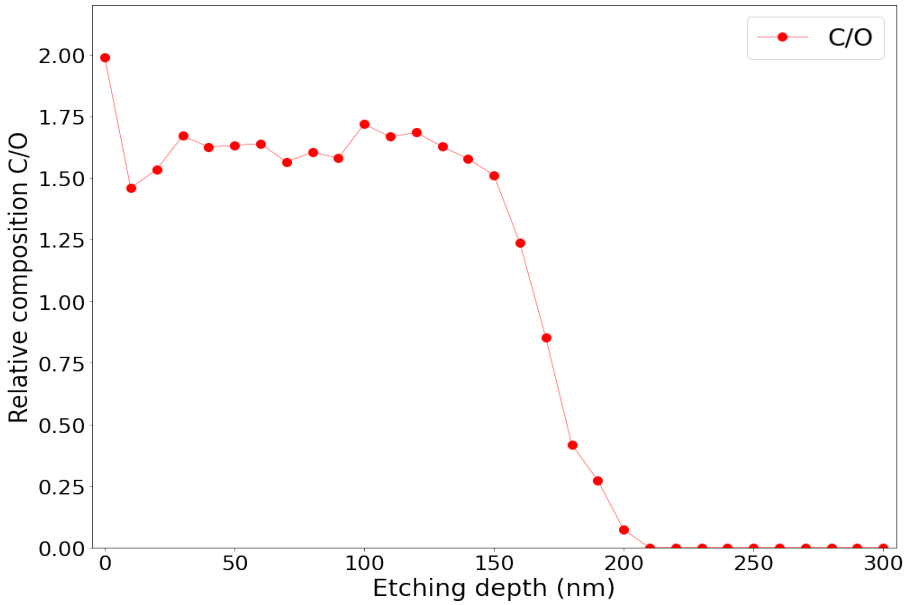

Figure 4.20: XPS atomic composition of carbon divided by atomic composition of oxygen through the depth profile of sample OFFSPEC 8 with an etch rate ≈ 10nm per 60s.

Considering again the XPS depth profile figure 4.19 we find some evidence for enrichment of silica at buried interface of the film near the substrate; the film is 211 nm thick, at an etch rate of 10 nm per 60 seconds we would expect the film to associated elemental spectra to decay as the substrate is reach after ≈ 1260 seconds, we can see that the C1s signal associated with the polymeric PDMS decays by this time as would be expected, a second etch at the location where the spectra in figure 4.18b was taken also shows carbon composition reaching a minimum after 1260s. However, the carbon composition of the surface has already begun to decline after

just 960s, which is ≈ 75% of the etch time for the film. This would be an etch dept of 160nm though the 211nm film, and should be tens of nanometers from the silicon substrate. Despite this, carbon C1s composition declines and O1s spectra with binding energy of 532.7eV [168] associated with silicon oxide or silica, could be discerned from the PDMS associated O1s of binding energy 532.0V [169] spectra showing the apparent presence of silica in the film well before the oxide layer of the substrate should be detectable. Similarly, The Si 2p signal, which could not be distinguished between silica and PDMS associated silicon, also rises at this stage in the etch.By normalising the carbon composition of the sample by the oxygen composition as per figure 4.20 we see that the carbon content falls sharply relative to oxygen at a depth of ≈ 160nm this would be consistent with the picture of an enriched volume fraction of silica and a depletion of the polymer in this region of the film. No evidence of any nitrogen containing species were detected in the film which would be indicative of the presence of ATPDMS catalyst. However the etch rate and depth profiling resolution of 10nm would be too high to necessarily detect such a small layer of sub nanometer according to neutron reflectivity fits.

A simple experiment that might be able to verify the enrichment of silica at the buried interface in these cured PDMS films would be to conduct XPS depth profiling on thinner films (perhaps 60nm films which would be viable to produce via spin coating) conducted with smaller etches between surface measurements perhaps 1nm per etch. If this was performed on a film formed from TES 40 and ATPDMS catalyst and a second film in which this same silica byproduct from crosslinking is not expected such as a thermally cured vinyl terminated PDMS, the depth profile and silicon, oxygen and carbon composition through the thickness of the film could then be compared between films. An enriched silica layer in TES 40 cured films would be indicated by a fall in carbon concentration, rise in silicon concentration and a change in the oxygen O1s spectra further from the substrate than in thermally cured PDMS films. Shorter etches, profiling the film nanometer by nanometer may also increase the likelihood of detecting a substrate wetting monolayer of ATPDMS, although this will still be challenging as the nitrogen content that differentiates the molecules from other components in the film is small in ATPDMS; the molecule only contains two nitrogen atoms and at least eight repeat units of the PDMS monomer so even a 100% amino propyl terminated PDMS bulk film would have a small nitrogen composition ≈ 2%.

4.5 Surface reconstruction in PDMS/PFPE-PEO topcoat films.

Having found no evidence of surface reconstruction in spin coated blend samples we consider the prospect that these model films could not be produced with both the desired thickness and controlled significant concentrations of PFPE-PEO to determine the surface activity of the amphiphile molecules in these foul release coatings. Without a viable way of producing these films that could be analysed with neutron reflectivity and had a good depth concentration of the additive we consider instead model thin films optimised solely for considering surface interfacial effects. We produced thin films of PDMS upon which a layer of PFPE-PEO was directly spin coated from a given solution from which surface analysis in air and on water would then be conducted(wetting behaviour, topography response to water).

Although crude in construction these models have the advantage of being far simpler to produce and allowing much more control and confidence over the applied PFPE-PEO content; by applying the amphiphile directly onto an already cured film we can have far more confidence in having applied a non negligible fraction of he additive to the system without the loses and ambiguity of using mixed solvent solutions and filtering aggregates from blend films.

PDMS based foul realise coatings were supplied to us for analysis by Akzo Nobel in which the PFPE-PEO Fluorolink E10/6 is mixed into PDMS elastomer (PFPE-PEO /PDMS FR). These coatings used HT-PDMS crosslinked using TES 40 and a dibutyltin dilaurate catalyst. Wet coatings were applied on perspex substrates and left to cure via hydrolysis, resulting in 300μm thick dry coatings. Inspection of these coatings using optical microscopy (figure 4.21) and AFM (figure 4.22) in air on both top and bottom surfaces provides evidence of droplet like features on the top surface.

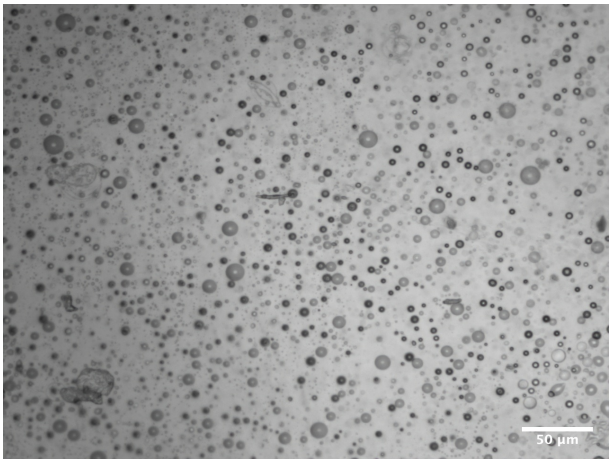

(a) topside of coating

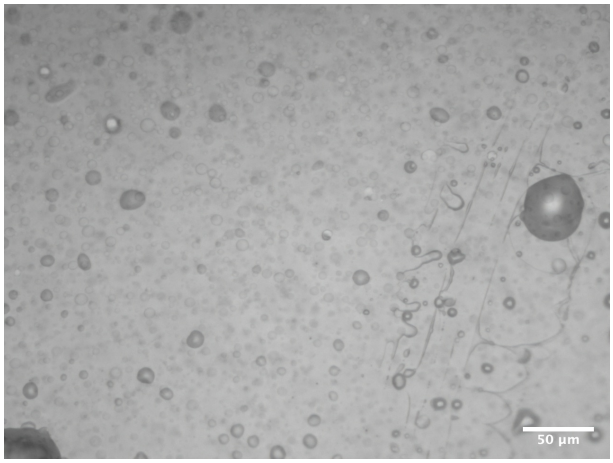

(b) Underside of coating.

Figure 4.21: 20x magnification optical images of PFPE-PEO /PDMS FR coating top side and underside.

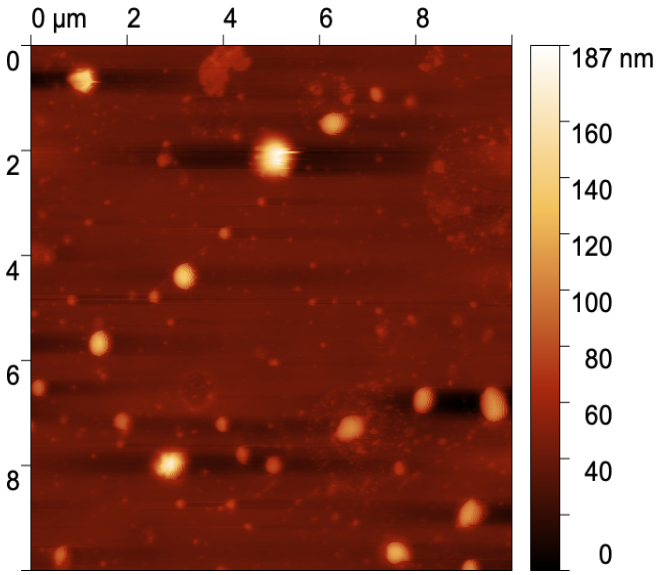

Figure 4.22: 1010μm AFM height image of top surface of PFPE-PEO/PDMS FR coating.

SIMS analysis of these coatings taken in preliminary data prior to the commencement of this project also indicated the dark droplet features in figure 4.43a are rich in fluorine suggesting these are droplet like features on the surface of the

coating. This would mean samples formed by the bilayer deposition of a topcoat of PFPE-PEO on PDMS would be representative of equivalent surfaces of bulk practical foul release coatings making findings from these thin films models directly applicable to their macro equivalent coatings.

4.5.1 PDMS/PFPE-PEO topcoat models films: methods

4.5.1.1 Topcoat preparation and in air analysis.

PDMS/PFPE-PEO topcoat models were prepared by first spin coating a thin film of PDMS on silicon. Typically these films were formed from HT-PDMS(3500Cst, M_w 43500, Sigma) , with TES 40 crosslinker(Wacker) and ATPDMS catalyst (Gelest) in n-hexane at recorded w/w ratios ones formed on silicon these films were left to cure in ambient conditions for at least 24 hours. Once crosslinked, PFPE-PEO (Fluorolink E10/6, Solvay) would then be spin coated directly on top of these PDMS films from solutions of acetone, acetyl acetone or methanol/ethanol at known concentrations w/w. These films were then analysed with optical microscopy to assess the wetting of PFPE-PEO on PDMS. The hydrophilicity of these systems was tested with water contact angle goniometry. AFM studies were performed of these surfaces with a particular focus on any droplet like formations on the surface. SIMS analysis of these surfaces was performed to ascertain the distribution of surface PFPE-PEO and whether partial or total dewetting of the amphiphile on PDMS occurs. To determine a surface energy value for PFPE-PEO, a pendant drop experiment was performed using the liquid PFPE-PEO Fluorolink E10/6.

4.5.1.2 D17 Neutron reflectivity of topcoat systems in air and in water.

Neutron reflectivity measurements of PDMS/PFPE-PEO topcoat films was conducted in air and in water using the D17 Reflectometer at the ILL.

Samples were prepared on 50x50x10mm silicon square blocks (sourced from Si'ltronix and Crystran). All PDMS films were produced by spin coating from the same solution of a HT-PDMS, M_w=43500 g/mol in n-hexane at a concentration of 1.5% w/w of solvent, with crosslinker TES 40(Wacker) 10.2% w/w$_{HT-PDMS}$ and ATPDMS catalyst(Gelest) 1.2% w/w$_{HT-PDMS}$. Four PDMS films were spin coated from this solution on silicon blocks at 3000 rpm. Films were left to cure in ambient conditions for 24 hours before PFPE-PEO (Fluorolink E10/6, Solvay) was

deposited on three of the samples at various concentrations; 2.5 % in methanol at 1500rpm, 11% in ethanol at 1500 rpm and 11% from ethanol at 3000 rpm. Equivalent PFPE-PEO films were spun onto pmma coated silicon a substrate upon which the films are stable enough to obtain an ellipsometry value of film thickness. All silicon oxide layers and PDMS thickness were measured with ellipsometry prior to the experiment.

A sample from the OFFSPEC reflectivity experiment is also presented here OFFSPEc 16: a PDMS thin film (spin coated and ambiently cured from a solution with 21.2% TES 40 crosslinker and 1.8% catalyst w/w$_{PDMS}$) with a layer of PFPE-PEO spin coated on top from a 16.3% w/w solution in acetone at 3000rpm, the size of this layer could not be verified as pmma is soluble in acetone so stable layers cannot be deposited on these substrates.

The D17 reflectometer was set in unpolarised time of flight mode capable of collecting the fastest measurements. Reflectivity was collected at 2 angles producing spectra across a Q range of 0.08 to 0.35$\mathring{A}^{-1}$. All samples were measured in air prior to performing neutron reflectivity in water. Samples were placed in ILL standard solid/liquid cells for 50x50mm substrates (figure 4.23). Cells had a liquid volume of $\approx$ 0.5 ml, cells were filled using an HPLC pump at a rate of 2 m per minute for 15 minutes (30ml through cell). Samples were measured in D_2O, H_2O and for some in silicon contrast matched water, produced by mixing volumes of H_2O and D_2O at volume fractions of 0.35:0.65 respectively.Each contrast was replaced by flushing through 30 ml of the new contrast over 15 minutes at a rate of 2ml/min for 60 times the cell volume. Spectra were collected for both angles over extended time periods depending on the contrast in order to ensure strong statistics; 105 minutes in air, 70 minutes in D_2O, 110 minutes for Si match water and 110 minutes for H_2O.

One PDMS/PFPE-PEO topcoat sample was aligned in an empty solid/liquid cell and then measured using rapid 1 minutes first angle scans during cell filling with D_2O in order to assess the fill rate and attempt to observe the kinetics of any surface reconstruction upon exposing the sample to water. Acquired reflectivity was fitted using Genx and motofit software.

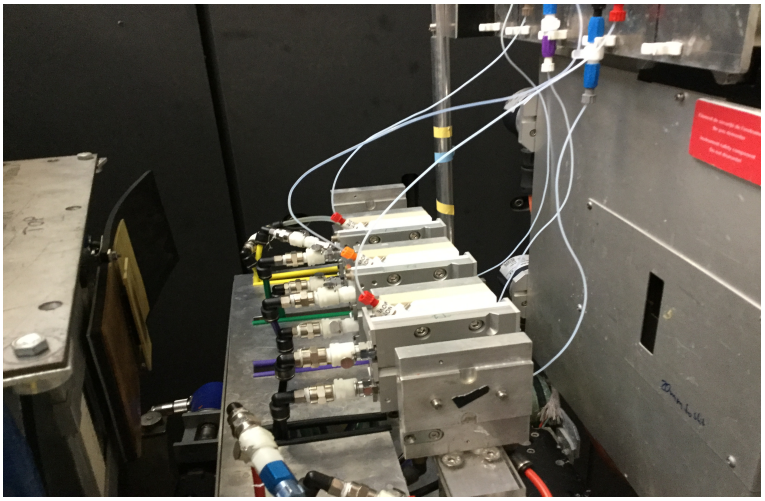

Figure 4.23: Reflectivity setup: 50x50mm square samples in ILL solid/liquid sample cells connected to a HPLC pump and aligned on the D17 sample stage.

4.5.1.3 Quantitative imaging(Qi) liquid AFM of PDMS/PFPE-PEO topcoat films

Quantitative imaging AFM in liquid was performed on a set of PDMS/PFPE-PEO topcoat thin films in deionised water using the JPK nanowizard AFM (Bruker). The cantilever tip used was a Fastscan-D with a tip radius of 5nm and a spring constant of 0.4N/m. Force curves were acquired and analysed using the JPK software alongside images of height and adhesion.

Films of PDMS were prepared from spin coated solutions with thickness $\approx$ 250nm. Once cured, layers of Fluorolink E10/6 PFPE-PEO were applied to two films; one from a 2.5% PFPFE-PEO dispersion in ethanol at 1500rpm and on a second sample a much larger layer of PFPE-PEO was applied from a 25% w/w in acetone solution. these two PDMS/PFPE-PEO topcoat samples were probed in water alongside a single PDMS thin film as a control.

Samples with PFPE-PEO layers applied from 25% w/w acetone solution were intended to act as a similar topcoat films to a sample measured with neutron reflectivity at the ILL; sample T1. This sample showed evidence of a complex structure forming at the solid liquid interface, the precise thickness of the deposited PFPE-PEO layer on PDMS could not be directly measured but films of PFPE-PEO 1μm thick on PMMA have been produced from the 25% solution at at a spin

rate of 1500rpm, forming a layer larger than that deposited on sample T1.

4.5.2 Results and analysis

4.5.2.1 PFPE-PEO topcoats in air

By Spin coating layers of PFPE-PEO on cured PDMS thin films we can assess the wetting behaviour and interaction of these two molecules in air.

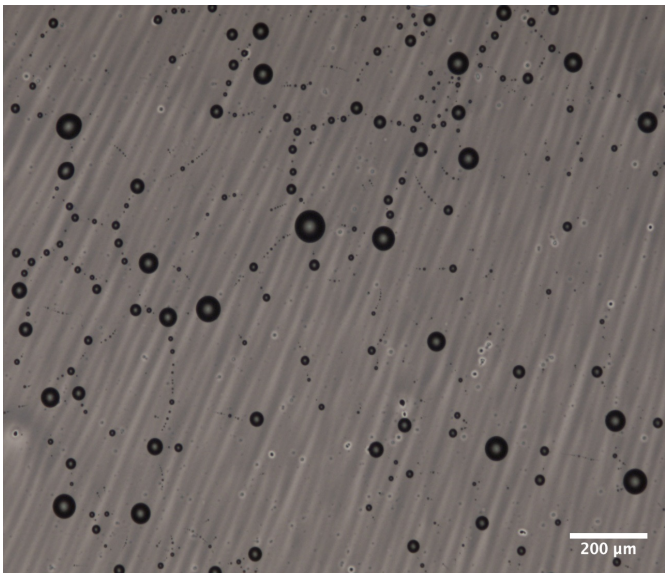

Figure 4.24: 10x magnification optical micrograph of a de-wetted PFPE-PEO on PDMS.

figure 4.24 shows that rather than forming a bilayer, when in air the spin coated liquid layer of PFPE-PEO de-wets readily, within the typical spin time of 60s. Forming optically visible microscopic droplets apparent on the surface. Testing these dewetted topcoats with deionised water contact angle we see markedly different wetting behaviour than was observed for PDMS/PFPE-PEO blend films.

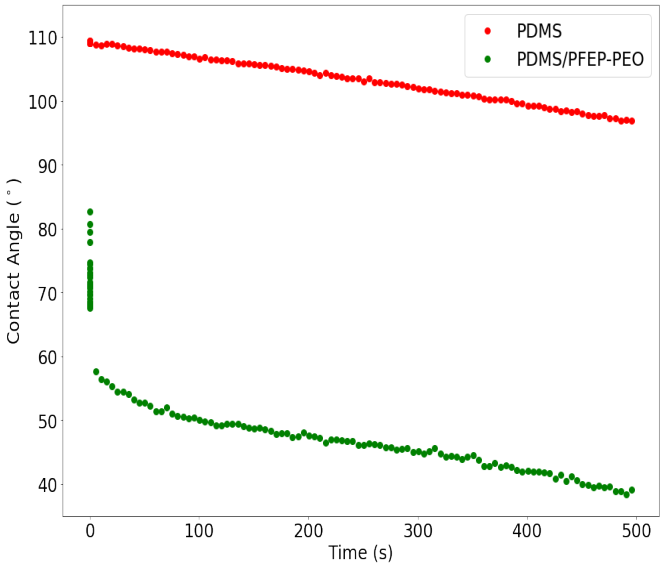

Figure 4.25: Water contact for thin films of PDMS and a dewetted PFPE-PEO topcoat layer on a PDMS film.

We can see in figure 4.25 that water rapidly wets on these topcoat films to a much more hydrophilic angle of 45° as the equivalent PDMS film sees only a small reduction of the contact angle due to evaporation loses over almost 10 minutes, whilst water spreads on these topcoat films a matter of seconds. This is a much greater and much faster change than observed in any attempted PDMS/PFPE-PEO blend films and is possible indicative of a change in the surface chemistry of the solid liquid interface that radically reduces the interfacial tension between water and the silicone film.

Similar topcoat films were fabricated using a very dilute dispersion of PFPFE-PEO; 0.1% PFPE-PEO w/w in acetone onto PDMS films. The AFM surface topography measurements in figure 4.26 show that this application of PFPE-PEO from solution produced droplets on the surface on the scale of micrometers.

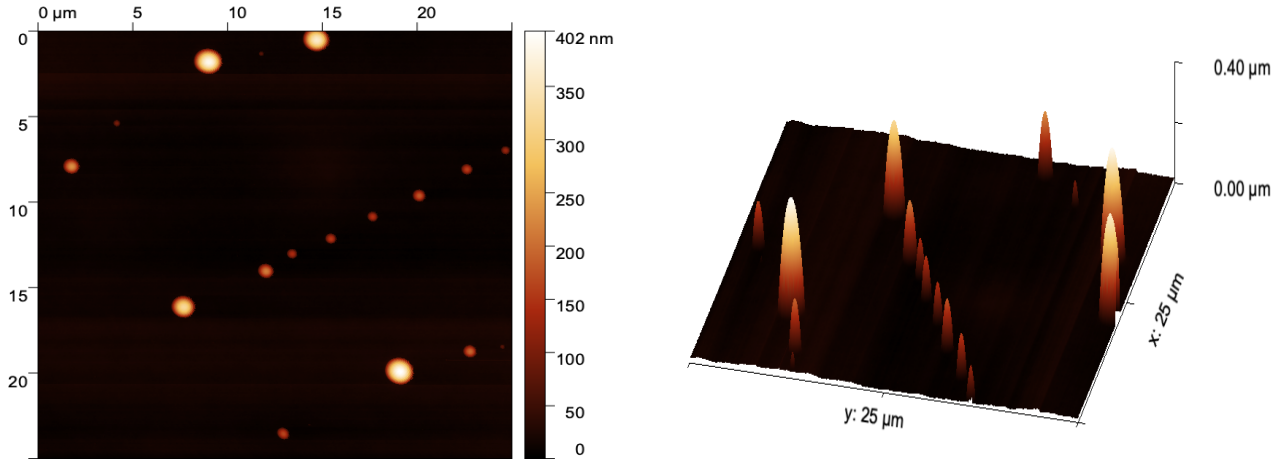

(a) 0.1%

(b) 3D projection.

Figure 4.26: 25x25 μm AFM height image of 0.1% PFPE-PEO spun on PDMS at 3000rpm.

Droplet formation can be observed on these surfaces which we consider to be individual droplets of PFPE-PEO de-wetted on the PDMS. By plotting the height profile of these observed droplets we can find values for the Contact angle of liquid PFPE-PEO on PDMS surfaces; as PFPE-PEO is a viscous liquid at room temperature it will from droplets with spherical cap geometry on the wetting surface, if the droplets have a wetting angle above 90° the formation will appear as semi capsule like shapes with large step heights at the edges of the features as the contact point will be underneath the diameter of the droplet and will not be captured by the top down imaging mode of an AFM cantilever tip. If the contact angle is less than 90° the height profiles can be observed from the peak height of the profile h and the base radius a. We can determine the radius R of the sphere of which this cap is a segment by the equation:

$$R = \frac{a^2 + h^2}{2h} \tag{4.1}$$

And the contact angle of the droplet α can be determined from the radius and cap height is:

$$\alpha = sin^{-1}\left(\frac{R-h}{R}\right) \tag{4.2}$$

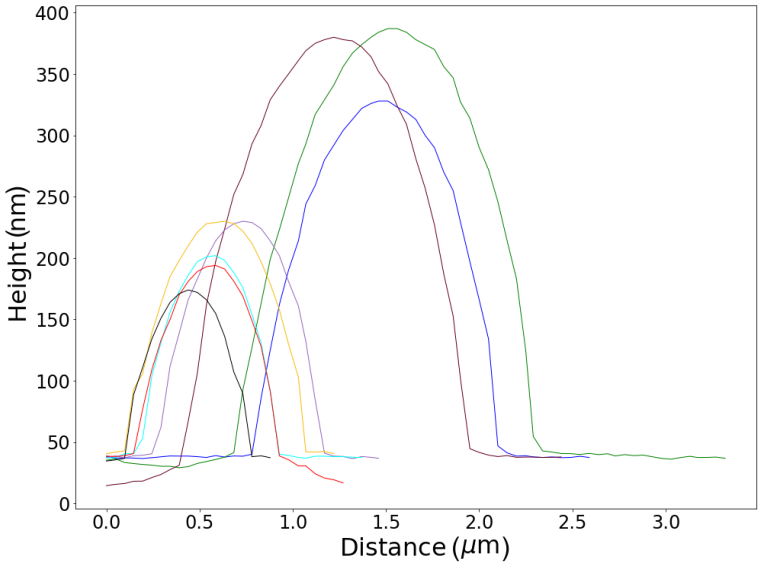

Figure 4.27: Height profiles of droplets of PFPE-PEO on PDMS observed in AFM image figure 4.26

Height profiles found in figure 4.27 yielded an average contact angle for these microdroplets of 45.2±1.3°, in good agreement with a single measurement of the contact angle of a macrodroplet of 45°. A value of the surface energy of PFPE-PEO was determined by carrying out a pendant drop experiment and using a density value of 1.77gcm^{-3} as 20.6mJm^{-2} with the method first verified by using deionised water which found for the surface energy of 71.2mJm^{-2} in good agreement with the accepted literature value of 72.8mJm^{-2}. With this value for PFPE-PEO surface tension, contact angle and a value for the PDMS surface tension of 22.8Jm^{-2} as determined from the PDMS thin film in Table 4.2 of 22.8mJm^{-2} the PFPE-PEO/PDMS interfacial tension in air was determined as$\gamma_{PFPE-PEO/PDMS}$= 8.28mJm^{-2}.

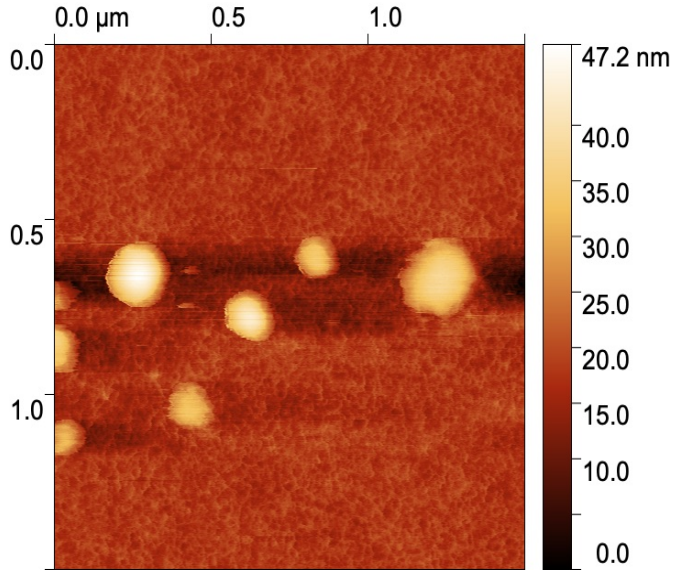

Figure 4.28: High resolution 1x1μm AFM height image of PFPE-PEO droplets on PDMS.

Figure 4.28 a higher resolution image taken of these surfaces showed the uncovered PDMS surface had a mesh topography characteristic of the crosslinkined PDMS surfaces[166]. In previous experiments spin coating PFPE-PEO onto silicon surfaces revealed a dewetting induced by the autophobic dewetting of the fluoropolymer from it's own bonded monolayer on silicon oxide. The appearance of characteristic PDMS surface structure of films coated with PFPE-PEO suggests that dewetting here is total and there is no monolayer of the amphiphile coating the PDMS. Nor would we expect such a monolayer to form on PDMS as it is a very non polar material so the OH termination groups of PFPE-PEO are unlikely to bond strongly to this surface as they would to an oxide.

To further confirm this, SIMS image analysis was performed on a sample of PDMS with a thin layer of PFPE-PEO spin coated on top from a 2% in ethanol solution at 1500 rpm. Droplets were identified on the surfaces and SIMS mass spectrometry was applied with a focus on the presence of fluorine (19 atomic mass units) and the signature mass fragment of the repeating PDMS block identified by fragments of 75 atomic mass units.

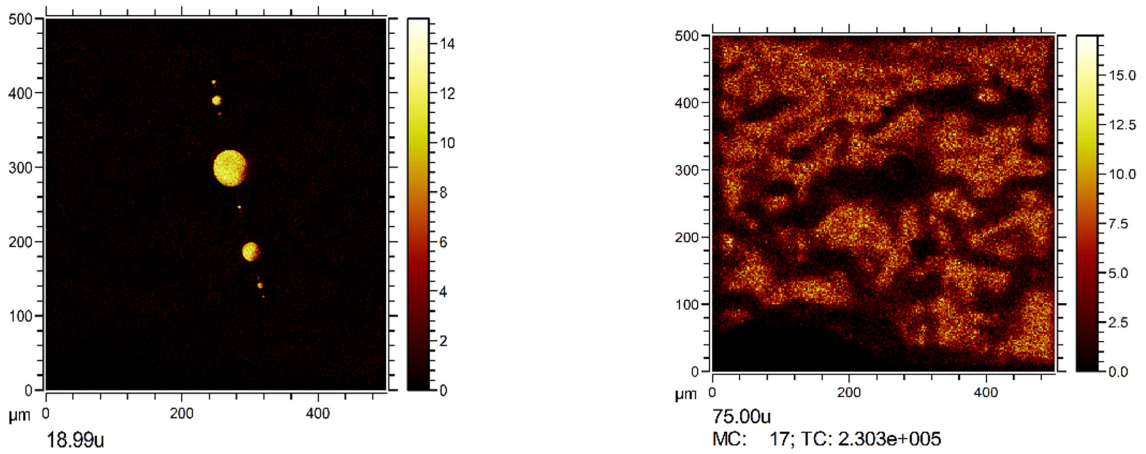

(a) 19 mass u (Fluorine).

(b) 75 atomic mass units (PDMS monomer)

Figure 4.29: 500x500 μm SIMS image of dewetted topcoat of PFPE-PEO on PDMS.

Figure 4.29 identifies surface droplet features rich in fluorine but little to no fluorine distributed across the rest of the surface where PDMS associated fragments are present at a much higher concentration (observe the dark circular region at 300x300 in 4.29b corresponding the the largest fluorinated droplet). In contrasts to dewetted blends on silicon we see no evidence of surface coverage of fluorine and no broad monolayer on the surface.

From these experiments the interfacial tension between PDMS and PFPE-PEO has been established with no indication of partial or total wetting of PFPE-PPEO on the surface in air but some evidence of a surface change in liquid.

4.5.3 Neutron analysis D17 ILL

Prior to performing Solid/Lquid neutron experiments all prepared samples were pre characterised with ellipsometry

Table 4.3: Table of Samples and basic dimensions derived from ellipsometry.

Sample	Oxide Thickness (nm)	PDMS Thickness (nm)	Equivalent PFPE-PEO thickness on PMMA (nm)
T1 PDMS with 3000rpm 11% PFPE-PEO in ethanol	1.85	104.39	330
T2 PDMS	1.71	80.32	N/A
T3 PDMS with 1500rpm 5% PFPE-PPEO from ethanol	1.69	82.88	45
T5 with 1500rpm 2.5% PFPE-PEO from ethanol	1.69	78.66	30
OFFSPEC 16 PDMS with 3000 rpm 16.3% PFPE-PEO in acetone	2.15	153.4	N/A

In stark contrast to the previous PDMS/PFPE-PEO blend samples examined at OFFSPEC, when measured in D_2O there was a stark difference between topcoat samples and the PDMS standard sample T2:

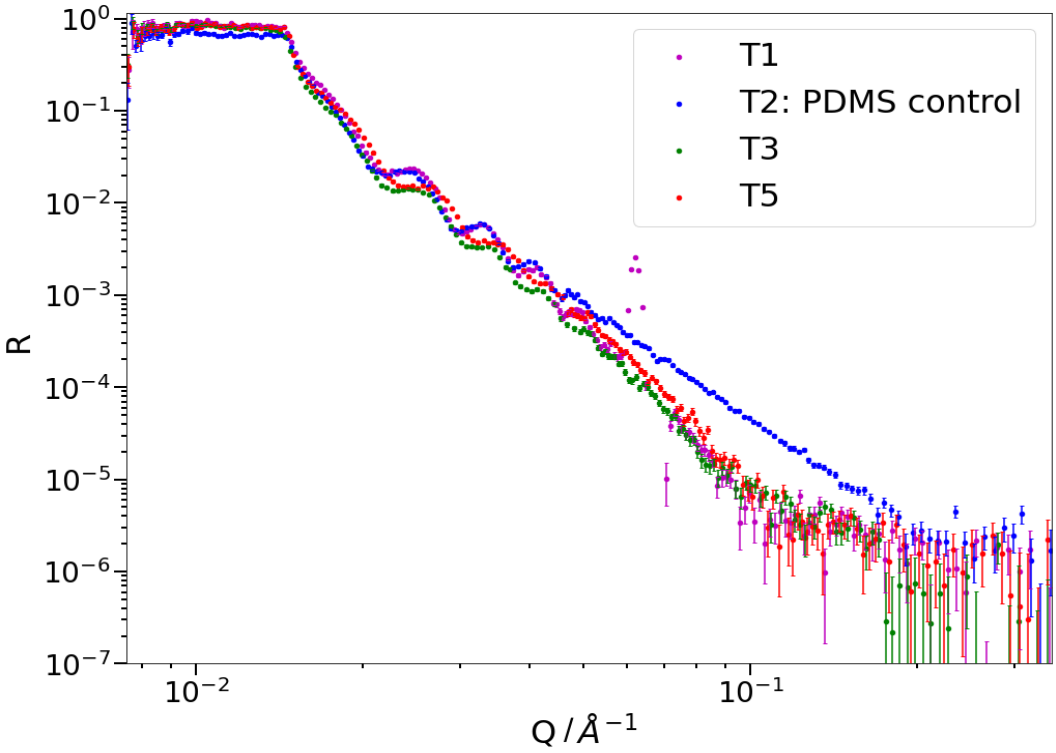

Figure 4.30: Neutron reflectivity curves for all T samples in D_2O.

The reflectivity measurements in figure 4.30 show that all PFPE-PEO containing samples follow the same reflectivity decay at higher Q and are in accord with each other. However, sample T1, upon which a much thicker layer of PFPE-PEO was applied, also shows a Bragg peak structure which shall be discussed later.

Considering first sample T5, in figures 4.31, 4.32 and 4.33 fits were obtained in D_2O, Si matched water and H_2O respectively, with low degree of error:

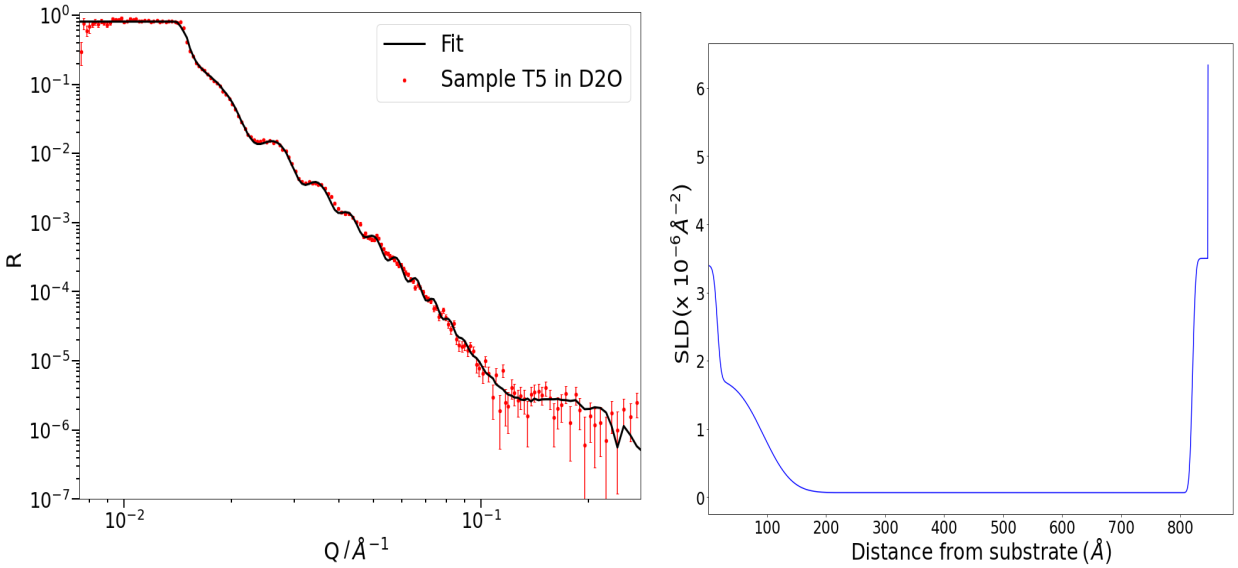

(a) T5 in D_2O (b) SLD for fit in D_2O

Figure 4.31: Neutron reflectivity for T5 thin film in D_2O

The simulation shown in figure 4.31b fit to data with an error of χ^2=5.99.

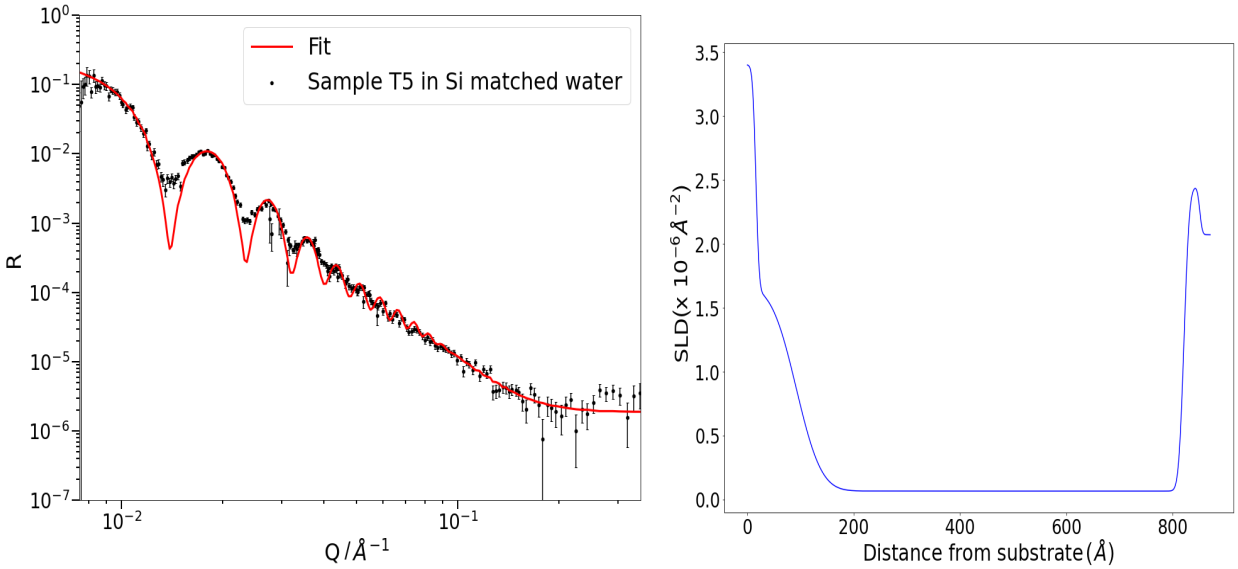

(a) T5 in Si matched water (b) SLD for fit in Si matched water

Figure 4.32: Neutron reflectivity for T5 thin film in Si matched water.

The simulation shown in figure 4.32 for sample T5 in Si matched water fit to data with an error of χ^2=7.27.

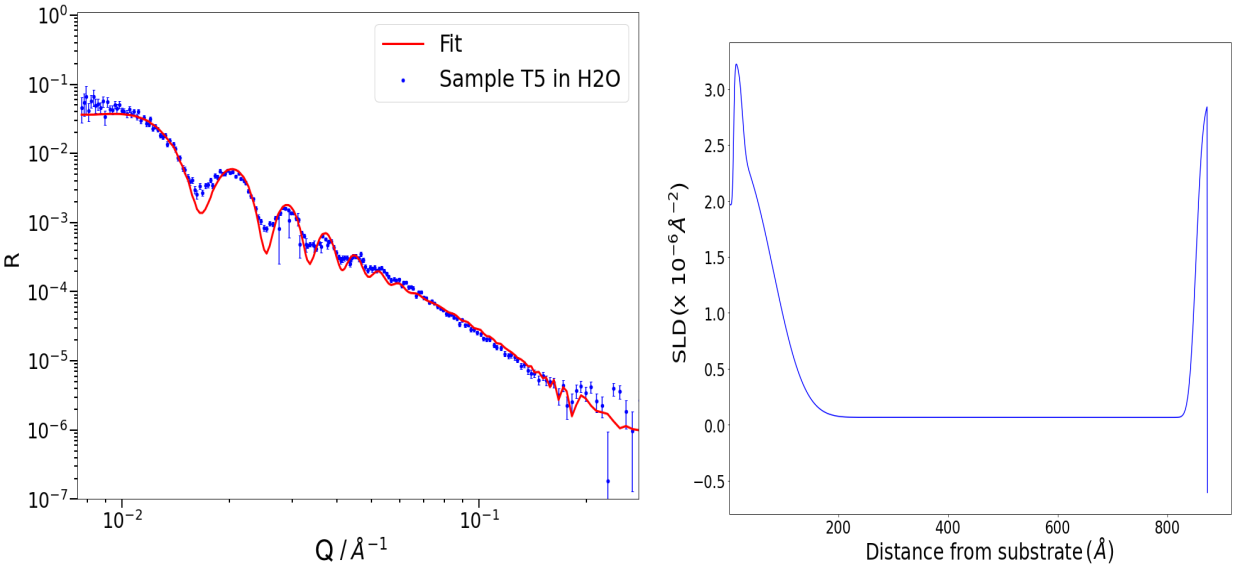

(a) T5 in H_2O (b) SLD for fit in H_2O

Figure 4.33: Neutron reflectivity for T5 thin film in H_2O

The simulation in figure 4.33 for sample T5 in H_2O achieved an error fit of χ^2=5.82. All fits were achieved using a very similar model of a small diffuse silica layer at the substrate and some small layer at the solid/liquid interface. In both fits we find evidence of a very thin layer at the surface in water with a much higher SLD than the PDMS film.

Considering also OFFSPEC 16 a PDMS/PFPE-PEO topcoat sample made and tested at the OFFSPEC Reflectometer also reveals a similar interfacial layer in water.

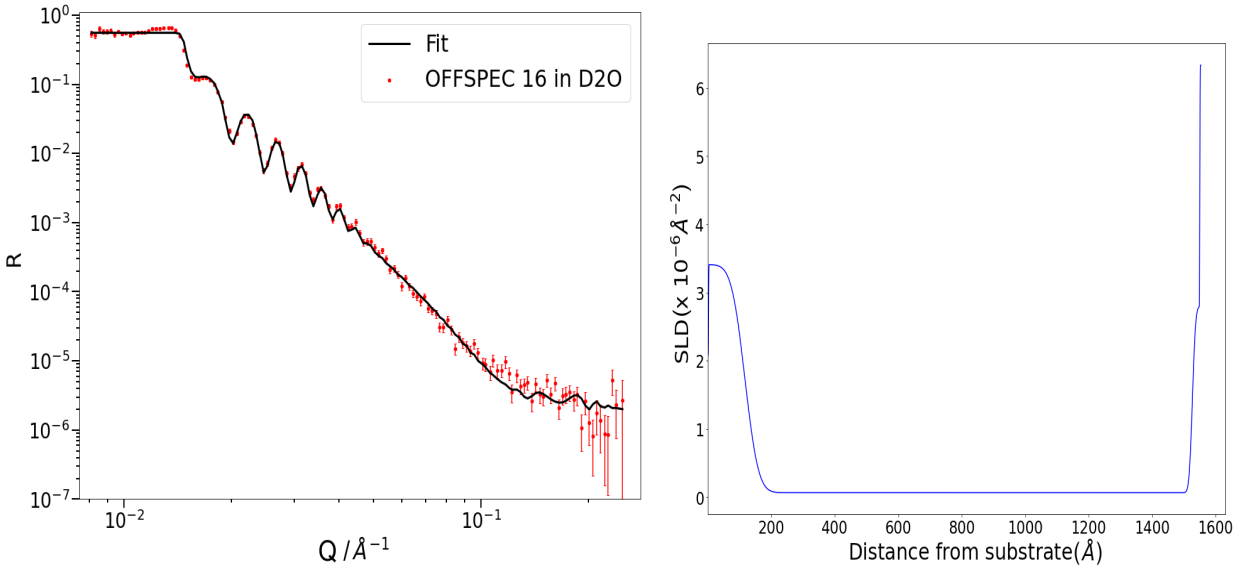

(a) OFFSPEC 16 in D_2O (b) SLD for fit in D_2O

Figure 4.34: Neutron reflectivity for OFFSPEC 16 thin film in D_2O

The simulation in figure 4.34 sample OFFSPEC16 in D_2O fit to data with an error of χ^2=3.12.

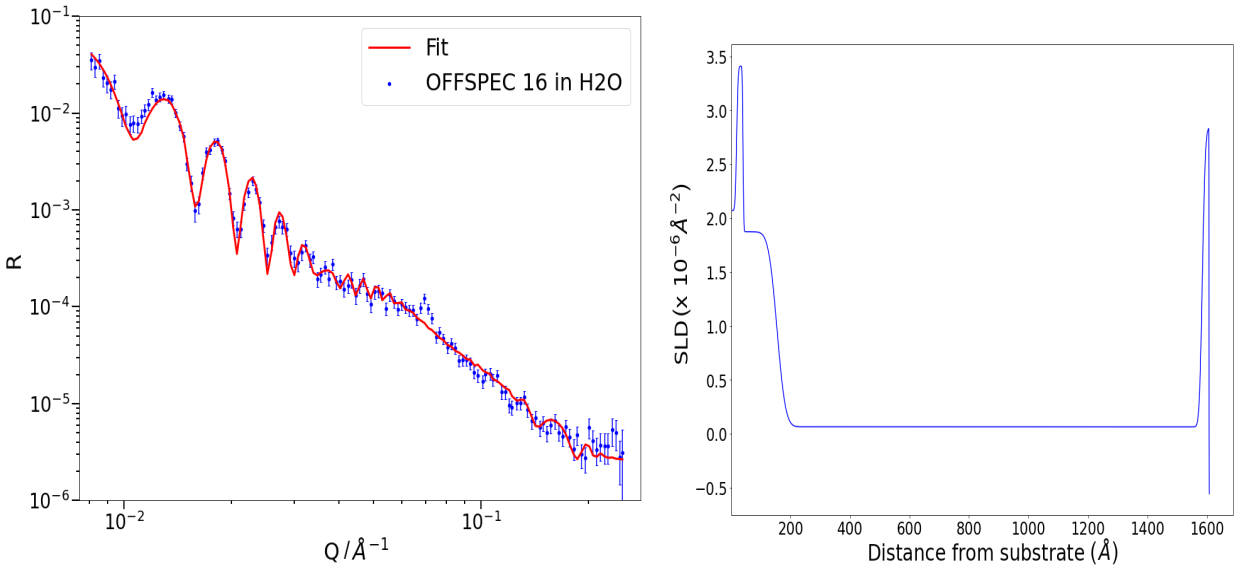

(a) OFFSPEC 16 in H_2O (b) SLD for fit in H_2O

Figure 4.35: Neutron reflectivity for OFFSPEC 16 thin film in H_2O

For sample OFFSPEC16 in H_2O the simulation achieved a fit to data with an error of χ^2=1.55. The result from this OFFSPEC measured sample shows that the interfacial layer that develops in liquid is repeatable and observable across experiments and sample types, independent of the batch of samples fabricated or the instrument used to measure the reflectivity. Although intensity of reflectivity spectra is reduced somewhat we were able to acquire good reflectivity spectra from these samples, many samples have large macro dewetted patterns on the surfaces as seen in figure 4.24 but these droplets are separated by micrometers, regions covered by micrometers will scatter neutrons in an irregular fashion and will not contribute to the scattering from the aligned surface interface so the overall reflectivity will be reduced but these droplet formations do not contribute to the specular reflectivity as the lateral coherence length of neutrons are ≈ 20-30μm [76].

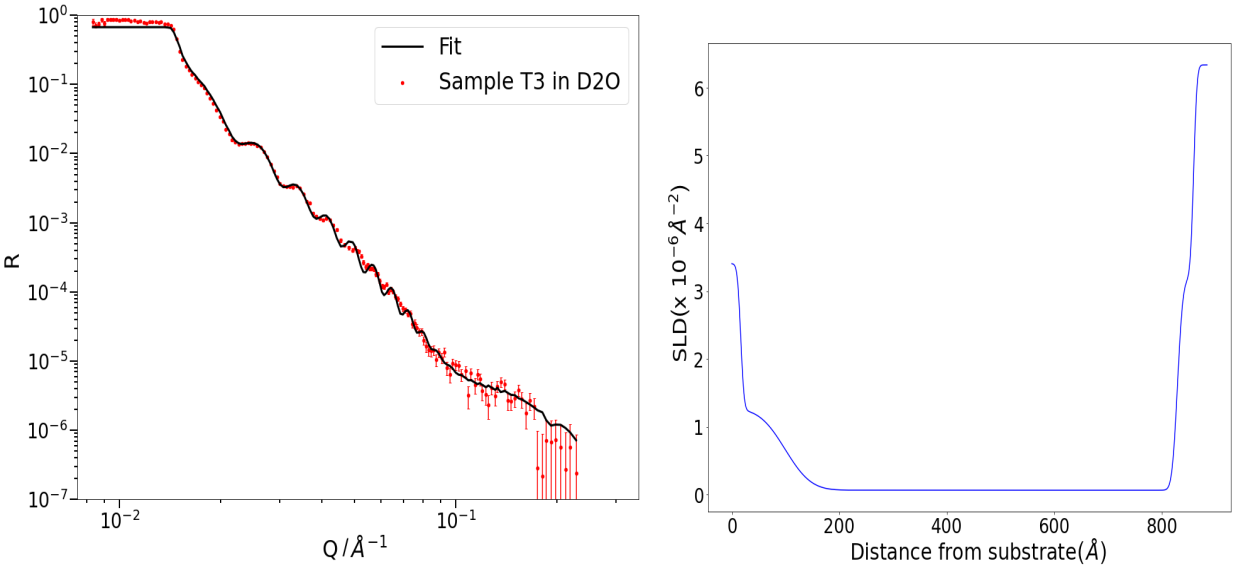

(a) T3 in D_2O (b) SLD for fit in D_2O

Figure 4.36: Neutron reflectivity for sample T3 in D_2O.

The model fit shown in figure 4.36 for sampleT3 in D_2O achieved an error of χ^2=14.0. Again we see strong evidence of an interfacial layer at the solid liquid interface. This interfacial layer was fitting as single layer on the top surface of the PDMS. The SLD value of this layer was fit specifically for each contrast but fit to an SLD of 2.5-3x$10^{-6}\mathring{A}^{-2}$ and a thickness of 30$\mathring{A}$. We can demonstrate that this layer is not present on the surface of these surfaces in air by fitting the specular reflectivity of these samples in air and modelling the same specular reflectivity with the surface interfacial layer determined from specular reflectivity in water.

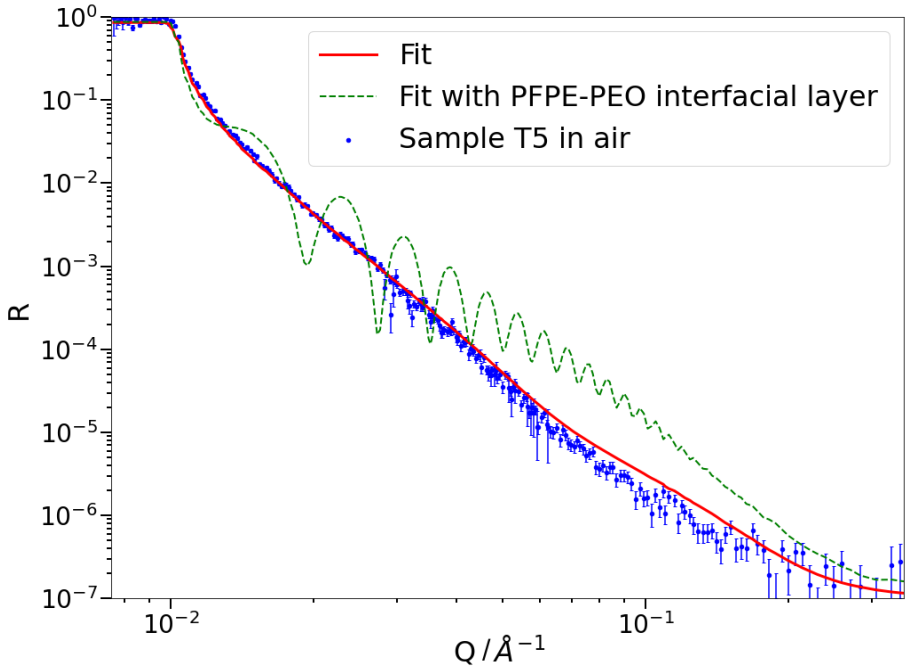

Figure 4.37: T5 fitted in air, with hypothetical surface layer.

The model fit shown in figure 4.37 for sample T5 in air used a small enriched silica sub layer and fit the data with an error of χ^2 of 4.99. The hypothetical layer modelled on the surface of sample T5 in air was set from the D_2O measurement of SLD 2.9x10^{-6}Å^{-2} and thickness 25.9Å. It is clear that if such a layer was present at the surface in air the specular reflectivity would be radically different from the obtained data, with the Keissig fringes for the full thickness of the sample present. Therefore there is a change in the surface structure when the surface is exposed to liquid water.

Sample T1 had a substantially larger layer of PFPE-PEO (a layer thickness 10 time the samples T3 and T5) with a much denser distribution of droplets on the surface than in the other PDMS/PFPE-PEO samples. Figure 4.38 shows the reflectivity for this sample in water, which is markedly different from the other samples. When this sample was measured in water a distinct structure was observed with a peak in the reflectivity structure at 0.05944 Å^{-1}, using Bragg's Law this peak represents length scale structure of 105 Å. In order to fit this a repeating structure of 10nm overall thickness was optimised for SLD and number of repetitions to minimise the error in the fit. We assume a similar interfacial layer at the surface of the PDMS seen in other PDMS PPFE-PEO interfacial layers. The repeating structure was designed as a 'sandwich' of 3 slabs two 2.5nm slabs

with an SLD equivalent to the liquid contrast capping a middle layer of thickness ≈ 5nm and an SLD intermediate between that of the fitted interfacial layer found for T5,T3 and OFFSPEC 16 and the given liquid contrast (i.e. in H_2O and Si matched water the middle layer has an SLD higher than the water contrast but in D_2O this middle layer has a lower SLD). The number of repetitions and the SLD of the repeating layer in order to minimise the fit error, we report the best results below.

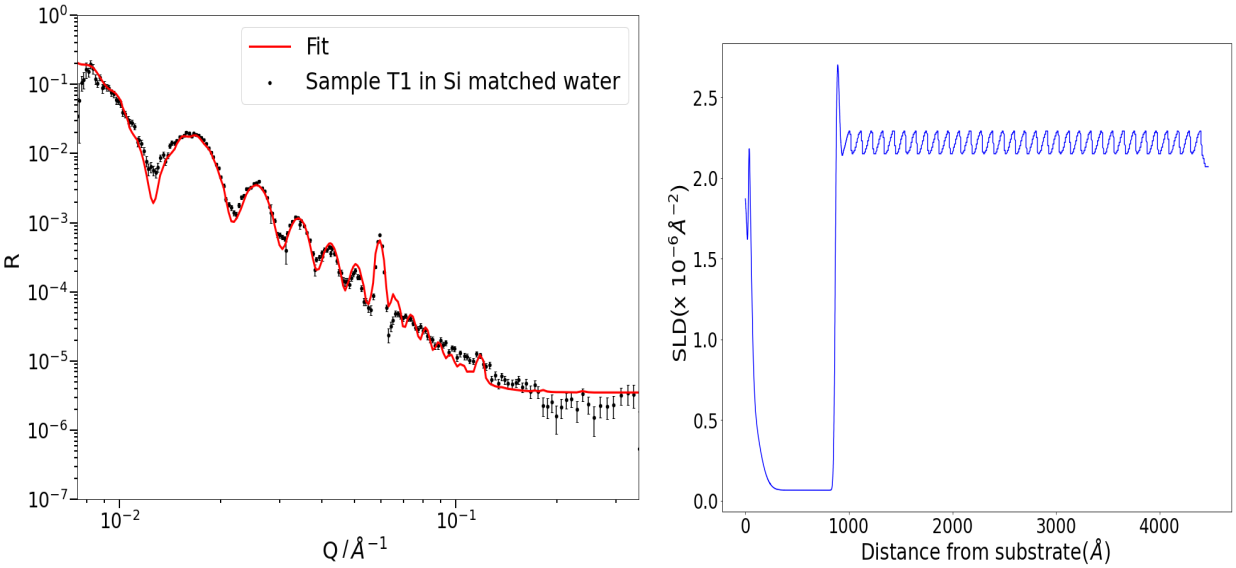

(a) T1 in Si matched water

(b) SLD for fit in Si matched water

Figure 4.38: Best fit for sample T1 in Si matched water.

The most successful fit was achieved in silicon matched water with an error χ^2=9.22. The repeating trilayer was optimised to 33 repetitions of ≈ 330nm. The simulated fit shown in figure refT1simatch shows a fluctuation in SLD between 2.11-2.28×$10^{-6}\mathring{A}^{-2}$, suggesting a high volume fraction of silicon matched water (of SLD 2.07×$10^{-6}\mathring{A}^{-2}$) throughout the repeating structure with small changes in the relative hydration giving rise to the observed structure.

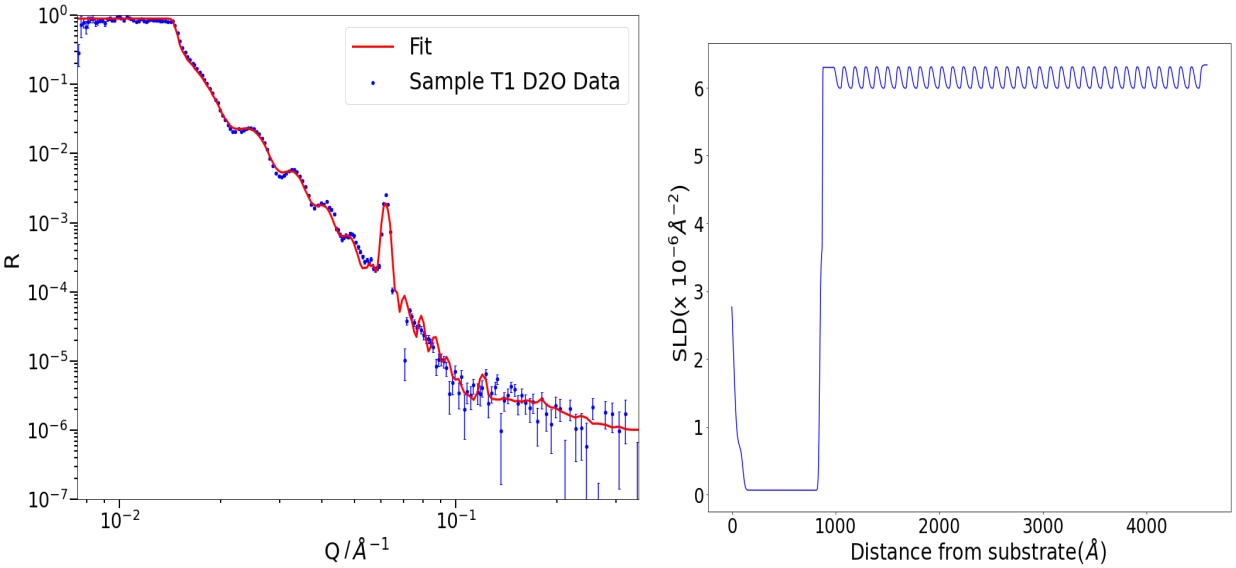

(a) T1 in D_2O

(b) SLD for fit in D_2O

Figure 4.39: Best fit for sample T1 in D_2O.

Figure 4.39 shows the current best model for the measured neutron reflectivity of sample T1 in D_2O. This model had a higher error χ^2=28.8, though if the high uncertainty data point at 0.0071 $\AA^{-1}$ is considered anomalous and removed (no model could be found that would produce a fit that captured this data point), the fit improves to an error χ^2 of 9.2. Fits were also attempted for measurements in H_2O but could only achieve a fit with an error χ^2=36. In each contrast the simulations are best optimised to a 10nm periodic structure that extends over 300nm. The physical interpretation of this observation is explored in the discussion.

Prior to filling with D_2O, sample T1 was aligned in an empty solid liquid cell, as the cell was filled with D_2O rapid, 1 minute reflectivity scans of the sample were taken in order to try and capture the timeframe of the surface transition.The rapid kinetic reflectivity measurements are presented in figure 4.40:

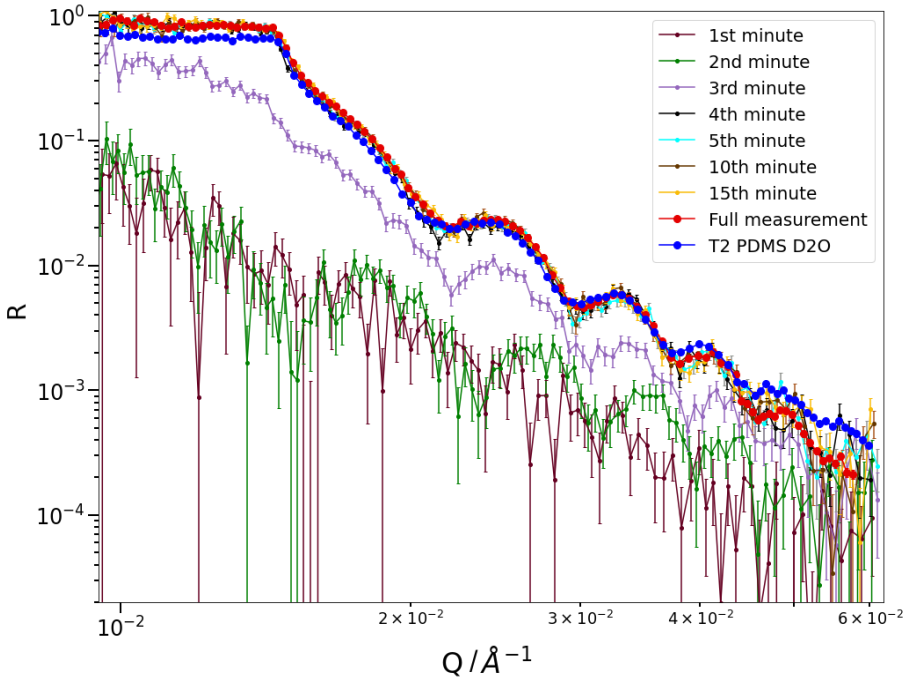

Figure 4.40: NR Spectra for T1 during filling with D_2O at 2 ml per minute, T2 PDMS sample included for comparison.

We can see that after 4 minutes of filling the cell at 2ml/min intensity reaches a maximum and the critical edge of the sample becomes clearly visible indicating that the cells are now nearly or completely full. After 4 minutes there was no appreciable difference in the scattering spectra collected each minute, data collected over these short timeframes had a higher degree of error than the full angle scans collected over 70 to 110 minutes, further as demonstrated by sample T2 PDMS shown in blue and also in figure 4.30 the divergence in specular scattering between PDMS and PDMS/PFPE-PEO topcoat films in liquid becomes clearer at higher Q values just as the error bars on the data begin to increase substantially, the Bragg peak seen for T1 would be the clearest indication of the surface reconstruction in liquid but cannot be detected accurately by these fast, first angle measurements. Nevertheless there appears to be some divergence between the rapid scans and full scan for T1 and the spectra of T2 between 0.04 and 0.06$\mathring{A}^{-1}$, as best as can be determined from this data the surface reconstruction has already occurred within the 4 minutes it takes to fill the solid liquid cell consistent with observation from contact angles tests of rapid wetting in response to water.

4.5.4 Liquid AFM

Liquid AFM images were obtained for three samples, additional sample (sample 3 in the original set) was attempted but images obtained from this sample were found to have false contact failing to image the surface. Images of height topography and adhesion are presented for each sample in liquid. With sample 1 the PDMS control, sample 2 PDMS with 2.5% PFPE-PEO from ethanol and sample 4 PDMS with 25% PFPE-PEO from acetone:

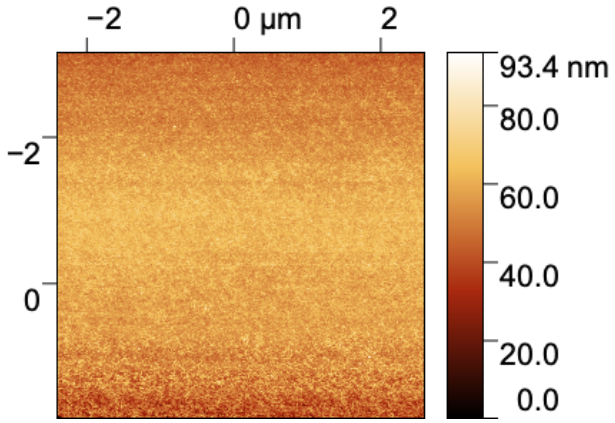

(a) Sample 1 image 3 height

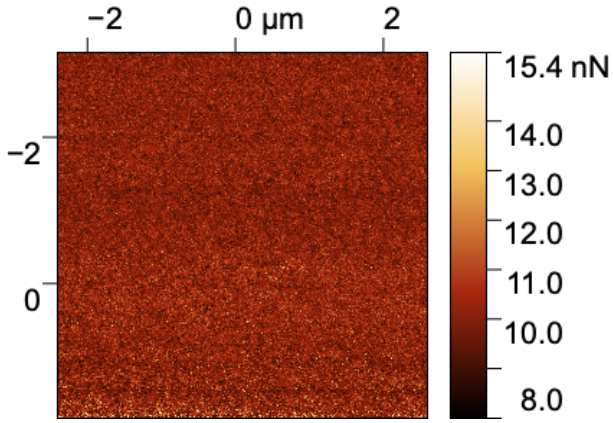

(b) Sample 1 image 3 adhesion

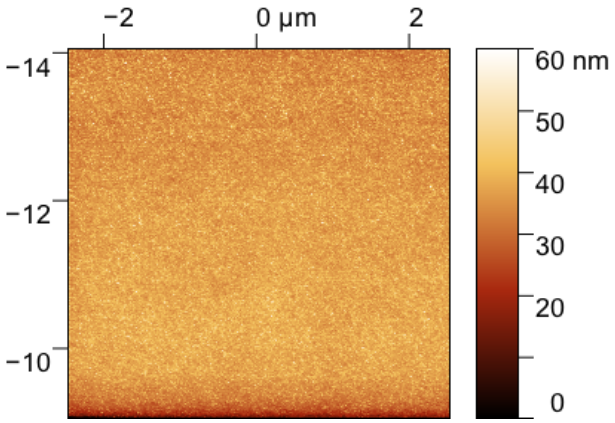

(c) Sample 2 image 1 height

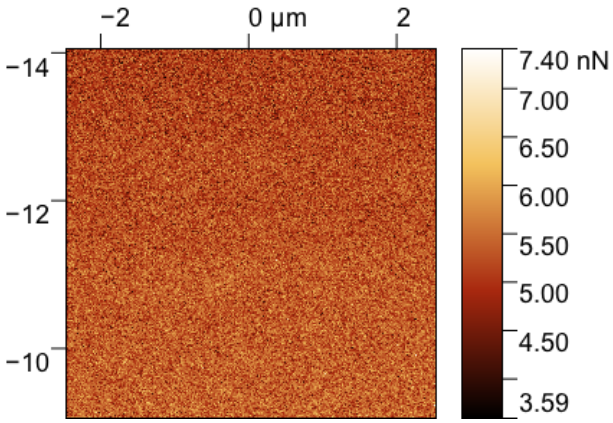

(d) Sample 2 image 1 adhesion

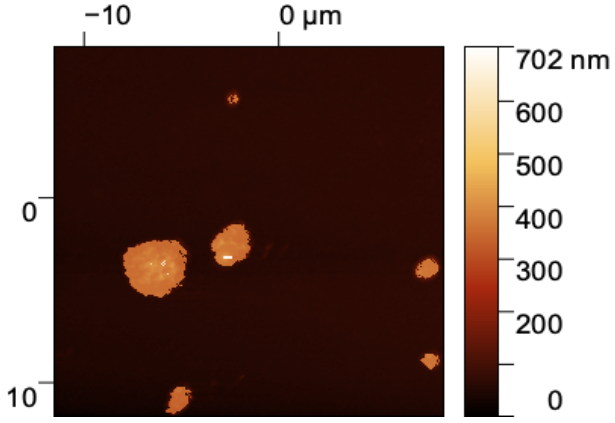

(e) Sample 4 image 2 height

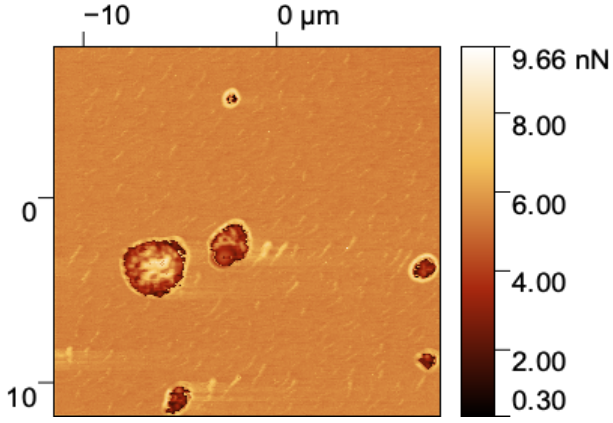

(f) Sample 4 image 2 adhesion

Figure 4.41: Height and adhesion Qi images for model thin films in deionised water.

Samples 1 (figures 4.41a and 4.41b) and 2(figures 4.41c and 4.41d) show very smooth topography and a uniform adhesive response. The image of sample 4 (figures 4.41e and 4.41f) was taken over a larger area and captures a number of droplet like features, likely small droplets of dewetted PFPE-PEO at the surface of the PDMS, with a much larger layer such droplets are much denser on the surface and so more likely to be captures in a surface scan. The adhesive behaviour of these droplets appears to be different of the surrounding surface. Force curves from each image were extracted including from sample 4 both in droplet features and the surrounding surface.

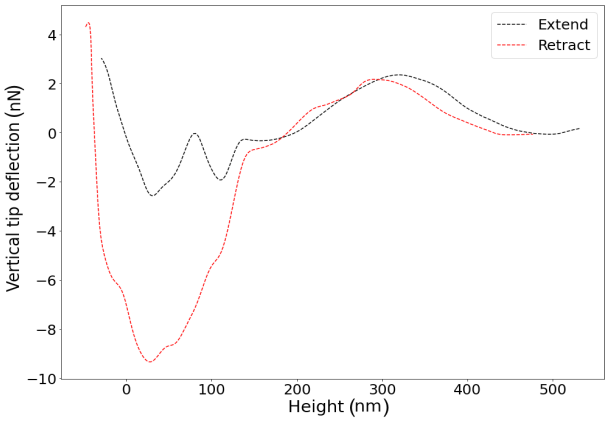

(a) Sample 1 (PDMS)

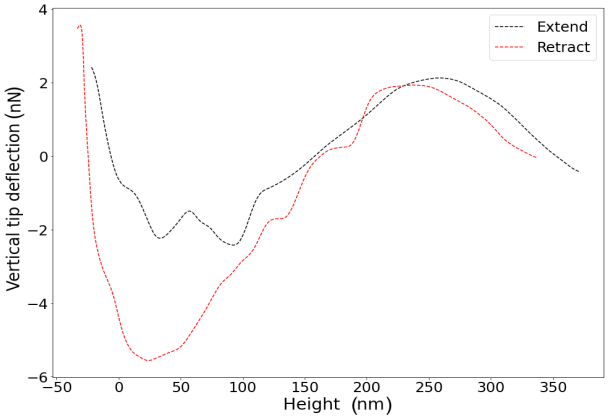

(b) Sample 2 (PDMS small PFPE-PEO layer)

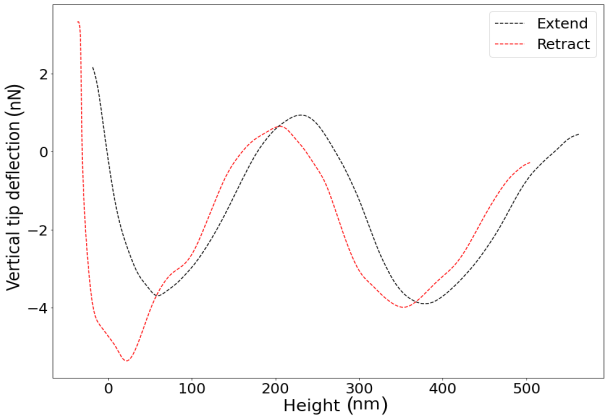

(c) Sample 4 (large PFPE-PEO layer)

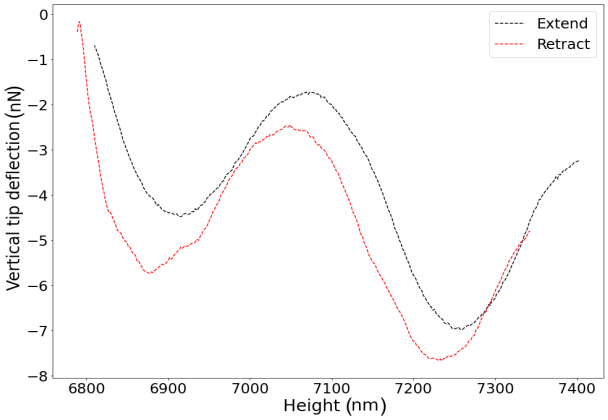

(d) Sample 4 droplet feature

Figure 4.42: Example force curves from Qi liquid AFM of PDMS/PFPE-PEO thin films.

These force curves in figure 4.42 show a reduced hysteresis between extension and retraction of the cantilever tip when comparing the PDMS control and sample 2 the thin PFPE-PEO topcoat. suggesting a less adhesive surface contact, fascinatingly sample 4 shows an unusual force distance curves with two minima separated by a large distance. This force curve shape is present not just from contact with the droplet features but also the flat surface regions of the image. The first minima in curve 4.42c appears to be entirely elastic and the second at the furthest extension shows hysteresis and is more likely to be the contact with the surface of the film, these curves were consistent in shape across the image and across further images taken of sample 4. Thirty curves were selected from 2 images of sample 4 at flat regions of the image, by using a python function to find the minimum points in the curves the distances between the first and second minima were found systematically, with the mean distance between the minimum points being 320±42nm. This is of a similar length scale to the size of the repeating lamella fit for sample T1 via reflectivity of 330-340nm.

All force distance curves obtained from AFM images were analysed to obtain statistical information about the adhesion and mechanical elastic modulus response of the surface to the cantilever probe yielding the histograms in figure 4.43 and the overall data summarised in table 4.4 . Force curves were analysed on mass once parameters were defined, curves from droplet features in sample 4 were not removed but the region selected for adhesion and Young's Modulus calculation was defined as the region around the second minima and greatest extension only.

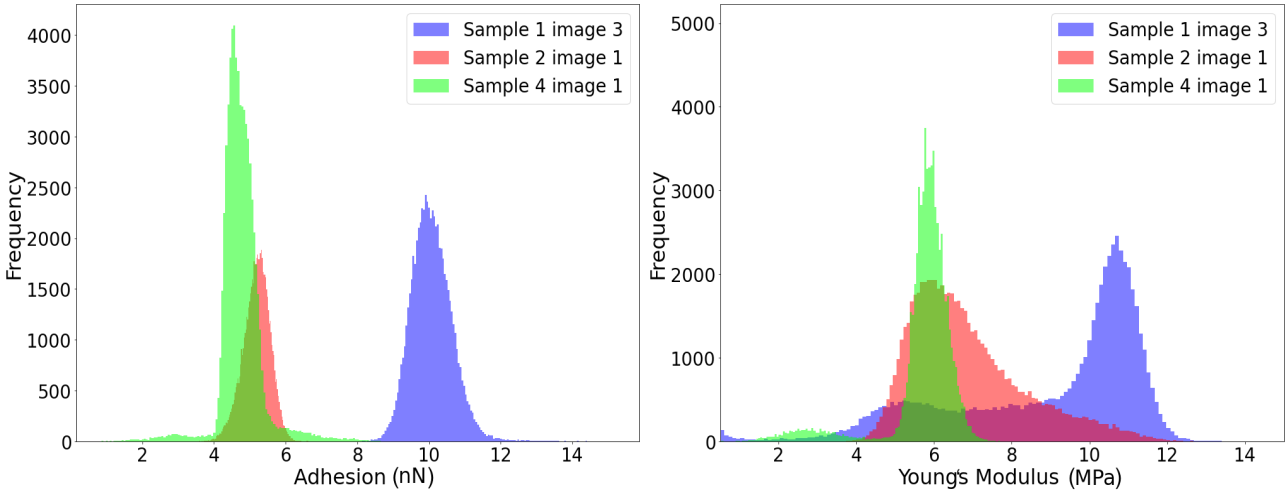

(a) Adhesion (b) Young's Modulus

Figure 4.43: Histograms summarising the adhesion and Young's modulus values calculated from the force curves obtained in Quantitate imaging AFM of model samples in liquid.

Table 4.4: Summary of properties determined for liquid AFM PDMS/PFPE-PEO samples.

Sample	Sample 1 image 1	Sample 1 image 2	Sample 2 image 1	Sample 2 image 2	Sample 4 image 1	Sample 4 image 2
Young's Modulus (MPa)	9.88±1.37	10.3±0.97	6.85± 1.49	7.51±2.51	5.62±1.12	6.9± 1.17
Adhesion (nN)	9.57± 0.56	9.57±0.53	5.19±0.37	5.6±0.37	4.76±0.6	4.76±0.6
rms Roughness (nm)	6.68	5.74	3.91	18.71	99.6	56.42

When compared to PDMS control sample 1, the adhesion of force contact for both topcoat samples 2 and 4 is reduced by 40-50% and the surface Young's modulus also decreases indicating the surface has become softer and more malleable when subject to force. The calculated values for the Young's Modulus are higher than would be expected fora PDMS surface particularly in the case of sample 1 with literature values ranging from 3.5 to 0.5MPa depending on the crosslinker ratio [170], however it should be acknowledged that these samples are not bulk PDMS but rather thin films of >300nm on a rigid silicon substrate. It has previously been

reported using polystyrene thin films that for soft thin films on hard substrates nano-indentations of greater than 1/5 of the film thickness results in significantly higher determined values of elastic modulus than bulk properties as influences from the much harder substrate effect the mechanical response [171]. In all the force curves it is clear the cantilever indents tens of nanometers from the contact point so the Young's moduli calculated here come from this substrate effect regime and can account for this apparent overestimation of the bulk modulus of PDMS.

The change in sample adhesion and elastic modulus for PDMS/PFPE-PEO topcoat samples across the entire measured surface when compared with PDMS films in water corroborate the observations from in situ neutron reflectivity of surface reconstruction of these systems in water and a solid liquid interface that is mechanically and chemically different when these PPFE-PEO containing surfaces are exposed to water.

4.5.5 Discussion: PDMS/PFPE-PEO surfaces in liquid.

Combining observations from contact angle, liquid AFM and neutron reflectivity it is clear that surface reconstruction occurs on PDMS/PFPE-PEO topcoat films in water. Several in air/vacuum techniques have demonstrated no evidence for a comprehensive coverage of PFPE-PEO on PDMS even if the molecule was initially applied across the whole surface as a film it will fully dewet. However in liquid some monolayer of $\approx 30\mathring{A}$ thickness. This effect can be achieved using even small quantities of PFPE-PEO eg. 30nm thin films deposited on PDMS surfaces which then dewet into disparate microdroplets, provided the entire surface is covered in water such that these dewetted droplets are exposed to water this surface transition can be seen to occur. Neutron reflectivity and liquid AFM topography measurements are in strong agreement about the general structure of this surface transformation; for small sub 100nm thick layers of PFPE-PEO applied to surfaces this takes the form of a uniform layer covering the surface of the PDMS film. Such uniform structure is necessary in order for the thin film to be visible in the neutron reflectivity spectra, structures that were too rough or too large such as micrometer sized droplets would not contribute to the coherent neutron scattering spectra and similarly as seen in figures 4.41a and 4.41c that the PDMS/PFPE-PEO sample was not significantly rougher than the equivalent PDMS standard film in water but nevertheless the adhesive and elastic properties of the surface measured from force distance curves changed significantly indicating a uniform change distributed across the surface which can be well explained by a small monolayer wetting the entire interface.

It is our interpretation of these results that when exposed to water PFPE-PEO

form the bulk dewetted droplets spreads as a single monolayer across the surface, with its hydrophobic central backbone of PFPE orientated into the hydrophobic PDMS substrate and its end block PEO groups orientated towards the water phase and solvated heavily with water, the PFPE backbone serving as an anchor to the surface tethering the molecule to the surface via hydrophobic interactions between PFPE and PDMS, both being highly hydrophobic and hence presenting a high work of adhesion cost in removing this layer and creating two high energy interfaces between water and the PDMS surface and water and the PFPE block of the amphiphile. Such solid liquid interfaces have been observed before in the case of Pluronic F108 on hydrophobic surfaces; pluronic the amphiphilic block copolymers of hydrophilic PEO and hydrophobic PPO in the form PEO-PPO-PEO could be grafted to surfaces from water solutions, if the surface was hydrophilic the block copolymer adsorbs in a pancake formation spreading broadly across the surface but if the surface is hydrophobic adsorption is brush like with the PPO backbone tethering to the surface and the PEO blocks solvating in water, this coating is considered to reduce the interfacial tension and render the coated surface hydrophilic, with such surfaces demonstrating improved resistance to protein fouling [172]. Further investigations by Nejadnik et al of this phenomenon, investigating the formation of brush layers of pluronic using QCM and the precise hydrophobicity of surfaces found that brush structures from via hydrophobic interactions for surfaces with water contact angles $>80^\circ$ with the layer thickness of wetting layer and the elastic modulus increasing with increasing hydrophobicity [173], a higher elastic modulus is also indicative of a higher grafting density of polymer brushes on a surface. In our case PDMS has a contact angle of 110-120° so should have a higher interfacial tension with water than is necessary for the formation of hydrophobic-ally induced brush formation. PFPE-PEO is not fully soluble in water but PEO domains can solvate in water and PFPE-PEO is liquid at room temperature so rather than absorption of amphiphiles from solution we argue a similar surface reconstruction occurs via liquid spreading.

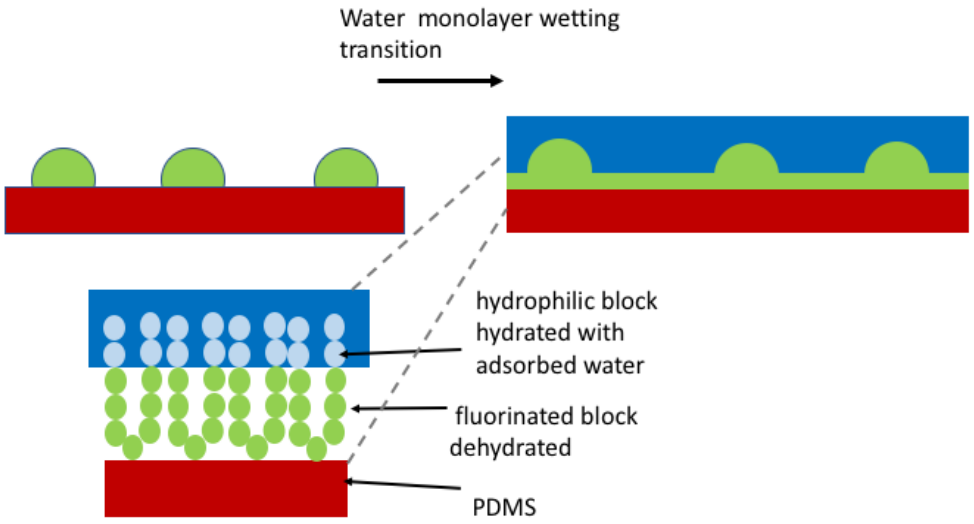

Figure 4.44: Proposed model of surface reconstruction due to water on PDMS/PFPE-PEO topcoat films.

Here in this proposed mechanism illustrated in figure 4.44 we see the formation of a single partial wetting layer with PEO solvated; note the bulk droplets of PFPE-PEO are still present, this is the case in both thin PFPE-PEO topcoats and the larger PFPE-PEO deposited layers. Observations of water droplets on surfaces using optical microscopy revealed the bulk micro-droplets on the surface were still visible on the surface. Prior to these experiments there was some ambiguity over the respective roles of each block in the amphiphile PEO and PFPE, with PEO offering protein resistance in brush form and PFPE representing a very low surface energy material which might be only weakly adhesive but given the structure of the wetting layer and the apparent hydrophilicity of the resulting it would appear the primary role the PFPE block plays at the interface is as a hydrophobic tether and not directly interfacial.

The precise mechanism of foul resistance this surface might exhibit is still unclear; similar Pluronic's are believed to form a brush with steric pressure inhibiting protein adhesion, the thicknesses of layers formed in Nejadnik et al's work varied depending on the surface but ranged from 5.5-8.5nm all considerably thicker than the observed layer of PFPE-PEO of 3nm. Further tests of PEG brushes and their optimum grafting density and length suggest grafting densities smaller than the typical protein dimensions are favourable for resisting fouling but that protein

resistance peaks for brush thickness of 9nm[34] again, much higher than the thickness of our observed layer. This would seem to counter the argument that this monolayer is performing as a self assembled brush layer.

An alternative explanation could be that the PEO layer induces strongly hydrogen bonded water layer on the surface leading to an enthalpic barrier to entry for any adhering substance and preventing direct contact with the surface. This theory of a tightly bound layer of water hydrogen bonded to the surface creating a strong, repulsive hydration force against protein fouling had been explored with self assembled alkanethiols bonded on gold with various chemical termination groups both experimentally and using molecular dynamics simulations. Specifically, experiments using short chain oligomeric ethylene glycol OEG end groups had found strong evidence of protein resistance and cell resistance[174] these monolayers on gold have a similar hydrophobic/hydrophilic bilayer structure as we propose with with the hydrophobic alkanethiol chemically anchored into the substrate and any oligo ethylene glycol solvated in the liquid phase. Computer simulations argued that these self assembled monolayers (SAMs) interact strongly with interfacial water molecules, with transient water molecules showing much greater residence times at the surface and simulated lysozyme molecules experiencing significantly greater repulsive forces in the near proximity of the surface [175]. Finally, Hayashi et al demonstrated that self assembled OEG monolayers in water could resist proteins with even a single terminating monomer of OEG but three was required for effective resistance to platelet adhesion, using AFM surface force analysis between two OEG SAMs they determined monolayers with at least two EG end groups experience strong repulsive forces upon coming within 5-6 nm of each other, such forces were not apparent with monolayers containing fewer EG groups and is attributed to the presence of a 2-3nm Hydration layer on the surface of these OEG SAMs[176]. It is not apparent whether much larger PEG/PEO brush layers also exhibit this hydration shell but given the very short nature of the absorbed layer observed in our experiments the concept of a highly hydrogen bonded interfacial layer of water induced by PEO should be seriously considered as the mechanism by which this layer augments the foul release/resistance properties of PDMS.

Considering the layer fitted from neutron reflectivity we found the SLD varies somewhat between the contrasts this can be interpreted as a degree of the layer by the particular contrast with H_2O reducing the fitted SLD and D_2O increasing it. In the interpreted model the layer forms a bilayer segregated by hydrophobicity and hydrophilicity but the layer was nonetheless fitted as a single uniform layer with a single SLD and some roughness. The SLD of the PFPE-PEO block copolymer in bulk is dependent on the individual blocks and their ratio but PFPE has an SLD calculated to be $3.8\text{x}10^{-6}\mathring{A}^{-2}$ and PEO has an SLD of $0.63\text{x}10^{-6}\mathring{A}^{-2}$. In

water we expect the PEO in this monolayer to be highly solvated with water so the effective SLD of the PEO will be much closer to the SLD of the given water contrast. There may also be some small amount of penetration of water into the PFPE segment the layer fit hypothesises a largely dehydrated layer with an SLD dictated by the PFPE segment of the amphiphile which then appears to decay into the SLD of the liquid contrast as more water penetrates the molecule further from the PDMS interface. A more accurate and structured model of the wetting layer is hard to achieve owing in part due to the complex structure of the underlying PDMS film and the relative thinness of this pertinent layer compared to the overall thickness of the sample. Despite this the model is not dissimilar more complex fitted interpretations of PEO at hydrophobic interfaces; Inutsuka et al observed surface reconstruction of a PDMS-PEG block copolymer containing PDMS film in water via neutron reflectivity in which the block copolymer would wet the interface in water and the PEG chains would solvate forming a spontaneous brush at the interface [162], they fitted the resulting layer in water as a series of ≈60 layers from the PDMS interface into the bulk water. Even with this multiplayer fit they still found an SLD profile in D_2O that was very much a step like profile with a shoulder at the interface 20nm thick with an SLD of $2.5\text{x}10^6 \mathring{A}^{-2}$ representing a solvated layer of PEG chains.

As discussed in the results section the Young's modulus calculated from AFM measurements is high and distorted by the rigid substrate, the adhesion values determined from these experiments must also be treated with caution as the experiment was conducted in pure deionised water, as such electrostatic charges between the tip and the surface could have effected the adhesion, if as hypothesised the surface interface is PEO this is unlikely as this is an uncharged molecule but to eliminate this possibility and ensure the reliability of these adhesion values the experiment would need to be repeated in an electrolyte buffer of 300mMKCl which will reduce electrostatic repulsive effects to zero [177]. Additional liquid AFM experiments were were intended however owing to Covid related lab restrictions on access to equipment and the departure of colleagues with the relevant skills in the technique this was not possible and the presented results were achieved using a single set of samples over one week. Although the exact values may not be wholly accurate the consistency of the determined values across images is high and there is good agreement between PDMS/PFPE-PEO topcoat samples suggesting that the wetting layer causes the sample to be softer and less adhesive relative to a PDMS surface. The QI results also suggest that under the structured multilayer that developed on hydrated thick layers of PFPE-PEO on PMDs (T1 and sample 4 from AFM) there is the same wetting monolayer of PFPE-PEO lining the PDMS interface, consistent with the fitted neutron SLD for sample T1.

The Bragg feature that developed on T1 in water was unexpected, this feature was observed twice as contrast Si match water had to be collected a second time with the sample being taken out of the liquid cell and rewetted with the feature again being seen as it had been in D_2O and H_2O contrasts. To interpret this feature we must again consider the amphiphilic nature of PFPE-PEO containing hydrophilic and hydrophobic domains, when subject to water the hydrophilic domains will become hydrated but the hydrophobic domains will week to minimise their exposure to water and so phase separated structures of hydrated and dehydrated polymeric blocks can form. Amphiphilic block copolymers of Polyethylene oxide and polybutadiene oxide have been shown to form ordered hydrated and dehydrated lamella blocks when subject to water vapour absorption. This has given rise to Bragg peak features in neutron reflectivity of such block copolymer surfaces [178]. We used this concept to attempt to model the repeating structure fit for the neutron spectra of T1; a series of ordered films based on hydrated and dehydrated blocks, upon fitting however the fluctuations are far smaller and oscillate around the SLD of the bulk liquid contrast implying that such layers would be made up of almost totally water layers and slightly less hydrated layers:

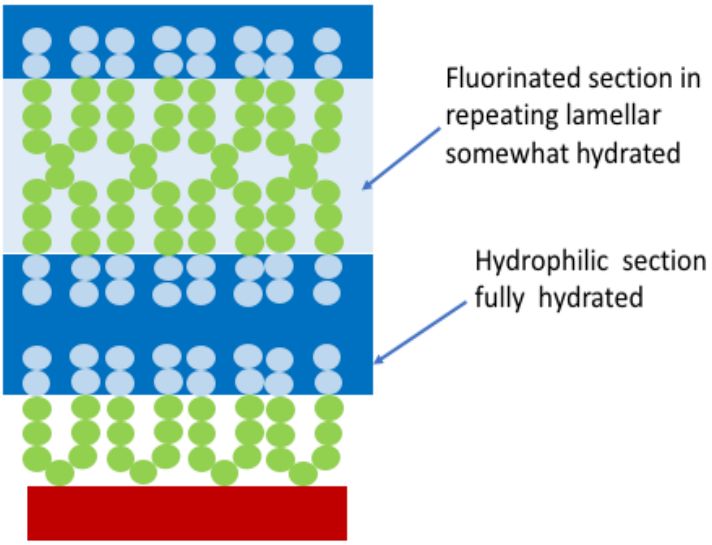

Figure 4.45: Model of estimated model lamella for sample T1 in water.

Physically, the fit structure depicted in figure 4.45 is not particularly credible. A structure is unlikely to form if the hydrophobic PFPE block cannot successfully

separate from the surrounding water. Further, with the exception of the fit in the Si match, fits based on this model had a high degree of error. Offspecular features were seen in the reflectivity spectra from this sample implying some lateral out of plane structure was present in the resulting layer, a number of effective systematic methods using python programs have been developed to analyse these out of plane offspecular correlation features in neutron reflectivity [179][180] however successful fits require strong fits from specular scattering in order to model the SLD off the offspecular features without which reliable analysis cannot be performed.

Amphiphilic molecules in water can also developed into self assembled structures in water such as micelles in which bundles of amphiphilic molecules form into 3-d structures to optimise the hydration/dehydration of the hydrophilic and hydrophobic polymer blocks . These structures can be spherical with the hydrophilic section aligned to the interface and the hydrophobic blocks contained within the micelle in order to remain dehydrated. Such aggregates may well be possible for PFPE-PEO and although micelles free floating within the liquid phase and should not be observable in a neutron reflectivity measurement sensitive to significant changes in the SLD close to the sample surface, there is in fact evidence in the literature for complex ordering of micelles at surfaces has been observed via neutron reflectivity showing similar sharp Bragg peaks indicating an extended repeating structure decaying into the bulk[181]. While we attempted to fit this structure as a consistent repeating layer Gerstenberg et al found such structures had a much more complex SLD profile, given the number of repeated layers are necessary to form the fitted thickness of this phase (AFM force distance curves showing the double contact are in agreement with neutron fits that this repeating structure is at least 300nm thick) without some understanding of the true structure of the ordered micelle surface phase, accurately fitting each layer individually will not be possible. If this is the explanation for the Bragg peak feature shown by sample T1 further experiments will need to be performed to demonstrate the presence of ordered micelles of PFPE-PEO at the surface and determine the length scales of their cohesion.

4.6 PB-PEO PDMS test films

With a working model of the behaviour of PFPE-PEO as a partial wetting layer at PDMS liquid interfaces we considered the prospect that the perfluoropolyether section of the molecule performs a largely structural role in the amphiphile at this wetting interface allowing the molecule to cover the PDMS in water via hydrophobic interactions and present hydrophilic PEG end blocks to the water interface,

in this model the perfluoropolyether plays only a limited role in the direct interfacial foul release/resistance properties of these coatings, given the expense of producing PFPE's we considered if an alternative non-fluorinated hydrophobic backbone could be employed. Ruffin et al had previously shown incorporating oligomeric amphiphilic block copolymer of PDMS and PEG with a cross-linked silane tether into a PDMS matrix resulted in a highly foul resistant surface with water driven restructuring of the PDMS/water interface driven by the amphiphilic block copolymer producing hydrophilic foul resistant surfaces [182]. Further, Khai et al demonstrated that the cross-linking silane tether was not necessary for foul release performance and that small oligomeric PDMS (ODMS) hydrophobic blocks were sufficient to physically tether PEG block copolymers to the solid liquid interface and produce highly effective foul release surfaces with hydrophilic interfaces significantly improving the foul release performance of the bulk PDMS coating; they found a viable ratio of hydrophobic tether and hydrophilic PEO blocks to be 13:8 [183].

We consider instead a simple low molecular weight co-block of hydrophobic polybutadiene and polyethylene oxide PEO, the structure is shown in figure 4.46.

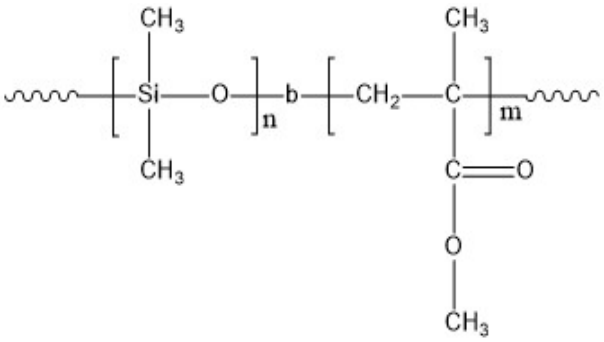

Figure 4.46: Polybutadiene Polyethylene oxide block copolymer.

Acquired from Polymer Source a M_w=2200 distrubuted in a ratio of 1.8-0.4 PB-PEO representing $\approx$ 33-9 repeat blocks respectively, similar to the stoichiometry of 30-8 hydrophobic to hydrophilic blocks reported by Khai et al. The material was an extremely viscous fluid.

4.6.1 Methods

Fractions of PB-PEO were dissolved in toluene and then spun onto pre prepared cured thin films of PDMS. The contact angle response of these surfaces to water was measured using the Ossila goniometer, further atomic force microscopy studies were taken of these PDMS/PB-PEO topcoat films. To asses the potential foul release applications of such films a protein exposure post situ experiment was performed, outlined in more detail in the upcoming chapter 5 briefly, protein solution was prepared by dissolving BSA in a solution of 200mM $CaCl_2$ in water at a concentration of 100μg/ml. PB-PEO/PDMS films were initially immersed in 200mM $CaCl_2$ solution and then the volume was doubled with BSA protein solution, resulting in the immersed films being exposed to a solution of 50 μg/ml. Films were left in solution for 50 minutes before being rinsed in buffer solution and dried. PDMS PB-PEO films were examined with AFM before and after protein exposure, a basic PDMS film exposed to a protein solution of the same concentration is also presented for comparison.

4.6.2 Results and Analysis.

As shown in figure 4.47 when PB-PEO is spin coated on PDMS thin films the resulting topcoat rapidly dewets in air just as we observe with PFPE-PEO.

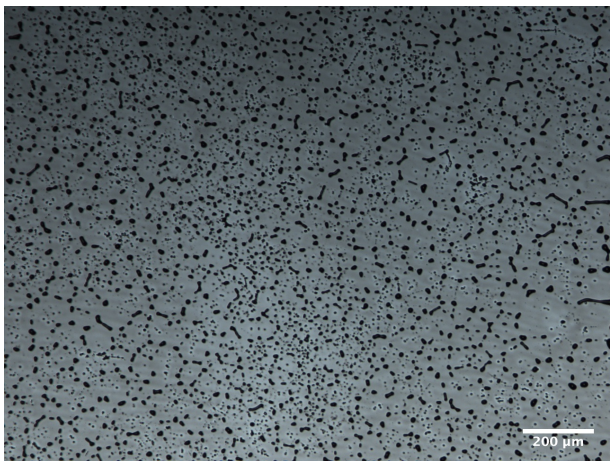

Figure 4.47: 5x magnification image of PB-PEO spontaneously dewetted on PDMS from 0.3% w/w solution in toluene.

However, the static water contact angle of the resulting is very different to PDMS/PFPE-PEO topcoat samples.

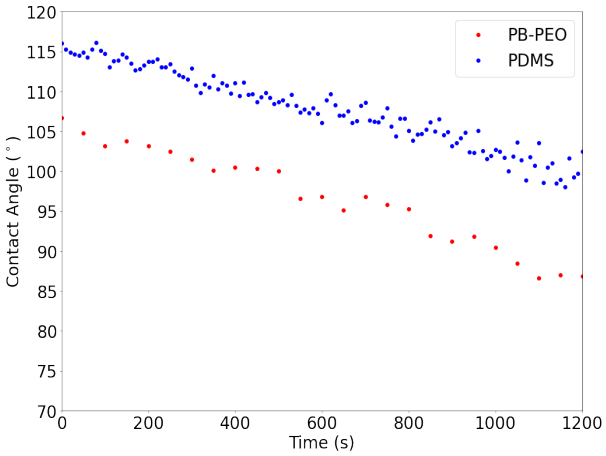

Figure 4.48: Change in water contact angle over time for PB-PEO 0.3% w/w in toluene spun PDMS, water contact angle response of basic PDMS film is shown for comparison.

The water contact angle data in figure 4.48 suggests that the surface is slightly more hydrophilic than PDMS but the rapid wetting shift is absent. The long term decline in the contact angle is not dissimilar to that seen for PDMS over 20-30 minutes as evaporation causes the droplet to recede slowly due to evaporation and not clearly indicative of a transition to a more hydrophilic surface.

Post situ studies of protein exposure shows little evidence of surface reconstruction or improved foul resistance due to PB-PEO, before and after images are presented in phase mode for clarity of features.

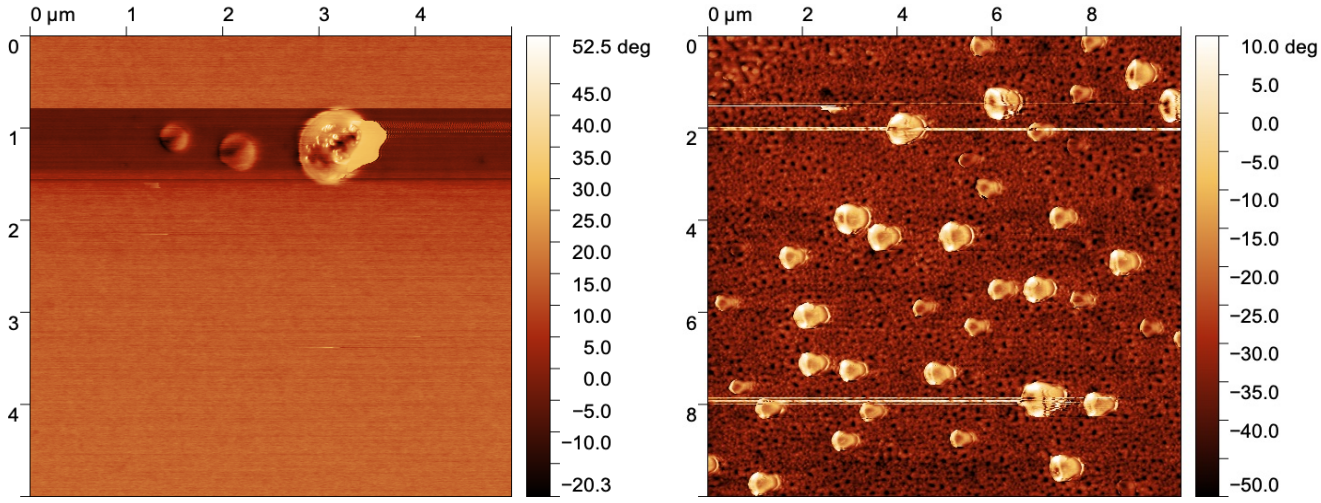

(a) Before (b) After

Figure 4.49: AFM phase images of PB-PEO treated PDMS before and after exposure to 50μg/ml BSA protein.

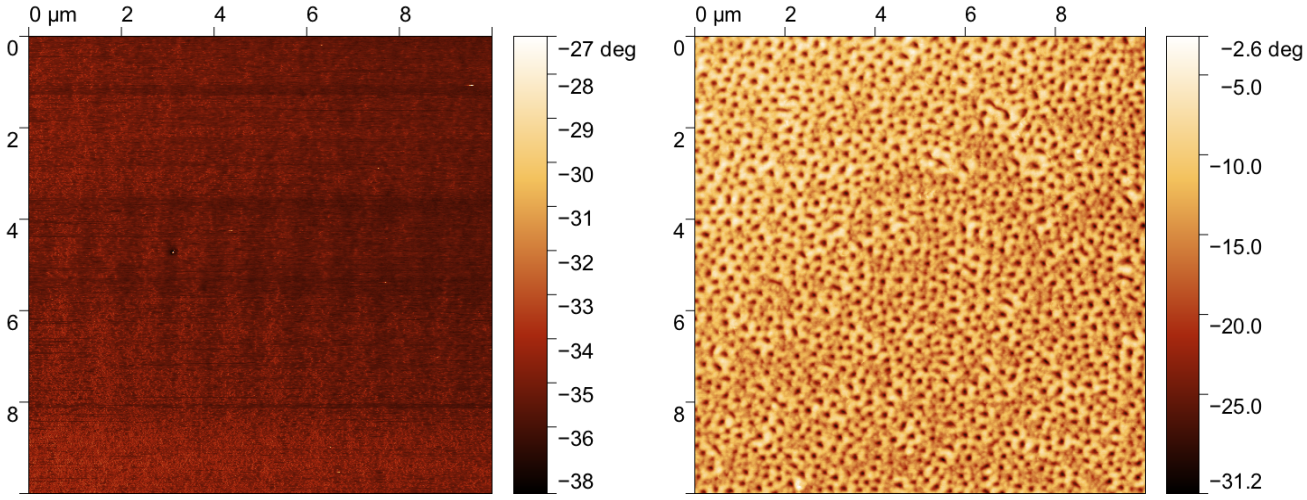

(a) Before (b) After

Figure 4.50: AFM phase images of PDMS before and after exposure to 50μg/ml BSA protein.

Comparing pre and post BSA exposure for the PB-PEO/PDMS film in figure 4.49 there appears to be a significant difference in the surface after protein exposure. We also see in figure 4.50 a similar change in the surface phase image for PDMS after exposure to BSA. This would suggests similar changes have occurred

to both surfaces, proteins are known to hydrophobically adsorb to PDMS and, as further elaborated in Bioadhesion chapter 5, the cross hatched pattern seen around droplet like globule features in figure 4.49b. and figure 4.50b is characteristic of the hydrophobic adsorption of BSA onto PDMS. However, result is not conclusive; only one sample was tested and the acquired AFM is of poor quality, phase images are presented here instead of typical height images to improve visual contrast as height images were too blurry, possibly indicating damage to the cantilever tip. Acknowledging the limitations of this data we would still argue that Pb-PEO does not induce surface reconstruction on PDMS when exposed to water or does not form an interface with water that resits protein adhesion. If PB-PEO/PDMS surfaces underwent surface reconstruction in response to water and improved protein resistance we would expect the AFM images acquired from that surface figures 4.49a and 4.49b to be very similar; if a monolayer formed in water that resisted biofouling no protein would attach to the surface, but as soon as the sample was dried again the layer would dewet just as PB-PEO dewets from PDMS when applied in air. This would result in a surface that was not significantly different after exposure to protein. Therefore changes that we do observe in the surface images imply the surface has been affected by protein adsorption.

The candidate block copolymer of PB-PEO does not appear to undergo surface reconstruction on PDMS surfaces when subject to water and does not assist the resistance of the surface to protein fouling and as such is not an effective additive for foul release coatings. The surprisingly hydrophobic response of these surfaces to water suggests that there is an insufficiently large PEG block in the chosen block copolymer perhaps an alternative block copolymer with a longer PEG block might drive surface reconstruction in order as a greater reduction in surface tension from solvating the PEG block might drive spreading of the polymer across the interface.

4.7 Conclusion

We have successfully identified surface reconstruction of amphiphilic block copolymer of PFPE-PEO on PDMS surfaces via hydrophobic interactions between the PFPE back bone and the PDMS surface, whilst the solvation of the PEO block at the liquid interface renders the hydrophobic PDMS coating effectively hydrophilic. This can occurs with relatively small quantities of PFPE-PEO and results in a single partially wetting layer of PFPE-PEO across the entire sample surface. This dense layer of surface PEO may be performing the role of a brush which can resist biofouling or augments the foul release properties of the coating by inducing a

strongly hydrogen bonded layer of water which inhibits biofouling by generating a repulsive hydration shell around the surface.

Attempts to identify novel non fluorinated amphiphiles to replicate this effect were unsuccessful at the first attempt but candidate fluorine free di block or tri block copolymers may exist which can replicate this effect. Ruffin et al recommend a large hydrophobic tether at least with at least 50% larger than the hydrophilic sections.We would further recommend that good candidate molecules are likely to be liquid at room temperature to ensure motility and insoluble/partially soluble in water.

Chapter 5

Investigation of the adsorption of biomolecules to model PFPE-PEO/PDMS surfaces.

5.1 Abstract

Model thin film coatings based on the topcoat deposition of PFPE-PEO on PDMS verified in previous chapters were tested for their resistance to a series of biomolecules. The absorption of proteins BSA, lysozyme and mefp-1 as well as the polysaccharide dextran were examined in real time using quartz crystal microbalance in a stop flow experiment. Adsorption was compared between hydrophilic and silicon surfaces, hydrophobic PDMS surfaces and model PFPE-PEO/PDMS surfaces. Protein adsorption on hydrophilic surfaces showed typical hydrophilic adsorption dynamics with proteins maintaining solution structure upon adsorption, adsorption on PDMS surfaces was hydrophobic with less overall mass adsorbed in the form of denatured proteins. PDMS/PFPE-PEO surfaces showed radically different responses to protein exposure with little or no apparent adsorption. dextran appeared to adsorb on all surfaces to a similar extent but desorbed readily upon rinsing. PFPE-PEO/PDMS protein fouling resistance was further examined by post immersion AFM surface characterisation again showing radically reduced protein adsorption of BSA on PDMS/PFPE-PEO surfaces. Finally, in situ adsorption studies on PDMS and PDMS/PFPE-PEO surfaces were performed in situ using neutron reflectivity obtaining real time adsorption kinetics of BSA adsorption on thin PDMS films, from this no BSA adsorption was observed for PDMS/PFPE-PEO surfaces suggesting a small surface treatment of PFPE-PEO on PDMS surfaces dramati-

cally improves a surfaces resistance to protein fouling.

5.2 Author Contributions

All QCM experiments, sample preparation and analysis were performed by myself. All post situ AFM images were acquired by myself. The neutron reflectivity experiment was conducted remotely with the assistance of Beam-line scientist Dr Samantha Micciulla at the ILL (whose assistance and consistent contact in preparation for the experiment was absolutely invaluable to its success) using on samples I had prepared and an experiment I had devised and proposed (with the consultation of Professor Richard Jones). All analysis and fitting of acquired neutron data was performed by myself. Neutron reflectivity blocks for the experiment were acquired with the assistance of Dr Stephanie Burg and Dr Andrew Parnell.

5.3 Introduction

In chapter 4 we showed that the model surfaces of PDMS with a thin deposited, de-wetted layer of PFPE-PEO on top undergo a surface reconstruction in response to water with a partial wetting layer of PFPE-PEO coating the PDMS interface at low densities and for larger deposited layers with higher dewetting density some hydrated lamella of PFPE-PEO forms parallel to the surface.

Having established this surface response of model coatings in the aquatic environment it was important to examine the performance of these surfaces to biofouling processes. A key processes in the early stages of biofouling is the adsorption of biomolecules onto a surface such as those found in the extracellular polymeric substances of a biofilm of which the key components are proteins, polysaccharides and extracellular DNA (E-DNA). These substances are particularly critical to the early adsorption processes and development of bioslimes and have innately adhesive qualities, with purified EPS fractions of any active bacteria still showing adhesive and aggregation effects [184]. Applying a wild type EPS to these model surfaces would be interesting but it would require first fully characterising the makeup of the particular EPS, which may not be consistently reproducible. Further, determining how each of the specific, constituent biomolecules that make up a given EPS were interact with the model foul release surfaces would be very challenging. Considering the adhesion of specific candidate biomolecules from these categories individually is a good way of investigating the performance of these model foul release coatings and potentially determining the mechanisms by which

these additives to silicone surface coatings are improving general foul release performance.

We should note again that the EPS is a highly diverse and heterogenous category, even a single biofilm will not have a homogenous mixture of EPS throughout the biofilm structure as these substances perform a number of functions beyond assisting bioadhesion and surface colonisation such as inter cellular communication, literature suggests that E-DNA is less critical to bioadhesion instead performing other functions within the biofilm such as contributing the structural stability of an established biofilm [185] and aiding resistance to predation or antimicrobials [186]. Polysaccharides and proteins have been found to constitute 75-89% of the EPS in bacterial biofilms [187] and colorimetric analysis of biofilm EPS compositions have found polysaccharides and proteins to be more concentrated in the adhesive layer of a biofilm suggesting that they have a particularly important role in bacterial adsorption and biofilm adhesion [188] as such it is this class of molecules, rather than E-DNA, that are likely to be most relevant to early biofouling mechanisms and it is these biomolecules that we have chosen to test that model foul release properties.

Protein adsorption to surfaces has long been a subject of scientific interest [189] the adsorption of a protein film on a surface has been identified in several processes as the initial stage of bacterial adhesion, this process is reliable enough that patterned surface protein adsorption has been used as a way of creating ordered arrays of attached cells for culturing[190]. The ready adsorption of proteins to PDMS elastomers is the primary failing of this material as an otherwise robust foul release surface, it is therefore of particular interest to consider protein adsorption on these model foul release surfaces.

For this study Quartz crystal microbalance was the primary technique employed, this highly sensitive technique is ideal for this kind of study enabling the monitor of mass changes and therefore biomolecule adsorption in situ in real time. The two surfaces of most interest are simple PDMS and PDMS/PFPE-PEO. As established PFPE-PEO forms a partial wetting monolayer at the solid/liquid monolayer of PDMS in water the effect this has on biomolecule adhesion will be purely interfacial, the bulk properties of a PDMS/PFPE-PEO surface and a PDMS surface will be the same. The comparative propensity to fouling should be directly attributable to this single wetting monolayer. As PDMS is a hydrophobic low energy surface we would expect proteins to adsorb to the surface via hydrophobic interactions and denature in the process, for comparison hydrophilic surfaces of gold and silica are also included in this study so the observed adsorption can be compared with well characterised surfaces regularly used in protein adsorption experiments. As seen in the last chapter the spin coated blended model surfaces did

not exhibit this solid/liquid interfacial PFPE-PEO layer, these surfaces were not included in this study due to the lack of clear and consistent surface structures and due to the challenges outlined in chapter3 which were further compounded when trying to prepare these as films on QCM crystal surfaces.

5.4 Biomolecules

5.4.1 Dextran Polysaccharide

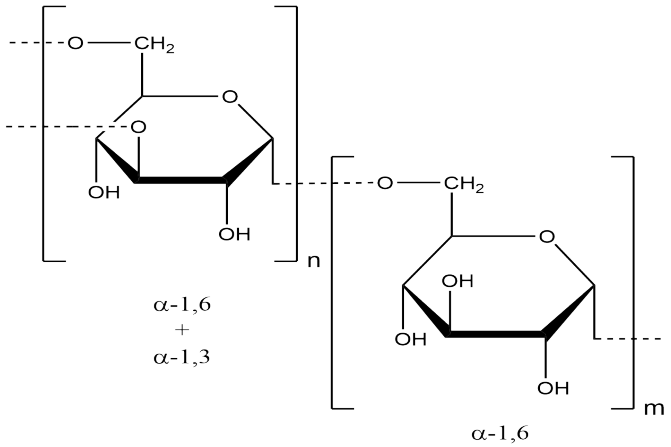

Figure 5.1: Chemical structure of the Polysaccharide Dextran

As the structure in figure 5.1 demonstrates, dextran is a branched, uncharged polysaccharide typically of high molecular weight derived from D-glucose mostly connected via $\alpha(\rightarrow 6)$ linkages. Branching increases with greater molecular weight. This polysaccharide is produced by bacterial microbes and is present throughout nature such as in dental plaque[191]. It is widely available commercially and one of the more comprehensively studied and understood polysaccharides owing to its clinical applications as a antithrombotic and blood plasma expander to treat anaemia [192]. This polysaccharide is of particular interest to questions of biofouling as it has been identified as an exopolysaccharide present in the EPS of bacterial biofilms, the adhesion of dextran on foul release surfaces should be assessed as there are indications this polysaccharide contributes to the adhesion and development of biofilms with prior research using the Dextran enzyeme dextranase showed that the breakdown of bacterial dextran inhibited the formation of biofilms[193][194].

Two Dextrans with average molecular weights of 20,000 and 150,000 Da were purchased from Sigma Aldrich. These Dextrans were produced from Leuconostoc mesenteroides bacterial cultures and were water soluble.

5.4.2 Protein: Bovine serum albumin

Bovine serum albumin (BSA) is a globular protein derived from cows and is the most common protein found in bovine blood. The protein has a molecular weight of 67kDa comprised of 583 amino acids. As a widely commercially available, water soluble and stable protein, BSA has been highly characterised and widely studied for a variety of protein interactions including adsorption to various model surfaces using QCM [195][196]. In solution this protein has a pseudo spherical shape with dimensions 40x 40x140$\mathring{A}$ [197].

BSA was purchased from Sigma Aldrich in lyophilised, freeze dried powder from.

5.4.3 Protein: Lysozyme

Lysozyme is a protein with a molecular mass of 14kDa, comprised of one polypeptide chain containing 129 amino acids. In nature this protein functions as an antimicrobial, acting as an enzyme which catalyses the hydrolysis of carbohydrates in the cell walls of Gram-positive bacteria. A globular protein but smaller than BSA with an ellipsoidal shape and solution dimensions of 45x30x30$\mathring{A}$ this protein is also ubiquitous in protein adsorption studies [198]as it can be readily extracted. from chicken egg white and is regarded as a stable protein in solution.

Lysozyme was purchased from Sigma Aldrich in lyophilised powder form from chicken egg white.

5.4.4 Protein: mefp-1

Mytilus Edulis foot protein 1 (mefp-1) is one of a series of 5 proteins found in the adhesive plaque that binds the sea mussel Mytilus Edulis to a fouling surface. In nature this adhesive glue forms rapidly from the 'foot' cavity of the mussel allowing the mussel to tether itself to a surface within 2-5 minutes this allows mussels to withstand significant hydrodynamic forces. preventing them from being washed ashore by tidal forces or waves. The adsorption of these proteins from liquid onto

solid surfaces is the first step in the formation of this strong bonding plaque, meaning unlike the other generic globular proteins considered, the fouling potential of this protein is known to be directly relevant to the mechanism of biofouling for this macro-fouler.
MEFP-1 is the best characterised of this class of adhesive proteins constituting 5% of the content of the mussel adhesive plaque[199]. mefp-1 is a large protein with molecular weight 130kDa and a comparatively simple structure for a protein that can be modelled as a random polymer composed of 75-85 units of a single repeating decapeptide; NH2-Ala-Lys-Pro-Ser-Tyr-Hyp-Hyp-Thr-L-DOPA-Lys-COOH. All MEFP proteins contain an atypical amino acid L-3-,4-dihydroxyphenylalanine (L-DOPA) (11-18 mol% for mefp-1) shown in figure 5.2, this DOPA component is thought to contribute to the adhesive properties of these proteins, with strong reported interactions with metals and metal oxides [200].

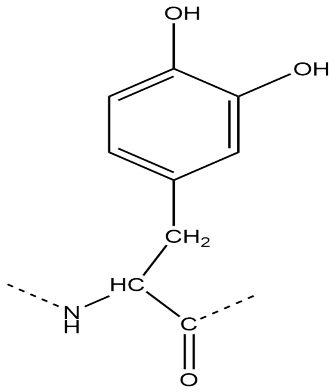

Figure 5.2: Dopa chemical group in mefp-1 which contributes to the adhesive property of the protein.

The DOPA residues have a second function in the protein; as well as contributing to adhesion these groups readily undergoes oxidation forming crosslinks between protein molecules, this reaction enables the rapid formation of the mussel foot plaque bond as covalent bonds between the proteins create a strong cohesive structure out of the adhesive mixture[201]. This oxidation can be induced by $NaIO_4$ or auto induced by in solutions with pH above 7[202]. As such most adhesion studies are conducted in acidic conditions to prevent solution aggregation.

Mefp-1 was purchased from Sigma Aldrich in solution form as 1 ml of 1mg/ml mefp-1 in a sterile, 1% citric acid solution.

5.5 Methods: QCM tests

5.5.1 Quartz Crystal Microbalance and sensor surface preparation

As previously stated in the techniques chapter 2 QCM-D measurements were performed using the Biolin Scientific Qsense D300 instrument show in figure 5.3. This instrument allows for temperature control and the monitoring of ΔF and ΔD for 3 overtones and the harmonic frequency for a single sensor at a time. The temperature selected for all measurements was 31.7°C, as temperature control required an above room temperature setpoint. This temperature was the stable temperature achieved in the earliest experiments and so was maintained for consistency. All experiments were conducted in a stop-flow batch orientation. Initially, frequencies for sensors were found in water buffer solution and QCM-D monitoring commenced, sensors were allowed to equilibrate until a stable baseline of F and D were achieved. Solutions were exchanged by flowing through 0.5ml of desired solution from pipette under gravity.

After each measurement the instrument was cleaned thoroughly by flushing at least 50ml of Hellemenex solution through all tubing and and the crystal chamber followed by 200ml of deionised water. to remove all traces of biomolecules or other buffer solute.

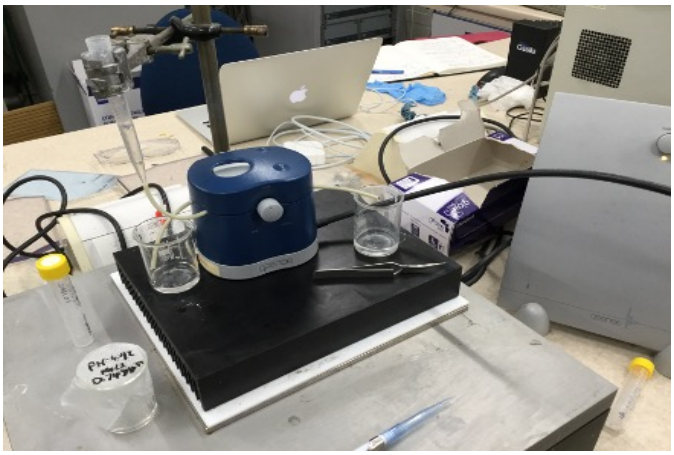

Figure 5.3: QCM-D D300 instrument in operaton

Quartz crystals were purchased from Biolin scientific and OpenQcm. All

quartz crystals were AT cut with 5MHz natural frequency. silicon dioxide coated quartz crystal sensors were purchased from Biolin scientific(QSX 303) with reported surface roughness of less than 1 nm. gold coated QCM crystals were sourced from open QCM with reported quartz thickness of $270\mu m$ and electrodes of gold/titanium deposited on the quartz crystal the gold surface was 200nm thick on a 10nm titanium substrate . Prior to use and reuse gold and silica coated sensors were cleaned with a cycle uv/ozone → sonication in SDS → uv/ozone → sonication in deionised water to remove any organic contaminants.

5.5.1.1 PDMS and PDMS/PFPE-PEO surface preparation

In order to mimic the PDMS/PFPE-PEO topcoat surfaces previously studied, PDMS thin films were deposited on gold coated QCM sensors via spin coating with resultant films depicted in figure 5.4. Solutions of 43500M_w HT-PDMS (Sigma) were formed at 1% in n-Hexane with crosslinker TES-40 (Wacker) and catalyst ATPDMS (Gelest) at 10% and 1% w/w_{PDMS} and spun on gold coated QCM crystals at 2000rpm. All crystals were tested after film deposition to determine the crystal resonances were still detectable, films were then left for at least 24 hours in ambient conditions for hydrolysis cure to ensure films were fully crosslinked before use. Equivalent films were deposited on silicon wafers at the same spin rate and measured with ellipsometry to have a thickness of 80nm. This thickness was found to provide good surface coverage whilst preserving crystal resonances.

PDMS/PFPE-PEO model sensors were prepared by preparing and curing thin films of PDMS on gold coated QCM crystals. Once the PDMS films were cured, the PFPE-PEO Fluorolink E10/6 (Solvay)was deposited onto these surfaces by spin coating from a 2% PFPE-PEO dispersion in ethanol at 2000 rpm resulting in a light coverage of de-wetted PFPE-PEO droplets on the PDMS/gold/quartz sensor surface.

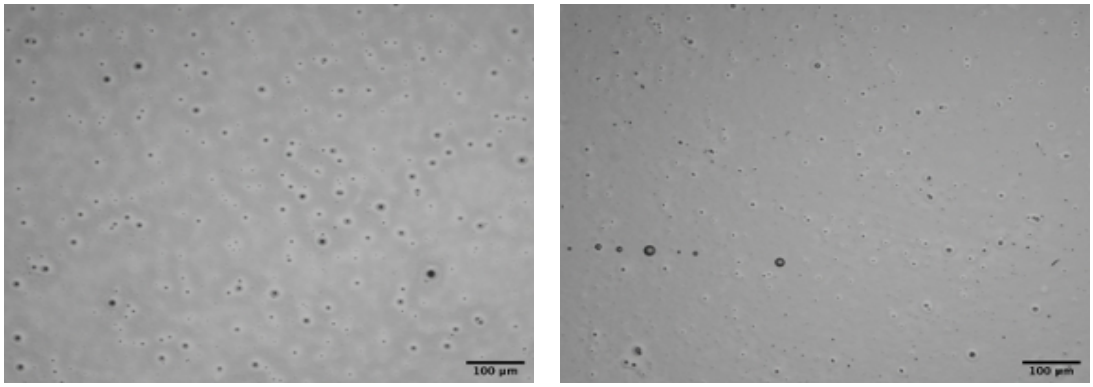

(a) PDMS on gold coated QCM sensor

(b) PFPE-PEO deposited on PDMS coated gold QCM sensor (note droplets bottom left of image)

Figure 5.4: 10x magnification optical micrographs of spin coated films of PDMS on gold coated crystal sensors and PFPE-PEO deposited on PDMS crystal sensors for model foul release analysis with QCM

5.5.2 QCM BSA adsorption tests

Buffer solutions for BSA (Sigma A7030) were prepared by dissolving 200mM of $CaCl_2$ in deionised water. BSA was dissolved in this buffer at a concentration of 50μg/ml. QCM sensors were monitored in salt buffer before introducing BSA protein to the chamber and F and D monitored. After the system reached equilibrium salt buffer was flowed through the chamber to monitor desorption. Tests were performed on silica coated, gold coated, PDMS and PDMS/PFPE-PEO sensors. Experiments for each surface were repeated at least 3 times so average adsorptions could be found.

5.5.2.1 BSA immersion AFM tests

Separate tests were also performed on PDMS and PFPE-PEO/PDMS model surfaces prepared on silicon wafers to the same protocol outlined in section 5.5.1.1. Ex situ protein adsorption of PDMS and PDMS/PFPE-PEO Surfaces were performed in a batch process with all films subject to the same protein solution in a protocol similar to that outlined by Taylor et al [203]. Surfaces first placed in a beaker and immersed in a volume of 10ml of salt buffer. Subsequently, 10ml of 100μg/ml BSA solution was added to the beaker to produce a solution with BSA concentration 50 μg/ml films were left for 90 minutes to allow protein adhesion.

Then additional salt buffer was added to the solution in order to heavily dilute the protein solution prior to sample removal, this was to prevent the film sample surface being exposed to a concentrated film of protein at the air liquid interface as they are pulled through the liquid meniscus [204]. Samples were further rinsed in salt buffer and then lightly dried with nitrogen before the surfaces were probed with AFM to observe evidence of adhered protein.

5.5.3 QCM lysozyme adsorption tests

Following established protocols [205] Lysozyme (Sigma Aldrich, L6876) solutions were prepared in PBS solutions (purchased from Sigma Aldrich No. P4417) with an ionic content of 0.0027M potassium chloride and 0.137M sodium chloride with a stabilised pH of 7.4. Solutions were prepared at concentrations of 50μg/ml and QCM adhesion test were performed in the same stop flow configuration as BSA. Lysozyme adhesion was tested on gold, PDMS and PDMS/PFPE-PEO surfaces.

5.5.4 QCM MEFP-1 adsorption tests

An initial solution 1ml of 1mg/ml of mefp-1 (Sigma Aldrich) was diluted in to a concentration of 25μg/ml by adapting established methods used for monitoring the surface adhesion of mefp-1 [206][207]. A solution of 1% citric acid in deionised water was formed before NaCl salt was added to a concentration of 0.75M. Small amounts of concentrated sodium hydroxide solution were then added to the solution to raise the pH to 4.9. The 1mg/ml mefp-1 fraction was mixed thoroughly with 40ml of this buffer to produce a protein solution of 25μg/ml. mefp-1 adhesion was tested against gold,PDMS and PDMS/PFPE-PEO surfaces.

5.5.4.1 MEFP-1 immersion AFM tests

A set of immersion tests were also attempted with Mefp-1 by preparing PDMS and PDMS/PFPE-PEO thin films in 10ml of buffer before adding 10ml of 25μg/ml mefp-1, exposing the films to a 12.5μg/ml concentration of mefp-1 protein. Protein exposure lasted 90 minutes before solution dilution and sample rinsing. The surfaces were then probed with AFM.

5.5.5 QCM Dextran adsorption tests

Dextran tests were performed following the protocol outlined by Kwon et al [208]. Dextrans of M_w 150kDa and 20KDa were utilised for experiment (Sigma Aldrich). 150kDa dextran was diluted in 100mM NaCl unbuffered salt solution at a series of concentrations 10,20,50 and 100μM/ml (150 mg/ml). Surfaces, initially monitored in salt solution, were exposed to 10μM dextran solution and allowed to reach saturation before successively higher concentrations of dextran are introduced to the chamber, once sensor frequency and dissipation responses have saturated for 100μM dextran solution the sensors were exposed to two rinsing salt buffer flows. Dextran adsorption measurements were performed on silica , PDMS and PDMS/PFPE-PEO coated sensors. An adsorption test using 100μM of 20kDa dextran was also performed on silica to compare the effect of molecular weight. Viscoelastic layer fits were performed using the Voigt mode [120] to estimate the layer thickness and and mass per unit area of adsorbed dextran. This data analysis was performed using the Qtools (Qsense) software.

5.6 Results and analysis: QCM tests

5.6.1 BSA adsorption

It should be noted prior to considering the observed QCM responses to protein that PDMS/PFPE-PEO coated crystals exhibited substantial long term frequency shifts when exposed to water.

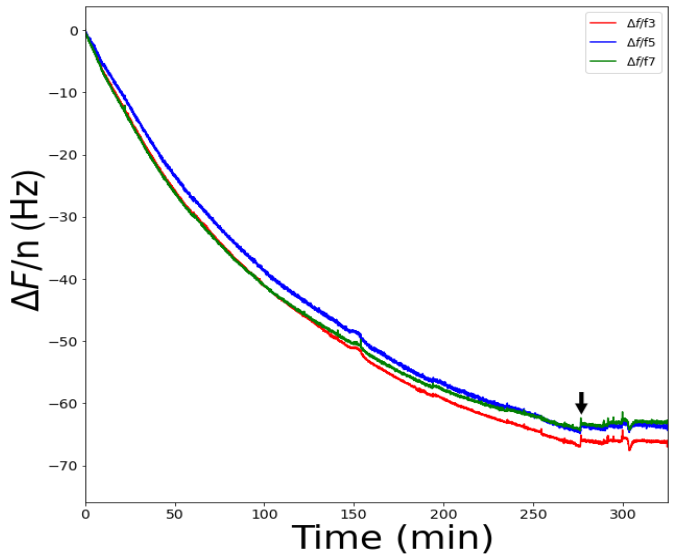

Figure 5.5: Frequency response of a PDMS/PFPE-PEO coated QCM sensor in 200mM $CaCl_2$ water solution from resonance detection, arrow represents a transient buffer flow.

The frequency response shown in figure 5.5 suggests substantial mass uptake in ambient conditions, this can be explained by the surface macro droplets of amphiphilic PFPE-PEO absorbing significant amounts of water. The recording of this process began as soon as resonances in liquid were determined but the process will have commenced as soon as the sensor surface was immersed in water, so the water uptake process cannot be fully recorded, drift is most significant initially and slows over time falling to $\frac{\delta F}{n} < 0.1 Hz min^{-1}$ after 270 minutes but stabilised almost completely after a transient flow was flushed through the sensor. Because the entire water uptake stage could not be captured and the timeframes were dependent on the sensor used and the delay between sensor/liquid immersion and data acquisition this data is not analysed with the drift monitored over hours until PDMS/PFPE-PEO frequency response stabilised.

Considering the BSA adsorption on the simple surfaces we observe the largest frequency shifts from hydrophilic, silicon and gold coated QCM sensors

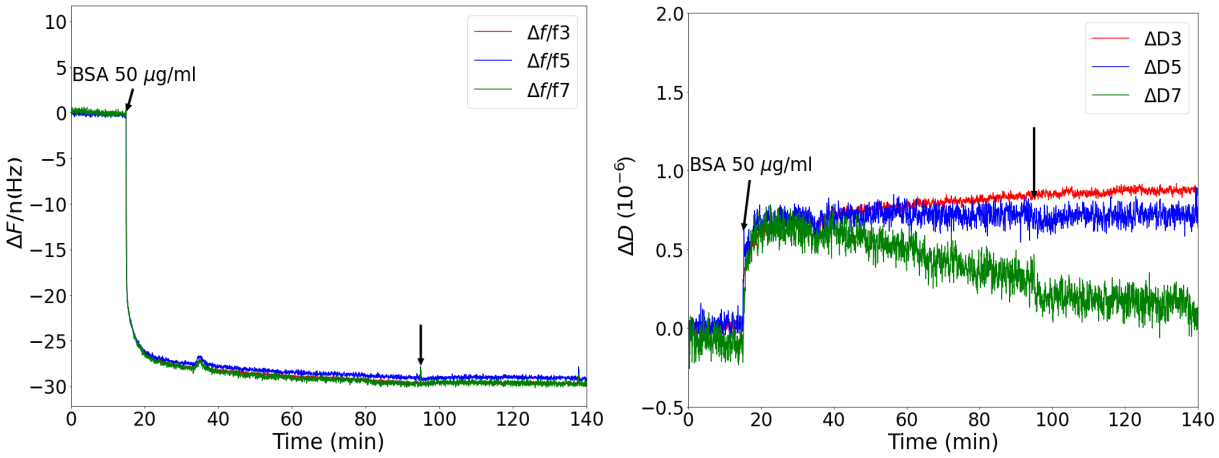

(a) Δ F/n (b) Δ D

Figure 5.6: ΔF and Δ D response of gold coated QCM crystals to 50μg/ml BSA (unannotated arrow at ≈ 95 minutes represents buffer flow for desorption).

With the frequency responses shown in figure 5.6, an areal mass can be derived using the Sauerbrey equation outlined in chapter2 outlined here as

$$\Delta m = \frac{17.7 \Delta F_n}{n} \tag{5.1}$$

The measured adsorbed mass calculated for the measured harmonics 15MHz 25MHz and 35MHz could be monitored in real time as shown in figure 5.7 for gold.

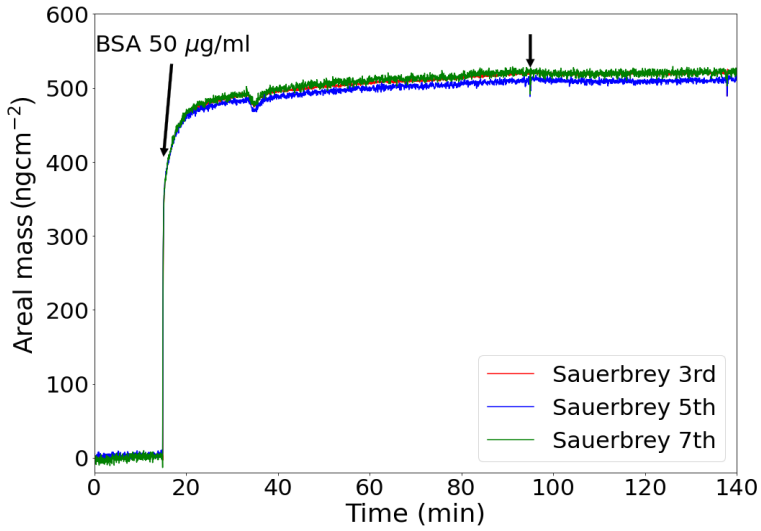

Figure 5.7: Calculated Sauerbrey mass per unit area for 50μg/ml BSA on gold.

Silica coated QCM crystals showed similar responses to BSA protein

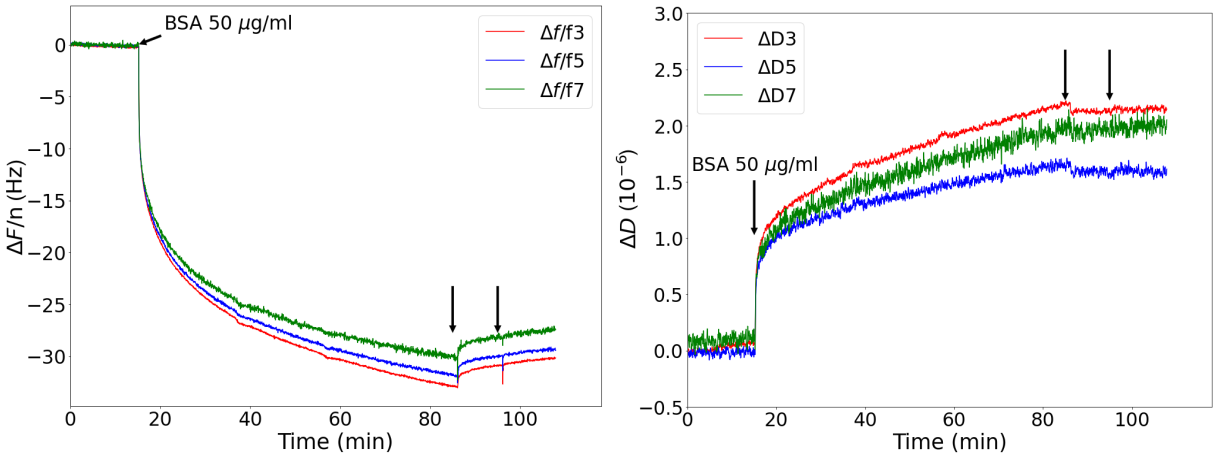

(a) Δ F/n (b) Δ D

Figure 5.8: ΔF and Δ D response of silica coated QCM crystals to 50μg/ml BSA (unannotated arrows represent buffer flow for desorption).

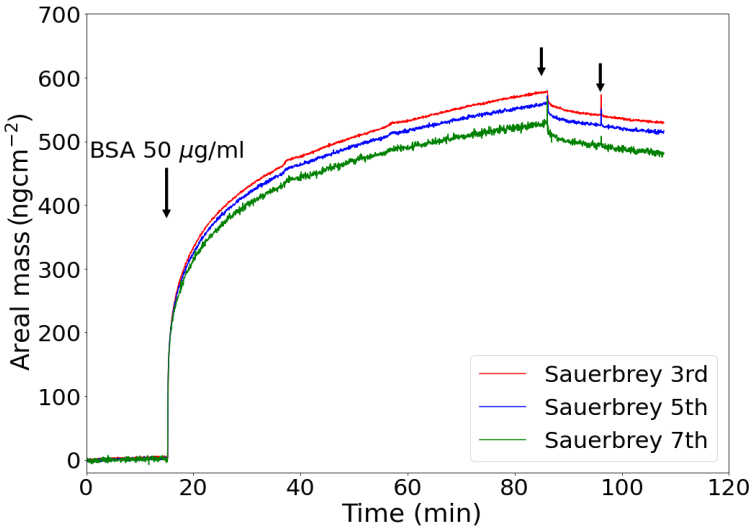

Figure 5.9: Calculated Sauerbrey mass per unit area for 50μg/ml BSA on silica.

Considering figures 5.6a and 5.8a, positive frequency shifts after buffer flow were small, suggesting very little adhered protein desorbed upon rinsing. We see in figures 5.7 and 5.9 that with both gold and silica hydrophilic surfaces the total mass absorbed reaches a value of $> 500\text{ngcm}^{-2}$ within 80 minutes of protein exposure.

The adsorption of BSA onto hydrophobic PDMS shown in figure 5.10 was smaller overall than for either of the hydrophilic surfaces.

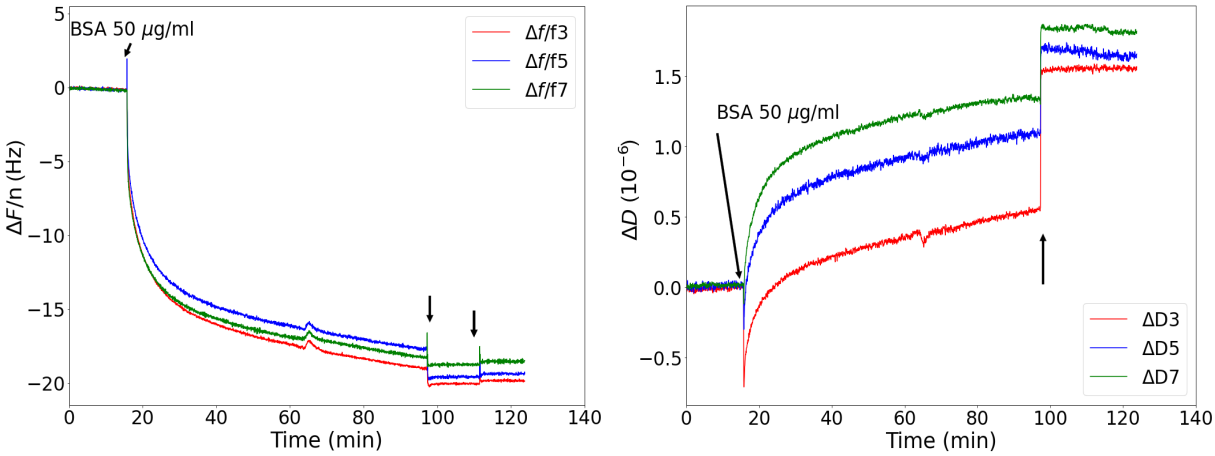

(a) Δ F/n (b) Δ D

Figure 5.10: ΔF and Δ D response of PDMS coated QCM crystals to 50μg/ml BSA (unannotated arrows represent buffer flow for desorption).

figure 5.11 shows that the smaller frequency shifts result in a smaller mass adsorbed at saturation.

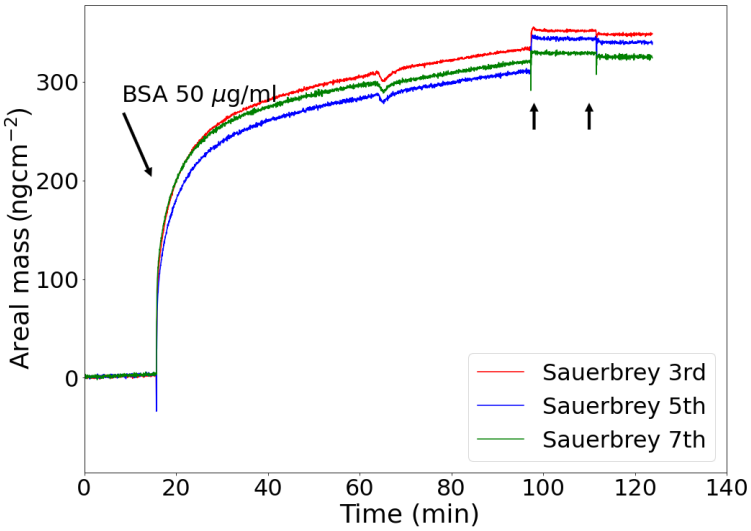

Figure 5.11: Calculated Sauerbrey mass per unit area for 50μg/ml BSA on PDMS (unannotated arrows represent buffer flow for desorption).

Note the small peak feature in figure 5.12a at around 65 minutes, this is due to a temperature fluctuation caused by loading salt buffer into the QCM circulation system prior to flowing through the sensor chamber. Small differences between ambient temperature solutions and the controlled temperature of the QCM can cause small temporary shifts in the temperature which translates into temperature dependent fluctuations in F and D[209].

The response to BSA from stabilised PDMS/PFPE-PEO, shown in figure 5.12, was in stark contrast to either hydrophilic or hydrophobic surfaces showing negligible response to protein exposure.

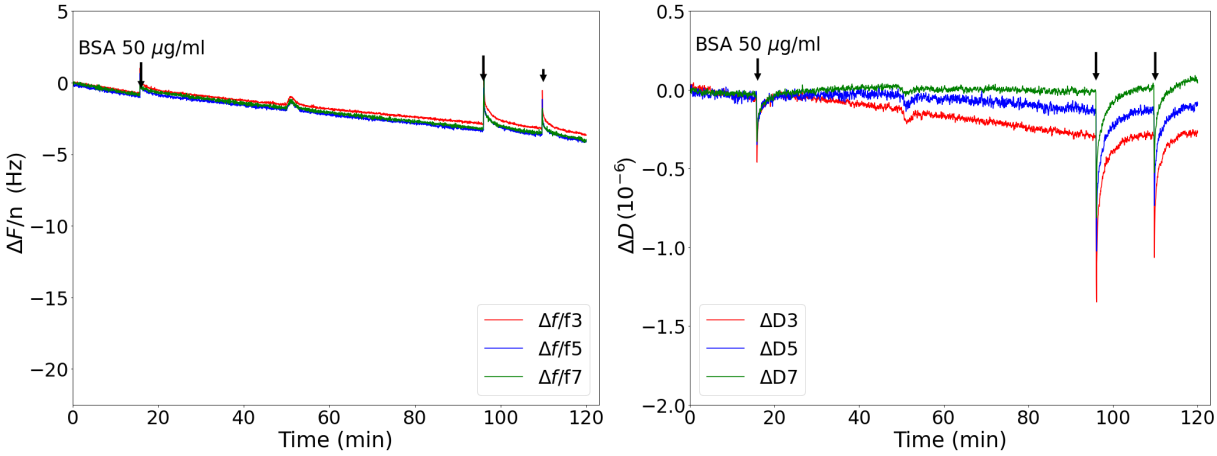

(a) Δ F/n (b) Δ D

Figure 5.12: ΔF and ΔD response of PDMS/PFPE-PEO coated QCM crystals to 50μg/ml BSA (unannotated arrows represent buffer flow for desorption).

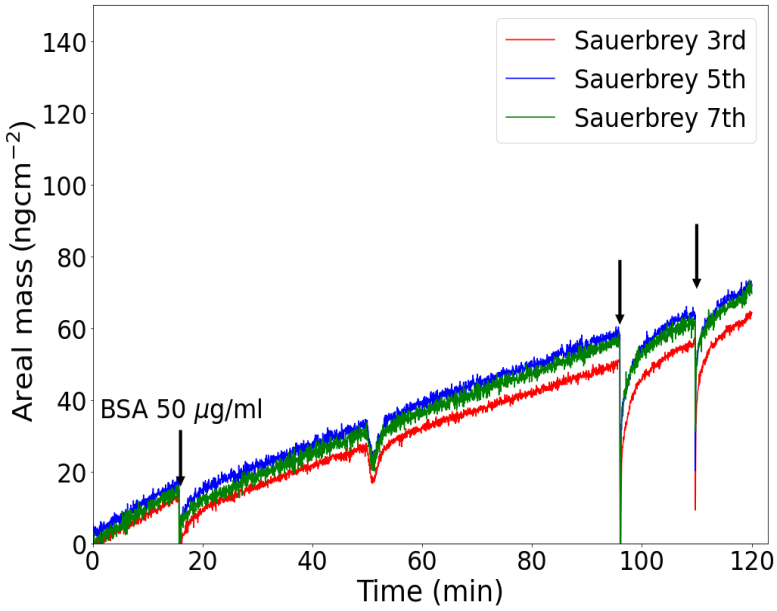

Figure 5.13: Calculated Sauerbrey mass per unit area for 50μg/ml of BSA on PDMS/PFPE-PEO coated QCM surfaces (unannotated arrows represent buffer flow for desorption).

The example experiment shown here is a fair and representative example of the series of experiments performed on PDMS/PFPE-PEO. Note that the Sauerbrey mass shown in figure 5.13 is highly linear and may not be real but rather simply the continuing drift in frequency that can be seen prior to protein flow at 15 minutes.

To further corroborate this behaviour an additional experiment was performed on a PDMS/PFPE-PEO coated QCM crystal using a series of different concentration of BSA protein on solution.

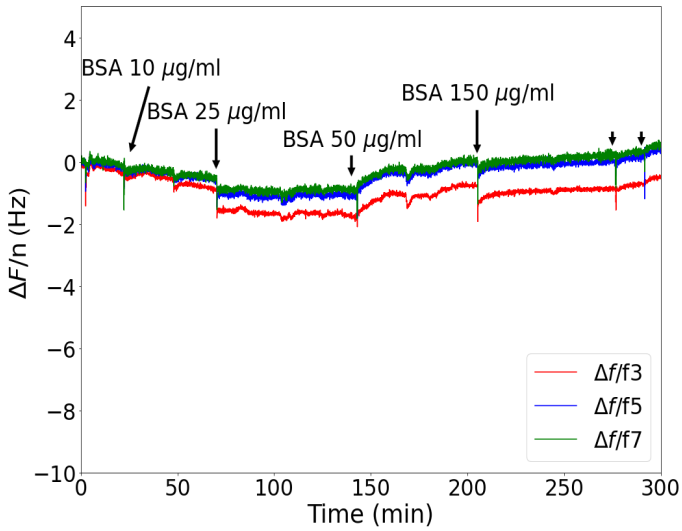

Figure 5.14: Frequency response of PDMS/PFPE-PEO coated QCM surface to a series of BSA concentrations.

The lack of any real response to protein concentrations up to 150μg/ml indicates that this technique finds little to no adsorption of BSA protein on these model foul release surfaces using the Sauerbrey equation for the data shown in figure 5.14. The maximum detected mass adsorbed throughout this experiment was 30ngcm^{-2}.

Averaging results across all harmonics for at least three experiments per surface we, show In figure 5.15 the overall mass adsorbed for each surface after 70 minutes of exposure to a 50 μg/ml BSA solution.

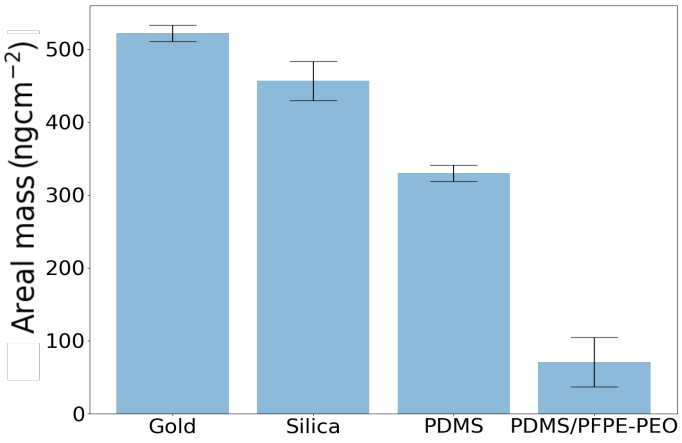

Figure 5.15: Average Sauerbrey BSA wet mass adsorbed for selected surfaces after 70 minutes of exposure to a 50 μg/ml BSA solution.

Table 5.1: Summary of BSA Sauerbrey wet mass adsorbed after 70 minutes.

Surface	Gold	Silica	PDMS	PDMS/PFPE-PEO
Sauerbrey Mass (ng cm^{-2})	522±11.2	457±26.9	330±11.1	70.9±34.1

Desorption on all surfaces was minimal on all surfaces amounting to less than 1% of mass adsorbed on each surface.

5.6.1.1 BSA Immersion Tests AFM

For post situ AFM analysis of protein adsorption, three samples were tested and examined by AFM each PDMS and PDMS/PFPE-PEO surface. A PDMS film immersed in pure water but no protein solution is shown as a control.

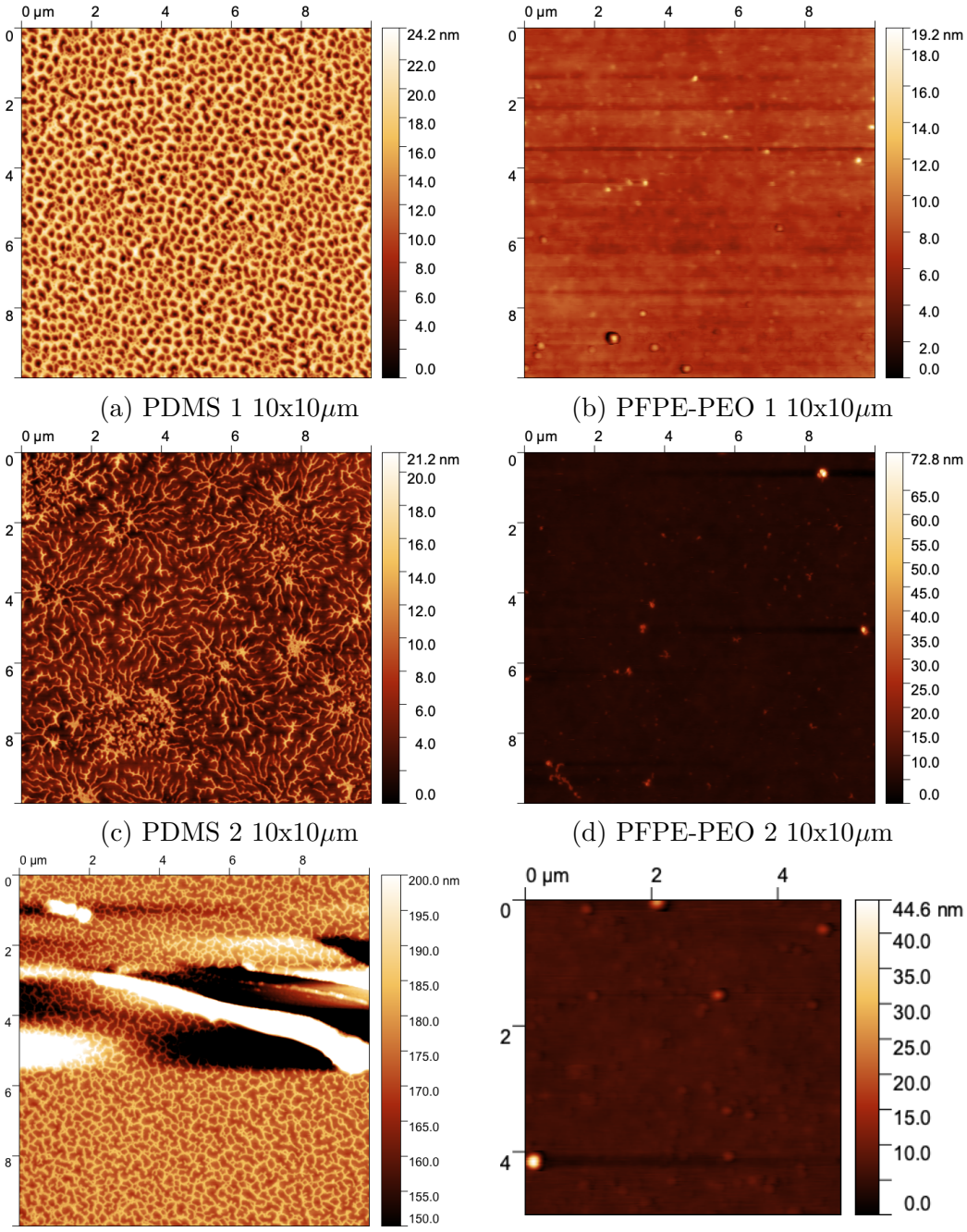

(a) PDMS 1 10x10μm

(b) PFPE-PEO 1 10x10μm

(c) PDMS 2 10x10μm

(d) PFPE-PEO 2 10x10μm

(e) PDMS 3 10x10 μm

(f) PFPE-PEO 3 5x5μm

Figure 5.16: AFM height Images for PDMS and PDMS/PFPE-PEO BSA exposed surfaces.

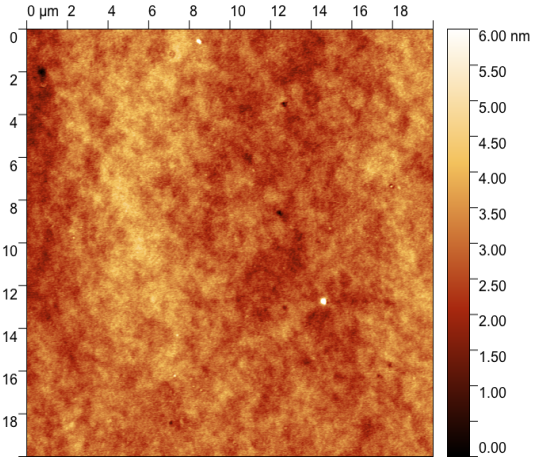

Figure 5.17: 20x20 μm AFM height image for a PDMS film after immersion in pure water.

Note that the image for PDMS 3 shown in figure 5.16e, the acquired image had a large scratch across the centre of the image. This distorted the image somewhat and made statistical analysis more challenging, so a smaller 4x4μm area of the image was selected for analysis. We show this in figure 5.18 alongside a similar area taken from the image in figure 5.16a for sample PDMS 1 which demonstrates that at the same scale the topography is quite similar.

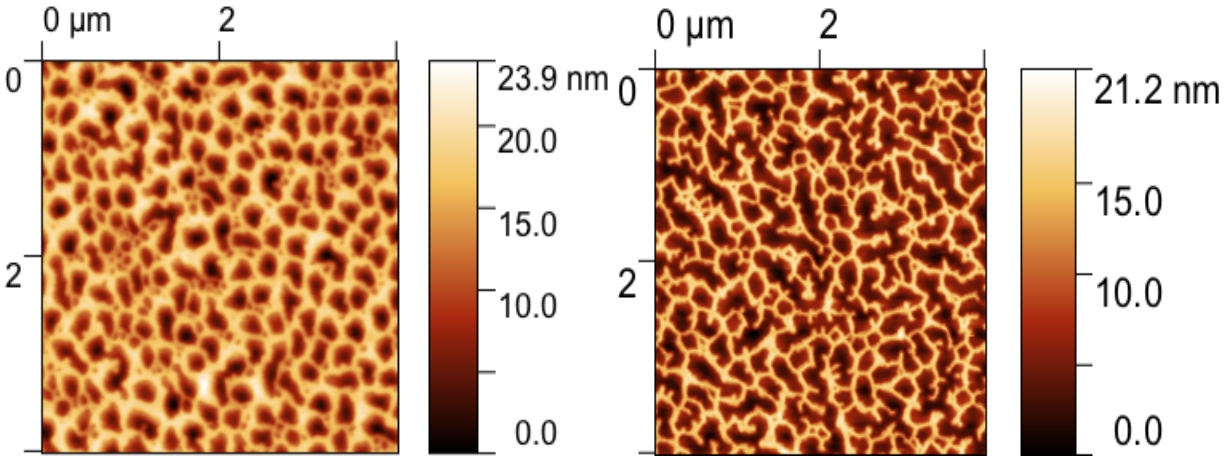

(a) PDMS 1 at 4x4μm (b) PDMS 3 at 4x4μm

Figure 5.18: Selected 4x4mum regions from sample PDMS 1 and PDMS 3.

Table 5.2: PDMS and PDMS/PFPE-PEO image roughness parameters and peak roughness from a series of height profiles.

Image	PDMS 1	PDMS 2	PDMS 3	PDMS/PFPE-PEO 1	PDMS/PFPE-PEO 2	PDMS/PFPE-PEO 3	PDMS control
rms roughness (nm)	4.22	2.85	4.35	1.53	1.07	0.79	0.53
Average maximum height of roughness (nm)	14.9±0.9	10.2±1	14.8±0.4	2.70± 2.43	1.98±0.19	1±0.03	0.99±0.06

There is little or no apparent adhesion of protein on PDMS/PFPE-PEO films post immersion. With table 5.2 showing PDMS/PFPE-PEO surfaces are far smoother than the PDMS surfaces, with only droplet like formations and no mesh like structure of PDMS surfaces. Comparing the PDMS surfaces in figure 5.16 with the image of the PDMS control sample figure 5.17 all three PDMS samples show dendritic mesh like patterns on the surface which are absent from the PDMS control. Assuming the mesh structures seen on post immersion PDMS surfaces are the result of adhered proteins on the surface we can determine the overall surface coverage and adsorbed mass. Otsu's grain analysis identified these structures clearly against the surface background and was used to determine overall surface coverage. A laplacian function found the overall volume of the identified grains (as defined as the volume lost if the identified grains were removed). Using the density of BSA and the size of each image it was possible to determine an areal mass of protein on surfaces. The same process is also applied to the control to demonstrate the validity.

Table 5.3: Grain analysis of PDMS.

Image	PDMS 1 10x10μm	PDMS 2 10x10μm	PDMS 3 4x4μm	PDMS control 20x20μm
Otsu's grain coverage	57.4%	27.7%	41.5%	48.52%
Laplacian grain volume (cm^3)	2.62×10^{-13}	3.45×10^{-14}	9.895×10^{-13}	1.01×10^{-13}
Dry Mass (ng cm^{-2})	357	134	293	34.3

These post situ tests appear to corroborate observations from QCM of very limited BSA adhesion to PDMS/PFPE-PEO. The dry mass adsorbed measured via this method is far greater for the PDMS post situ samples than the PDMS control, upon which there is negligible mass adsorbed measured by this method as expected. There is strong consistency between the mass adsorbed on PDMS 1 and PDMS 3. PDMS 3 has significantly lower mass adsorbed in agreement with inspection of figure 5.16 where the mesh on PDMS 2 is less comprehensive than PDMS 1 and 3. A possible explanation is that mishandling of the drying process of samples post immersion could have resulted in some removal of protein on surface PDMS 2.

Further consideration of protein adsorption yielded further evidence of the highly protein resistant nature of the partial wetting monolayer of PFPE-PEO.

5.6.2 Lysozyme adhesion

Figure 5.19 shows a typical QCM response for a gold surface subject to lysozyme. The Sauerbrey mass adsorbed as calculated in figure 5.20 suggests a lower overall adsorbed but generally fast kinetics of adhesion with the saturation value being reached faster than in the case of PDMS.

PDMS and PDMS/PFPE-PEO showed similar results though the general kinetics of adsorption were faster with lower overall adhesion and faster adhesion to saturation levels.

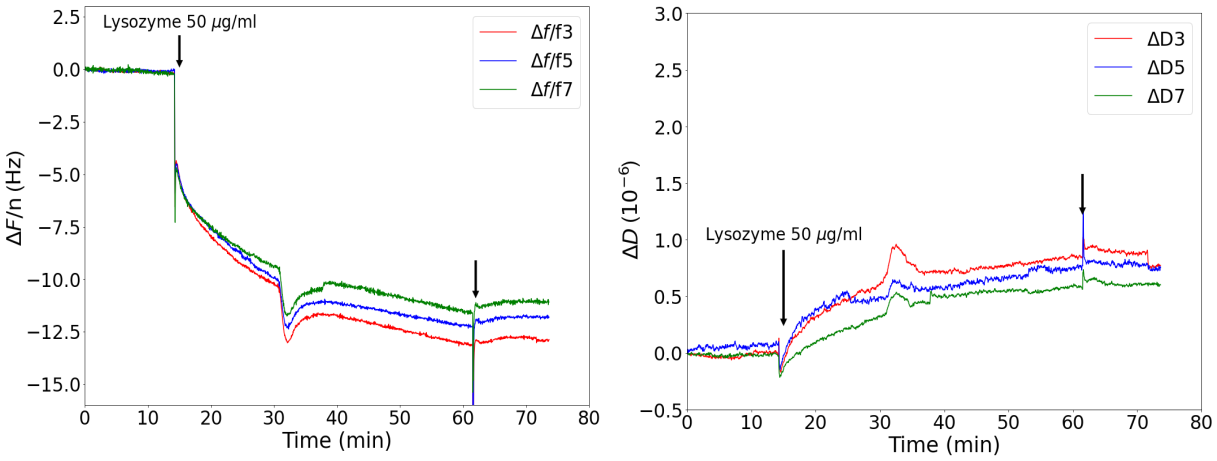

(a) Δ F/n (b) Δ D

Figure 5.19: ΔF and ΔD response of gold coated QCM crystals to 50μg/ml lysozyme(unannotated arrow represents buffer flow for desorption).

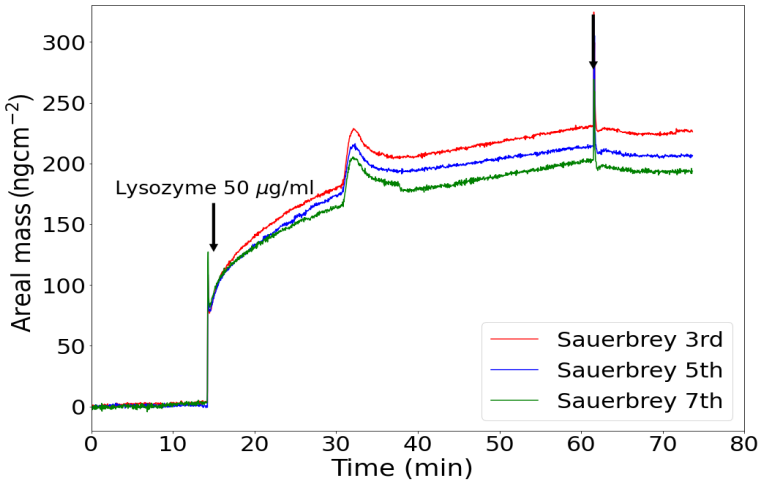

Figure 5.20: Calculated Sauerbrey mass per unit area for 50μg/ml lysozyme on gold (unannotated arrow represents buffer flow for desorption).

Figures 5.21 and 5.22 shows lysozyme adhesion to PDMS follows the same pattern with as BSA, with a reduced adsorption compared to gold.

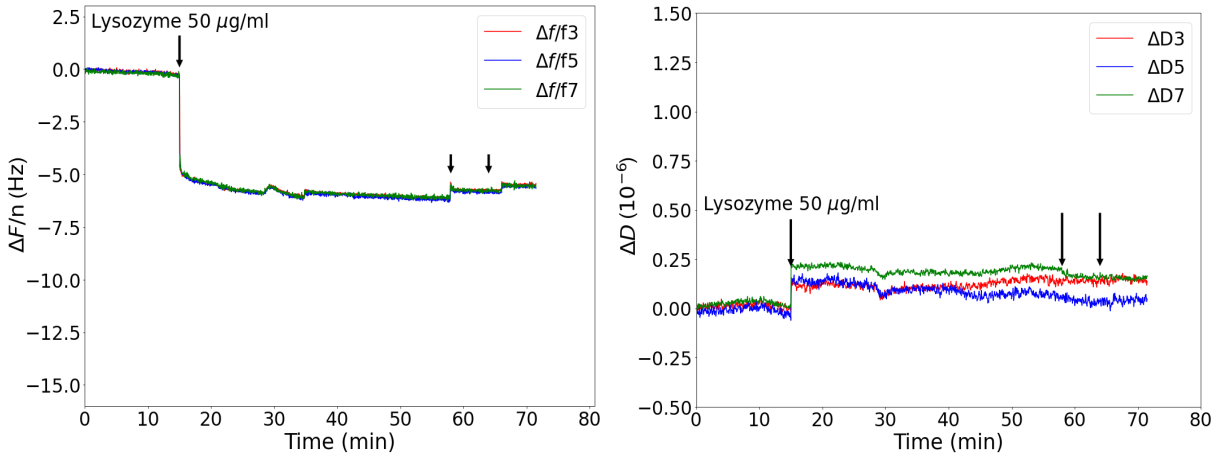

(a) Δ F/n (b) Δ D

Figure 5.21: ΔF and ΔD response of PDMS coated QCM crystals to 50μg/ml lysozyme (unannotated arrow represents buffer flow for desorption).

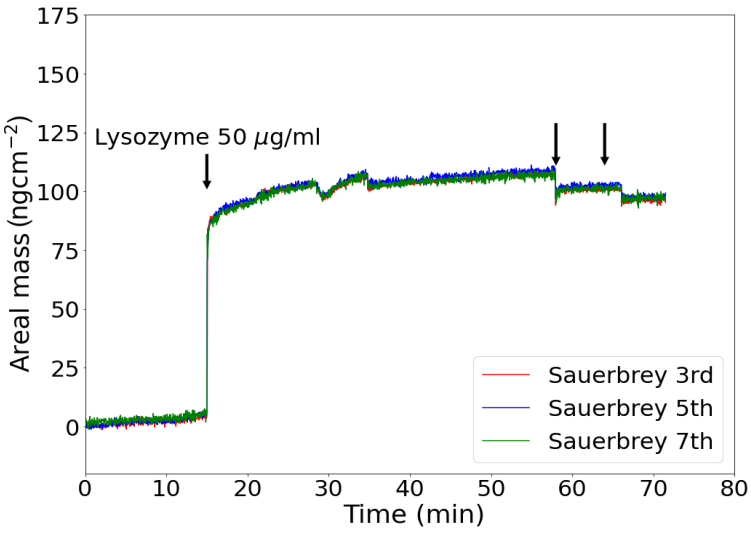

Figure 5.22: Calculated Sauerbrey mass per unit area for 50μg/ml lysozyme on PDMS unannotated arrow represents buffer flow for desorption).

From figure 5.23 and 5.24 PDMS/PFPE-PEO surfaces show minimal response to lysozyme suggesting little or no adsorption.

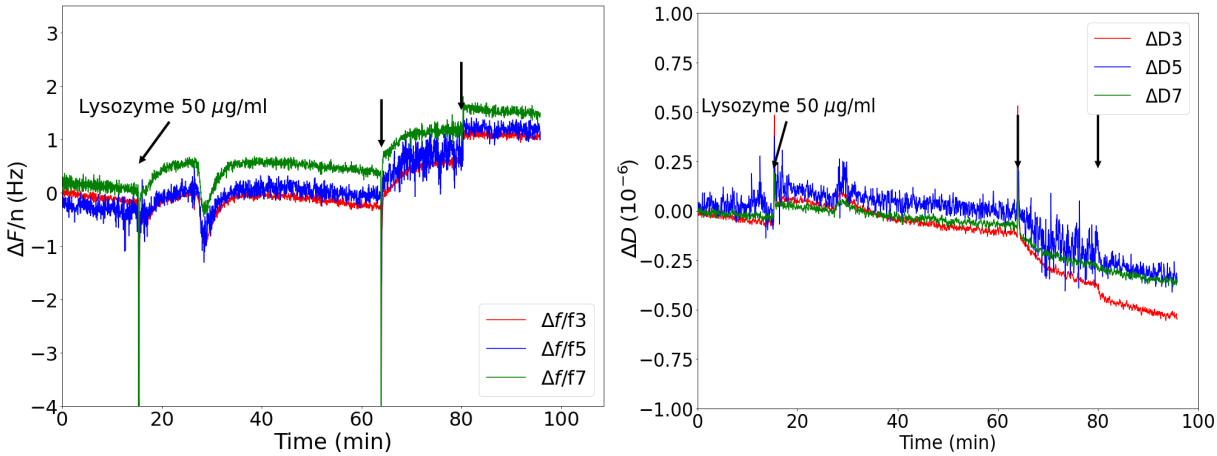

(a) Δ F/n (b) Δ D

Figure 5.23: ΔF and Δ D response of PDMS/PFPE-PEO coated QCM crystals to 50μg/ml lysozyme (unannotated arrow represents buffer flow for desorption).

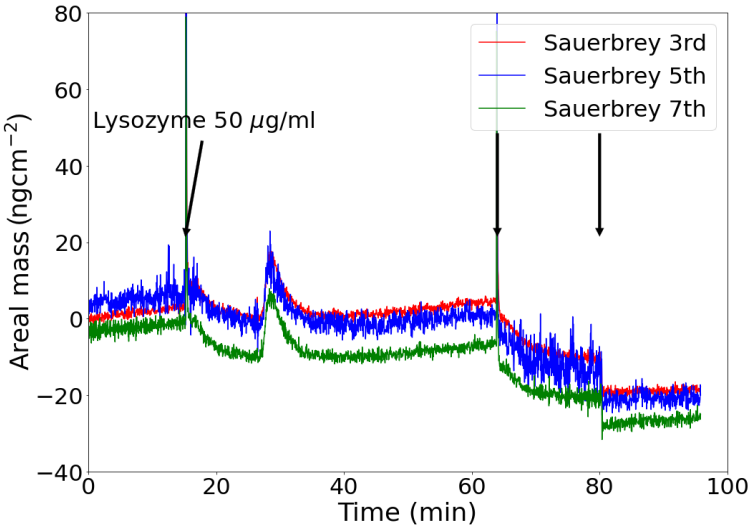

Figure 5.24: Calculated Sauerbrey mass per unit area for 50μg/ml lysozyme on PDMS/PFPE-PEO (unannotated arrow represents buffer flow for desorption).

Taking the Sauerbrey mass from all experiments after 35 minutes of protein exposure at which saturation was reached, we summarise the observed protein absorbance in figure 5.25.

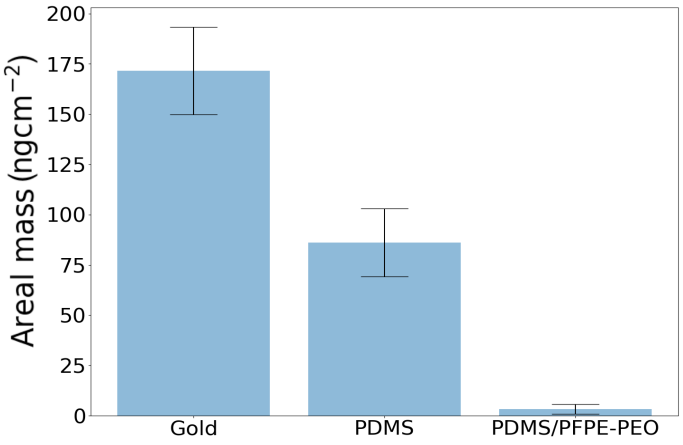

Figure 5.25: The average Sauerbrey wet mass of lysozyme adsorbed after 70 minutes for tested surfaces.

Table 5.4: Summary of Sauerbrey mass adsorbed after 40 minutes.

Surface	Gold	PDMS	PDMS/PFPE-PEO
Sauerbrey Mass (ng cm^{-2})	171.6± 21.7	86.1 ± 16.9	3.4± 2.4

In summary, we see from table 5.57b that PDMS coated surfaces show less overall mass of lysozyme adsorbed to QCM sensors than simple gold surfaces, in this case effectively no protein fouling by lysozyme was observed on the PDMS/PFPE-PEO surfaces.

5.6.3 MEFP-1 Adsorption

Experiments attempted with mefp-1 in pH 4.9 controlled solution were attempted using QCM but observed results were significantly inconsistent for gold and PDMS surfaces presented here in figure 5.26 and 5.27 are the frequency responses from tests on two examples of each surface:

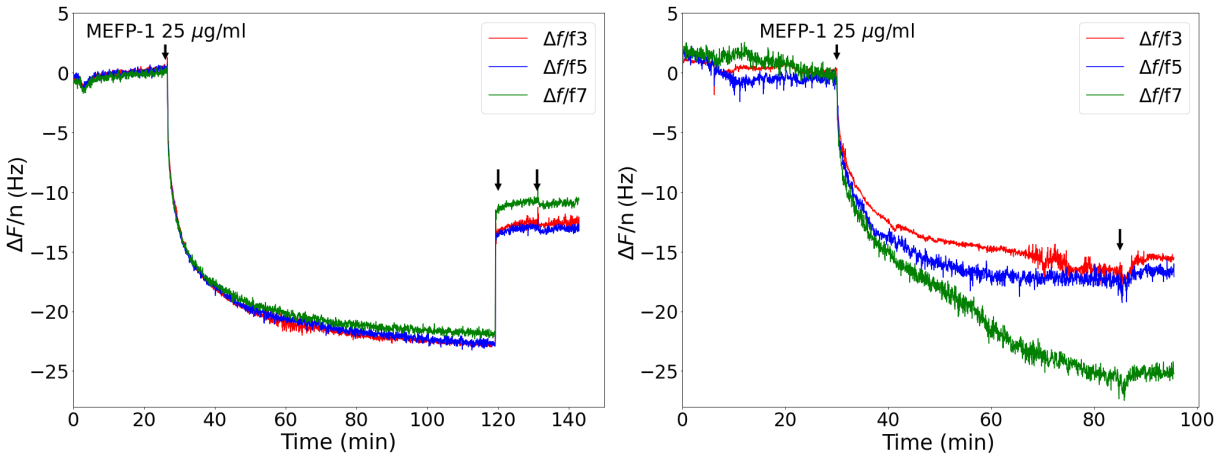

(a) Gold test 1 (b) Gold test 2

Figure 5.26: Frequency responses ΔF from two tests of the adsorption of 25μg/ml mefp-1 on gold coated QCM sensors (unannotated arrow represents buffer flow for desorption).

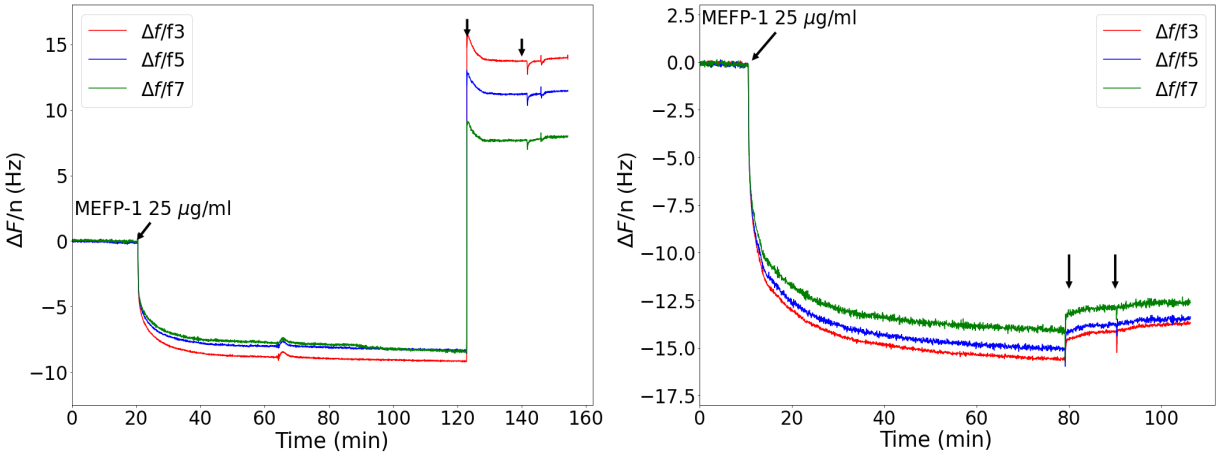

(a) PDMS test 1 (b) PDMS test 2

Figure 5.27: Frequency responses ΔF from two tests of the adsorption of 25μg/ml mefp-1 on PDMS coated QCM sensors (unannotated arrow represents buffer flow for desorption).

As can be seen in figure 5.26a and 5.27a large positive frequency shifts were observed upon buffer rinsing but these shifts are not consistent for each surface with the same shifts absent in tests 5.26b and 5.27b. Note also the frequency response ΔF between both PDMS tests shown in figure 5.27 are very different

peak ΔF in 5.27b is 70% higher than in 5.27a we would not expect this kind of discrepancy between identical experiments on the the same surface, the Sauerbrey absorbed mass after 50 minutes was 147ng cm^{-2} for test 5.27 and 256 ng cm^{-2} for test 5.27b. As such it is not possible to draw clear conclusions from these tests. We attribute this to the limitation of the experimental method; insufficient buffer solution was produced when making the protein solution and had to be remade for later experiments, this may have resulted in small but significant differences in pH and salinity between the protein solution and the new buffer solution.

However, comparing these results with figure 5.28 showing the QCM response of PDMS/PFPE-PEO surfaces to mefp-1 protein we see that there is still little or no evidence of a change due to protein exposure on these surfaces and little evidence of adhesion:

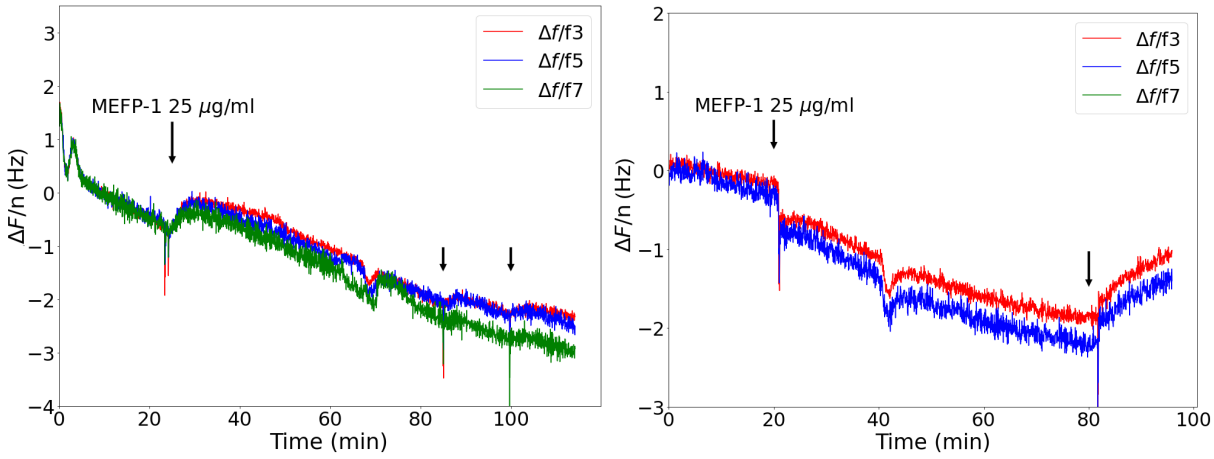

(a) PDMS/PFPE-PEOTest 1

(b) PDMS/PFPE-PEO

Figure 5.28: Frequency responses ΔF from two tests of the adsorption of 25μg/ml mefp-1 on PDMS/PFPE-PEO.

Sauerbrey averages from limited tests are summarised in table 5.5.

Table 5.5: Summary of Sauerbrey mefp-1 mass adsorbed after 50 minutes.

Surface	Gold	PDMS	PDMS/PFPE-PEO
Sauerbrey Mass (ng cm^{-2})	342.8±67.4	245.4±93.8	33.1±3.4

With such high uncertainty in the measurements, limited conclusions can be drawn from these experiments, further mefp-1 tests attempted using immersion and post situ AFM analysis are presented below.

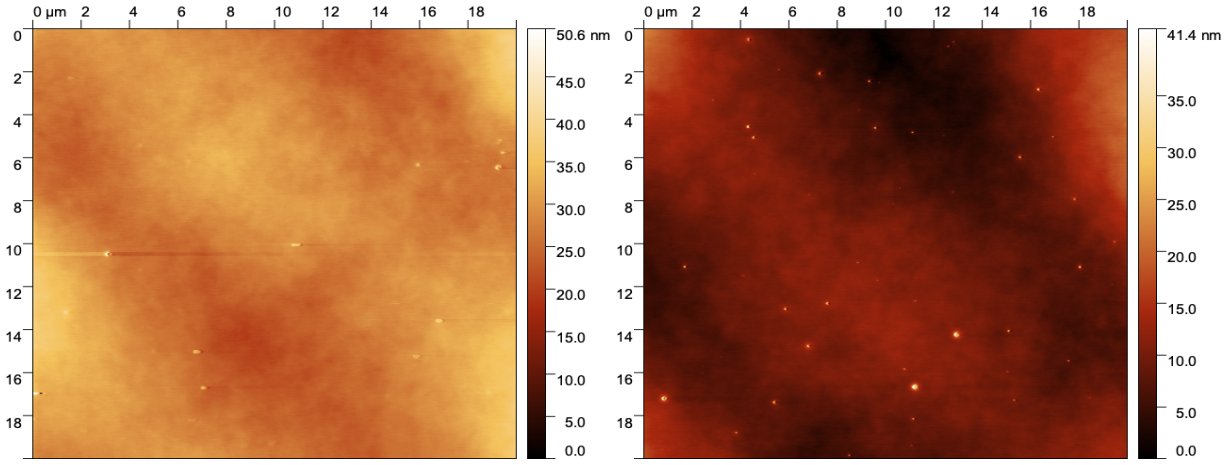

(a) PDMS/PFPE-PEO surface (b) PDMS surface

Figure 5.29: Post situ AFM images for selected PDMS/PFPE-PEO and PDMS surfaces immersed in a 12.5 μg/ml mefp-1 protein solution.

Across 20x20μm areas probed in figure 5.29 there is a limited difference between the two surfaces from these immersion tests. The rms roughness for both images were almost the same, 5.29a is 3.30nm and for 5.29b 3.29nm. Ultimately, there appears to be limited evidence of adhesion on either surface this may be in part due to the highly dilute nature of the immersion solution and the fact that fresh buffer had to be produced to dilute the protein solution which may have caused similar effects as seen in the QCM measurements. Despite the limitations of the data we see from these two experiments very limited ΔF shifts upon protein exposure suggesting little or no absorbance as is consistent with results from BSA and lysozyme tests.

5.6.4 Dextran adsorption

Dextran polysaccharide adhesion on silica(figure 5.30), PDMS(figure 5.31) resulted in frequency and dissipation responses that were distinct from those caused for the absorbance of proteins.

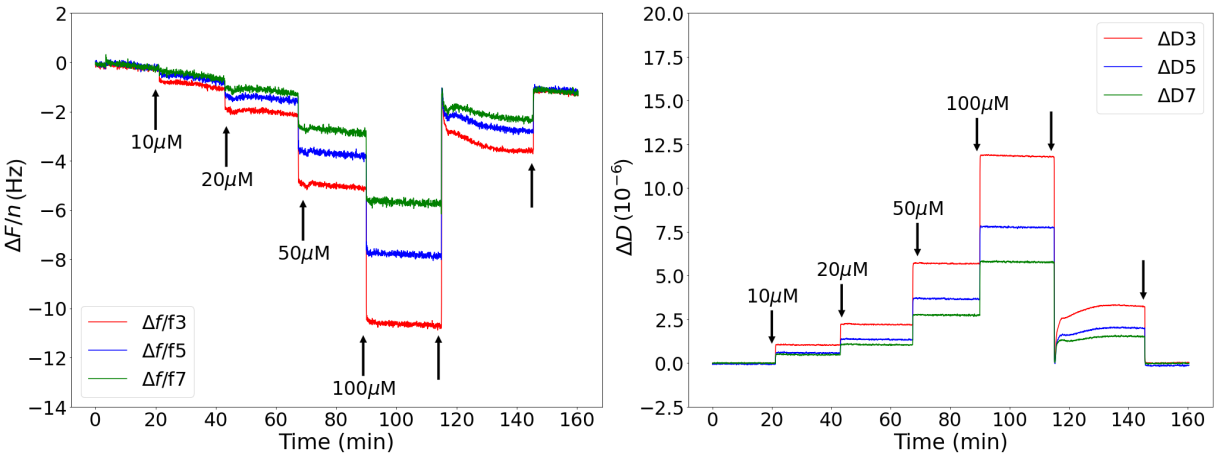

(a) Δ F/n (b) Δ D

Figure 5.30: ΔF and Δ D response of silica coated QCM sensors to 150kDa of dextran for a series of increasing dextran concentrations.

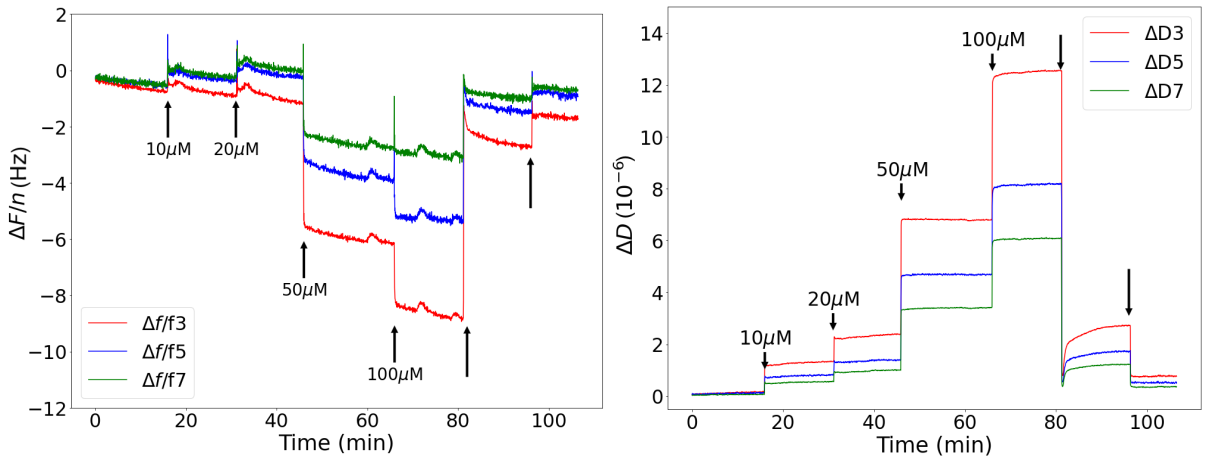

(a) Δ F/n (b) Δ D

Figure 5.31: ΔF and Δ D response of PDMS coated QCM sensors to 150kDa of dextran for a series of increasing dextran concentrations.

We can see clearly that the substantial dissipation caused by the introduction of dextran. Dissipation shifts ΔD due to dextran (figure 5.30b and figure 5.31b), were much larger than the dissipation responses that occurred in any of the protein adsorption experiments (eg. figure 5.12b). For proteins, Δ D does not increase to more than 2x10^{-6} Hz and in all cases the ratio of $\frac{\Delta D}{\Delta F}$ <<1 this ratio is much higher in the case of dextran with the ratio reaching $\gtrsim$1 for the highest concentrations of

dextran 100μM. This indicates that the dissipative losses in the energy of oscillation are much higher in these adhered dextran layers, suggesting these layers are softer and viscoelastic.Note also that for both silica and PDMS surfaces, the normalised frequency response ΔF varies significantly across the three monitored overtones in the case of silica in figure 5.30a when exposed to 100μM dextran solution ΔF/n for the 3rd overtone is $\approx$ twice ΔF/n for the 7th overtone, therefore this adhered layer is not in the Sauerbrey regime as a Sauerbrey modelled layer will be rigid, not soft and dissipative, the Sauerbrey equation cannot accurately determine the adhered mass as F3 and F7 will yield values twice each other, contrary to the values determined for measured protein absorption eg. figure 5.11 where there is at most a 20% variation across the harmonics. This Frequency and dissipation behaviour strongly suggests that the film is in the viscoelastic regime and so voigt modelling rather than Sauerbrey model analysis is necessary. In figure 5.32, the ratio $\frac{\Delta D}{\Delta F}$ was plotted across the 4 concentrations for both surfaces to elucidate any changes in the ratio with increasing dextran concentration and by implication increasing dextran adhesion.

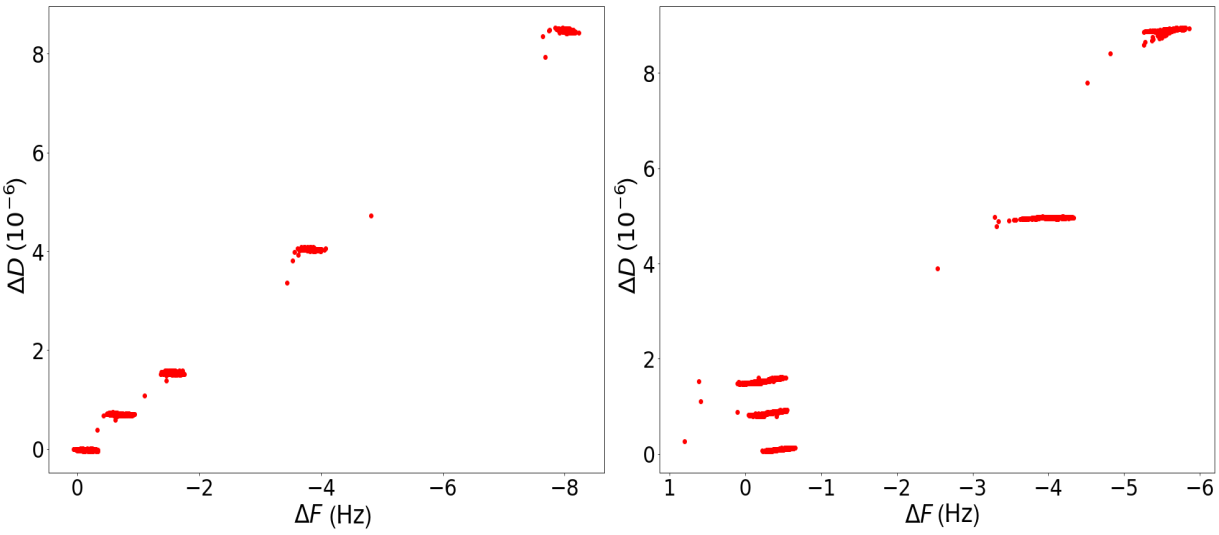

(a) Silica (b) PDMS

Figure 5.32: ΔD versus ΔF for the stages of absorbed dextran on silica and PDMS (taken from the averages of ΔF and ΔD accross 3 harmonics).

In figure 5.33, the adhesion of shorter chain 20kDa dextran on silica at 100 μM also showed smaller overall responses but with a similar ratio of $\frac{\Delta D}{\Delta F}$ to that of 150kDa dextran on silica.

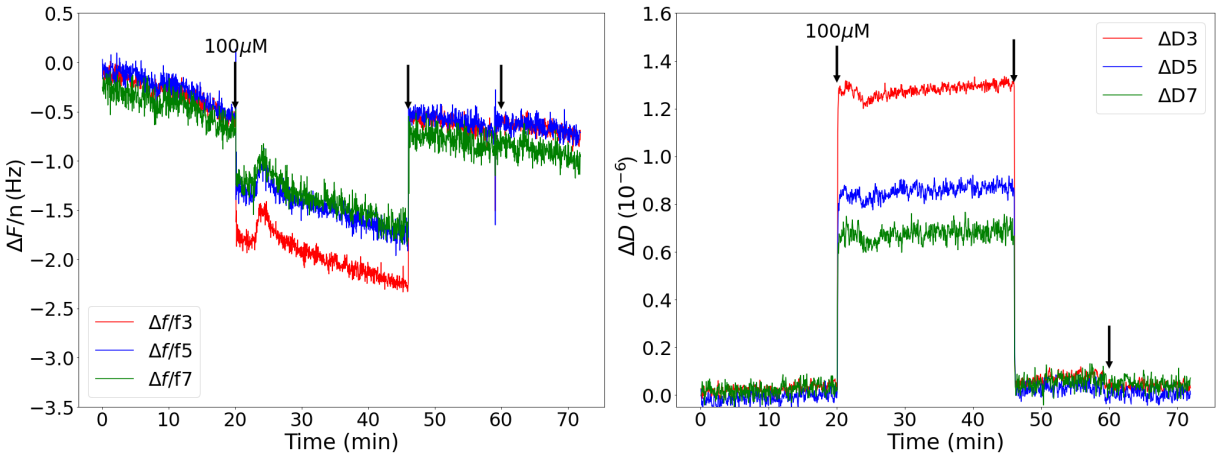

(a) Δ F/n (b) Δ D

Figure 5.33: ΔF and ΔD response of silica coated QCM sensors to dextran of M_w 20 K Da at a concentration of 100μM.

Briefly, post situ immersion and post rinsing AFM tests of 20kDa and 150kDa dextran on PDMS at concentrations of 100μM were conducted after rinsing in salt buffer to demonstrate the effect of molecular weight on the size and branching structure of the polysaccharide. the results are presented in figure 5.35.

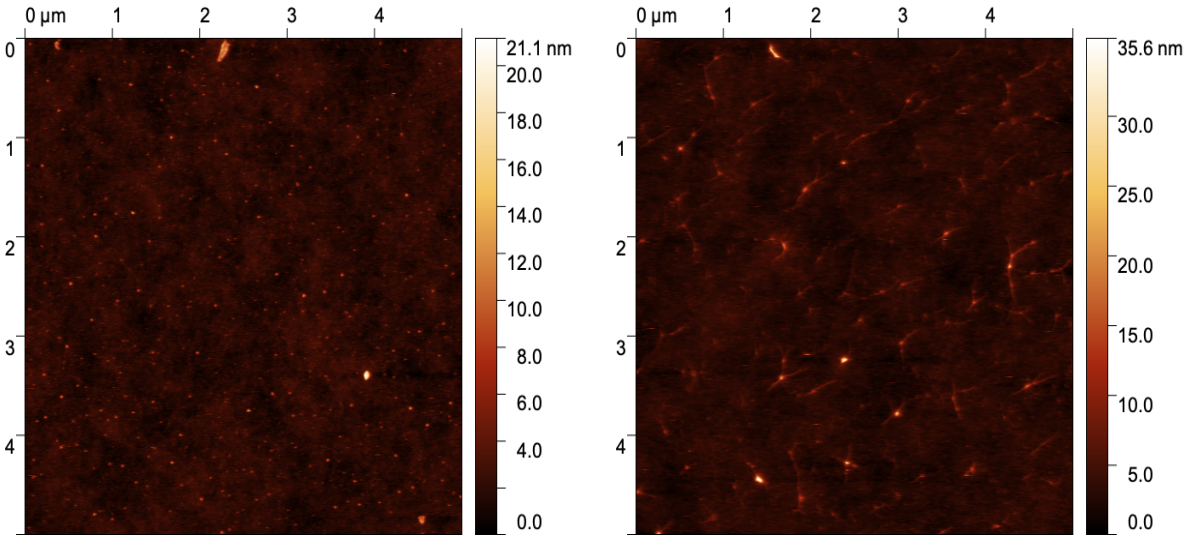

(a) 20kDa on PDMS (b) 150kDa on PDMS

Figure 5.34: Post situ AFM 5x5 μm images of dextran of M_w 20kDa and 150kDa at a concentration of 100μM on PDMS after rinsing with salt buffer.

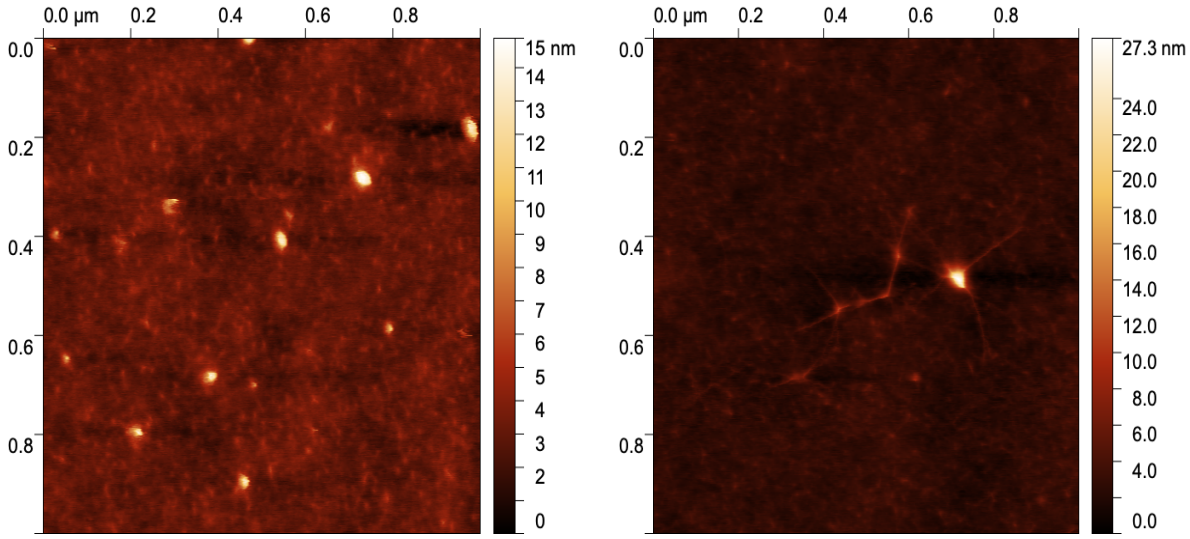

(a) 20kDa on PDMS

(b) 150kDa on PDMS

Figure 5.35: Post situ AFM 5x5 μm images of dextran of M_w 20kDa and 150kDa at a concentration of 100μM on PDMS after rinsing with salt buffer.

The features on dextran 20kDa exposed surfaces are more particle like, whereas the features on surfaces exposed to 150kDa of dextran show more strand like features. Height profiles of features in figures 5.34a and 5.56a suggest a typical height of $\underline{9.57 \pm 0.66}$ and from grain analysis a surface area of $\underline{300nm^2}$. A series of height profiles across the strands seen in figures 5.34b and 5.35b yields an average height of $\underline{3.11 \pm 0.82nm}$ if we consider these strands as immobilised individual molecules of dextran we could consider this value as either the molecular chain thickness or a small bundle of dextran molecules, the latter is more likely, with similar experiments using height profiles to determine the thickness of polysaccharide chains finding height values of 1-1.2nm for the thickness of single chain triple helix polysaccharides [210] and 0.6-1nm for double helix polysaccharides [211], with the structures in figure 5.34b being at least twice this thickness it is more likely these are small fibrils of polysaccharide rather than individual polymer chains.

Finally, in figure 5.36, we present the QCM data from PDMS/PFPE-PEO surfaces exposed to 100μM 150 kDa dextran, in contrast to protein absorbances, shows very similar ΔF and ΔD responses to the silica and PDMS surfaces.

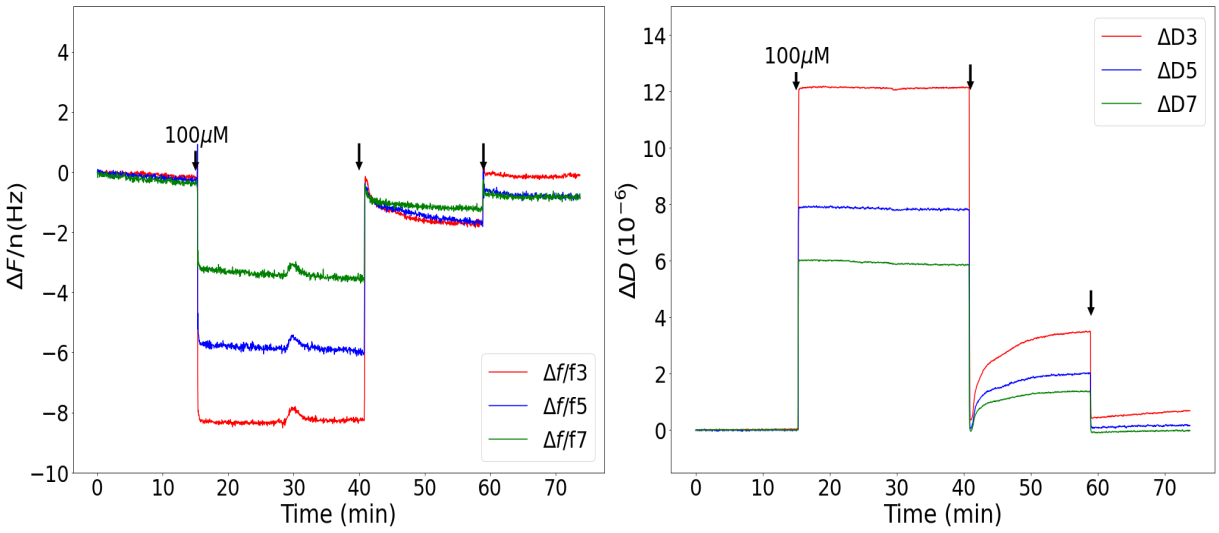

(a) Δ F/n (b) Δ D

Figure 5.36: ΔF and Δ D response of PDMS/PFPE-PEO coated QCM crystals to 50μg/ml BSA (unannotated arrow represents buffer flow for desorption).

Of all the biomolecules tested, this is the first clear non null surface response upon exposure to biomolecule solution. We consider this significant as it shows these PDMS/PFPE-PEO coated QCM surfaces are valid sensors and would show a response to some adhesion, therefore the null/minimal responses for protein adhesion can be considered real and not the result of the complex sensor surface and substantial water uptake inhibiting the effectiveness of the sensor.

The thickness of adhered dextran layers were modelled using the Voigt model of viscoelasticity and modelling tools in the Qtools software, the density of the adhered layer was fitted as a variable alongside viscosity, shear modulus and thickness. The bounds for the density were set to be between the density of water and the density of dextran found from values of specific volume to be 1.66 gcm^{-3}[212]. Figure 5.37 shows the Voigt thickness for the peak concentration and after the second rinsing buffer flow to determine both peak adhesion and the extent of bound dextran layer after rinsing. This Voigt thickness is also converted into a calculated mass per unit area for the layer based on the modelled layer density, summarised in table 5.6.

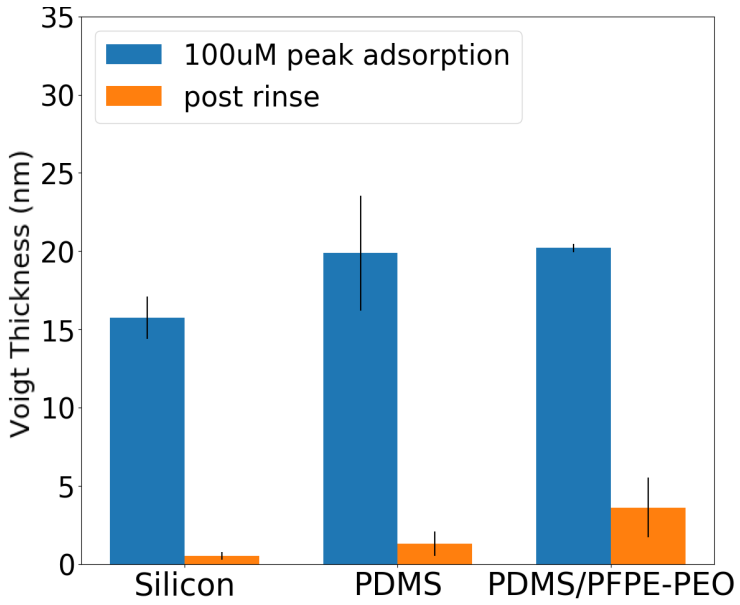

Figure 5.37: Average Voigt thickness of viscoelastic dextran layer calculated for highest concentration and after final rinsing.

Table 5.6: Summary of viscoelastic modelled dextran adhesion to surfaces.

Surface	Dextran 100μM Voigt Thickness (nm)	Post rinse Voigt Thickness (nm)	Mass per unit area (ng cm^{-2})	Post rinse mass per unit area (ng cm^{-2})
Silica 150kDa	15.8±1.6	0.5±0.3	2500±460	76± 48
Silica 20kDa	2.0	0.1	278	20
PDMS	19.9± 4.5	1.3±0.9 278	2780± 220	200±156
PDMS/PFPE-PEO	20.2±3.6	3.61±2.7	3360± 80	381± 293

From this we see that PDMS/PFPE-PEO appears to have the largest absorbance of dextran at the maximum concentration but the standard error found from average values suggests overall mass adhesion is similar between PDMS and PDMS/PFPE-PEO, on all surfaces desorption is very significant upon buffer flow (97 % and 93% for silica 93% for PDMS and 89% for PDMS/PFPE-PEO). This is

consistent with ready desorption of dextran on silica and alumina surfaces observed by Kwon et al using QCM [208].

5.7 Neutron reflectivity of BSA adsorption to PDMS and PDMS/PFPE-PEO surfaces

The results of these QCM in situ tests and the post situ, post immersion AFM tests strongly suggest that PDMS/PFPE-PEO is highly resistant to protein fouling compared to PDMS, potentially totally resistant to the fouling of BSA, lysozyme and mefp-1 at the examined concentrations.

To confirm this, alternative techniques were required to monitor in situ protein adsorption to further corroborate these results. The significant water uptake of these surfaces has a large effect on the frequency response of the QCM sensors so it is necessary to validate the results determined here through other methods. Post-situ AFM tests could be complicated by the transition from liquid to air. For example, this transition is expected to induce the dewetting of the PFPE-PEO monolayer at the PDMS-water interface. This means PFPE-PEO/PDMS surfaces are definitively distinct in air and in water whether or not protein has adhered to the surface. Although we might expect to see some evidence of adhered protein remaining on the surface after drying, this dewetting phenomena might disrupt any protein layer that develops. It was therefore necessary that further investigations of possible protein adhesion on a PDMS/PPFE-PEO surface be performed in situ. For this additional experiment neutron reflectivity was employed.

Protein adsorption onto well characterised surfaces has been studied extensively with Su et al probing and classifying the hydrophilic adsorption of lysozyme to hydrophilic silica [213] and the conformation of BSA on hydrophilic silica [214] in both cases the proteins maintain their bulk solution structure, experiments have also been conducted showing the denaturing of lysozyme due to hydrophobic interactions upon adsorption to hydrophobic monolayers [215]. these seminal papers demonstrated the viability of studying protein adsorption using neutron reflectivity and revealed the unique utility of this particular method; Neutron reflectivity can probe in situ the size and structure of an adhered protein layer revealing conformational changes upon adsorption, the volume fraction of protein in an adhered layer and hence both the degree of hydration and the true protein mass adsorbed in the layer.

For the proposed experiment the adsorption of BSA on a thin film of PDMS and a thin film PDMS/PFPE-PEO model surface would be compared with neu-

tron reflectivity, this would both characterise the mode of protein adsorption on PDMS, a known failure mechanism of PDMS as a foul release material and establish PDMS/PFPE-PEO liquid wetting layers do truly inhibit the adsorption of protein.

5.7.1 Materials and Methods

For this experiment very well defined thin films had to be prepared so that changes in the scattering upon protein exposure could be reliably attributed to protein adsorption. As such, the diffuse SLD layer near the silicon substrate that developed in the previous neutron reflectivity thin films as the result of the TES 40 cross-linker hydrolysing to silica would need to be eliminated. With blended PFPE-PEO/PDMS films no longer an objective, alternative methods of creating thin film PDMS could be utilised. Previous groups report using a vinyl terminated PDMS with (30–35%) methylhydro-(65–70%) dimethylsiloxane as thermal cross-linker to produce thin PDMS films for neutron reflectivity the resultant cross-linked thin films had a uniform SLD throughout the thickness of the layer [216].

Vinyl, terminated PDMS M_w 25,000 was purchased from Sigma Aldrich alongside 950 M_w (50%) methylhydro- co- (50%) dimethylsiloxane and Karstedt's catalyst platinum complex 1% in Xylene (see figure 5.38 for chemical structures). 50x50x10mm silicon reflectivity blocks were purchased from Sil'tronix for use as substrates.

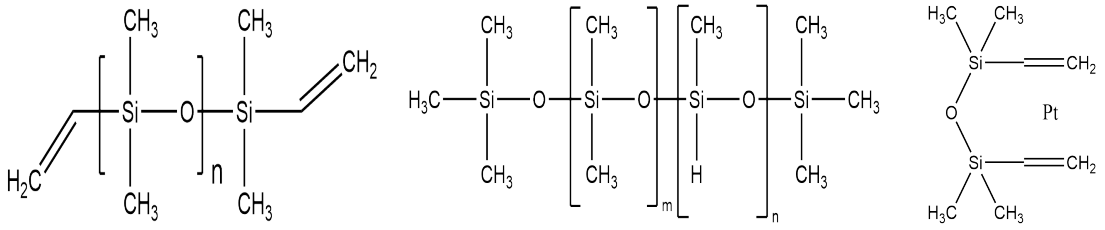

(a) Vinyl terminated PDMS

(b) Poly(dimethylsiloxane-co-methylhydrosiloxane), trimethylsilyl terminated

(c) Karstedt's Catlyst

Figure 5.38: Chemical of the components in thermally cured PDMS films.

Thin films of PDMS were prepared by spin coating from solution, the crosslinker PDMS-co-PMHS was mixed with vinyl terminated PDMS at a ratio of 10% the mass of PDMS and then dissolved in Hexane to a concentration of 1% by wt.

Karstedt's catayst was diluted from original concentration of 1% in xylene to a concentration of 0.01% in Hexane then added to the PDMS solution at a concentration of 13ppm of the overall solution (this was found to be optimal to allow for early curing upon film formation during spin coating to prevent dewetting without being too concentrated as to cause crosslinking in solution and gelation).

PDMS films were formed by spin coating this solution on silicon blocks at 3000rpm and then curing the films at 65C° for 4 hours. Before film deposition the oxide layer on both silicon blocks was measured with ellipsometry, which was used again to characterise the thickness of each PDMS film once crosslinked.

The PDMS/PFPE-PEO surface was prepared by selecting one of these blocks and depositing a dewetting layer of PFPE-PEO (Fluorolink E10/6 Solvay) on top from a 2% dispersion in ethanol at 3000 rpm. Surfaces formed uniform thin films with few defects as shown in figure 5.39. The surface of both thin films was characterised with AFM prior to the experiment.

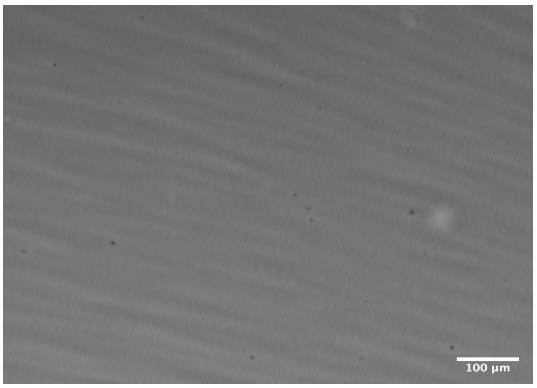

(a) Thermally cured vinyl terminated PDMS.

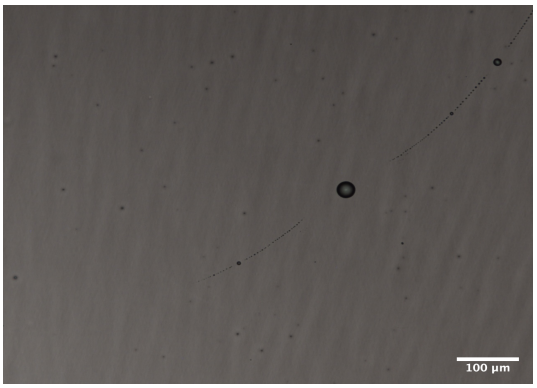

(b) Thermally cured PDMS with PFPE-PEO deposited on top (droplet arc from top right).

Figure 5.39: 10x magnification micrograph image of thin cured PDMS films prepared on silicon blocks.

Bovine serum albumin was prepared in a buffer of 200mM $CaCl_2$ dissolved in deionised H_2O. D_2O was provided by the ILL and 200mM $CaCl_2$ was added to D_2O to produce a deuterated salt buffer.

5.7.1.1 Procedure

Neutron experiments were conducted at the ILL in ToF mode. PDMS and PDMS/PFPE-PEO surfaces were placed in custom ILL 50x50mm solid/liquid cells with a liquid volume of 0.5ml. Initially, cells were filled with D_2O buffer and an initial full reflectivity measurement was conducted across 2 angles θ_1=1.01 θ_2=3.51° yielding reflectivity across a Q range of $0.009 < Q < 0.35\mathring{A}^{-1}$. This allowed the initial state of both samples in liquid to be characterised, with cells throughly filled prior to measurement as such we expect the PDMS/PFPE-PEO sample to have a partially wetting layer of PFPE-PEO at the solid liquid interface which will be well characterised. Subsequently, the liquid buffer was exchanged from D_2O to H_2O using an HPLC pump (flushing approximately 30ml through the cell at a rate of 2ml/min, totalling $\approx$ 60 times the cell volume to completely exchange water contrasts). A second two angle reflectivity measurement in H_2O was then conducted for both samples, between these two SLD contrasts both samples should be fully characterised for SLD and thickness pre adhesion.

Once these initial contrasts had been performed on both samples 50 μg/ml BSA in 200mM $CaCL_2$ in H_2O was injected into the PDMS solid liquid cell for 15 minutes at a rate of 2 ml/min to expose the PDMS film to BSA during this time period rapid kinetic tof measurements were conducted at a single angle (θ=1.01 $0.0088< Q < 0.071\mathring{A}^{-1}$) and recorded every minute for 80 minutes (15 minutes during protein flow and 65 minutes of post flow protein exposure). This sample was left immersed in protein containing buffer whilst the second sample PDMS/PFPE-PEO was aligned in the neutron beam and the same protein exposure and rapid kinetic measurements were conducted. Once both kinetic BSA measurements had been performed the PDMS sample was realigned in the beam and a full angle static measurement was again performed in H_2O to fully characterise any adhered BSA layer in H_2O buffer (this measurement would be performed at least 2.5 hours after the initial protein exposure which should be ample time for an adhered layer to reach saturation concentration as indicated by the QCM adsorption tests). The sample was then subjected to 15 minutes of 2ml/min 200mM $CaCl_2$ H_2O buffer as a rinsing flow to induce any desorption, kinetic 1 angle reflectivity measurements were taken during this process. Once the rinsing flow had ben completed a second rinsing two angle measurement was conducted to obtain a full angle measurement of any change to the adhered protein layer. The same series of measurements was then repeated on the PDMS/PFPE-PEO sample, simultaneous to this set of measurements the buffer in the PDMS sample cell was exchanged with a D_2O buffer. The time period for this set of measurements is close to 3 hours which should allow for labile hydrogen-deuteron exchange between BSA in the protein layer with the D_2O buffer , this is an uncontrollable process that can effect the

effective SLD of BSA in different H_2O/D_2O contrasts but allowing 3 hours for this process should be sufficient for proton exchange to have reached equilibrium by the time the sample is probed in D_2O (the process of proton exchange at pH 7 and 0C for BSA has been found to be 90+% complete within 2 hours with 75% of potential labile exchange occurring almost instantly[217]) so we can model the BSA layer according to its SLD in D_2O of $3.24x10^{-6}\mathring{A}^{-2}$[214]. After the cycle of H_2O measurements on the PDMS/PFPE-PE sample is complete the PDMS surface was measured across two angles in a static mode in D_2O buffer whilst D_2O was exchanged into the PDMS/PFPE-PEO cell. This series of measurements, summarised in a flow chart 5.40, ensured good characterisation of the initial sample in liquid using two contrasts followed by in situ kinetic measurements of potential protein adsorption, characterisation of adsorbed layers at saturation observation of desorption upon buffer flow and a full characterisation of any adsorbed layer post desorption in two contrasts.

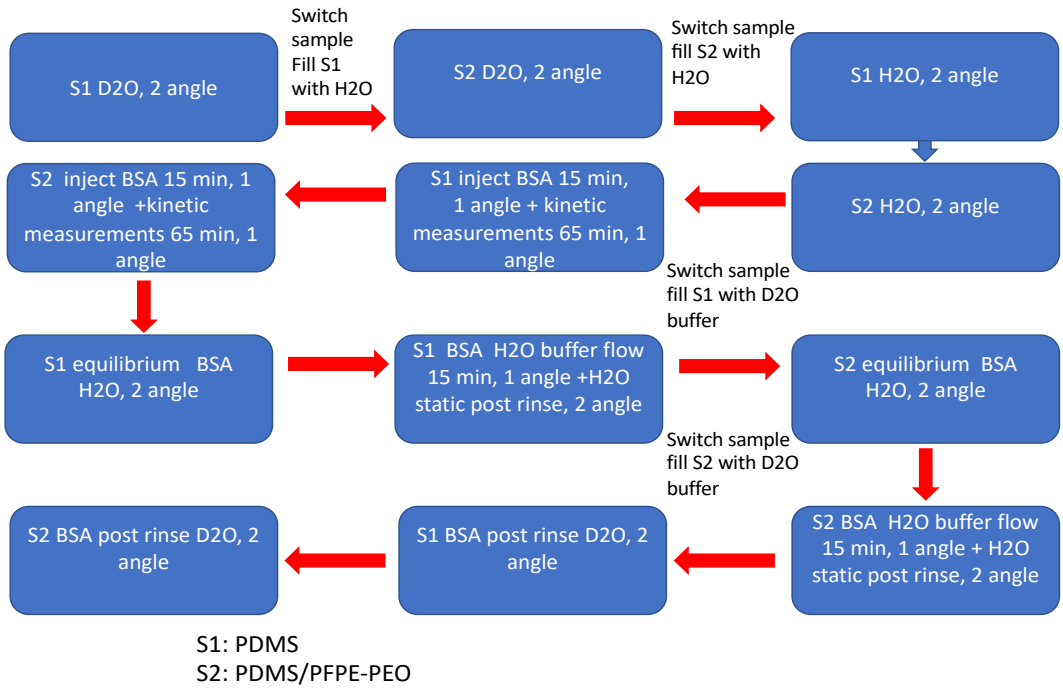

Figure 5.40: Illustrative sequence of neutron measurements for sample 1(S1) PDMS and sample 2 (S2) PDMS/PFPE-PEO.

Post experiment measurements were conducted upon the return of samples

from the ILL, post situ AFM, ellipsometry and water contact angle measurements were also conducted.

5.8 Results: neutron reflectivity of BSA adsorption to PDMS and PDMS/PFPE-PEO surfaces

Ellipsometry fits for sample 1 PDMS had an oxide layer of 1.41nm and a dry thickness of 67.4nm. For Sample 2 PDMS/PFPE-PEO, the oxide layer was measured as 1.4nm and the PDMS thickness prior the deposition of PFPE-PEO was measured to 66.6nm. Clear reflectivity measurements were obtained for sample 1 before protein adsorption with strong and consistent fits. These fits agree strongly with respect to the overall thickness of the PDMS layer within 1nm for both fits (68.6 and 69.3 nm). The simulated fits depicted in figure 5.41 found normalised χ^2 error for H_2O and D_2O as 1.17 and 1.54 respectively.

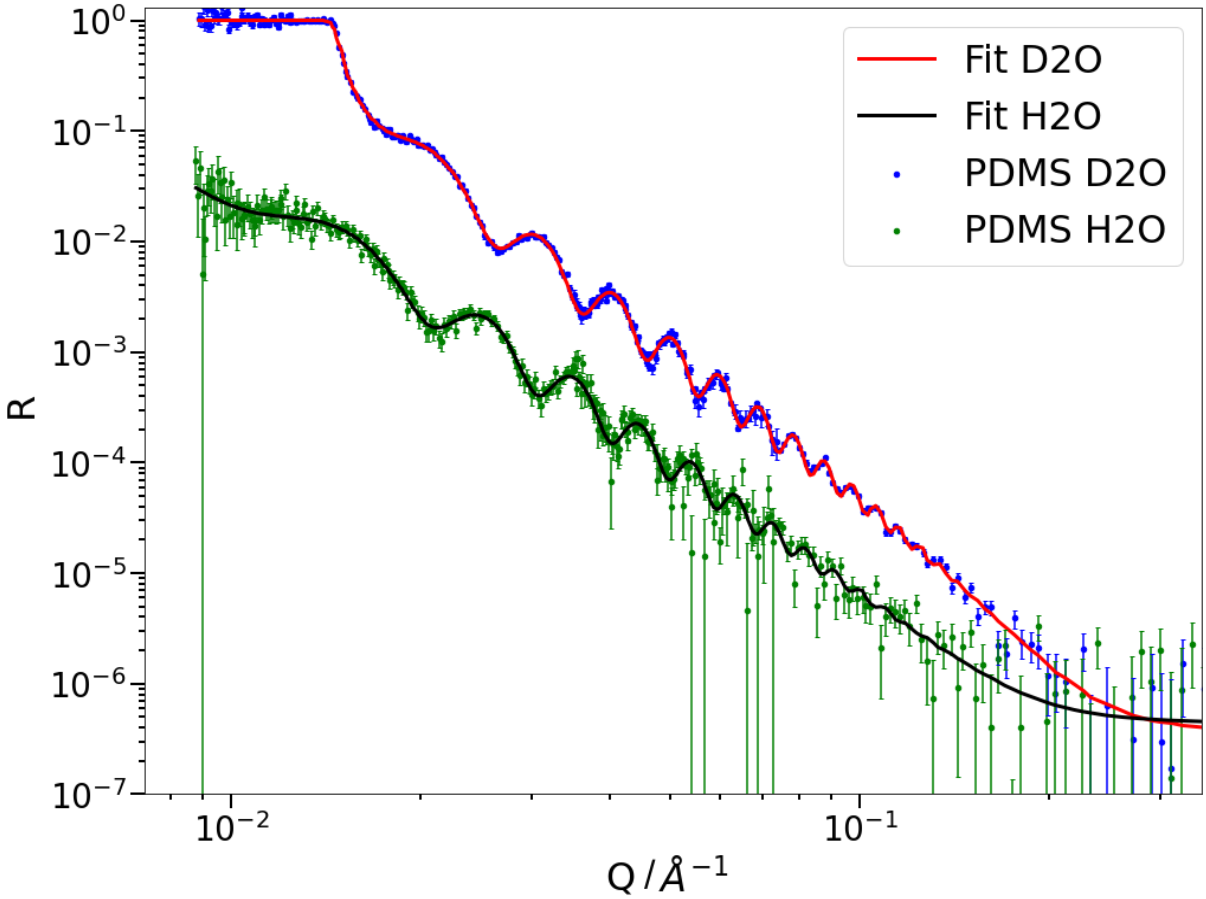

Figure 5.41: Sample 1 PDMS in D_2O and H_2O prior to BSA adsorption.

As can been seen in figures 5.42b and 5.43b the the PDMS layer could be accurately fitted as a single layer of uniform SLD, demonstrating that this crosslinked layer is free of the structure seen in previous tests.

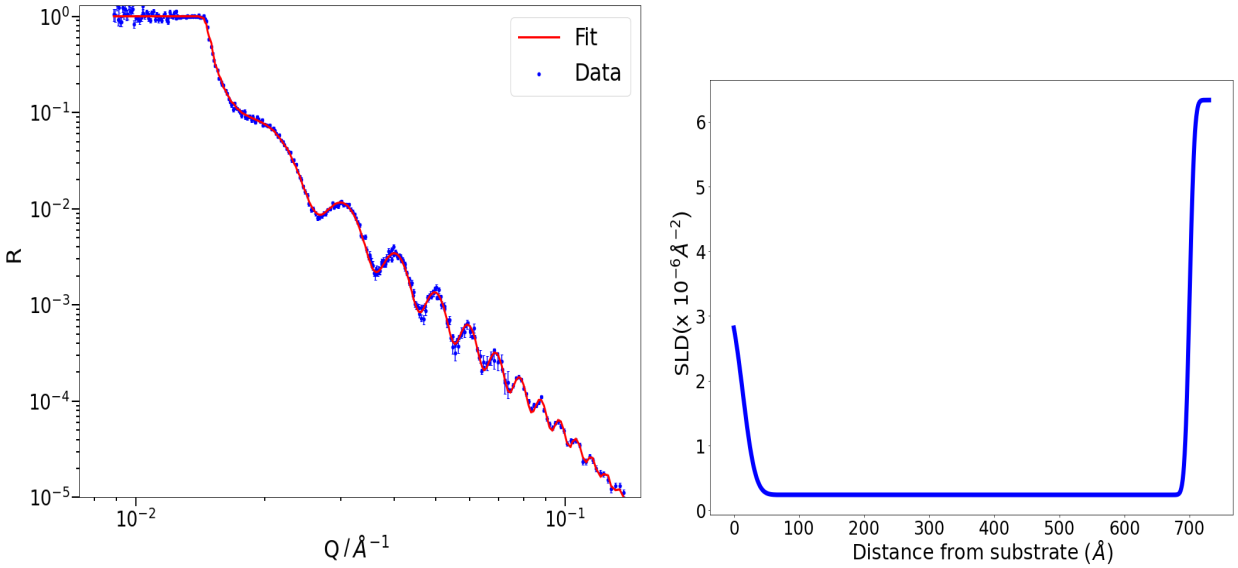

(a) S1 PDMS in D_2O. (b) Fitted SLD in D_2O

Figure 5.42: Neutron reflectivity, model and SLD for S1 PDMS thin film in D_2O.

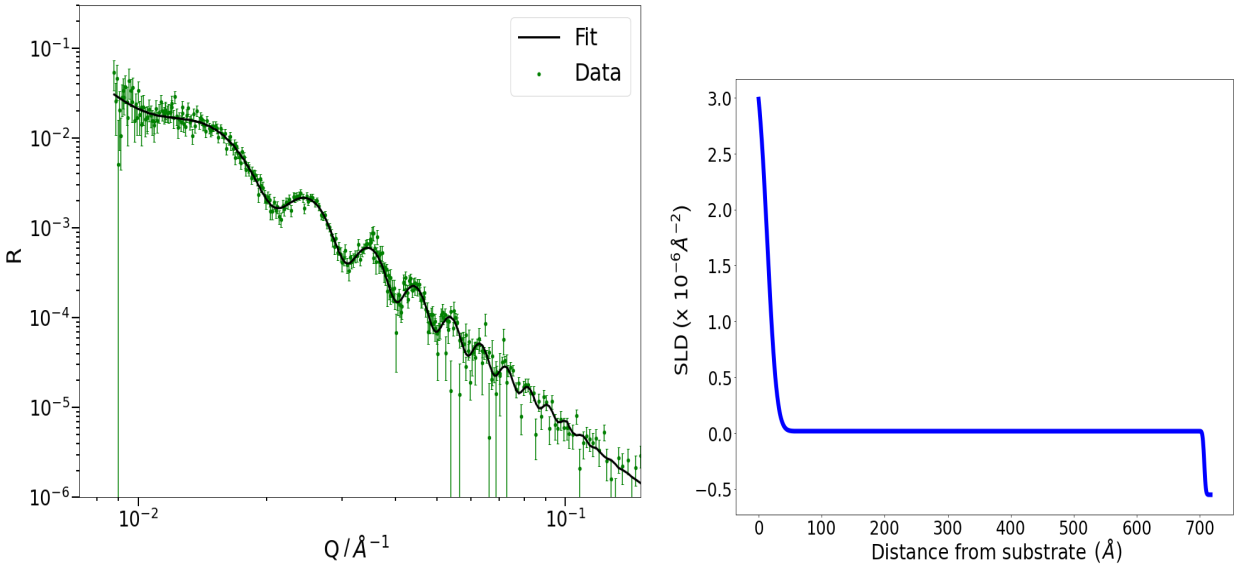

(a) S1 PDMS in H_2O. (b) Fitted SLD in H_2O

Figure 5.43: Neutron reflectivity, model and SLD for S1 PDMS thin film in H_2O.

Sample 2 PDMS/PFPE-PEO could also be fitted clearly in both contrasts (summarised in figure 5.44 as a PDMS film with a small wetting layer with a

rough interface with the liquid. Considering the simulation for S2 in D_2O in figure 5.45b, the interface was modelled as a layer of SLD 3.9x10^{-6}Å^{-2} and thickness 3.1nm with a surface roughness of 1.16nm for a χ^2 1.58. in H_2O, the simulation presented in figure 5.46 found this layer was best fit to an SLD of 3x10^{-6}Å^{-2} and a thickness of 3.0nm with a roughness of 1.06nm fitting to a χ^2 of 1.83. We conclude that, as intended this sample has a wetting monolayer of PFPE-PEO covering the PDMS/water interface prior to protein exposure.

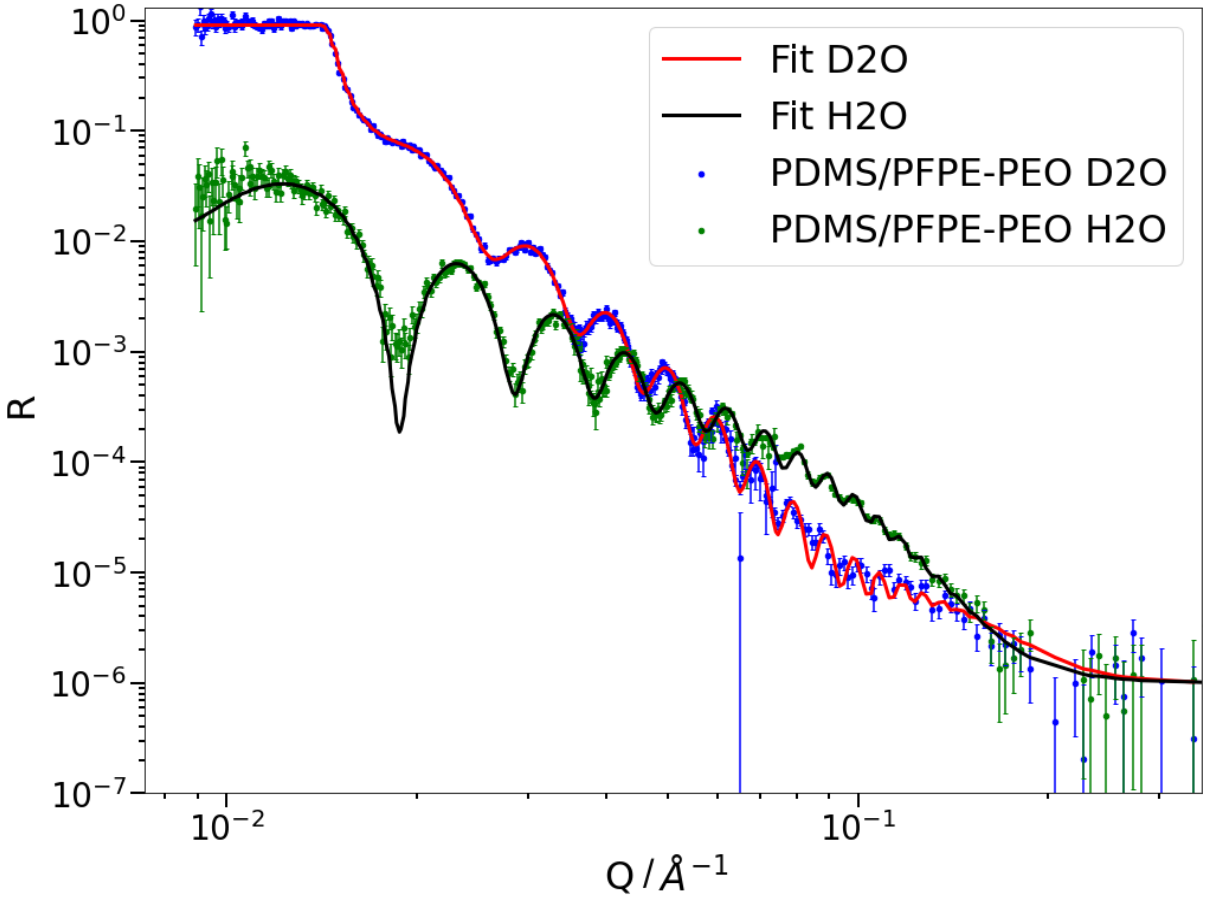

Figure 5.44: Neutro reflectivity for sample 2 PDMS/PFPE-PEO in D_2O and H_2O prior to BSA adsorption.

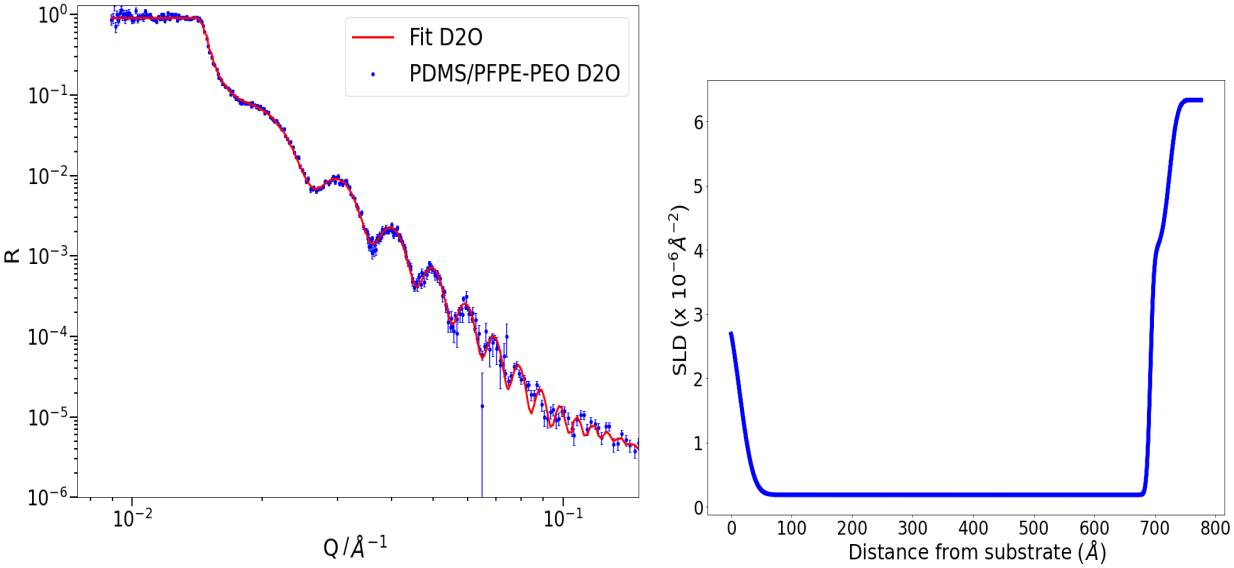

(a) S2 PDMS/PFPE-PEO neutron reflectivity in D_2O .

(b) Fitted SLD in D_2O

Figure 5.45: Neutron reflectivity, model and SLD for S2 PDMS/PFPE-PEO thin film in H_2O.

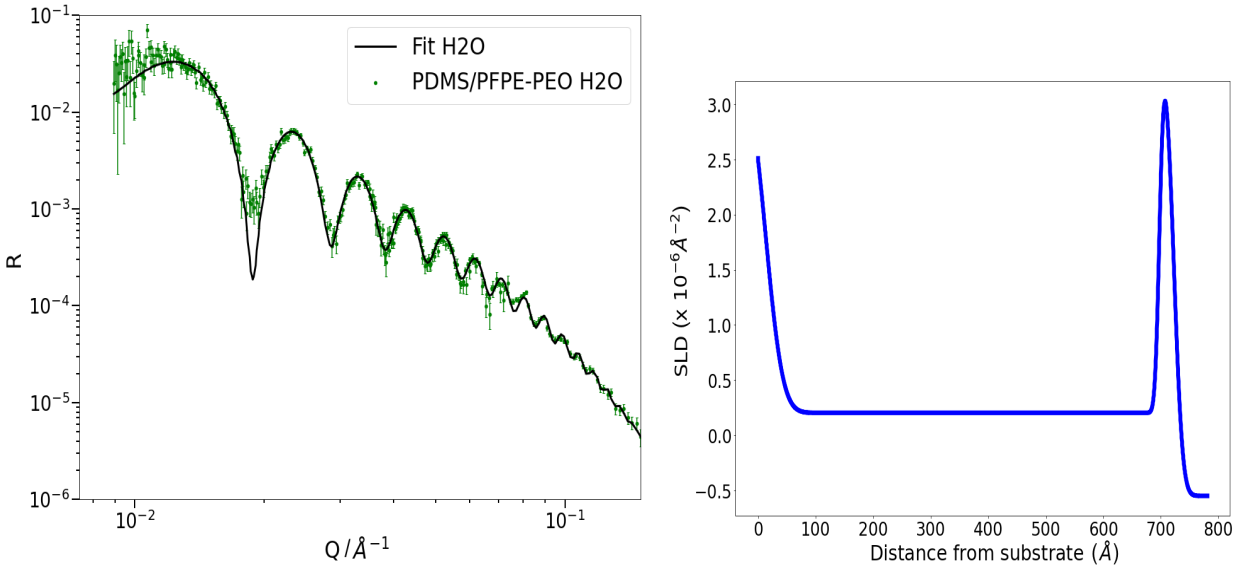

(a) S2 PDMS/PFPE-PEO neutron reflectivity in H_2O.

(b) Fitted SLD in H_2O

Figure 5.46: Neutron reflectivity, model and SLD for S2 PDMS/PFPE-PEO thin film in H_2O.

Sample 1 PDMS thin film was exposed to 50μg/ml BSA in salt buffered H_2O. Figure 5.47 presents the change in neutron reflectivity at equilibrium after 2 hours of exposure. The 2 angle reflectivity measurement of the sample shows a shift in the Kiessig fringes of reflectivity after protein exposure. This indicates some small change in layer thickness due to protein adsorption on the surface.

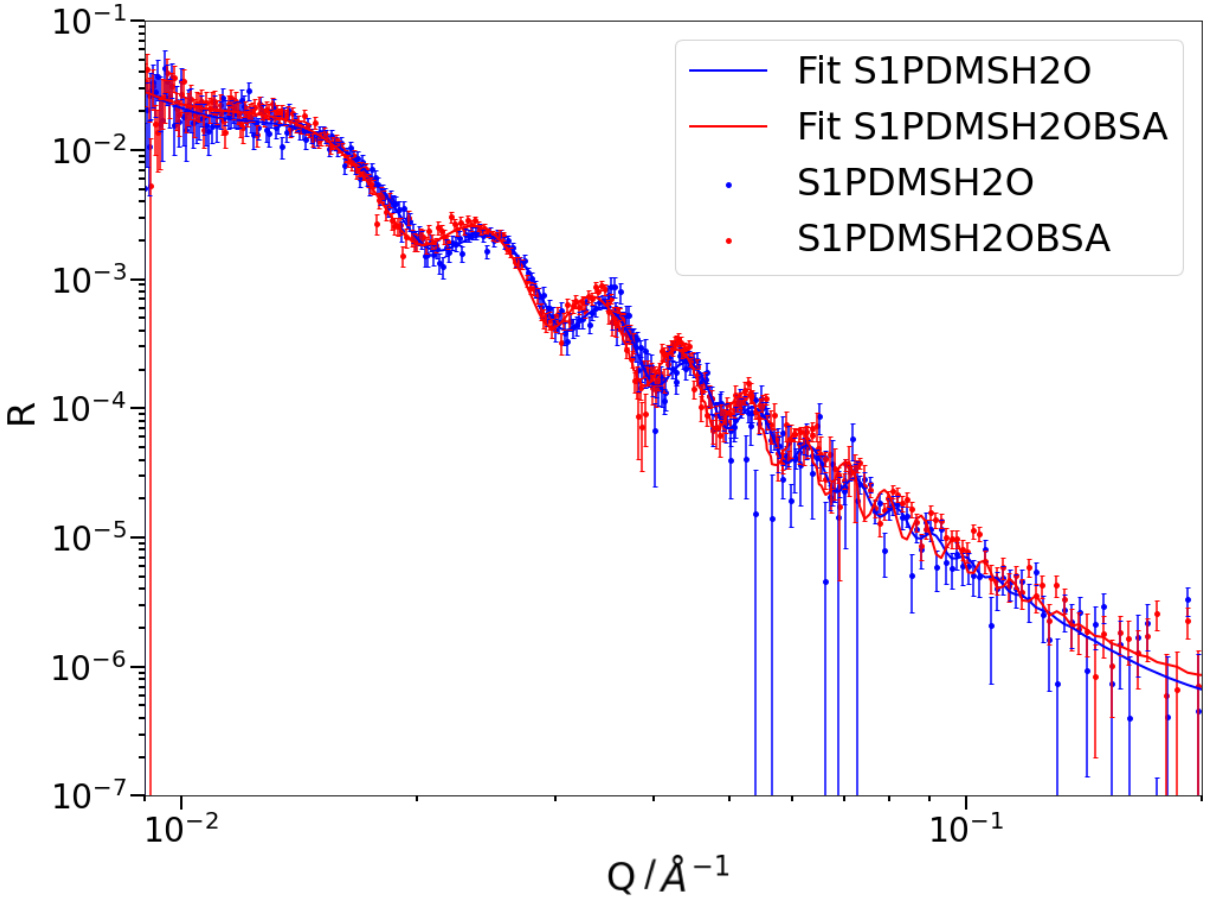

Figure 5.47: 2 Angle reflectivity measurements of sample 1 PDMS in H_2O prior to BSA adsorption and after equilibrium protein adsorption.

Kinetic reflectivity adsorption measurements taken during initial adsorption stages at 1 minute intervals proved to be excessively noisy with high uncertainty in the data points making clear conclusions impossible to draw from possible changes between intervals. Recombining this data into 8 minute scans and 4 minute scans, as depicted in figure 5.48 and figure 5.48b respectively, greatly reduced the error bars on data points. This made the changes in scattering over time clearer, albeit at a lower time resolution. The quality of the 8 and 4 minute kinetic simulations are summarised in tables 5.7 and 5.8 respectively.

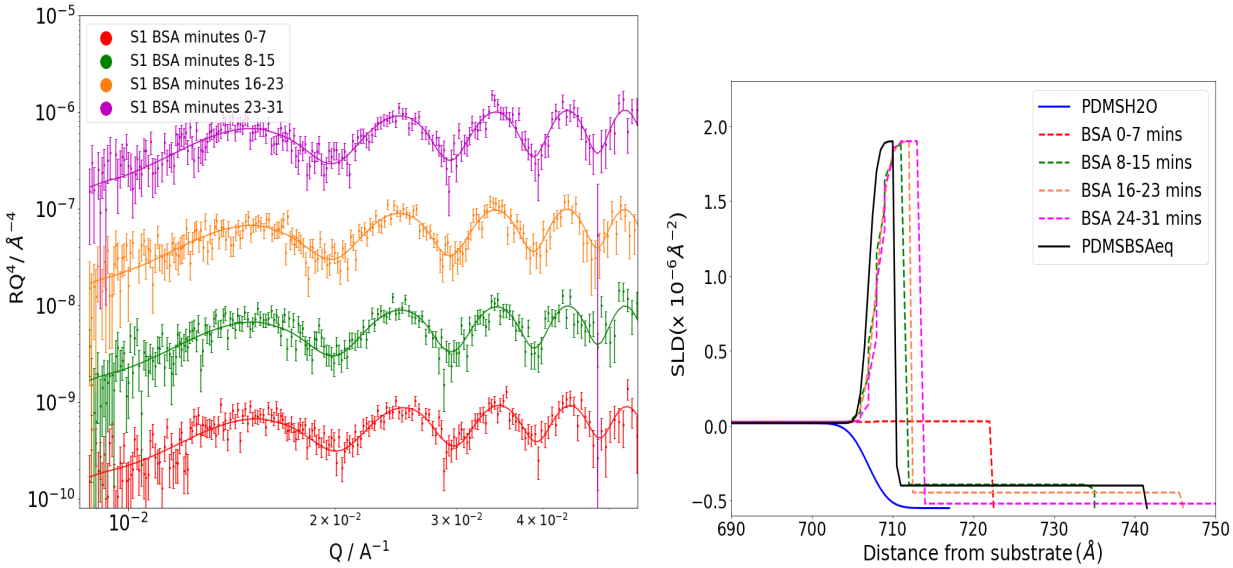

(a) Porod RQ^4 reflectivity data and simulations for 8 minute scans, each data set offset by a factor of ten.

(b) Fitted SLD in H_2O.

Figure 5.48: Neutron reflectivity, model and SLD for sample 1 (S1) PDMS film in H_2O exposed to BSA acquired in 8 minute scans, SLD model of the initial and equilibrium reflectivity also included.

The quality of 8 minute kinetic is summarised in table 5.7.

Table 5.7: Error on kinetic 8 minute simulations presented in figure 5.48.

8 minute scans	χ^2 error
0-7 mins	1.1
8-15 mins	1.18
16-23 mins	1.11
24-31 mins	1.07

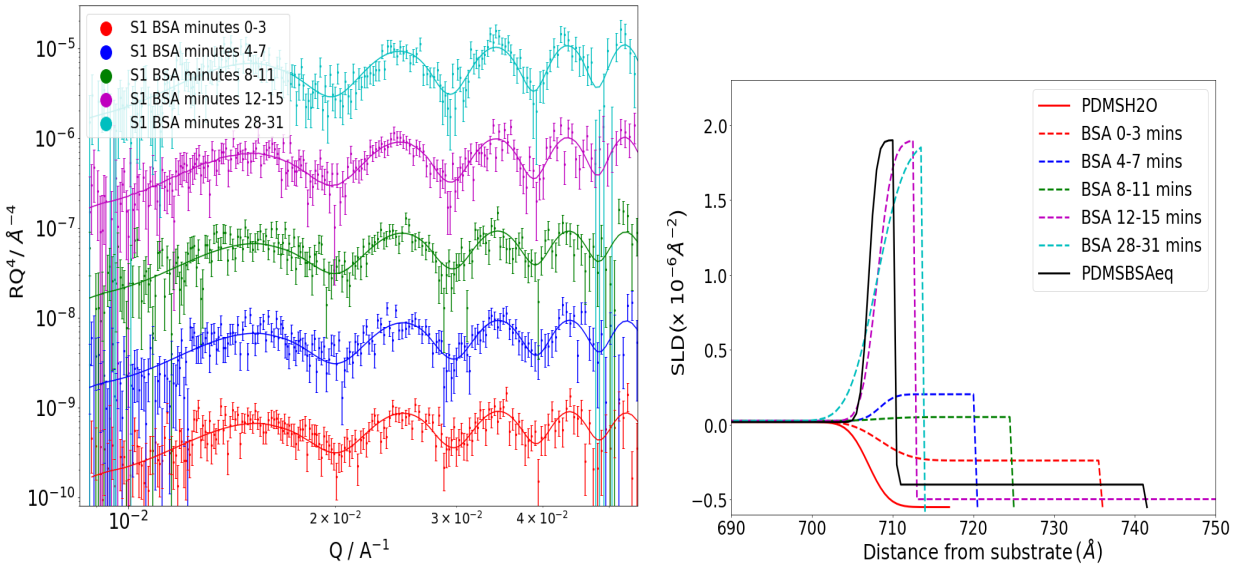

(a) Porod RQ^4 reflectivity data and simulations for 4 minute scans, each data set offset by a factor of ten.

(b) Fitted SLD in H_2O.

Figure 5.49: Neutron reflectivity, model and SLD for sample 1 (S1) PDMS film in H_2O exposed to BSA acquired in 4 minute scans, SLD model of the initial and equilibrium reflectivity also included.

Table 5.8: Error on kinetic 4 minute simulations presented in figure 5.49.

4 minute scans	χ^2 error
0-3 mins	1.06
4-7 mins	1.58
8-11 mins	1.22
12-15 mins	0.99
28-31 mins	1.16

In figure 5.50, the reflectivity from sample 1 prior to BSA exposure is depicted alongside kinetic reflectivity measurements collected at 8 minute intervals during BSA adsorption and the reflectivity obtained at equilibrium BSA adsorption.

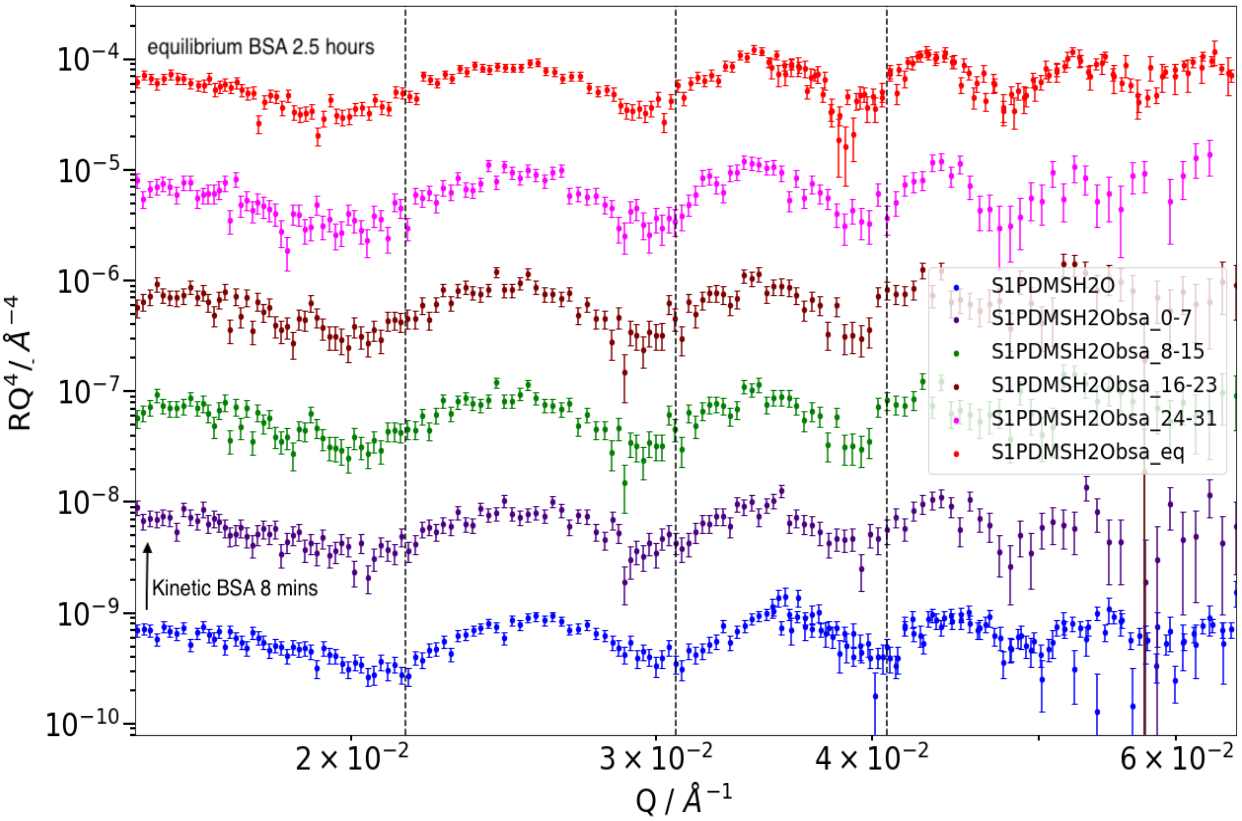

Figure 5.50: Porod RQ^4 reflectivity plot of 8 minute kinetic BSA tests; initial PDMS, for 32 minutes of adsorption and the final equilibrium state after 2.5 hours.

We can see from figure 5.50, that there is a clear shift in fringe spacing between the initial reflectivity from sample 1 and first kinetic reflectivity measurement taken after just 8 minutes of exposure. this implies that protein adsorption occurs rapidly after the PDMS sample is exposed to the BSA solution. Reflectivity curves were fitted for each of these intervals using a single layer or bilayer fit on the surface of the PDMS film using an SLD of 1.9x10^{-6}Å^{-2} in hydrogenous water. In the bilayer fit, the adhered layer we modelled as a thin layer with high SLD (limited to 1.9x1x10^{-6}Å^{-2} for a volume fraction of BSA of 1) and a larger layer on top with a lower SLD. The equilibrium angle NR curve taken after 2.5 hours protein adsorption fits best to a bilayer depicted as the black curve in figures 5.48b and 5.49b with a thin layer of 3.5Å with an SLD of 1.9x10^{-6}Å^{-2} and a larger upper layer of thickness 3.09nm but with a much lower SLD of -0.4x10^{-6}Å^{-2}.

The volume fraction of protein in this SLD layer can be determined via the

equation[215]

$$\phi_{BSA} = \frac{\rho - \rho_w}{\rho_{BSA} - \rho_w} \tag{5.2}$$

Using equation 5.2 we found the volume fraction of protein in the adhered layer: the thin 3.5$\mathring{A}$ layer closest to the interface had a volume fraction of $\phi = 1$, whereas the protein volume fraction in the larger 30.9$\mathring{A}$ thick outer layer is ϕ=0.06.

This structure does not fit with the known dimensions of BSA in solution but would be consistent with a denatured adhered layer of protein. In which the protein has unravelled from its equilibrium solution structure and adhered to the surface via hydrophobic interactions, with the hydrophobic moieties of BSA bonded to the hydrophobic PDMS surface and it's hydrophilic moieties presented to the solid/liquid interface and heavily solvated with water. This would be consistent with the fitted model of a very thin wholly dehydrated protein layer directly on top of the PDMS and a much larger much more hydrated layer on top.

When fitting the 8 minute kinetic adsorption data, the denatured protein model was found to be the best fit for the reflectivity data acquired after the first scan at 8 minutes. The precise size of the hydrated thicker layer varied somewhat between scans, perhaps due to the data range and higher overall uncertainty in these 1 angle kinetic reflectivity curves. Interestingly, the first kinetic reflectivity spectra (0-7 minutes) does not fit optimally as a bilayer; during fitting, an initial bilayer model tends towards the higher SLD layer shifting infinitesimally small thickness and the adhered BSA fitting best as a uniform layer of length 14.5$\mathring{A}$ and SLD of 0.03x10$^{-6}\mathring{A}^{-2}$ and a volume fraction of ϕ= 23.7. Having identified this first with 8 minute reflectivity scans reflectivity was refitted with 4 minute resolution. The same structural model for early BSA absorption is observed as seen in figure 5.49b for the earliest 4 minute spectra a layer of 27.5 $\mathring{A}$ at an SLD of -0.24x10$^{-6}\mathring{A}^{-2}$, volume fraction: ϕ=0.122. For subsequent scans the layer becomes thinner but with a higher SLD before converting to a bilayer fit with the similar high SLD-low SLD structure to the equilibrium layer. This conversion occurs within 12 minutes, consistent with the timeframe of structure conversion fitted from the 8 minute scans. The rapid maturation of protein layer structure shown in the reflectivity data is consistent with observation from QCM seen in figure 5.10 in which the majority of the mass adsorbed in the first few minutes after protein flow.

After rinsing through H_2O buffer for 15 minutes to remove protein solution and induce protein desorption from the surface. Figure 5.51 shows that the post rinse reflectivity data is indistinguishable from the reflectivity obtained from the sample after equilibrium protein adsorption (figure 5.47), suggesting little or no

surface desorption. This is in accord with the findings from the QCM tests which observed little or no desorption upon buffer rinsing and agrees with the model of expected hydrophobic adsorption between BSA and PDMS with the protein layer now energetically stabilised to minimise contact between hydrophobic protein moieties and water, making desorption and water immersion of the protein unfavourable.

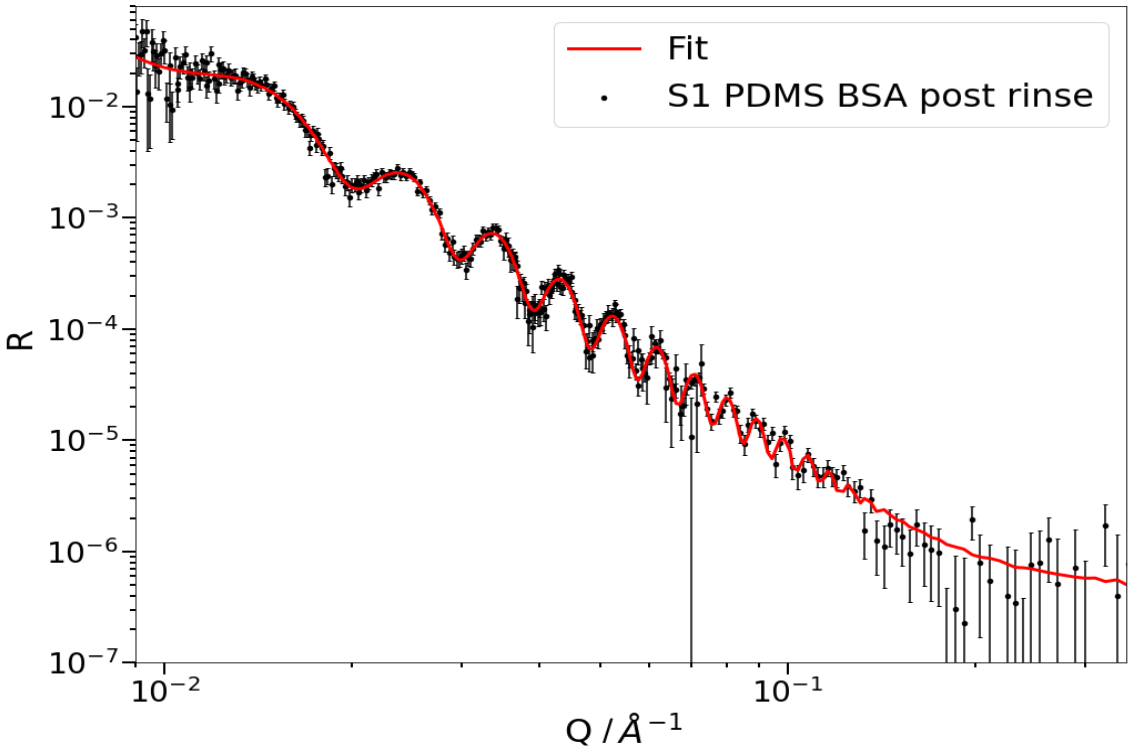

Figure 5.51: Neutron reflectivity for sample 1 PDMS film in H_2O after BSA exposure and rinsing with salt buffer.

The final state of sample 1 PDMS post BSA adsorption and rinsing was easily fitted with the simulation in figure 5.51 achieved a normalised χ^2 error value of 1.28 for the fit. With the adsorbed layer modelled with a very similar structure to the fit for the pre rinse equilibrium adsorption a bilayer with a thin layer on top of the PDMS of 3.91Å thickness and SLD 1.9x10^{-6}Å^{-2} (ϕ= 1) and an outer layer 33.5Å thick with an SLD -0.467x10^{-6}Å^{-2}. (ϕ= 0.035). The surface excess of BSA can be determined from the thickness, protein density and volume fraction by the equation

$$\eta = \rho'_{BSA} \cdot \tau \cdot \phi \tag{5.3}$$

with ρ_{BSA}' being the mass density of BSA, τ, the thickness of protein layer and ϕ, the effective volume fraction of protein in the layer.

A summation of the surface excess across the modelled bilayer was obtained using equation 5.3 from the reflectivity data both after equilibrium protein adsorption η_{eq} and after rinsing η_{rinse}. We find that the surface excess was η_{eq}=72.4 ng cm^{-2} and η_{rinse}=71.2 ng cm^{-2} respectively, implying no meaningful desorption of the attached BSA layer upon rinsing.

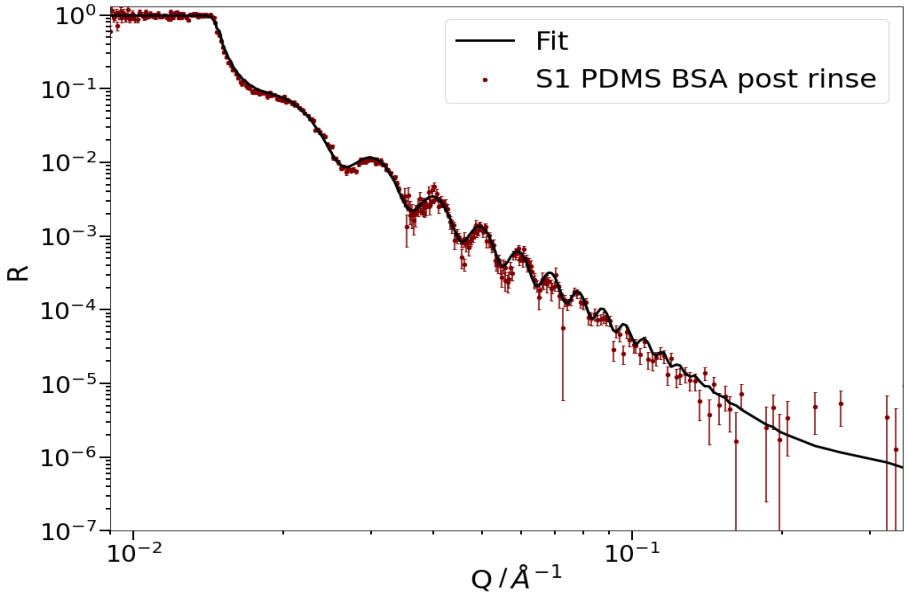

Figure 5.52: Sample 1 PDMS in D_2O after BSA and rinsing

Fitting the PDMS post BSA and rinse in D_2O, it's apparent from figure 5.52 that the scattering contrast of the samples before and after BSA was much smaller than in H_2O, attempting to fit the sample with the value of scattering length density in D_2O of 3.24x10^{-6}Å^{-2} [214]. The data could be modelled to a low degree of fit error χ^2 2.2, though the BSA layer was modelled with a different structure to that used for the H_2O contrast; the adhered layer was best modelled as a single layer of SLD of 5.35x10^{-6}Å^{-2} (ϕ=0.318) and thickness 16.2Å. This yielded a surface excess of 71.9 ng cm^{-2} which agrees strongly with the surface excess derived for the protein layer in H_2O. The difference in fitted structure may

be the result of poor scattering difference in the D_2O contrast, we therefore regard the modelled layer fit for the H_2O contrast to be more reliable.

Having characterised sample 2 PDMS/PFPE-PEO and identified the partial wetting layer of PFPE-PEO on the solid liquid interface we observed the effect of BSA injection on this surface. As presented in figure 5.53, in stark contrast to the simple PDMS thin film there is no observable difference in the scattering spectra between the pristine surface and after protein exposure , either in the kinetic rapidly acquired spectra or in the 2 angle measurement at equilibrium adsorption 2.5 hours after the introduction of protein.

This is consistent with the observations from QCM tests and post situ AFM imaging which suggest little to no protein adsorption on these surfaces.

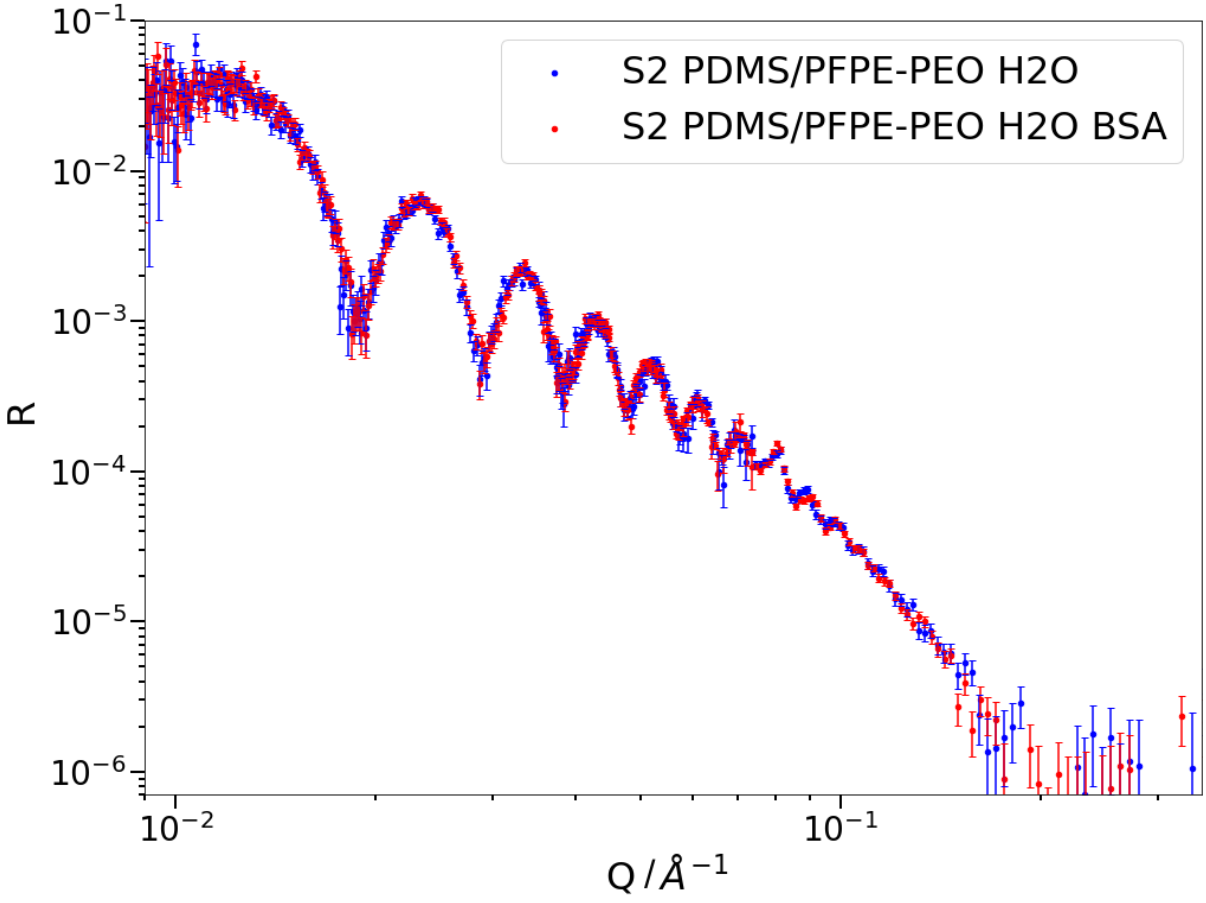

Figure 5.53: Sample 2 PDMS/PFPE-PEO in H_2O before and after BSA exposure.

Without any appreciable difference in scattering it's hard to justify

attempting to fit any kind of adhered layer to the surface, as the reflectivity can be adequately modelled by the existing fit for the pristine film.

To demonstrate the effect of BSA protein adsorption on this surface would have on the reflectivity spectra we present in figure 5.54 fits for the PDMS/PFPE-POE surface post BSA exposure and buffer rinse with fits from the original pristine PDMS/PFPE-PEO in D_2O and H_2O contrasts but also fits for the same surface modelling a hypothetical layer of BSA absorbed on top. We model a denatured layer of BSA caused by hydrophobic interactions modelled from the fit of BSA adhesion sample 1 PDMS.

We also fit an alternative mode of protein adsorption to this surface; our model of the mode of surface reconstruction in which PFPE-PEO forms a wetting monolayer where the PFPE backbone aggregates onto the PDMS surface whilst the end capping PEO groups are solvated by water, considering also dynamic contact angle measurements of water droplets on model PDMS/PFPE-PEO surfaces which become significantly more hydrophilic post transition we consider the case where these model surfaces present a hydrophilic solid/liquid interface. Hydrophilic adsorption of BSA to surfaces has been studied before on silica by Su et al[214], they report for 150mg dm^{-3} BSA (150 μgml), that a BSA layer forms on silica 36$\mathring{A}$ thick, modelling a BSA proteins as adsorbing in a side on configuration on silica, with it's layer thickness similar to the shortest dimension of the protein in solution 40$\mathring{A}$. From the calculated surface excess 2.5mg m^{-2} a volume fraction and effective SLD of ϕ=0.51 and ρ=0.7 in H_2O and ρ=4.75 in D_2O, with this thickness and SLD it is possible to model a potential hydrophilic monolayer on the PDMS/PFPE-PEO surface.

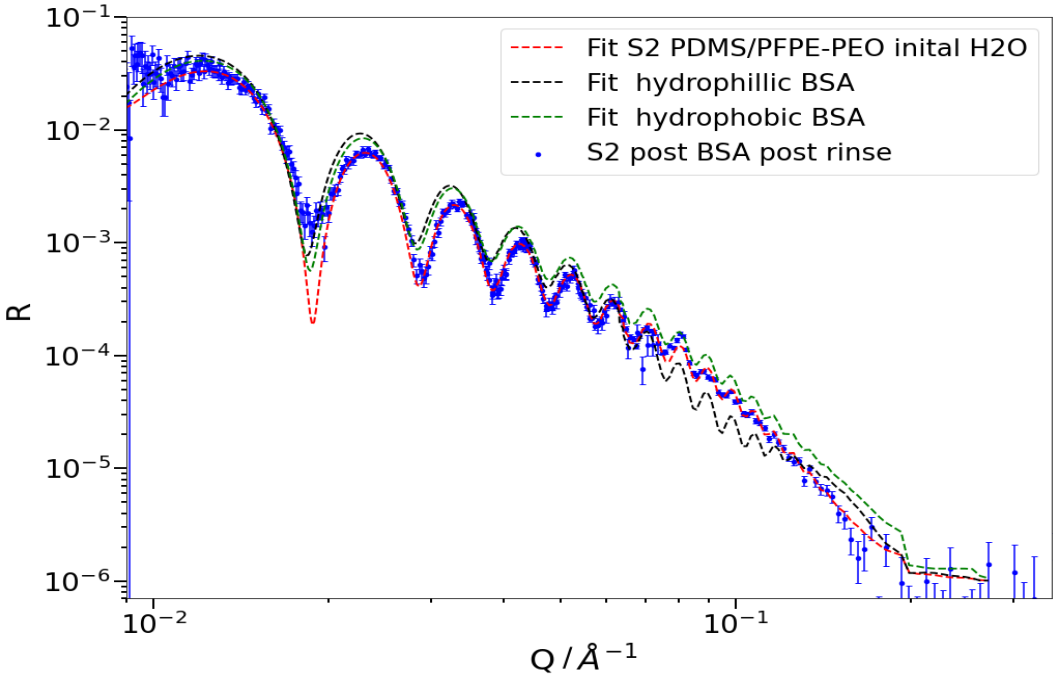

(a) S2 PDMS/PFPE-PEO post BSA and post rinsing in H_2O.

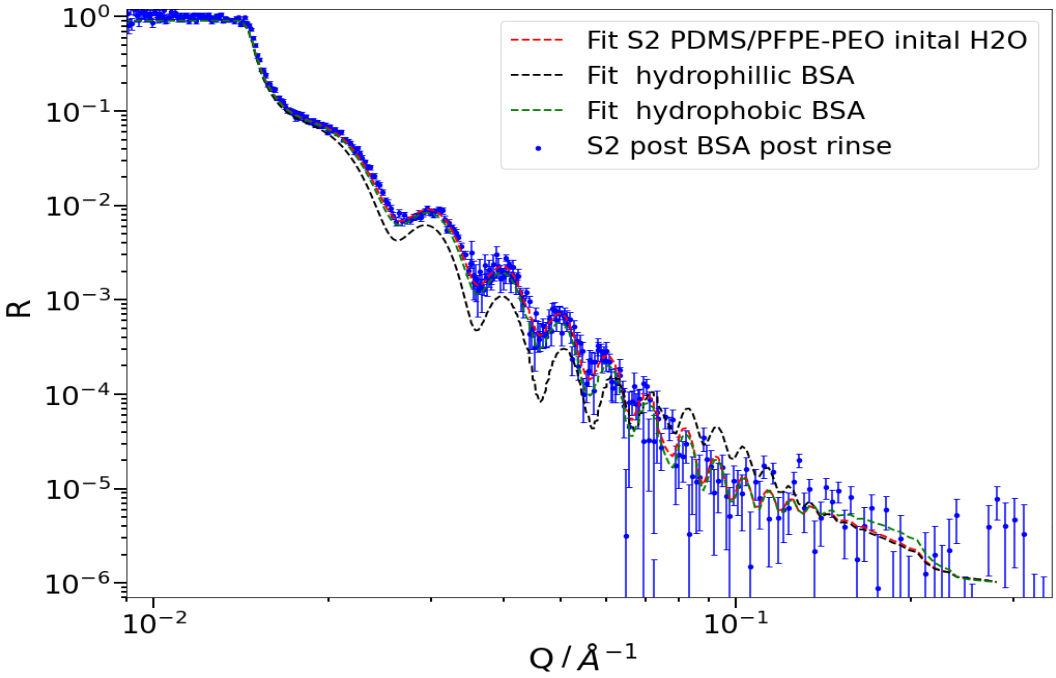

(b) S2 PDMS/PFPE-PEO post BSA and post rinsing in D_2O.

Figure 5.54: S2 PDMS/PFPE-PEO post BSA and post rinsing with fits for pristine PDMS and modelled hydrophobic and hydrophilic BSA protein layers.

Inspecting the simulated fits in figure 5.54, neither hydrophobic nor hydrophilic models of BSA on this sample fit credibly in H_2O, with the model for predicted hydrophilic adsorption departing radically from the obtained scattering data in both scattering contrasts. Fitting data using simulations from pre exposure reflectivity data in H_2O and D_2O contrasts (found in figures 5.46 and 5.42) the fit error was χ^2=2.95 in H_2O and χ^2=1.68 in D_2O without any alteration. We argue therefore that there was no adsorption of protein on this surface or at such low surface concentrations that the adhered layer had an effective SLD insufficiently distinct from the ambient H_2O to observe with neutrons.

Upon completion of this experiment the samples were returned and post situ analysis was conducted as seen in figures 5.55 and 5.56 topographical evidence of the development of a mesh like structure on the PDMS sample post BSA adhesion tests corroborates the neutron reflectivity confirming protein adsorption. Sample S2 PDMS/PFPE-PEO suffered some damage in transit with surface abrasion but surface measurements did not indicate the same mesh structure forming in this surface consistent with the absence of protein adsorption. Rms roughness values for both 5.56 was 1.83nm and a height profile across the image indicted a average peak roughness of 3.63nm, for 5.56b the rms was 1.89nm but once the larger blobs (suspected PFPE-PEO micro droplets) the rms roughness for the remainder of the surface was 1.1nm. Height profiles from this image give an average peak height for the roughness of 1.35nm.

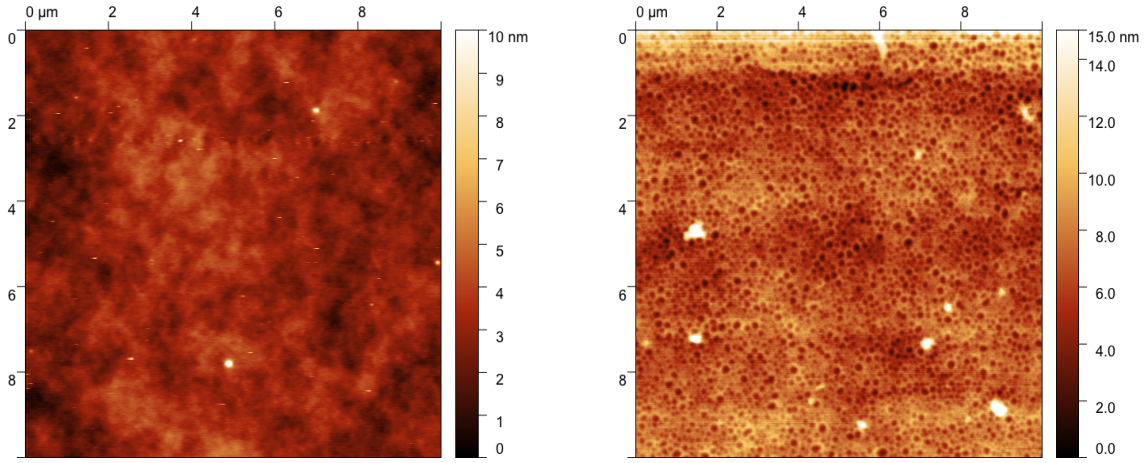

(a) Sample 1 PDMS pre experiment

(b) Sample 1 PDMS post BSA exposure

Figure 5.55: Pre and post experiment AFM images for Sample 1 PDMS.

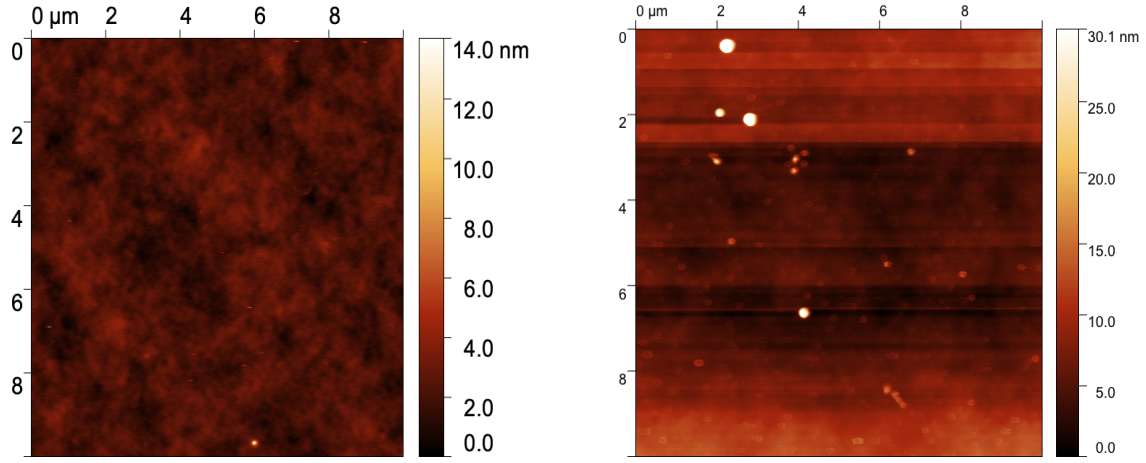

(a) Sample 2 PDMS/PFPE-PEO pre experiment

(b) Sample 2 PDMS/PFPE-PEO post BSA exposure

Figure 5.56: Pre and post experiment AFM images for Sample 2 PDMS/PFPE-PEO (note sample suffered some surface abrasion during transit).

5.9 Discussion

5.9.1 Protein adsorption

Experiments for the adsorption of protein using BSA,mefp-1 and lysozyme all show radically reduced protein adsorption on PDMS/PFPE–PEO surfaces, in the case of BSA, 3 independent experimental techniques were used to verify minimal protein adsorption to this surface, with in situ neutron reflectivity confirming the in situ QCM observations that even a single monolayer of PFPE-PEO ordered at the solid liquid interface prevents the adhesion of protein on the surface. Considering the summaries shown in figure 5.57 this behaviour is seen for both lysozyme and BSA. Attempted experiments using mefp-1 proteins were less conclusive with inconsistent frequency responses between repeated experiments on the same surfaces preventing statistically robust results. If there are inconsistencies between the pH or ionic strength of the buffer, this could have induced some desorption of the protein layer as has been seen by varying the ionic strength of lysozyme adsorption [213] and may explain the apparent desorption effects observed in these experiments, see figure 5.27a. However, the resistance of the PDMS/PFPE-PEO surface to protein adhesion appears to be similarly high for both attempted experiments and consistent with verified observations of minimal protein adhesion on these model surfaces. If these mefp-1 experiments could be repeated using a single

prepared buffer solution for the protein and rinsing buffer for all experiments we anticipate consistent results should have been achievable, the cost of this protein was prohibitive. Attempting to repeat these experiments for each PDMS QCM crystal was challenging as each crystal only be used once as there was no effective way of cleaning adsorbed protein from the surface after use (typical methods used for metal surfaces such as uv/ozone can chemically alter the PDMS interface from PDMS to silica[218] and surfactant cleaning was not fully effective) but we argue the qualitative results are valid and in accord with the finding of high resistance to protein adsorption for PFPE-PEO monolayers.

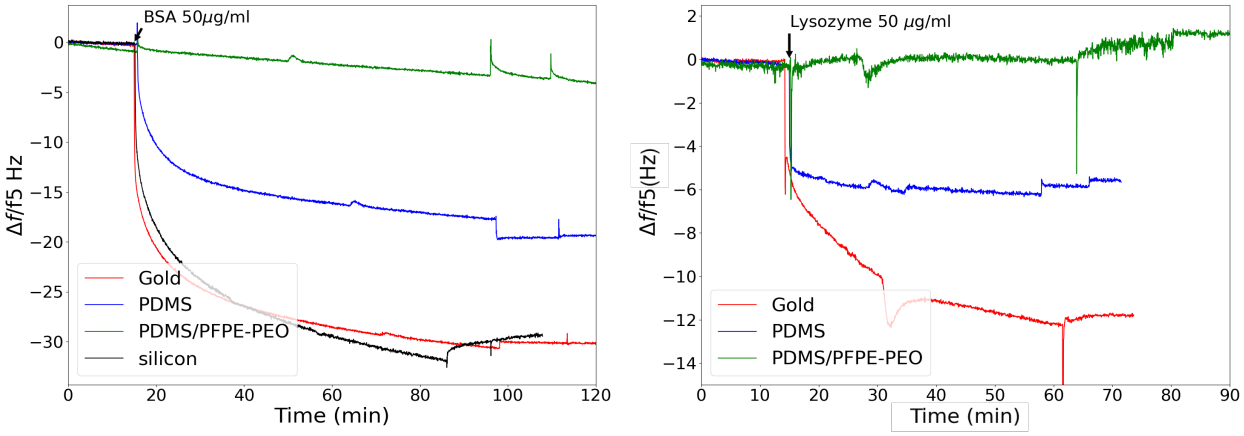

(a) BSA summary

(b) Lysozyme summary

Figure 5.57: Summary of protein adsorption tests on various surfaces for BSA and lysozyme taken from the 5th harmonic.

Considering the total mass of protein adsorption on gold and PDMS as observed by QCM we can make some inferences about the structure and mechanics of protein adsorption on these surfaces. For BSA, gold and silica, the average adsorption after 50 minutes was determined as 521ng cm^{-2} and 457 ng cm^{-2} respectively if we simply use the density of BSA protein these adsorbed masses would be equivalent to protein thicknesses of 3.83 and 3.35nm. However, these numbers are not likely to be accurate as the Sauerbrey mass measured in water is the wet mass not the true dry mass of the protein. The Sauerbrey determined masses are a summation of the mass of the adhered protein but also the mass of water in the adsorbed layer i.e. equation 5.4:

$$\Delta M_{wet} = \Delta M_{protein} + \Delta M_{water} \tag{5.4}$$

The water in these hydrated protein layers is always significant; our own neutron reflection studies of BSA adsorption on PDMS models a highly hydrated upper layer of protein with a small volume fraction, Su et al found a volume fraction for BSA on silica to be only 0.55 of the layer [214] and when considering lysozyme adsorption on silica they found the volume fraction of a single protein monolayer adsorbed from a $30\mu g$/ml solution to be as low as 0.39 [213]. Indeed, comparing QCM measurements with other techniques that can be used to infer or model the dry adhered mass of protein without the associated water such as ellipsometry[207][219], surface plasmon resonance (SPR) [220] and optical waveguide lightmode spectroscopy (OWLS), all have indicated that the wet Sauerbrey mass can overestimate the true mass of adsorbed protein by 2-3 times dependent on the protein. Goda et al estimated that the thickness of Sauerbrey and Voigt modelled layer of a self assembled by using an intermediate density value for the layer between the protein density and water to find the thickness of the protein of either 1.1 and 1.18gcm^{-1} [220].

Instead, we consider the density implied by the volume fractions of BSA and lysozyme on silica found by Su et al using neutron reflectivity. For BSA a the layer volume fraction of ϕ=0.44[214] yields a density of 1.138gcm^{-3} and for lysozyme, a layer volume fraction of 0.39 [213] yields a density of 1.158gcm^{-3}. With these estimated densities the thickness of the BSA layer on gold and silica are found to be 4.5 nm and 3.9 nm. Using the BSA dimension values of 40x140 $\mathring{A}$ the adhered layer fits best as a single monolayer of BSA in the side on conformation with a $\approx 40\mathring{A}$ thickness, the silica fit agrees particularly well with the model found of Su et al of hydrophilic adsorption on silica. In contrast the measured thickness of lysozyme on gold using the approximated density is only 1.48nm, this less than any of the dimensions of lysozyme in solution and suggests that overall layer coverage of lysozyme is less comprehensive than BSA.

Using these intermediate density values provides some credible notion of the protein thickness. We should also acknowledge that the lower effective density of these hydrated layers implies that the area footprint per adhered protein is significantly higher than the maximum packing value of a potential monolayer. A side on perfectly packed monolayer of BSA would have a footprint per protein of 40x140$\mathring{A}$ yielding a dry adsorbed mass per unit area from equation 5.5:

$$\eta = \frac{M_{protein}}{n_a \cdot A_{protein}} \tag{5.5}$$

with n_a is Avagdaro's constant we find the maximum packing protein mass for a monolayer of BSA as 200ngcm^{-2} in the side on configuration and 180ngcm^{-2} for lysozyme in the side on configuration. However, these configurations are unphysical when we consider the mechanism by which proteins attach to the surface;

proteins will adhere to the surface in a random configuration individual proteins will land at a given site with their areal footprint dependent on their orientation (we assume here side on based on previous literature and the indicated mass from experiments). As more proteins attach to the surface more of the surface will be covered in a random configuration of proteins and there will be fewer open sites for new proteins to land, this process is known as random sequential adsorption (RSA) [221] and is depicted in figure 5.58. Once enough of the surface is covered additional adsorption is inhibited by the jamming limit; the surface still has uncovered areas but there are no contiguous free spaces large enough to accommodate the footprint of adhering proteins and they are blocked from sticking to the surface. As a result of this process, mass uptake saturates below the limit of the optimal mass of a protein layer in a close packed formation but such an orientation is not achievable in the RSA mode. Modelling conducted by Hinrichsen et al determined that 2 dimensional discs (much like the ellipsoidal proteins) will saturate at a surface coverage of 0.55 [222] demonstrating that equilibrium coverage from random adsorption will be significantly lower than the optimal close packed adhesion. Although in practice proteins are more malleable in shape than simple discs and are capable of adsorbing in both side on and end on conformations, the RSA modal does describe the limitations preventing optimal protein adhesion to surfaces.

Understanding this process also explains aspects of the adhesion mode, the 'hockey stick' like nature of the frequency response to proteins can be explained by the rsa process, as at early times random adsorption occurs readily on the empty surface but as the space becomes more constrained and free sites for proteins become restricted the rate of adsorption declines as proteins are less frequently arriving on the surface at viable sites, the rate of adsorption will decline further as more proteins attach and geometric blockage becomes more frequent until the jamming limit is reached. Notably, the hydrophilic adsorption of proteins on silica and gold also results in minimal desorption upon rinsing, this has been attributed to two factors; the development of hydrogen bonds between hydroxy groups in the adsorbed proteins and the silica surface which must be broken in order to induce desorption and secondly mild structural changes to adhered proteins that increase the entropy of adsorption and a greater cost to removing the proteins, these changes have been observed in the adsorption of BSA on silica [223] which in this hydrophilic case has been shown to be reversible upon forced desorption.

For both proteins on PDMS the thickness of BSA on PDMS of 330ngcm^{-2} fits a layer of 2.84nm and for lysozyme 86ngcm^{-2} a Sauerbrey thickness of 0.75nm. On hydrophobic PDMS the layer thickness of proteins cannot be modelled to the thickness of any of the protein dimensions in solution, this agrees well with existing

understanding of protein adsorption on hydrophobic surfaces and the structure of protein adsorption observed using neutron reflectivity; proteins denature on these surfaces via hydrophobic interactions to form stable bonds between hydrophobic groups within the protein and the hydrophobic surface.

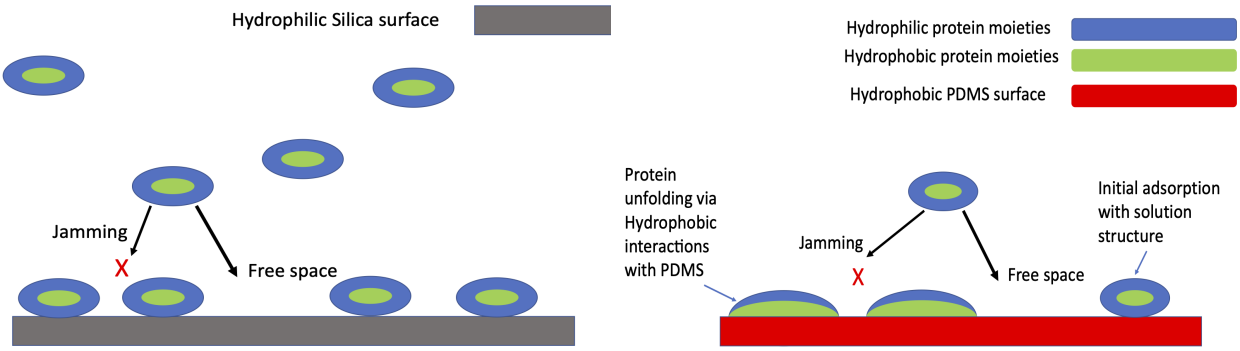

(a) Hydrophilic Protein Adsorption (b) Hydrophobic Protein Adsorption

Figure 5.58: Models of hydrophilic and hydrophobic protein adsorption showing jamming effects from inefficient surface adsorption and protein unfolding on hydrophobic surfaces.

With reference to the diagram in figure 5.58 and the RSA model for the protein adsorption process we can understand the lower overall mass adsorption as being a result of protein footprint growth during hydrophobic adsorption; after the initial, random adsorption of a protein with it's original solution structure (in either side on or end on orientation). A second process occurs in which the protein undergoes a radical restructuring and spreads across the surface, such that the area footprint A, of each hydrophobic-ally adsorbed protein is larger than the footprint of a hydrophilically adsorbed protein $A_{hydrophobic} > A_{hydrophilic}$. As depicted in figure 5.58b, each denatured protein takes up a greater randomly orientated area, thus the overall free space that can accommodate the original protein footprint is even smaller and so fewer proteins can adsorb to the surface before the jamming limit is reached. This footprint growth due to hydrophobic interaction induced protein denaturing results in a lower overall adhered mass when compared with saturation adsorption on hydrophilic surfaces [224].

The denaturing, unfolding nature of proteins on hydrophobic surfaces has been well characterised before in studies utilising FT-IR ATR analysing the conformational structure of adsorbed proteins on surfaces of varying wettability. Green et al observed that the amide *ii* IR band at 1540cm^{-1} of lysozyme protein which corresponds to the α helix structure declined rapidly in absorbed proteins on hy-

drophobic polystyrene and EDPM rubber, this change in IR bands was reflective of a process of protein unfolding [225]. Notably, they observe this change in bands occurring rapidly after initial adsorption, on the timescale of minutes. Similar timescales for hydrophobic partial unfolding were seen by Yokoyama et al who observed a decline in α helix content of adsorbed lysozyme on hydrophobic surfaces upon first measurement 0.25 hours after adsorption suggesting the process occurs no later than 15 minutes [226].

The best fit kinetic models for BSA protein adsorption on PDMS found for 4 minute and 8 minute spectra shown in figures 5.49 and 5.48 concur with these observed timeframes for protein unfolding. The protein layer structure observed from SLD shifted from a uniform monolayer to an unfolded dehydrated -hydrated bilayer within 15 minutes. The modelled structure for this unfolded protein bilayer is in agreement with the general findings of Lu et al observing lysozyme on hydrophobic monolayers. However, the fit we obtain is comparatively crude with the Su model using a smoother, multilayer fit from a high SLD, high protein volume fraction layer at the solid liquid interface falling to a lower SLD, lower volume fraction layer projecting further into the water over several intervals[215]. Such a fit could not be replicated credibly as fits already had low error and were not sensitive to increasing thin layers at the interface much smaller than the overall thickness of the sample. In the case of Lu et al protein adsorption occurred on a thin monolayer of oxide on a silicon block which allowed a more detailed modelling of the adsorbed layer as it a represented most of the scattering material in the reflectivity spectra. More recent studies using neutron reflectivity to study the adsorption of protein in hydrophobic polymers utilised a 3nm polystyrene monolayer grafter onto silicon from solution [227] with this much thinner hydrophobic polymer layer. Brouette et al also fit the adsorption of myoglobin protein in a bilayer form with a thin, high SLD region close to the hydrophobic polymer surface followed by a larger more hydrated layer. It may have been possible to form a similar monolayer of PDMS on silicon for reflectivity experiments which may have enabled a more detailed fitting of the resultant adsorbed protein layer. However, the primary objective of this experiment was to verify the comparative resistance of PDMS/PFPE-PEO surfaces to protein adsorption compared to equivalent PDMS surfaces and validate prior QCM and AFM studies. It was therefore important to remain faithful to the design of the model systems used in previous tests, with a crosslinked thin film of PDMS being more representative of a true foul release coating than a single bonded monolayer. The neutron reflectivity data presented here was acquired across a single 24 hour period which was used optimally with the excellent assistance of the local beam-line scientists. Additional samples could not have been examined in the time allotted but a future study using a thinner PDMS interface might be able to better characterise the resultant protein layer.

Interestingly, when considering the basic fitted monolayer for the PDMS monolayer we found a value of 71.2ngcm^{-2} for the adsorbed mass of protein, this model used a completely dehydrated small layer and a larger highly hydrated layer of thickness 33.5$\mathring{A}$ and a volume fraction of 0.035. If we consider the mass of water in this hydrated layer the total mass in the modelled protein layer of both protein and water is 391ngcm^{-2} this is much closer to the Sauerbrey wet mass found as 330$\pm$11 ngcm^{-2} though this does suggest that the overall hydrated layer thickness may be slightly overestimated in our fit.

Comparing QCM and neutron reflectivity with the dry AFM analysis in figure 5.16 and the calculated mass adsorbed shown in table 5.2 we find that this method overestimates the mass adsorbed compared o the other two methods with the dry mass from two samples $\approx$300ngcm^{-2}, comparable to the wet mass measured by QCM. Post situ AFM measurements were valuable as a way of demonstrating a qualitative change in surface topography due to protein adhesion. To assess the validity of this technique for measuring mass absorption it would be useful to directly compare the mass adsorbed on a surface using QCM and AFM on the same surface.

5.9.2 Dextran

Dextran adsorption was distinct from the response from proteins with more adsorption on both PDMS and PDMS/PFPE-PEO than on silica. The overall mechanism of adsorption is also different with much sharper step like adsorption of dextran compared to the hockey stick like form of protein time dependent adsorption. The lower adsorption modelled for 20kDa compared to 150kDa can be interpreted as a consequence of the lower molecular weight with a similar overall adsorption but the mass per adhered molecule being considerably higher such that the overall mass adsorbed is greater, this would also concur with Kwon et al's prior study of dextran on silica using a 66kDa molecular weight dextran in which the peak adsorbed amount was determined to be 550ngcm^{-2}[208] intermediate between the values we found for the two selected weights of dextran. Prior studies for the adsorption of polysaccharides do indicate that higher molecular weight polysaccharides have a greater affinity to surfaces with cooperative adsorption of neighbour monomers in the polymer chain strengthening the overall adhesion [228]. This study also argues from FT-IR measurements that polysaccharide adsorption is mediated by hydrogen bonds, this might explain the affinity of adsorption on PDMS/PFPE-PEO surfaces we postulate that the wetting monolayer of PFPE-PEO is orientated such that the PEO groups are presented to the water interface, these groups are capable of forming strong hydrogen bonds to water and other hydrogen bonding species

and so may allow for the adhesion of polysaccharide.

The adsorption behaviour of dextran on PDMS was somewhat less expected as this is a hydrophobic surface, a recent study by Kädorf et al found fairly small amounts of adsorbed dextran on PDMS QCM sensors; a Sauerbrey wet mass of 93ng cm^{-2} [229] however this experiment was conducted at a concentration of 1mg/ml less than the initial concentration of 10 μM employed used in our experiment (equivalent to 1.5 mg/ml with the final 100 μM concentration being equivalent to 15 mg/ml) which for PDMS found an initial adsorption of 90gcm^{-2} in good agreement with their value. It's possible uncured oligomeric chains of HT-PDMS ,may have played a role in dextran adsorption with uncross-linked OH termination groups at the solid liquid interface creating sites for hydrogen bonding, a comparison of adsorption at a full range of dextran concentrations using a vinyl terminated PDMS might show different adsorption behaviour.

Considering the comparison of F versus D for silica and PDMS seen in figure 5.32 we can see some interesting behaviour as the concentration of dextran and adsorbed mass increases. The ratio of ΔD over ΔF remains linear across all concentrations this is consistent with the relationship Kwon et al found suggesting that the structure of dextran on silica is consistent and independent of the increase in mass adsorbed. In contrast, dextran on PDMS appears to have a two stage relationship between ΔF and ΔD, with the ratio of D to F much higher at lower concentrations 10 and 20 μM before transitioning to a much lower ratio $\approx$ 1.5 ΔF upon the adsorption of 50μM dextran. As D relates to dissipation processes in the film the early stage adsorption could be interpreted as having a more open flexible with more water coupling and more viscoelastic losses, then as concentration increases and overall adsorption increases the lower ratio of $\frac{\Delta D}{\Delta F}$ is indicative of the structure becoming more rigid as the film becomes more close packed with adsorbed dextran chains.

5.10 Conclusion

A powerful set of experimental techniques have been used to independently investigate the resistance of PDMS/PFPE-PEO coatings to protein and polysaccharide adsorption. The protein adsorption behaviour on hydrophobic PDMS surfaces have also been studied and were found to be consistent with the fields understanding of hydrophobic protein adsorption mechanisms.

A single wetting monolayer of PFPE-PEO on PDMS greatly improves resistance to protein adsorption over PDMS but offers no apparent improvement in the

removal of dextran, an adhesive polysaccharide found in EPS. Given the important role proteins have in early micro-fouling processes, we believe this interfacial PFPE-PEO monolayer is plays a crucial role in the overall efficacy of foul release coatings that incorporate these oligomeric amphiphiles. We recommend that future, alternative foul release additives be subject to similar tests to determine whether they can also demonstrate this high protein resistance without compromising the overall mechanical properties of robust foul release platforms such as PDMS.

Chapter 6

Studies of amphiphilic diffusion through PDMS silicone

6.1 Abstract

Attempts were made to determine the diffusion coefficient of PFPE-PEO amphiphiles through PDMS silicone membranes. Initially, experiments were attempted using Fourier transform Infra red absorption spectroscopy using an attenuated total reflectance crystal (FT-IR ATR) following the 1-d Fickian Diffusion equation. However, owing to poor identifying bands and low overall concentration this method failed to yield results. Raman spectroscopy was considered before settling on a tensiometer based method utilising the diffusive time lag as outlined by Daynes. This method was validated using two small branched block copolymers of PDMS-PEG. When this method was applied to PFPE-PEO results were more challenging indicating much slower diffusion times with much lower initial surface concentrations after the time lag. Experiments using this method with a PFPE-PEO containing bulk foul release coatings as reservoirs for the penetrant yielded a diffusion coefficient of $3.55\pm0\ 0.24 \times 10^{-12}\mathrm{m}^2\mathrm{s}^{-1}$. Model diffusive bilayers made and prepared for ion milling XPS probed surface and depth composition. These measurements found a peak fluorine elemental bulk composition of 3% yielding an implicit limit on the solubility of PFPE-PEO in PDMS. Further XPS experiments determined that the diffusion of PFPE-PEO through 262um thick PDMS was detectable within 18 hours placing an absolute lower limit on the diffusion coefficient of $1.77\times\ 10^{-}13\ \mathrm{m}^2\mathrm{s}^{-1}$.

6.2 Introduction

6.2.1 Fickian Diffusion

The Physics of Diffusion are well characterised and are of significant relevance for our studies. Understanding the relative transport rate of the additive amphiphiles in a greater matrix can inform the necessary concentrations that should be incorporated into a given coating to ensure the overall coating efficacy. This concentration can then be optimised to achieve reliable longevity without requiring excess and cost ineffective use of additives.

For Fickian diffusion in 1 dimension, consider a cross section of a medium in which there is some concentration of a diffusing solute, the rate of diffusion will be primarily defined by the equation 6.1: Fick's first law of diffusion [230]

$$F = -D\frac{\partial C}{\partial x} \tag{6.1}$$

where F represents the flux of diffusant through a given area, C is the concentration of the diffusant, D is the diffusion coefficient and x is the spatial coordinate normal to the cross section. This equation assumes an isotropic medium and a constant diffusion coefficient, a reasonable assumption in dilute systems. From this equation we can see that Diffusion of solutes occurs from regions of high concentration to low concentration.; if $\frac{\partial c}{\partial x} > 0$ i.e. concentration C increases. As one moves further in the positive direction from the cross section the flux of diffusing solvent will be in the negative direction towards the cross section. We can also see that in the case that there is no flux of diffusing solute in the case when $\frac{\partial c}{\partial x} = 0$, this is consistent with an understanding of the of movement of solute in a medium where the concentration has equilibrated; in a system where a given solute is uniformly distributed at a single concentration there will be no net transfer of diffusing material.

Equation 6.2, Fick's second law of diffusion in one dimension relates the rate of change of concentration with the spatial distribution of concentration[231]:

$$\frac{\partial C}{\partial t} = D\frac{\partial^2 C}{\partial x^2} \tag{6.2}$$

The solutions to this can be used to solve and find the diffusion coefficient in a variety of scenarios. For the determination of the diffusion coefficient of PFPE-PEO in PDMS silicone the first model considered was that of small molecule penetrants in a bulk film. [232] If we consider a simple uniform polymer film that

is initially free of diffusive penetrant (hence C=0) and is effectively infinite in the x and y dimension but has finite thickness 2L (defined around the middle of the film at z=0). If this film is immersed entirely into a large reservoir of liquid penetrant both the top and bottom surface (+z,-z) will be exposed to an instantaneous, maximum concentration C_{sat}.

Using Fourier series to solve equation 6.2 it has been determined that the concentration within the film across space and time can be found as:

$$\frac{C}{C_{sat}} = 1 - \frac{4}{\pi}\sum_{n=0}^{\infty}\left[\frac{-D(2n+1)^2\pi^2 t}{4L^2}\right] \times \cos\left[\frac{(2n+1)\pi z}{2L}\right] \tag{6.3}$$

Integrating over this space the mass of penetrant M_t, adsorbed into the polymer film at a given time t can be determined relative to mass adsorbed upon equilibrium at infinite time M_∞:

$$\frac{M_t}{M_\infty} = 1 - \sum_{n=0}^{\infty}\frac{8}{(2n+1)^2\pi^2}\exp\left[\frac{-D(2n+1)^2\pi^2 t}{4L^2}\right] \tag{6.4}$$

equation 6.4 is also a summation but the expression can be simplified for intermediate times where $\frac{M_t}{M_\infty} \geq 0.5$

$$\ln\left(1 - \frac{M_t}{M_\infty}\right) = \ln\left(\frac{8}{\pi^2}\right) - \frac{D\pi^2 t}{4L^2} \tag{6.5}$$

Using Equation 6.5 it is possible to determine the diffusion coefficient of a penetrant through a given polymer by monitoring mass uptake of diffusant over time and then finding the linear relationship between $\ln\left(1 - \frac{M_t}{M_\infty}\right)$ against the time dependant expression $\frac{D\pi^2 t}{4L^2}$. This relationship provides us with a viable method of determining diffusivity provided when can obtain accurate time dependent data on the mass uptake of the diffusing penetrant. A number of methods have been utilised historically for such an experiment. For very small gaseous particles adsorbing or desorbing from small polymer films Quartz Crystal Microbalances (QCM see chapter2) have been used to measure time dependent mass changes with a high degree of sensitivity, for liquid penetrants this method can be more challenging as immersing the crystal surface in a liquid will significantly effect the crystal resonance. A polymer coated QCM crystal will often need to be calibrated and it's resonance frequency in liquid determined before data can be acquired, given that polymer coatings on QCM crystals are typically very thin (10s of nm-10s of μm)

the lost measurement time during the initial setup could be quite significant to the overall diffusion process. Crude techniques for larger bulky samples simple pat and weigh methods (in which a sample is simply dipped in the penetrant liquid for a given time, then removed and any excess, non adsorbed liquid shaken off before re-weighing the sample to determine the mass of penetrant absorbed) could also be used to measure mass uptake albeit to a much lower degree of accuracy.

One drawback with simply measuring the mass change in the sample after diffusion is that without strict sample control one cannot guarantee the mass gain or loss is solely the result of the chosen particle. A better alternative is to use a spectroscopic technique that can be used to specifically identify the prescience and concentration of the diffusing penetrant. This is most typically done using infrared absorption spectroscopy.

6.2.2 Measuring diffusion using Fourier transform infra red absorption spectroscopy

Infra-red absorption spectroscopy is a ubiquitous technique for identifying molecules, particularly polymers, via their chemical functional groups. In the simplest case when a molecule is exposed to photons γ of frequencies within the infra red range (700nm$<\lambda<$1mm) the molecules will absorb photons which have a frequency that matches the vibrational resonant frequencies of chemical bonds within the molecule. Because different chemical bonds have different resonant frequencies dependent on the elements involved and the adjacent functional groups it is possible to identify the bonding and signature chemical groups of a polymer or molecule based on the frequencies of IR light which are most absorbed by the substance.

For diffusion experiments a particularly useful innovation in infra red spectroscopy is attenuated total reflectance spectroscopy (FT-IR ATR). A crystal is used (typically made of sapphire) which the analysis sample is placed in contact with. The IR light is guided through the crystal to the crystal/sample interface at such an angle to ensure total internal reflection of the light at the boundary. At this reflection boundary an evanescent infra red light wave will be induced in the sample medium. As this wave penetrates the sample medium it will decay exponentially and, depending on the ATR crystal material, will only penetrate 0.5-4μm into the sample. This decay is described by equation6.6

$$E = E_0 exp(-\gamma z) \tag{6.6}$$

where E_0 is the initial electric field strength, z is the depth and γ is the reciprocal of the penetration depth, the distance at which the evanescent wave decays to 1/e

of the original value. This factor γ is determined by equation6.7:

$$\gamma = \frac{2n_2\pi\sqrt{\sin^2\theta - \left(\frac{n_1}{n_2}\right)^2}}{\lambda} \tag{6.7}$$

we see from this that the wave will have a greater effective depth penetration the lower n_2 the refractive index of the ATR crystal is.

Generally, the angle will be fixed and the technique demands the use of a broad fixed range of wavelengths λ so the choice of crystal is the only thing that can increase the depth of IR penetration. Recognising that with this experimental setup we can place a sample of a given thickness L in contact with an ATR crystal at one side, this FT-IR ATR can generate an evanescent wave penetrating the sample to a finite depth. In this ATR experiment the infra red absorption spectra of the sample is produced from an evanescent wave with a penetration depth, d$\approx 4\mu$m from the crystal sample interface. For a diffusion experiment, with the sample exposed to liquid penetrant distance L from the ATR crystal diffusion can be determined by adapting equation 6.4 to account for the convolution of the ATR evanescent wave described by equation 6.6. The IR absorbance due to the diffusing penetrant can be described over time by:

$$\frac{A_t}{A_\infty} = 1 - \frac{8\gamma}{\pi[1-\exp(-2\gamma L)]} \times \left[\frac{\exp\left(\frac{-D\pi^2 t}{4L^2}\right)\left(\frac{\pi}{2L}\exp\left(-2\gamma L\right) + (2\gamma)\right)}{\left(4\gamma^2 + \frac{\pi^2}{4L^2}\right)}\right] \tag{6.8}$$

where A_t and A_∞ are the IR absorbance due to the penetrant at time t and at infinite time respectively. If we make the assumption that in most cases, the ATR penetration depth is much smaller than the overall thickness then $4\gamma^2 >> \frac{\pi^2}{4L^2}$ and $1 >> \exp(-2\gamma L)$. Therefore equation 6.8 can be simplified to[233]:

$$\ln\left(1 - \frac{A_t}{A_\infty}\right) = \ln\left(\frac{4}{\pi}\right) - \frac{D\pi^2}{4L^2}t \tag{6.9}$$

From equation 6.9 it is clear how an FT-IR ATR experiment could be performed to determine the diffusion coefficient for a penetrant in a thin film by monitoring the absorbance for a selected IR band over time. Much like QCM but unlike 'pat and weigh' methods it is possible to monitor the increase in penetrant concentration in realtime. This is the method that was initially attempted to determine the diffusion coefficient of PFPE-PEO in PDMS.

6.2.3 Methodology of FT-IR ATR diffusion for PFPE-PEO in PDMS

6.2.3.1 Curing of PDMS elastomers and PFPE-PEO doped silicone of controlled concentrations

For these initial methods Sylgard 184(Dow chemical) was used as the PDMS. The PFPE-PEO diffusant studied was Fluorolink E10/6 (Solvay) supplied by Akzo Nobel. Bulk IR absorbance measurements of the spectra of PFPE-PEO and liquid uncured Sylgard were taken to identify signature absorbance bands and any distinct groupings. In previous diffusion experiments thin $\approx 20\mu$m thick thin films of polymer were spin coated directly onto ATR crystals, this was not viable with the FT-IR available a ficsher scientific model with a penetration depth of 4μm. Elastomers of PDMS were made by mixing Sylgard A with curing agent Sylgard B at a ratio of 10:1 by mass, these mixtures were then cured at 65 °C for 4 hours. Mixed PFPE-PEO/PDMS elastomers were also made by mixing Sylgard PDMS and PFPE-PEO together in solvent before evaporation and curing.

The solvent utilised for this was tert butanol which was found to be a mutual solvent for both PDMS and PFPE-PEO. PDMS (10:1 by mass cross-linker to base) was dissolved into tert butanol at a concentration of 40% by mass. PFPE-PEO was added to fractions of this solution to create solutions with PFPE-PEO mass content relative to PDMS content of w/w$_{PDMS}$=0.45,0.85,1.5 and 2.5%. Once mixed, the solvent was allowed to evaporate leaving behind partially mixed PFPE-PEO/PDMS elastomers which were then cured at 65C for 4 hours. The IR absorbances of these mixed elastomers were measured to determine if PFPE-PEO was identifiable in the PDMS elastomer.

6.2.3.2 Long term diffusion monitoring using liquid volumes of PDMS

Finally, an experiment was conducted over 24 hours using uncured Sylgard and liquid PFPE-PEO). as illustrated in figure 6.1, a volume of uncured liquid PDMS was deposited onto the ATR crystal encapsulated by an O-ring of diameter 11.1mm,. By measuring the mass deposited into the o-ring it was found a mass of 0.13g of PDMS was used which given a density of 0.965g/cm^3 and corresponds to a volume of $135mm^3$, divided by the O-ring area of $387mm^2$ the thickness of the PDMS layer and also the distance for diffusion in 1 dimension would is 350μm. Subsequently, a mass of PFPE-PEO was deposited fully covering the top surface of the liquid Sylgard layer. The Ir spectrum was normalised by taking an initial background for the experiment whist the ATR crystal was covered with PDMS thus normalising

for this spectrum, the system was left overnight and a second Ir measurement was taken to assess the change in Ir bands due to diffusion of PFPE-PEO.

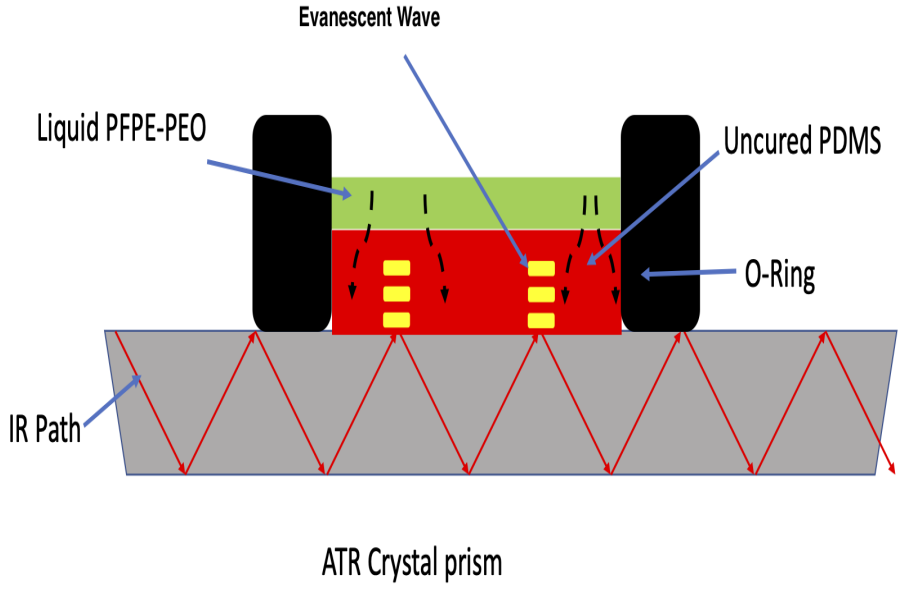

Figure 6.1: Cross sectional view of the FT-IR ATR setup for the diffusion of liquid PFPE-PEO through uncured PDMS.

6.2.3.3 IR bands of PFPE-PEO and PDMS: lack of detectable PFPE-PEO in PDMS

From FT-IR of bulk PFPE-PEO and Sylgard measurements of their respective Infra red absorption spectrums were obtained.

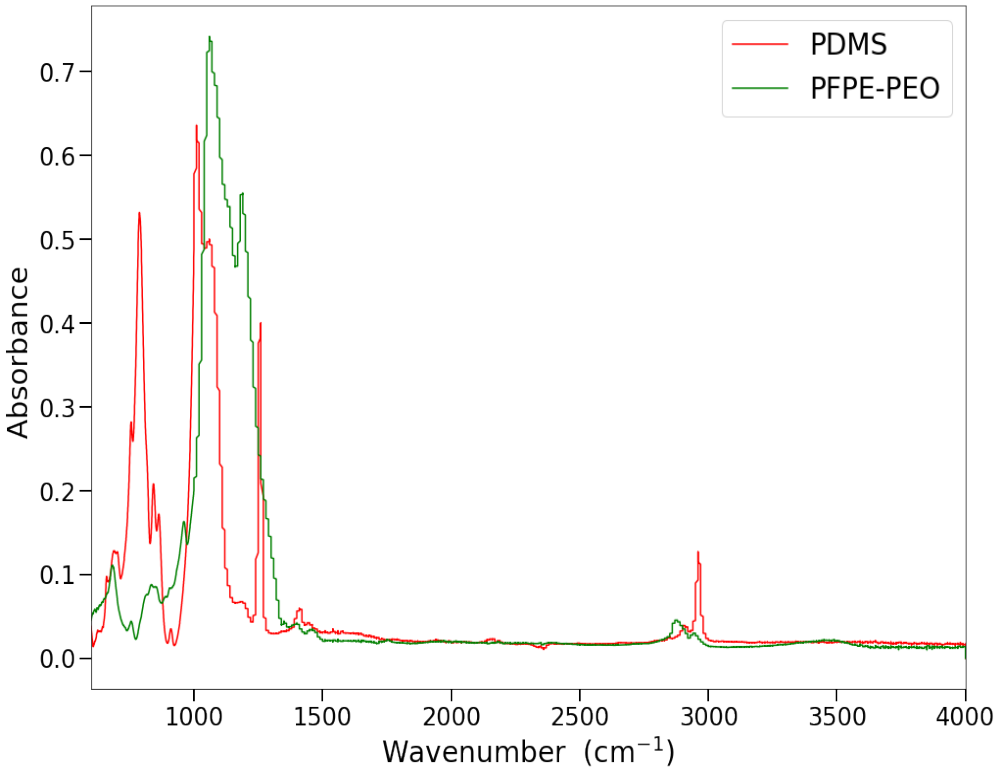

Figure 6.2: IR absorbance spectra for PDMS and PFPE-PEO.

It is clear immediately from figure 6.2 that there is a lack of clear and distinct absorption bands between the two materials; the largest peaks outside the fingerprint region for both materials are in the region of 2800-3000cm^{-1} which corresponds to the ubiquitous methyl CH3 CH2 groups seen in both polymers. the only other unique IR absorbance for PFPE-PEO occurs in the region of 3200-3600cm^{-1} this can be attributed to the OH diol groups terminating the ends of the PFPE-PEO molecule. However, this band is clearly very broad and weak so will be very difficult to see at low concentrations and given this OH stretch is also found in water longterm variance in the environment humidity and moisture absorbance could very easily influence this absorbance band making this band very hard to utilise reliable over long time frames.

For the time dependent IR diffusion tests the initial infra red spectrum was normalised for PDMS so any shift in the absorbance spectra should be more clearly attributable to PFPE-PEO. However after more than 12 hours there was no evidence of PFPE-PEO around the distinct 3200-3600cm^{-1} band.

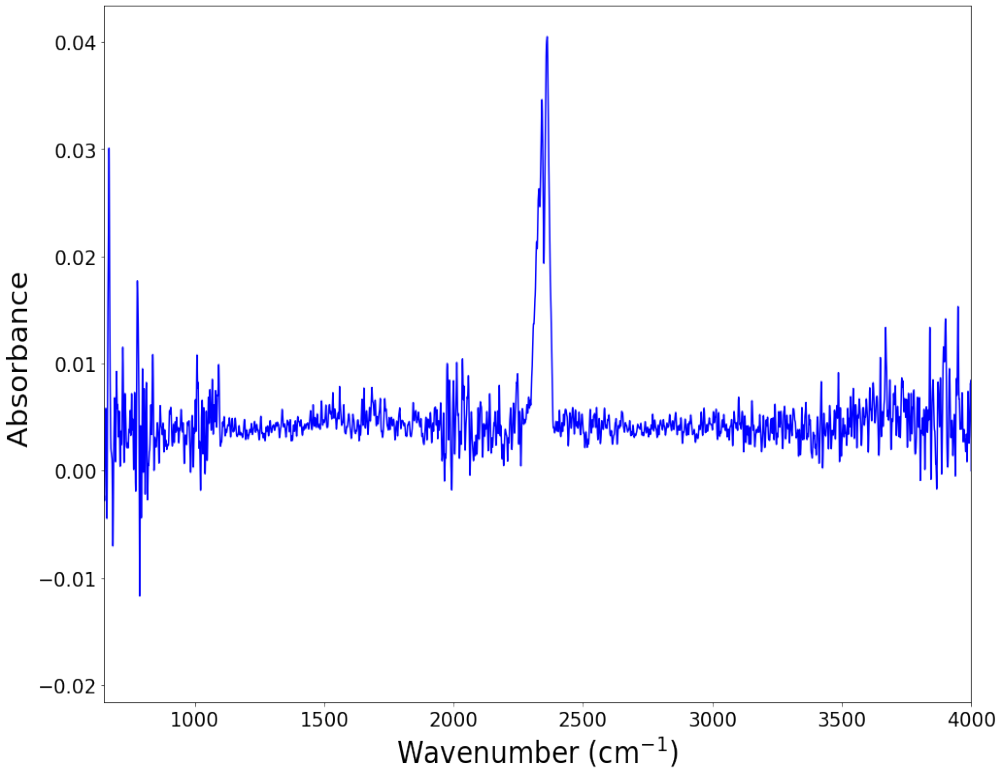

Figure 6.3: Initial IR spectra for diffusion sample normalised for the PDMS liquid.

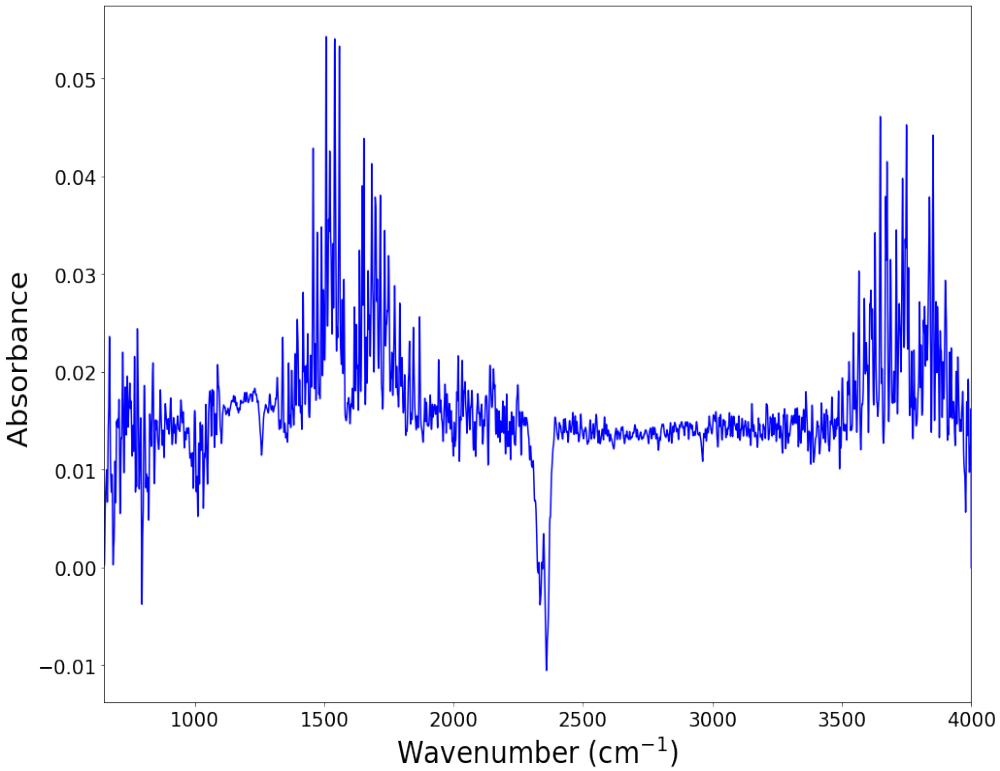

Figure 6.4: IR spectra for the liquid diffusion sample after 17 hours of diffusion.

Inspecting figures 6.3 and 6.4 over the 17 hours of the diffusion experiment there is some change in the IR spectra but none of the shifts could be associated with the presence of PFPE-PEO. The only clear and identifiable feature relates to a doublet absorbance peak around $2350cm^{-1}$ this doesn't correspond to either PDMS or PFPE-PEO but rather to CO_2 [234]. We observe a clear shift in this absorbance peak over the timeframe for diffusion in which this shifts from a very small positive absorbance of less than 4% at the beginning of the experiment to an inverted and unphysical negative absorbance after 17 hours. Both these peak features are very small; compared to the absorbances seen for Sylgard PDMS and PFPE-PEO in figure 6.2 these absorbances are an order of magnitude smaller. This is to be expected given that these experiments took the PDMS in contact with the ATR crystal as an IR background, indeed it is somewhat surprising that the CO_2 absorbance bands are as prominent as they are in figure 6.3 as the background was taken only a few minutes earlier. The change in this band can be attributed to a small fluctuation in the carbon dioxide content of the room over the timeframe of the experiment. The FT-IR was not encapsulated and so changes in the overall

concentration of CO_2 over extended timeframes would result in a change in the nature and intensity of these bands in this case a slight decrease in the overall carbon dioxide concentration over the period. Outside of this doublet peak and a very rough broad absorbance around 3500-4000cm^{-1} which are also associated with CO_2 there is no clear evidence of PFPE-PEO, without any peaks that can be clearly attributed to this penetrating molecule no concentration can be determined from this method.

When examining cured elastomers of PDMS with set concentrations it is not clear what absorbance bands should be used but a pure PDMS elastomer was used to subtract as a background for the spectra an example residual spectra is shown below.

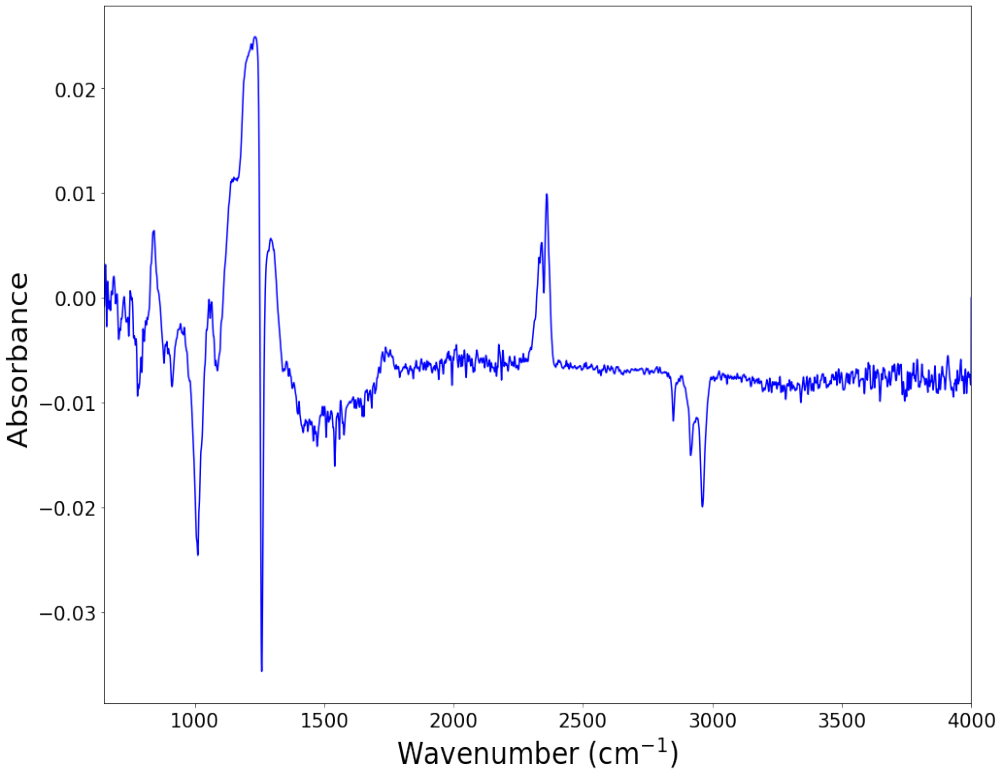

Figure 6.5: Residual IR spectra for a cured PDMS elastomer with1.5% PFPE-PEO by wt. after the subtraction of a standard PDMS spectrum.

For this residual spectrum seen in figure 6.5 there do appear to be some weak absorbances once the PDMS control signal is subtracted. Most clearly this residual

absorbance occurs around 1000-1250 cm^{-1}, this corresponds roughly to well known infra red absorbances for C-F carbon fluorine bonds which are in abundance in the perfluoroinated section of PFPE-PEO. These absorbances were integrated for the whole range of PFPE-PEO concentrations in mixed PDMS elastomers in order to determine whether the intensity of the peaks do correlate with increasing concentrations of PFPE-PEO. Indeed over the range of mixed silicones formed there is a positive correlation between the residual intensity of this peak and PFPE-PEO concentration.

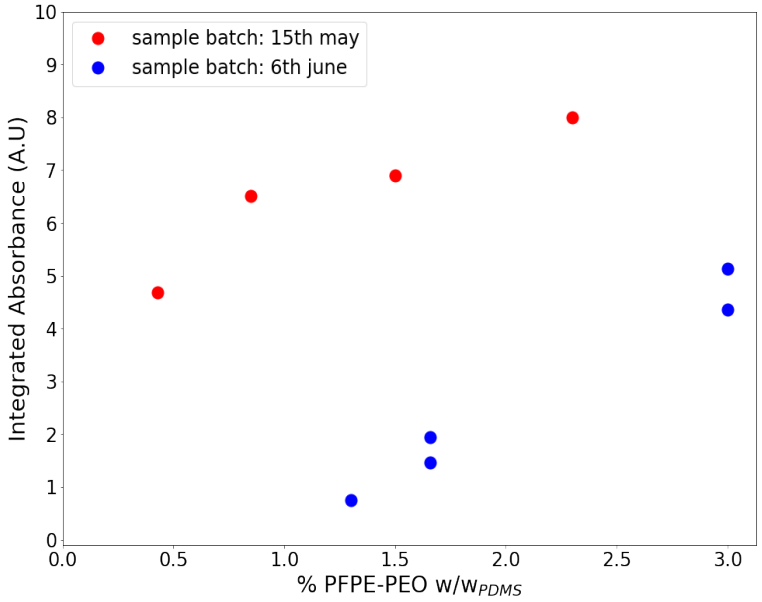

Figure 6.6: integrated intensity for 1000-1250cm^{-1} residual IR peak for two sets of calibration samples of varying PFPE-PEO % w/w in PDMS elastomers.

However, despite the linear correlation between these integrated peak and PFPE-PEO concentration the absolute intensity could not be measured reliably: figure 6.6, the intensity of these integrated, residual peaks were not consistent across samples nor was the linear relationship between signal though the relationship between increasing intensity with increasing concentration. As such, it is unlikely that a true value of the penetrant concentration could be found by using these values as a calibration curve. It should also be noted that these residual signals are in a region with significant absorbances for both PDMS and PFPE-PEO, the integrated peaks are not from distinct isolated absorbances native to PFPE-PEO only.

Overall, despite the historic success of this method for finding diffusion coefficients this ATR FT-IR infra red spectroscopy method was deemed unfeasible for this system. We attribute this to a series of limitations

1. The ATR-IR is not in an enclosed air tight chamber and so the environmental background effects like CO_2 air content cannot be controlled which means measurements are not comparable over time and the modest residual intensities are dominated by these effects.
2. For solid cured samples maintaining consistent contact between the sample and the ATR crystal is hard to control meaning signal intensities are often inconsistent from measurement to measurement.
3. The absorbances found in residual IR signals are in the fingerprint region of 800-1500cm^{-1} in which both PDMS and PFPE have significant and complicated absorbances it's not clear that increasing concentration of each material will lead to clear linear increases in the residual signals in this region.

The challenges faced with this method have meant it is not possible to reliably and clearly obtain a diffusion coefficient from 1 dimensional tests using ATR IR. This method may have been viable if only there was a clear and wholly distinct absorbance between the two materials, but attempts to use normalisation of spectra subtraction were not able to provide substantive results so other methods had to be considered.

6.3 Determining the diffusion coefficient of amphiphiles using surface functionalisation at the solid liquid interface and the diffusive time lag

Having found severe difficulties with more conventional methods of measuring diffusion alternative material specific methods were researched. A recent novel method developed by Noguer[235] specifically for small amphiphile molecules relies on observing the contact angle of small sessile droplets of water on a membrane surface over time to observe the effect of any diffusing amphiphile in the coating. These additives are small molecules relative to the effectively infinite molecular weight of the cross linked elastomer and due to their amphiphilic nature containing both hydrophilic and hydrophobic moieties will diffuse to and preferentially functionalise the solid liquid interface of a coating in contact with water [236] [237].

In the case of a coating of PDMS silicone this is especially true as the coating is highly hydrophobic with measured contact angles for water of PDMS often in the range of 115-120° with values of surface energy in the region of 22mJm^{-2} [238] silicone's water interfacial tension is around 58mJm^{-2} providing a strong energetic justification for a more hydrophilic additive to surface segregate and reduce the solid\liquid interfacial tension.

In the case of a sessile drop of liquid water, when the droplet is in contact with a PDMS coating containing some concentration of a an amphiphile the contact angle the droplet forms with the surface will initially be similar to that with a pure PDMS surface ($\sim 120^o$) but the droplet will then spread on the surface further with a reduced contact angle as the amphiphile begins to functionalise this solid liquid interface and reduce the surface tension. This is particularly the case in PEO\PEG containing amphiphile as this polymeric block is so hydrophilic and provides a profound energetic driving force for segregation at aqueous interfaces. It is this surface segregation effect Noguer et al used to determine diffusion coefficient for PEG containing amphiphiles.: PDMS coatings of known thicknesses were used as diffusive membranes exposed to reservoirs of a given amphiphile with the time taken for water droplet relaxation to occur. This time frame was related to a concept known as diffusive time lag from which the diffusion coefficient can be derived.

6.3.1 The time lag for diffusion across 1-dimensional membranes

The diffusive time lag is a concept originally determined by Daynes to determine the diffusion of gaseous hydrogen across rubber membranes [239]. In his model we consider a situation in which initially, at time t=0, a reservoir of gaseous hydrogen of a give concentration C_L is present on one side of a rubber membrane of thickness L. This reservoir is sufficiently large that the concentration does not fall appreciably throughout the timeframe of the experiment such that the rubber membrane is initially empty of any hydrogen. Likewise, on the other side of this membrane at distance L from the gaseous reservoir the concentration of hydrogen is also 0 C_0=0. The general Fickian solution for these boundary conditions is defined as [240]:

$$\begin{aligned} C(x) = C_0 + \frac{C_L - C_0}{L}x + \frac{2}{\pi}\sum_{n=1}^{\infty} \frac{C_L\ cos\ n\pi}{n} \cdot sin\frac{n\pi x}{L} \cdot e^{-\frac{D\pi^2 n^2 t}{L^2}} \\ + \frac{2}{L}\sum_{n=1}^{\infty} sin\frac{n\pi x}{L} \cdot e^{-\frac{D\pi^2 n^2 t}{L^2}} \int_0^x f(x') sin\frac{n\pi x'}{L} \cdot dx' \end{aligned} \tag{6.10}$$

For the aforementioned system, an empty membrane is instantaneously exposed to gas on one side the initial boundary conditions of C(x)=0 and C_0=0 at time t=0 this general equation simplifies to:

$$C = \frac{C_L}{L}x + \frac{2}{\pi}\sum_{n=1}^{\infty}\frac{C_L\ cos\ n\pi}{n}\cdot sin\frac{n\pi x}{L}\cdot e^{-\frac{D\pi^2n^2t}{L^2}} \tag{6.11}$$

with identity $cos\ n\pi = (-1)^n$ this leads to [239]

$$C = \frac{C_L}{L}x + \frac{2}{\pi}C_L\sum_{n=1}^{\infty}\frac{(-1)^n}{n}\cdot sin\frac{n\pi x}{L}\cdot e^{-\frac{D\pi^2n^2t}{L^2}} \tag{6.12}$$

so at small time the concentration gradient near the boundary x→0 is found to be

$$\left(\frac{\partial C}{\partial x}\right)_{x\to 0} = \frac{C_L}{L} + \frac{2nC_L}{L}\sum_{n=1}^{\infty}\frac{(-1)^n}{n}\cdot cos\frac{n\pi x}{L}\cdot e^{-\frac{D\pi^2n^2t}{L^2}} \tag{6.13}$$

If we imagine that the gaseous diffusant flows through the membrane over time and out the face at x=0 . The gas that passes through the membrane and into this initially empty volume V, the flow rate into this volume is given by

$$V\cdot\frac{\partial C}{\partial t} = D\left(\frac{\partial C}{\partial x}\right)_{x\to 0} \tag{6.14}$$

$$dC_{out} = \frac{D}{V}\frac{C_L}{L}\int_0^t\left(1 + 2n\sum_{n=1}^{\infty}\frac{(-1)^n}{n}\cdot cos\frac{n\pi x}{L}\cdot e^{-\frac{D\pi^2n^2t}{L^2}}\right)\cdot dt \tag{6.15}$$

$$C_{out} = \frac{DC_L}{VL}\left(t + \frac{2L^2}{D\pi^2}\sum_{n=1}^{\infty}\frac{(-1)^n}{n}\cdot\left(1 - e^{-\frac{D\pi^2n^2t}{L^2}}\right)\right) \tag{6.16}$$

Using the identity $\sum_{n=1}^{\infty}\frac{(-1)^n}{n^2} = \frac{-\pi^2}{12}$ allows us to simplify the summation and find the time dependent concentration into this volume as:

$$C_{out} = \frac{DC_L}{VL}\left(t + \frac{2L^2}{D\pi^2}\left(-\frac{\pi^2}{12}\right)\left(1 - e^{-\frac{D\pi^2n^2t}{L^2}}\right)\right) \tag{6.17}$$

We now have a function for the time dependent change in the overall concentration of the diffusive material the other side of the diffusion membrane from the reservoir.

Considering the case at long times after initial exposure to penetrant,
as t$\rightarrow \infty$ $C_{out} = \frac{DC_L}{VL}\left(t + \frac{2L^2}{D\pi^2}\left(-\frac{\pi^2}{12}\right)\right)$

$$C_{out} = \frac{DC_L}{VL}\left(t + \frac{L^2}{6D}\right) \tag{6.18}$$

This function C_{out} is unphysical or zero until the time of diffusion t is equal or greater to:

$$t_{lag} = \left(\frac{L^2}{6D}\right) \tag{6.19}$$

This factor t_{lag} is the definition of diffusive time lag. In the initial experiments by Daynes in which this factor was first defined, this time factor enabled the determination of diffusion coefficients through membranes of differing rubber materials by measuring the time lag between exposing a membrane to the gaseous hydrogen the first detection of hydrogen gas on the other side of the membrane from the penetrant reservoir or more simply the time it takes for a penetrant to first diffuse across the entire thickness of the membrane. This method has been used successfully to find the gaseous diffusion coefficient of oxygen trough silica using a permeation cell [241] and to determine the diffusion of sodium dodecyl sulphate surfactant through polymeric elastomers using spectrophotometry [242] This time lag concept was also applied more recently to amphiphiles in coatings with some success, instead of measuring the concentration of gas in the outgoing volume diffusive time lag was reframed as the time until non-zero concentration of amphiphile was detected across a membrane of thickness L. The non zero concentration of amphiphile at the top surface of a diffusive membrane was determined by water sesslie droplets; when the contact angle of the droplet with the surface fell clearly and further spreading of the droplet on the surface was induced, the presence of an amphiphilic species was inferred at the surface capable of reducing the solid liquid surface tension. Defining this time as the diffusive time lag in this case a number of diffusion coefficients were determined successfully for small amphiphiles in PDMS silicone. With more conventional methods proving challenging, this context specific method of finding diffusion coefficients for very similar systems was highly appealing. Although less accurate (as will be discussed in the

discussion) this method requires little pre preparation of the system An adapted methodology to suit our system will now be described.

6.3.2 Methodology: determining the diffusion coefficient from time lag contact angle measurements

Initially, coatings of amphiphile free PDMS silicone were formed using Sylgard 184 by mixing the two components A and B at a ratio of 10:1. In most cases Hexane was added to the silicone to help aid the mixing of silicone and curing agent, as both are soluble in Hexane. This had the added benefit of reducing the viscosity of uncured Sylgard to aid coating and reduce the prevalence of micro-bubbles in the film as well as enabling a greater variation of final thicknesses by utilising different Sylgard volume fractions in Hexane at deposition as a thinner coating will remain once the Hexane evaporates. For each experiment a range of films were formed by spreading mixtures of uncured Sylgard on PMMA slides using a series of RK print hand coaters ranging from 120-500μm. Once spread the films were initially left in a fume hood for 15 minutes to enable hexane solvent to evaporate (with a boiling point of 56°C this will happen readily in a short time frame) and then placed in a pre heated oven at 65°C for 4 hours in order to crosslink the PDMS creating thin solid rubber films. For each amphiphile a single set of cured coating films were formed such that the cross-linker ratio in each of these cured films is equivalent, so there should be no difference in the diffusion membranes material structure.

For each amphiphile a set of experiments across a range of PDMS coating thicknesses, for each experiment the specific thickness of the coating was measured using a micrometer and then the coating would be placed in contact with a reservoir of penetrating diffusant. A liquid droplet of initial volume 50μl was placed immediately on top of this coating surface and then the contact angle of this droplet was recorded over time using the Osilla Goniometer. Any minor time delay between membrane exposure and recording contact angle was recorded and accounted into observed timeframes. All recorded videos of contact angles were reprocessed for ease of analysis into videos with a frame rate of ten seconds per frame allowing the contact angle to be found using analysis software at 10 second intervals. For each diffusion measurement the time at which the contact angle falls is recorded from these dynamic contact angle measurements and this shift was defined as the time lag for a given amphiphile at a given coating thickness. Multiple measurements were performed across the range of thicknesses from which a diffusion coefficient using a linear fit, plotting the time lag against the the square from membrane thickness L $T_{lag} = \frac{L^2}{6D} + \partial T$ from which the diffusion coefficient D can be found from the gradient m of a linear fit of of this data $D = \frac{1}{6m}$. The y

intercept of this equation ∂dT is a factor not mentioned in the original definition equation 6.19 of Fickian time lag. This is a term we associate with non Fickian diffusion anomalies which may be related to initial barrier resistance to diffusion into the membrane or ,as will be discussed later, an innate delay in the time for amphiphiles to surface segregate to the solid liquid boundary. This y-intercept factor ∂dT could relate to real non Fickian effects on diffusion but we do note that this factor is membrane thickness independent and this factor must be positive as a negative time lag at thin membranes would be unphysical.

6.3.2.1 Method validation using small PDMS-PEG branched amphiphiles DBE-411 and DBE-712r

In order to verify this version of the Noguer method, two short amphiphiles were tested to determine if the Fickian diffusion relation of contact angle time lag increasing with membrane thickness[2] and a viable diffusion coefficient could be found. The chosen amphiphiles were branched PDMS-PEG oligomers DBE-712r and DBE-411(see figure 6.7 for general structure). DBE-712r has recently been shown to act as an effective foul release additive in silicone coatings[243]. The amphiphile was incorporated as an additive in cured silicone coatings and showed clear surface active behaviour from contact angle measurements. As such, these branched molecules are capable of diffusing in bulk PDMS silicone and functionalising the solid liquid interface, therefore this method should be highly suited to determining their diffusion coefficient through silicone.

DBE 712r (reduced volatility variant) has a M_w of 600 Da of which. 60-70% is PEG and a dynamic viscosity of 20cSt. DBE 411 has a total molecular weight of M_w 400-500 of which 45-50% is PEG and a dynamic viscosity of 5-10cSt. These molecules were purchased from Gelest chemical company (via Fluorochem supplier). For diffusion tests thin layers of either DBE-411/712r were spin coated at 1500 rpm from bulk onto silicon wafers treated with a 100nm layer of PMMA to encourage film stability. These layers were micrometers thick and acted as the penetrant reservoirs which PDMS coatings were placed on for 1 dimensional diffusion.

In the case of DBE-712r an attempt to repeated the diffusion experiment using the aforementioned FT-IR ATR method outlined in section 6.2.2 is also shown.

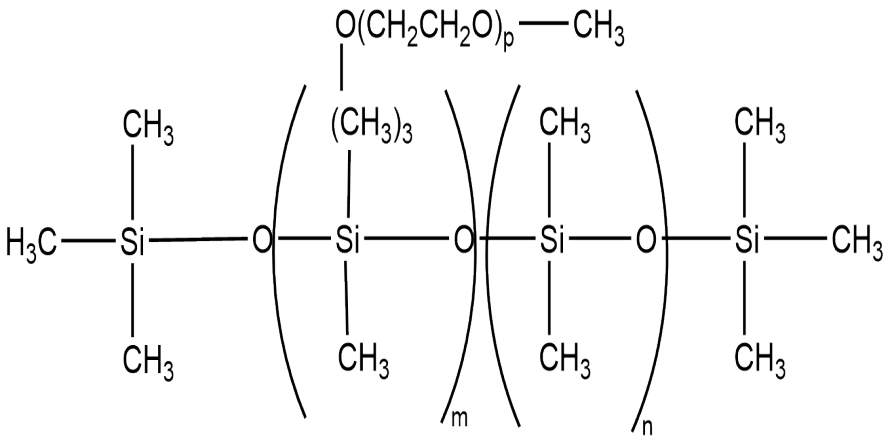

Figure 6.7: Chemical structure of amphiphile PDMS-PEG branched copolymers DBE-411 DBE-712r.

Because of the apparatus structure it was not possible to enclose the environment of the droplet so that over time, these droplets are subject to evaporation effects and will lose volume and result causing a decline in the contact angle without surface reconstruction as demonstrated by figure 6.8 in which the contact angle steadily declines over 30 minutes due to water evaporation.

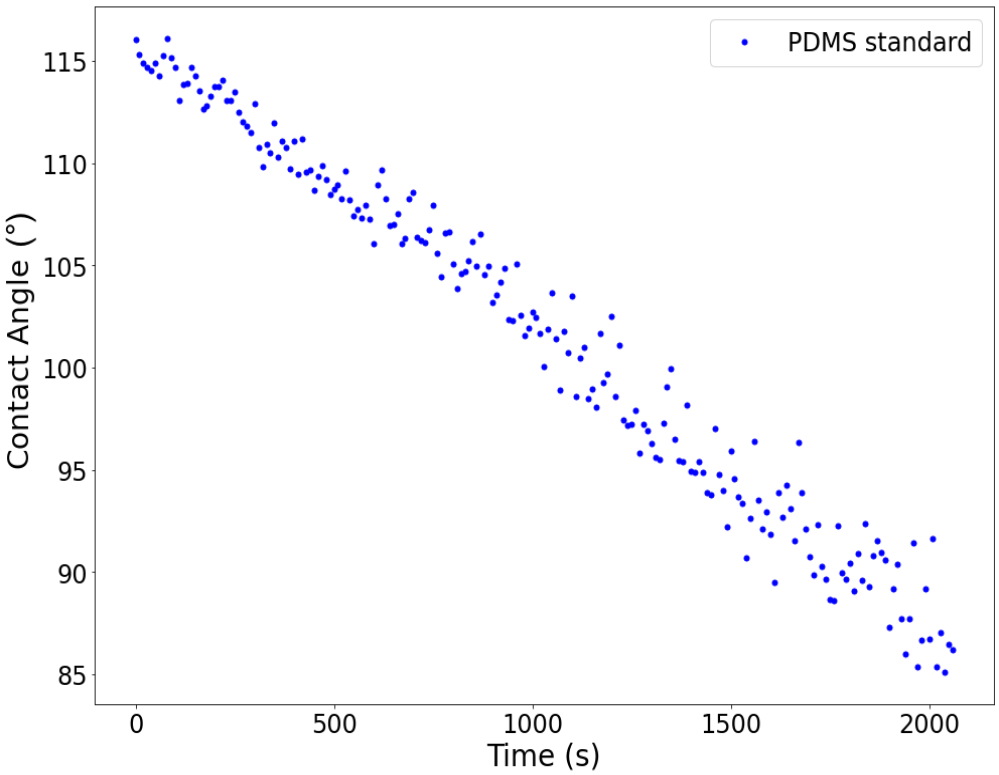

Figure 6.8: Contact Angle change over 30 minutes for a water droplet on an amphiphile free PDMS.

To help account for this the contact angle drop was identified using a numpy based piecewise fitting function to identify inflection points in the change of contact angle over time as exemplified by figure 6.9 which shows how the piecewise function identifies the wetting shift as caused by the diffusion of the amphiphile DBE-712r through PDMS.

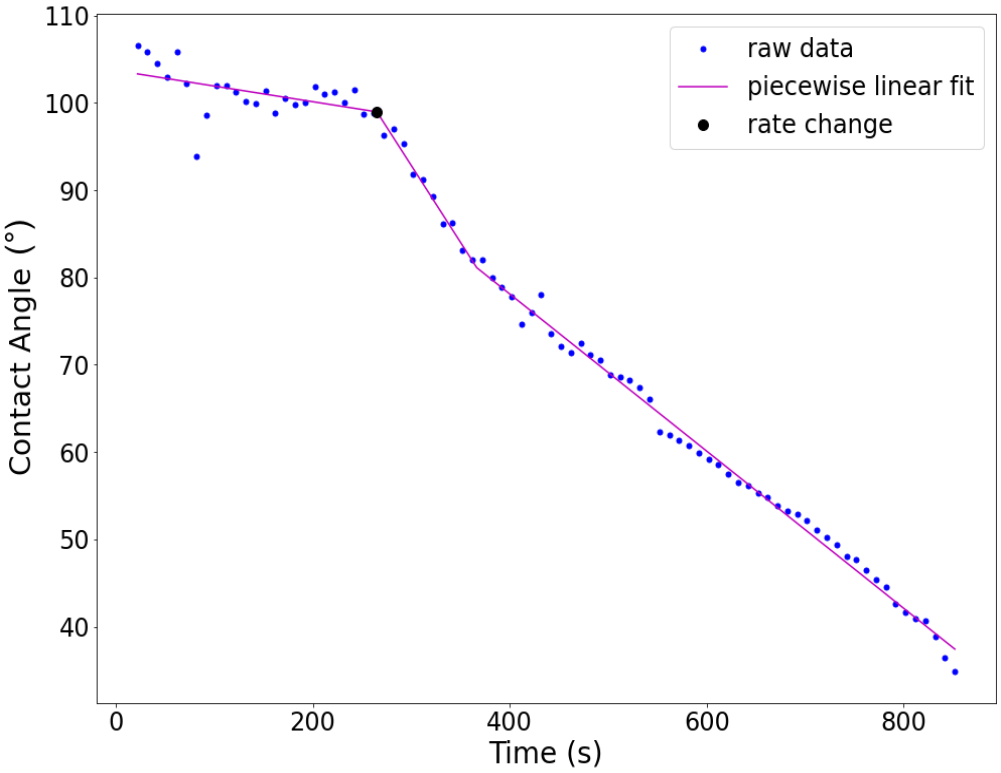

Figure 6.9: Contact Angle and piecewise fitting for a 105.3μm thick membrane with the Penetrant DBE 712r, time lag inflection point found from a 3 point function at 265s.

Once a data series of time lags for various membrane thicknesses had been acquired, linear fits and diffusion coefficients were found using the Python package scipy orthogonal distance regression function to account for uncertainties both in the thickness and time lag property of each measurement.

6.3.2.2 Methods: diffusion of PFPE-PEO in PDMS using bulk PFPE-PEO and PFPE-PEO containing silicone coating

Following tests using branched PDMS-PEG amphiphiles, measurements were made to find D for a PFPE-PEO amphiphile (Fluorolink E10/6, Solvay) in PDMS silicone. Two methods were employed; one similar to the DBE tests using a thin liquid layer of PFPE-PEO as a reservoir, these were formed by spin coating a layer of PFPE-PEO from solution at a concentration of 20% in methanol at 1500 rpm onto PMMA coated silicon wafer. This yielded a stable thin film determined to

be 1.5-1.7μm thick from ellipsometry, coatings were placed on top of this reservoir and the contact angle of water droplets observed.

A second set of measurements were also made in which pieces of a PFPE-PEO containing silicone based foul release coating (PFPE-PEO FR) were used as the reservoir for diffusion. The coating was formed by mixing of HT-PDMS with Fluorolink E10/6 and curing the PDMS with TES 40 crosslinker. PFPE-PEO FR coating was supplied by Akzo Nobel as a 300μm thick film. This PDMS based foul release coating incorporates PFPE-PEO as a key surface active additive and should be able to act as a reservoir of this amphiphile for PDMS membranes. To use this coating as a reservoir of PFPE-PEO, PDMS membranes of known thickness were brought into contact with the coating immediately before monitoring time dependent water contact angles. This method is similar to the Noguer paper technique [235] in which diffusion reservoirs were formed by making cured coatings containing 4% of a desired additive and placing a free PDMS membrane into contact with this film.

Initially the contact angle for PFPE-PEO FR was found on both the top surface and the under surface (the surface in contact with glass during film cure) the PDMS based foul release coating which incorporates PFPE-PEO as a key surface active additive and should be instructive as to the expected response of an PFPE-PEO containing film to water.

6.3.3 Contact angle diffusion results

For DBE-411 time lags were determined for a range of thicknesses from 90 to 360μm, transitions were observed at time intervals that were demonstrably thickness dependent. In order to verify this contact angle shift does represent the diffusion of the amphiphile DBE-411 we repeated tests after the initial diffusion and observed the wetting behaviour t>> T_{lag}

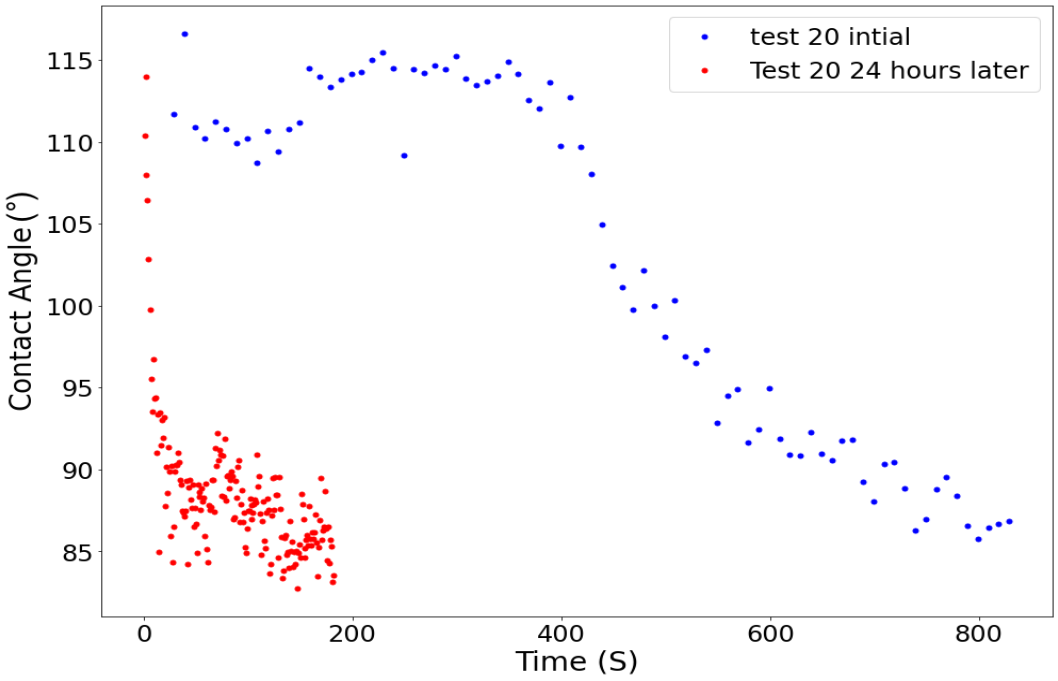

Figure 6.10: Time dependent contact angle for test 20 a 209μm thick membrane immediately after exposure to DBE-411 penetrant and again 24 hours later.

In figure 6.10, the initial diffusive time lag from the contact angle shift was fit to 399s but the following day a wetting shift occurs almost immediately upon adding a droplet to the surface. From the series of thickness dependent time lags the relationship between diffusion and membrane thickness was determined as shown in figure 6.11.

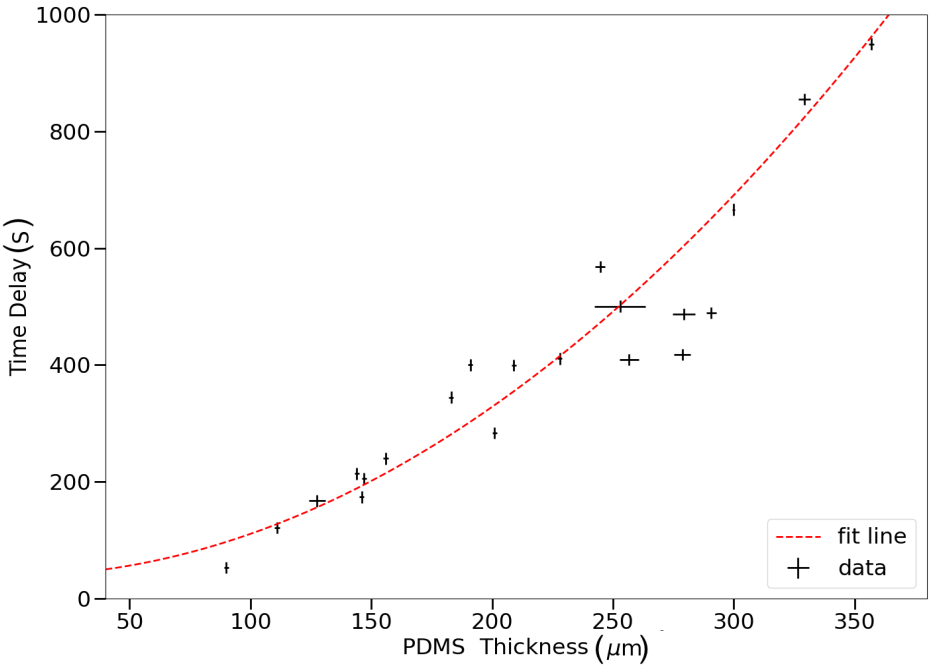

(a) Measured diffusive time lag against membrane thickness with fit line=mx^2+c

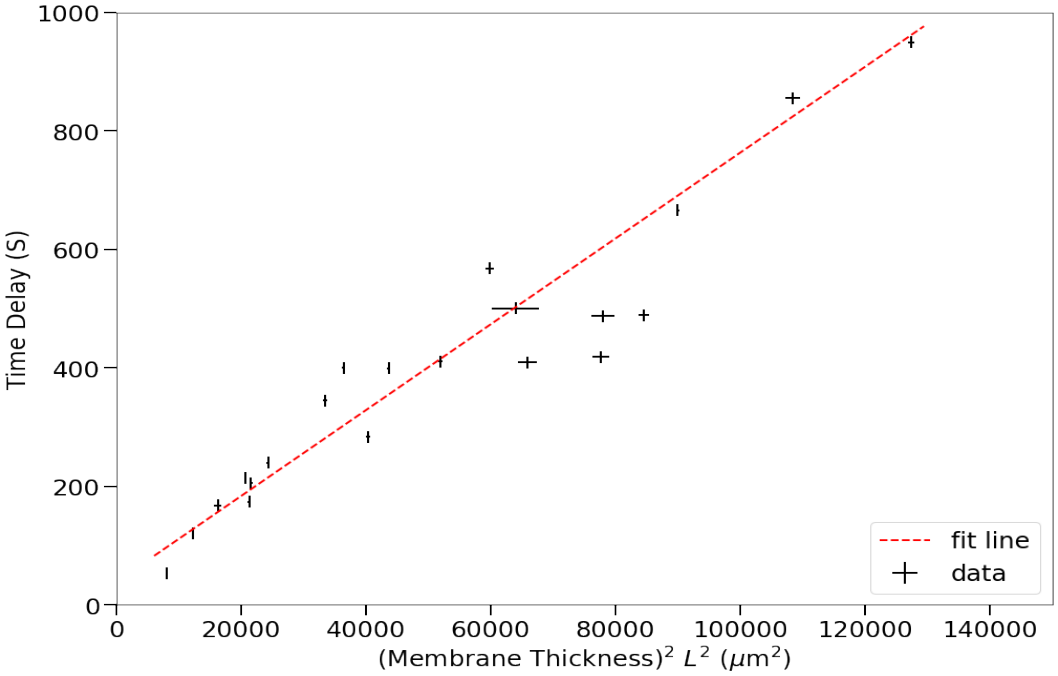

(b) Measured diffusive time lag against the square of membrane thickness with linear fit line

Figure 6.11: Experimental time lag measurements for DBE-411 in cured PDMS membranes.

The fit line in figure 6.11b was found to have a y intercept ∂dT of 38.3±27s and a gradient m=0.00725±0.000446 from which a diffusion coefficient for DBE 411 through silicone was determined using equation6.19 to be D=$7.46\pm1.41\times10^{-12}m^2s^{-1}$. As seen in figure 6.12, it was similarly possible to obtain time lag measurements at varying membrane thicknesses for the diffusion of DBE-712r in PDMS. From which it was possible to derive the diffusion coefficient.

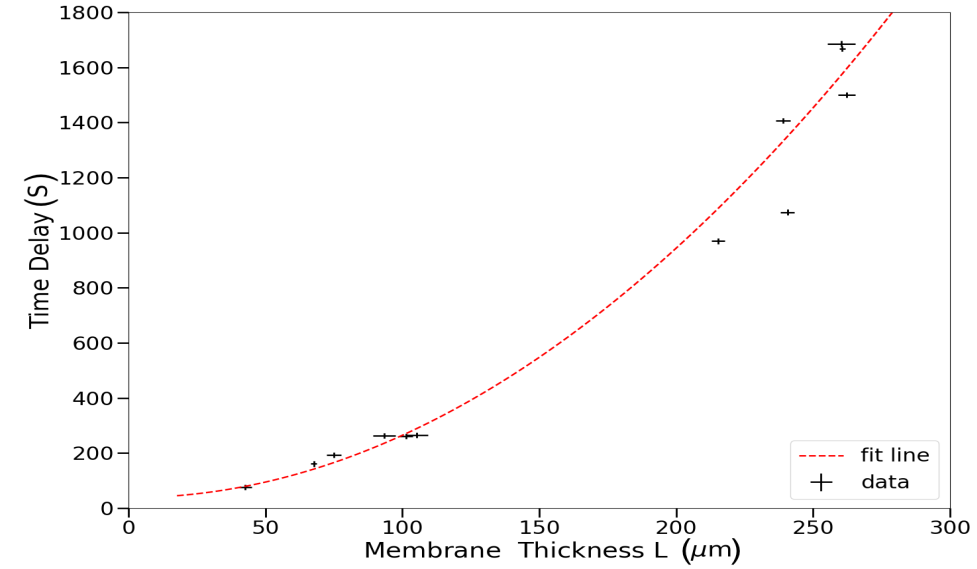

(a) Measured diffusive time lag against membrane thickness with fit line=mx^2+c

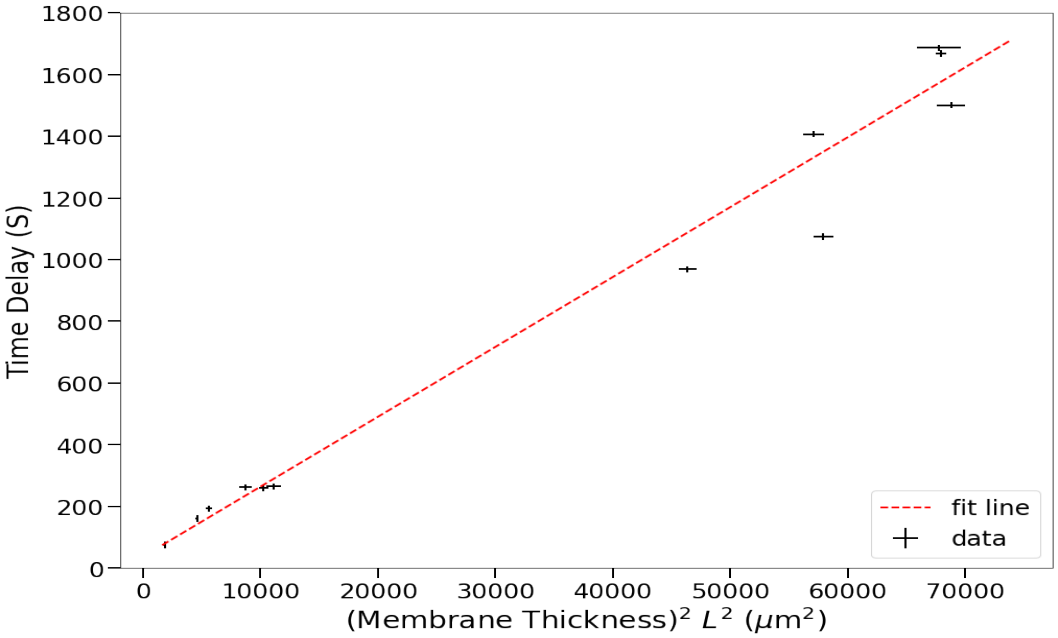

(b) Measured diffusive time lag against the square of membrane thickness with linear fit line

Figure 6.12: Experimental time lag measurements for DBE-712r in cured PDMS membranes.

The linear fit line found in figure 6.12b indicates that the diffusion coefficient for DBE-712r through PDMS silicone is D=7.36±0.31×$10^{-12}m^2s^{-1}$ with a y intercept ∂T of 38.1±29.9s.

Having determined a value of the diffusion coefficients and having identified the 1-D time frames for diffusion for DBE-712r, FT-IR based diffusion measurements were attempted by exposing a 240μm membrane to DBE-712r for 5 days before measuring the IR spectra to determine the concentration of the penetrant can be resolved. For this thickness the time lag for 1-D diffusion would be 1300s after which there would be a non zero concentration throughout the whole film. After 5 days (4.32×10^5s) we expect penetrant to achieve equilibrium at or near saturation concentration in the membrane.

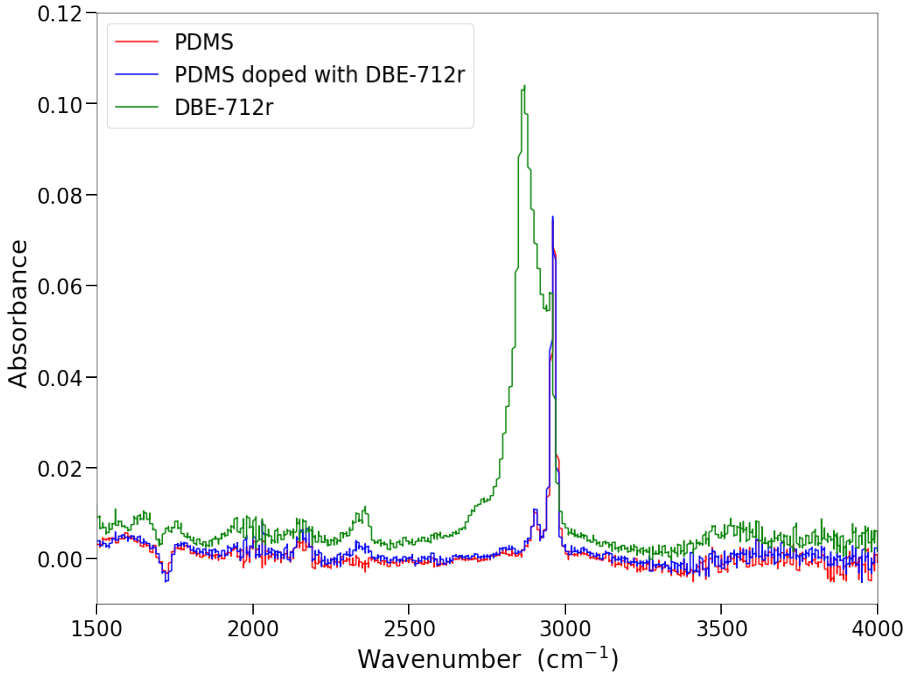

Figure 6.13: Comparison of IR absorbance spectra from liquid DBE-712r, cured PDMS and a 5 day exposed PDMS DBE712 240μm film.

Surprisingly, figure 6.13 shows that despite the presence of distinct absorbance spectra between DBE-712r and PDMS due to an independent peak at 2870cm^{-1} for DBE-712r, there was no corresponding absorbance perturbation in the IR spectra for the PDMS coating exposed to penetrant. The lack of a clear, resolvable difference between the penetrant free PDMS spectra and the sample subject to

diffusion demonstrates the limitations of ATR diffusion method for our samples. Given the diffusion timeframes, we know there must be some non zero concentration of DBE-712r throughout the coating and yet this concentration is undetectable from it's IR absorbance spectra, we conclude that the concentrations involved in this diffusion are not high enough to be detected using the instrument employed. In contrast, the contact angle time lag method applied in this chapter, despite being wholly unable to quantify penetrant concentrations, is able detect the diffusion of amphiphile penetrants even at concentrations too low for our FT-IR ATR.

For PFPE-PEO diffusion in PDMS we first present the contact angle behaviour of PFPE-PEO containing silicone based foul release costing (referred to as PFPE-PEO FR coating).

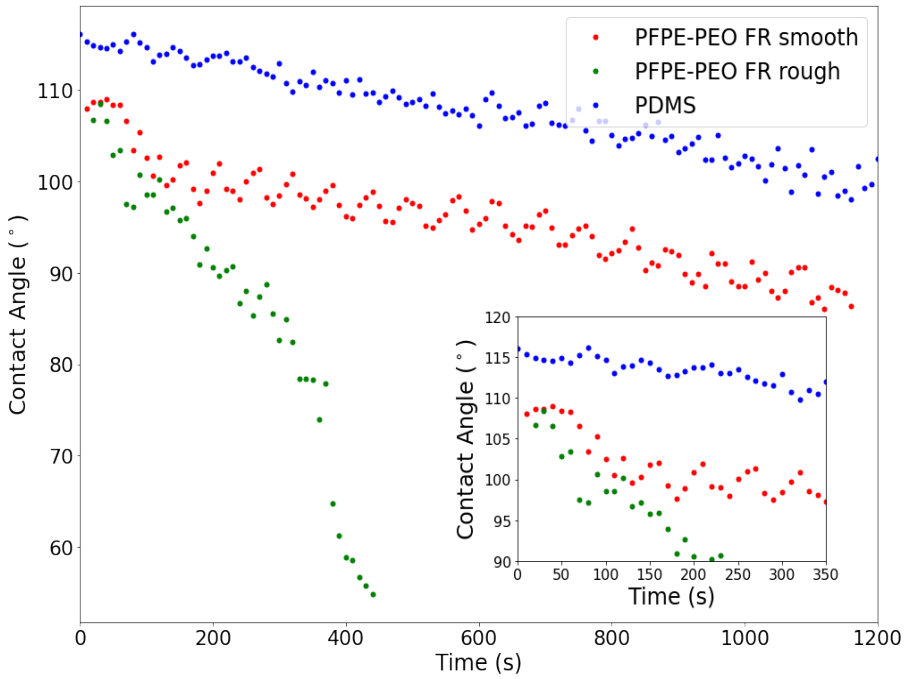

Figure 6.14: Comparison of contact angle response of a droplet on a coating of PFPE-PEO FR on both rough top surface and smooth bottom surface, PDMS control included for reference.

We see from figure 6.14 that there is a considerably greater and more sudden wetting shift on the top surface of the coating than the smooth underside we attribute this to a greater concentration of PFPE-PEO on the top surface in the form of bulk surface droplets of PFPE-PEO which are absent from the smooth

undersurface. Despite a lower overall surface concentration of PFPE-PEO on the smooth surface there is still a wetting shift of 10 degrees in the first 120 s of wetting suggesting some amphiphile is present in the coating. This wetting transition is nevertheless smaller than seen with either DBE-411 or DBE-712r.

It is not possible to infer directly the surface energy or the interfacial tension of the surface during this water induced functionalisation. However, the work of adhesion of the water droplet can be determined; initial contact angles for both the smooth and rough PFPE-PEO FR coating begins were 108° with a W_{SL}=50.3mJm^{-2}. The initial shoulder in contact angle seen around 50-150s sees the droplet spread and the work of adhesion for the rough upper side increases to 65.5mJm^{-2}. After the same time frame the smooth side of the coating sees the work of adhesion increase to 58.0mJm^{-2}. For the rough upper side of the PFPE-PEO FR coating there is a second wetting shift in the contact angle around 350s at which point the work of adhesion rises from 87.6 to 114.7mJm^{-2}.

Looking at figure 6.14 there appear to be oscillations in the contact angles measured for PFPE-PEO FR coating smooth side and PDMS. It is not immediately clear why this would be observed. However, given that for PDMS the primary driver for the fall in contact angle is evaporation of the water droplet, this long term oscillation may be due to pinning effects at the solid liquid contact line. Over time these droplets lose volume and reduce their contact area with the surface, if this process is discrete rather than continuous due to pinning of the water contact boundary we may see small oscillations in the contact angle due pinning and un-pinning of this boundary. However, similar effects are absent in for the time dependent PDMS contact angle for the PDMS in figure 6.8. Another explanation could be that these small oscillations are caused by vibrations from the environment causing oscillations in otherwise static water droplets, this would explain the inconsistency between samples as such vibrations may not be present from experiment to experiment. Without isolating the contact angle system from the environment and preventing vibrations and evaporation from effecting water droplets it is difficult to comment further on these oscillations.

PDMS membrane diffusion tests using PFPE-PEO FR coating as a penetrant reservoir were performed for a range of thicknesses, to account for the comparatively slight wetting shift successive droplets were placed on the coating surface over time to mitigate the long term effect of evaporation and pinning effects causing the contact angle of a single static droplet to fall over time [244]. A typical contact angle measurement is shown for a membrane 150.3μm.

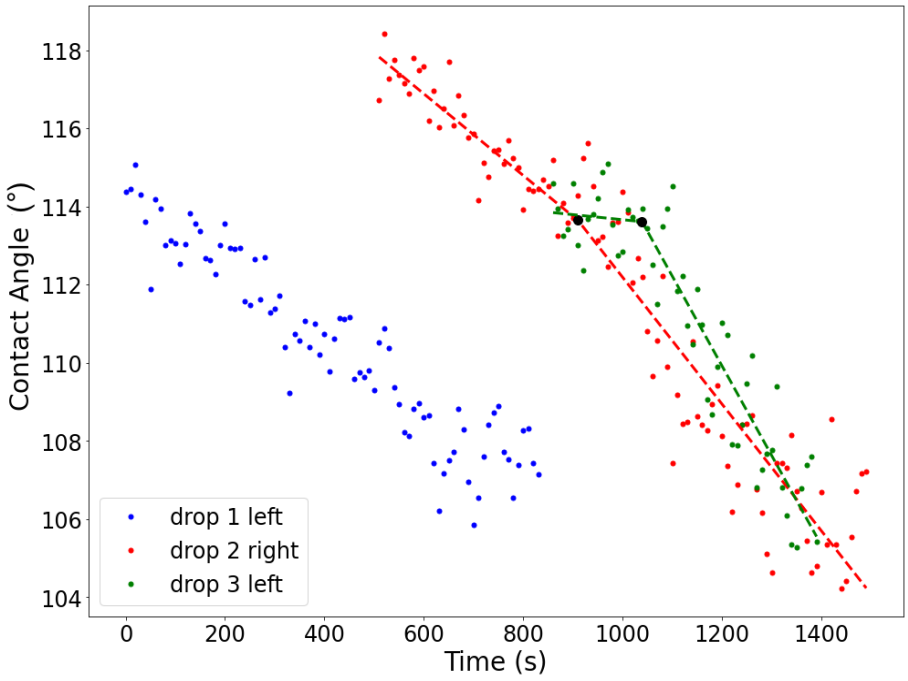

Figure 6.15: Time dependent contact angle measurements for 3 droplets on a 150.3μm thick PDMS membrane subject to the diffusion of PFPE-PEO from a PFPE-PEO FR coating.

From figure 6.15 the first wetting shift is seen from the second droplet at 960s, we also see a similar wetting transition in the third droplet that is slightly later but at a much earlier stage in the droplet's lifetime. This is consistent with the expectation that a penetrant has diffused through the membrane and after t=960s post the time lag it is now present through the entire film and can now much more rapidly functionalise the solid liquid interface.The initial droplet does not show this wetting shift indicating no surface functionalisation.

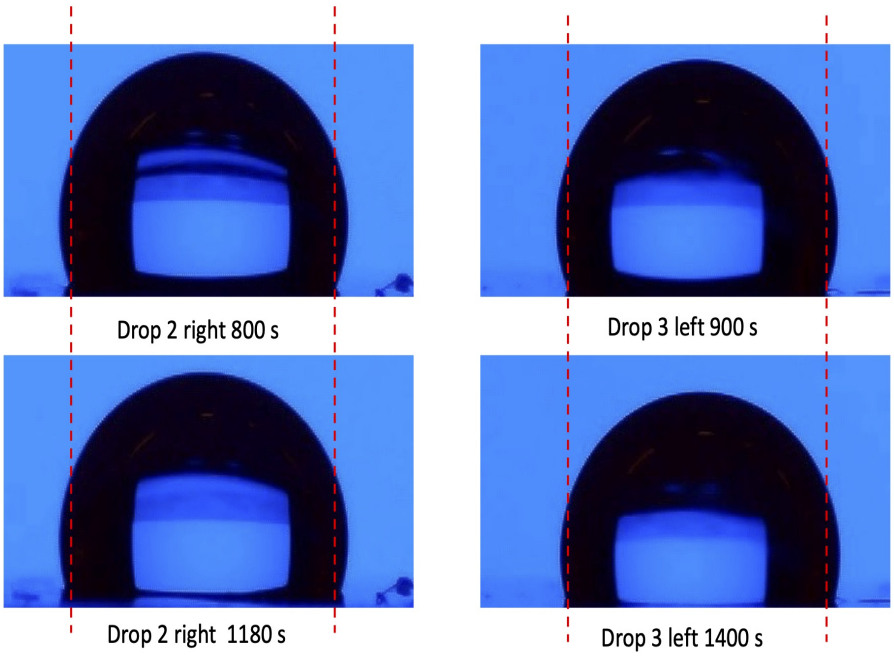

Figure 6.16: Selected frames from the video recorded of the experiment in figure 6.15 for droplet 2 and droplet 3 pre and post wetting transition demonstrating the spreading of water droplets on the silicone surface (all images cropped to the same pixel size 200x400).

Figure 6.16 shows frames from the recorded video of droplets on the surface of 150.3μm thick PDMS membrane. Upon inspection, it is clear that droplets do spread and increase their surface coverage on PDMS during this contact angle shift and this fall in contact angle is not the result of pinning and evaporation effects. Using imageJ analysis the length of the sideview droplet contact diameter with the surface was assessed; for droplet 2 this was 262 pixels long at 800s and 271 pixels long at 1180s, for droplet 3 at 90s the contact length was 253.6 pixels and post transition at 1400s it had grown to 265 pixels long. Although small this shift does indicate a real spreading and a reduction in interfacial tension due to the surface segregation of some low concentration of amphiphile. When a given membrane was left in contact with an PFPE-PEO FR coating as a reservoir, these wetting shifts continued to developed over time.

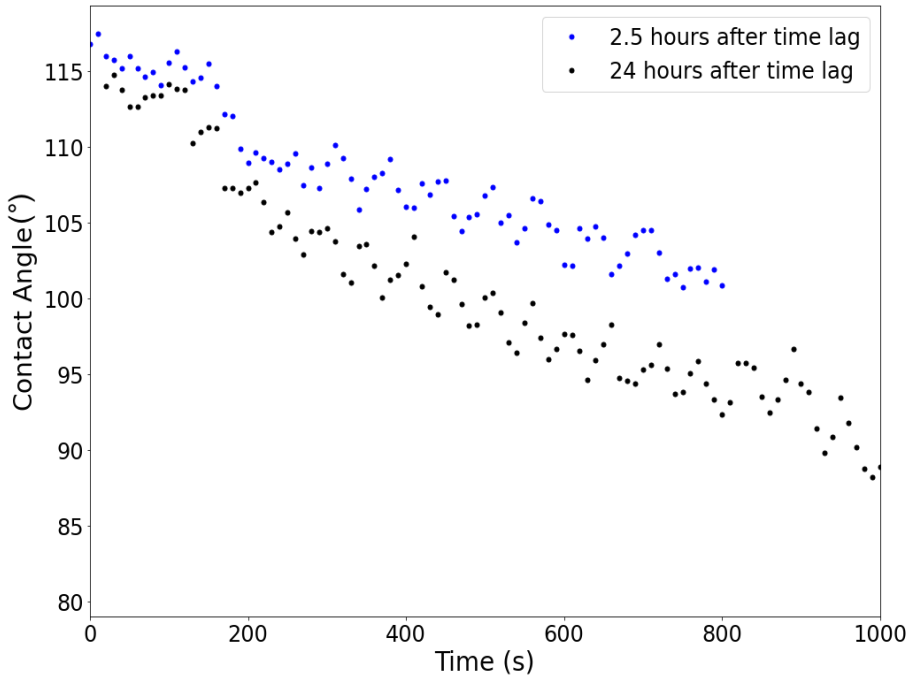

Figure 6.17: Static contact angles for a 310.3μm membrane exposed to PFPE-PEO FR coating 2.5 hours after the detected time lag and again 1 day later (time lag was measured to be 67 minutes).

For the 310.3μm membrane shown in figure 6.17, the hydrophilic wetting shift of water contact angles on this diffusive membrane had become greater 24 hours after the initial, with the interfacial tension falling faster seen after the initial time lag for diffusion. In both cases we see an initial shoulder in the wetting shift around 150s. For the 2.5 hour post time lag test the contact angle changes from an initial angle of 115.5° and a work of adhesion of 41.5mJm^{-2} at 150s to an angle of 108.9° and a work of adhesion of 49.2mJm^{-2} by 200s. The measurement taken 24 hours later shows a change from a CA=113.7° and W$_{SL}$=43.4mJm^{-2} at120s to a Ca=107.3° and W$_{SL}$=51.2mJm^{-2} at 170s. Indicating that in a relatively short period of time there is a significant increase in the adhesion of the water droplet to the surface. At 800s the measurement after 2.5 hours shows the work of adhesion has increased to 59.1mJm^{-2}, whereas the measurement after 24 hours shows the work of adhesion increasing to 69.8mJm^{-2} after 800s hence this increased wetting is indicative of an increased bonding between the surface and the water droplet, likely caused by an increased concentration of PFPE-PEO amphiphiles at the interface. Just as with DBE-411 and DBE-712r the series of obtained time lags for

PDMS membranes with PFPE-PEO (from the PFPE-PEO FR coating) followed a linear relationship $T_{lag} \sim L^2$

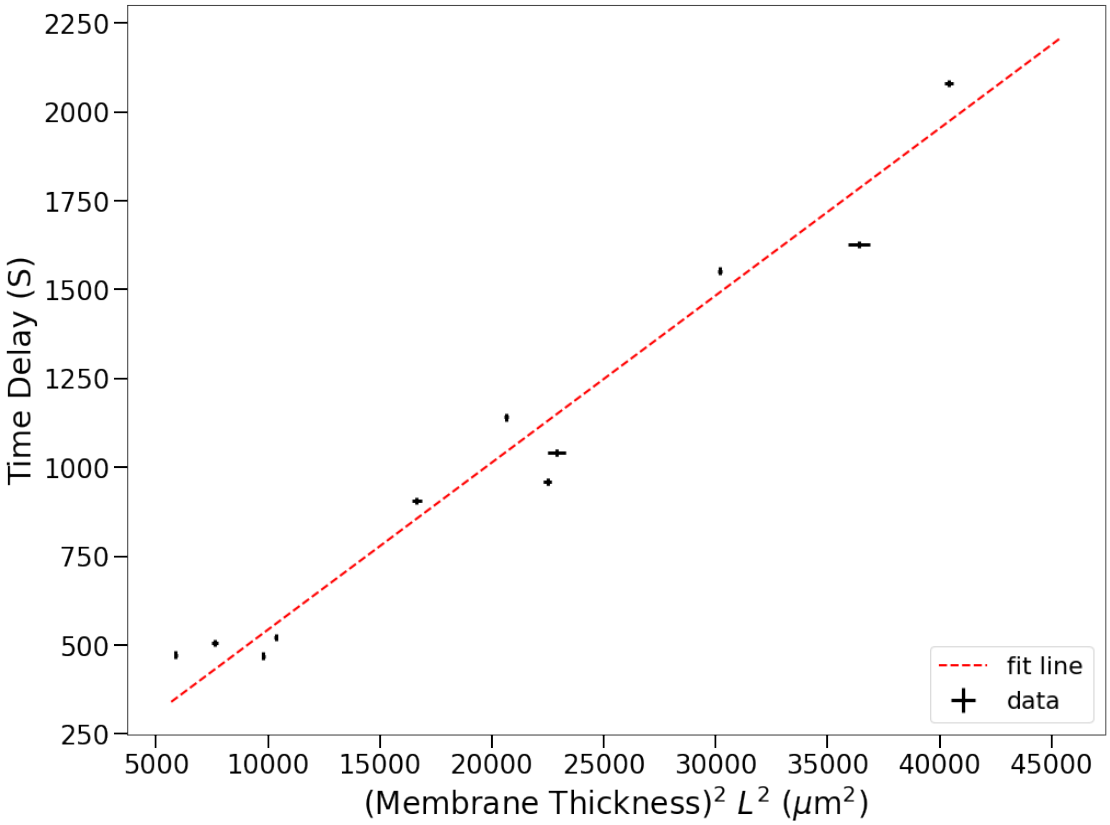

Figure 6.18: Diffusive time lag T_{lag} against the square thickness L^2 of PDMS membranes exposed to PFPE-PEO FR as a reservoir for PFPE-PEO.

From the fit in found in figure 6.18 a value for the diffusion coefficient of PFPE-PEO through PDMS silicone was found to be D=3.55±0.24 $\times 10^{-12} m^2 s^{-1}$ and $\partial T = 73.2 \pm 64.6 s$

6.3.3.1 Discussion of time lag diffusion results

Considering the initial test amphiphiles DBE-411 and 712 demonstrates the validity of the time lag contact angle method; previous literature has already demonstrated that these molecules are compatible with PDMS silicone , will surface segregate at the silicone/water interface and will diffuse through PDMS membranes.

The contact angle method utilised here is able to convincingly determine the diffusion coefficient for these molecules figures 6.11 and 6.12 show that the diffusion times determined from wetting transitions do follow the expected relationship of increasing linearly with the square thickness of the length of the membrane i.e if 2L$\rightarrow 4T_{lag}$. We therefore do believe that this is a successful and valid method for determining the diffusion coefficient for these surface active molecules. The values found for DBE-411 and DBE-712r are consistent with the general range of diffusion coefficients of small molecule penetrants in silicone found by Noguer [235] which were in the order of $10^{-11} - 10^{-12} m^2 s^{-1}$ similarly alternative, conventional methods have found smaller molecules like hexadecanethiol have diffusion coefficients D=$5.6 \times 10^{-12} m^2 s^{-1}$ [245] and larger uncured chains of PDMS diffusing though a cured membrane have been determined within the literature to be D=$1 \times 10^{-12} m^2 s^{-1}$ for $M_w = 11500$[246]. Comparing DBE-411 and DBE-712r we can also see that DBE-411 has a diffusion coefficient roughly twice as large as DBE-712r and therefore has a faster diffusion rate in PDMS silicone. Again this is as expected; given that DBE-712r has a higher molecular weight and viscosity we would initially predict that the diffusion of this version of the branched PDMS-PEG would be slower following an established relation that $D = k_w \ M_w^a$ [247] . However, the constant α for silicone networks has previous been determined to be -1< α <-1.3[248] so the increase in molecular weight of 33% alone cannot account for this decrease in the coefficient. The change in PEG:PDMS ratio likely also reduced the diffusion rate of DBE-712r in silicone as the content of PEG is now higher at 70% the higher PDMS content DBE-411 may have a smaller interaction parameter with silicone owing to it's more silicone like molecular structure which may aid diffusion compared to the more lipophobic PEG heavy DBE712. Although the overall lipophilic to hydrophilic ratio of these molecules must play some role in the diffusion rate previous experiments did not find a clear relationship between the stoichiometry of various block copolymer amphiphiles and the diffusion coefficient, although as yet unproven, it remains a reasonable inference that within a single class of amphiphiles there would be a relationship between diffusion and lipophilic hydrophilic block ratio. For a partially PDMS branched polymer diffusing in a PDMS network miscibility and diffusivity should increase with increasing PDMS ratio in the polymer.

It should be noted that the water droplets used to measure the diffusive time lag do not themselves induce the diffusion which would occur undetected without a sessile droplet on the surface, we can see in figure 6.10 that at time long after diffusion the wetting transition occurs rapidly despite there not being a constant solid liquid interface at the top surface of the membrane throughout the diffusion time. This solid liquid interface does however induce the surface functionalisation which causes the observed wetting shift and more hydrophilic interfacial tension after

the diffusive time lag for the amphiphile. In the original Daynes case the model assumes that the concentration just outside the membrane is kept at zero as the gas enters into the volume outside the membrane but in this case the amphiphile is liquid and cannot do that, instead when a molecule of the amphiphile reaches the solid liquid interface of the droplet it surface segregates with the PEG section solvating and covering the interface reducing the interfacial tension, because this is energetically favourable these molecules are no longer moving randomly through the coating diffusively but are instead fixed in place. As more and more of these molecules reach and functionalise the interface eventually the concentration of amphiphile at the solid liquid interface C_{SL} is sufficiently high that γ_{SL} falls enough for the droplet to spread further and the contact angle to reduce. So in the case of our method we should consider that at the observed time delay $C_{bulk} < C_{SL}$ and there is a critical interfacial concentration needed for the wetting shift to occur. This may be one source of non Fickian time lag ∂T although fitted to a significant uncertainty all measured ∂T were positive and as such, physical. Surface segregation is itself a time dependent process so would add some minimum time delay to any measurement using this method. Gauging the true concentrations of the diffusant in the samples after diffusion are not possible using this method and as shown in figure 6.13 without very distinct absorbance bands it is very difficult to use alternative methods to determine this value.

It should be considered that these amphiphilic molecules have bulk behaviour in solution and may be able to form together into self assembled stable structures within the membrane called micelles, it has previously been suggested this hinders the diffusion of amphiphiles through media [246] and we should therefore treat the diffusion here as governed by the transit of unimers of the amphiphile.

For PFPE-PEO the result was somewhat surprising, based initially on expectations of a very hydrophilic response to water as demonstrated by the top surface of the PFPE-PEO FR coating (figure 6.14) the much smaller contact angle shift observed in tests such as figure 6.15 were not initially identified as evidence of the diffusive time lag. As such, little reliable data was obtained from liquid PFPE-PEO based samples, these tests were performed first and without a clear expectations of the likely wetting shift, most of these measurements were not recorded for long enough to find the time lag. Only with the PFPE-PEO FR based tests was the diffusive time lag consistently identified first using the thinnest membrane, which yielded the necessary timescale for these measurements. As will be reported in the next section, bulk PFPE-PEO reservoir diffusion samples that were preserved for extended time frames did eventually show evidence of more dramatic surface wetting (days to weeks after the fact) but again from early tests it was unclear this was the result of diffusion or surface contamination from repeated sample han-

dling. Examining again the contact angle response of the underside of PFPE-PEO shown in figure 6.14 we conclude that the underside does show some surface segregation in response to water with a rapid but small initial wetting shift of around 10 degrees, as the underside lacks bulk droplets of PFPE-PEO on the silicone surface the initial surface concentration is in effect much lower. This smaller wetting shift is totally absent from the response of control PDMS to water droplets, so it is reasonable to infer that this is the result of the presence of a surface active molecule.

The PFPE-PEO FR tests were more successful, having been performed after initial XPS studies discussed in the following section which established clearly evidence of PFPE-PEO diffusion in silicone. The determined Diffusion coefficient of D=$3.55\pm0.24\times10^{-12}m^2s^{-1}$ is considerably slower than the DBE class amphiphiles. This may in part be due to the comparatively higher molecular mass but may also be due to overall miscibility and other factors. The smaller contact angle shifts seen in figures 6.14 and 6.18 have implications for the overall concentrations of PFPE-PEO in silicone; if the bulk concentration is quite small then there will be less PFPE-PEO available at the surface to functionalise the interface and reduce the contact angle so this process will be much slower. In principle we would expect that if this experiment could be performed in a controlled atmosphere of saturated water vapour to inhibit droplet evaporation, the water contact angles for PFPE-PEO FR and post time-lag diffusion samples would eventually fall to the levels seen for the top side of PFPE-PEO FR (and from the PFPE-PEO/ PDMS bilayer model systems discussed in chapter 4) as eventually the interfacial concentration of PFPE-PEO would become comparable. This effect is inhibited here due to droplet evaporation over time and pinning effects at the 3 phase contact line[244].

Before conclusions should be drawn from this determined diffusion coefficient the validity of the result must be further considered. The advantages of using a PFPE-PEO FR coating as a bulk reservoir for these tests are twofold; first as the basis of an industrially used coating a diffusion coefficient found using this system can confidently be applied to the coating itself. Further, when compared to the diffusion tests using thin film reservoirs of PFPE-PEO, the PFPE-PEO FR coating represents a substantially larger overall reservoir of PFPE-PEO; on average thin layers of PFPE-PEO were deposited at a thickness of 1.5-1.7μm, when used as a reservoir for a PDMS membrane of thickness 200μm the maximum possible concentration of PFPE-PEO in the membrane if the entire reservoir was absorbed would only be 0.85% by volume if fully equilibrated. This is a very low concentration and depending on the diffusive timeframes and the maximum concentration of PFPE-PEO of PDMS it may be the case that the entire reservoir would be depleted before the diffusive time lag has occurred. Given that the 1-D

time lag as outlined by Daynes requires that C_L the time lag method break down if this boundary condition cannot be sustained with such small reservoirs.

Conversely, as an industrial coating rather than a purpose made coating the composition is less controlled; PFPE-PEO is the additive intended to be surface active within this coating and most likely be the cause of the measured time lag but this wetting shift cannot be specifically attributed to this PFPE-PEO amphiphile without further analysis, as impurities or additional additives in the coating (e.g. catalyst) could also be having a diffusive effect and resulting in this wetting shift. For the determined diffusion coefficient, the time lags observed proved to be quite long; ranging from 8 to 35 minutes. As discussed in the results the evaporation of the sessile droplets was significant over this timeframe so the time lag could not be observed from a single, initial droplet. The necessity of using multiple droplets reduced the accuracy of these measurements, as any successful measurement required the droplet to be replenished in good time to detect the time lag. This could have been mitigated with a larger series of membranes of thinner but more strictly defined thicknesses around 70-130μm where the time-lags would be shorter but such controlled thicknesses were not possible with the k-bars available. This could also have been prevented if the measurement could be conducted within a water vapour saturated environment so as to prevent droplet mass loss.The time lags measured here were difficult to measure accurately with the current method due to the necessary repeated measurements, though the error in this case would be to overestimate the diffusion time lag (if the droplet is replenished only after the time lag has already taken place).

In order to validate that the diffusive behaviour of PFPE-PEO in PDMS and the diffusion coefficient measured here, additional experiments were undertaken using XPS.

6.4 Observations of PFPE-PEO diffusion using ion milling X-ray photo-electric spectroscopy

X-ray Photoelectron Spectroscopy is not typically used to determine diffusion coefficients for polymers. This is partly because the technique requires ultra high vacuum conditions, this causes a significant sample setup timeframe during which diffusion cannot be monitored. When considering the diffusion of organic penetrants in organic materials, XPS is of limited value as there is no distinction in the elemental species of either the membrane or penetrant molecule so the penetrant cannot be easily identified by the presence of a particular element. For

example, the DBE class of molecules would be very hard to identify in PDMS silicone as they each contain silicon, carbon and oxygen. Any attempt to distinguish them would require very close examination of the slight difference in oxygen energy levels due to the oxygen the PEG block of DBE molecules; with the Si-O bond having a binding energy of 284.2eV and C-O bonds associated with PEG having a binding energy corresponding to 286.3eV[249] but as both PDMS and DBE411,712r contain Si-O bonds, distinguishing them from the O1s spectra will be challenging.

In the case of PFPE-PEO and PDMS however, the matrix and penetrant can be identified clearly by the distinct photoelectrons F1s and Si 2p respectively. This allows us to determine the diffusion of PFPE-PEO into PDMS and, via ion milling, some measure of the depth profile assessing potential surface enrichment.

6.4.1 Methods and control experiments

All XPS measurements were facilitated by Dr Hammond at the University of Sheffield's Surface Science Analysis Centre (SSAC) using the Kratos Axis Supra X-ray photoelectron spectrometer using an Argon gas cluster Ar^{+}_{1000} for ion milling to etch samples and perform depth measurements. All cans were performed at high resolution with energy intervals of 0.1eV, 40e pass energy at 60s/sweep. The spectra was collected for the relevant elements C 1s O 1s Si 2p and F1s.
Prior to full measurements the etch rate for PDMS silicone was first determined using a calibration sample of thin film PDMS 240nm thick spin coated on a silicon wafer (HT-PDMS $\approx$ 2% in hexane with TES 40 crosslinker 10%w/w$_{HT-PDMS}$ and ATPDMS catalyst 1% w/w$_{HT-PDMS}$). For this sample figure 6.19 an etch series of varying energy and etch time were performed through the entire depth of the sample to determine the time taken to etch the full thickness with each mode, summarised in table 6.1.

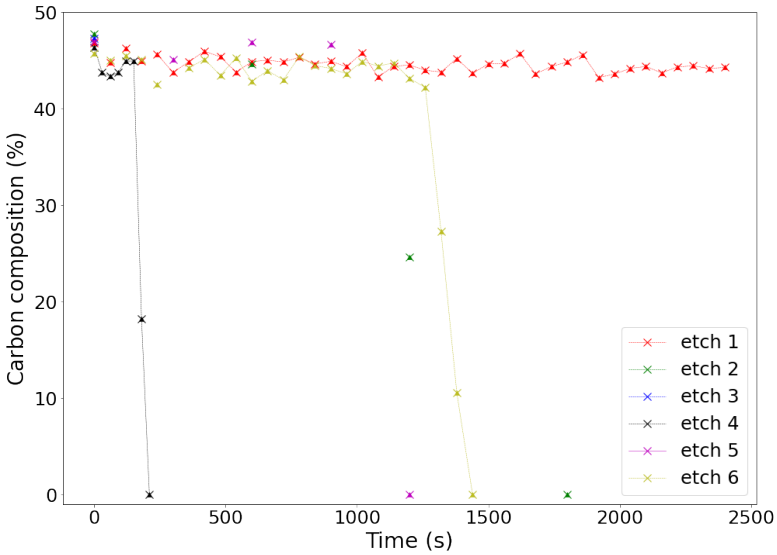

Figure 6.19: Determined % carbon atomic composition for 240nm PDMS film on silicon at various etch rates.

Table 6.1: Etch scan conditions for PDMS calibration sample.

Etch	Etch Energy (keV)	Crater Diameter (mm)	Time per Etch (s)
1	10	3	60
2	10	2	600
3	20	1.5	240
4	20	1.5	30
5	10	1.5	300
6	10	1.5	60

By monitoring the strength of the carbon signal and inferring relative sample composition it is possible to infer the etch rate through the full thickness of the PDMS, as once the ion beam has etched totally though the polymer film and into the silicon/oxide substrate the carbon composition of the XPS spectra will fall to zero. In the case of etch scan 6 the fall in carbon composition is observed after 1320s of etching implying an etch rate of 0.18nm/s and 10-11nm between each 60s etch. For small etches of 10s of nanometers this etch condition was chosen: 10 keV across a 1.5mm diameter. For larger etches a longer etch interval was taken of 600s (ten minutes) using the same etch size and energy.

6.4.1.1 CYTOP PDMS bilayer control for diffusive fluorine fragments

The first sample tested using this etch rate was a thin bilayer sample of PDMS and CYTOP on silicon wafer. The amorphous fluoropolymer CYTOP is a highly fluorinated polymer of interest to the electronics industry as an insulator with a glass temperature of $T_g = 108^o$ [250] it is solid at room temperature, the structure is shown in figure 6.20. CYTOP was sourced from AGC and prepared in CT-SOLV180 according to a reported protocol [251] when spin coated at 1500rpm this solution formed a layer of CYTOP 6nm thick on silicon as verified by ellipsometry.

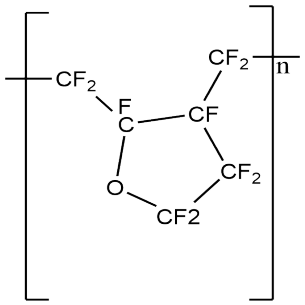

Figure 6.20: Chemical structure for CYTOP amorphous fluoropolymer.

A thin film of PDMS was spin coated and cured onto a thin layer of polystyrene sulfonate (PSS) on glass. The PSS acts as a sacrificial layer allowing the PDMS to be floated onto water and then onto the CYTOP layer forming a bilayer of CYTOP and PDMS on silicon wafer as illustrated in figure 6.21. Ellipsometry verified the thickness of the floated PDMS layer as 220nm. An etch was performed through the full thickness of this sample. As a non diffusive sample this sample acts as a measure of the effect of ion milling on the specificity of polymer layers. Ion milling can induce fluorinated fragments to form free radicals not dissimilar to those seen in TOF-SIMS diffusion of these fragments could cause fluorine photoelectrons beyond the true thickness of the CYTOP layer which we would have to account for in our analysis of the concentration profile of PFPE-PEO in PDMS.

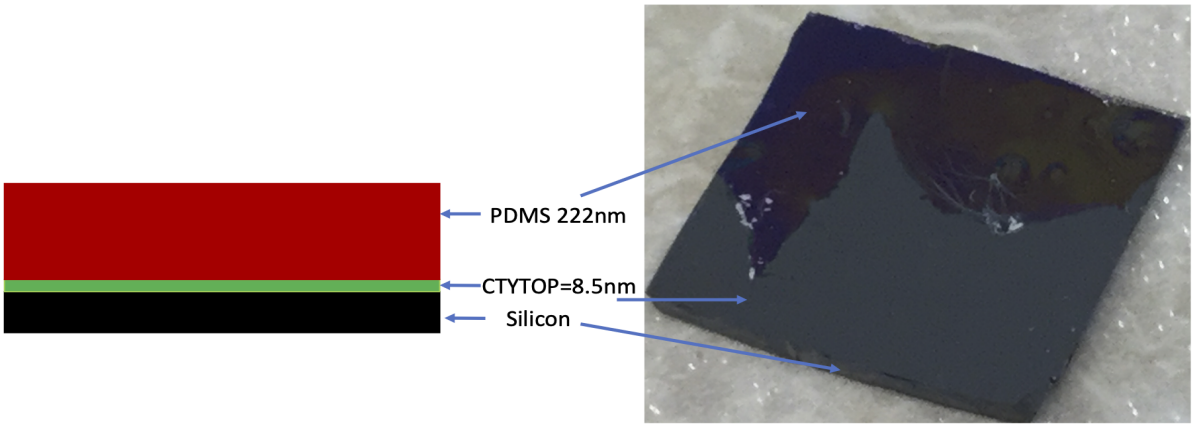

Figure 6.21: Schematic of bilayer of PDMS on CYTOP with image of sample of thin (partial) film layer of floated on top of CYTOP coated silicon wafer.

6.4.1.2 Bilayers of PFPE-PEO and PDMS.

A thin bilayer of PDMS PFPE-PEO was prepared by spin coating a solution of PFPE-PEO (Fluorolink E10/6, Solvay) from methanol at a concentration of 20% by mass onto a silicon wafer treated with a thin film of PMMA as a stabilising layer. Ellipsometry determined this layer to be 1.5μm thick. SYLGARD 184 PDMS (10:1 A:B mixture) was prepared and spin coated from hexane at 25% by mass on PSS treated glass and cured for 4 hours at 65°C. This layer was floated from water onto the PFPE-PEO reservoir which acts as a penetrant reservoir. Once the bilayer was formed this sample was measured with ellipsometry and the PDMS layer thickness was found to be 2μm. A full ion mill was attempted of the sample.

A bulk sample was prepared by preparing a thin PFPE-PEO reservoir on PMMA before placing a 219μm thick cured PDMS membrane onto the reservoir to induce diffusion as illustrated by the diagram figure 6.22. Surface and small depth profiles were performed on this sample several days after the initial penetrant exposure. Duplicate samples of the same thickness were also produced at the same time and contact angle measurements were taken over the same timeframe to produce equivalent measurements of diffusion.

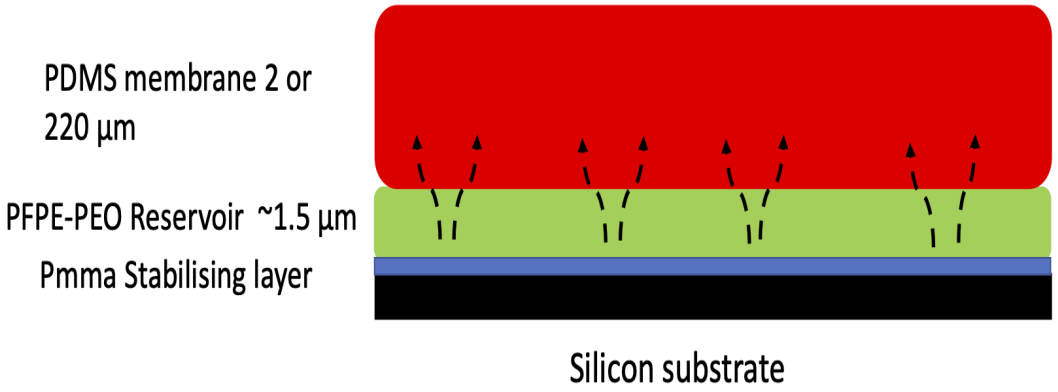

Figure 6.22: Diagram of diffusion bilayers with PDMS membranes on small liquid reservoirs of PFPE-PEO on PMMA treated silicon.

6.4.1.3 PFPE-PEO containing silicone coating as reservoir for diffusion into pristine PDMS.

In order to validate the determination of the diffusion coefficient from contact angle time lag measurements using 300μm thick PFPE-PEO FR coatings as PFPE-PEO reservoirs, a bulk diffusion sample was also prepared using PFPE-PEO FR as the reservoir for a 262μm thick PDMS membrane. Using the calculated diffusion coefficient the time lag for a membrane of this thickness would be $\approx$ 54 minutes. This sample was prepared immediately before XPS measurements were performed, with the PDMS membrane being placed on top of the PFPE-PEO FR coating just prior to insertion in the XPS analysis chamber. The instrument setup and time to vacuum conditions caused a $\approx$ 30 minute delay between diffusion commencement and surface analysis such that the first XPS measurement of the membrane should be prior to expected diffusive time lag. This sample was measured a second time 2.5 hours later (over twice the calculated time lag for diffusion). Surface XPS measurements were then repeated 24 hours later and 1 week after initial sample formation.

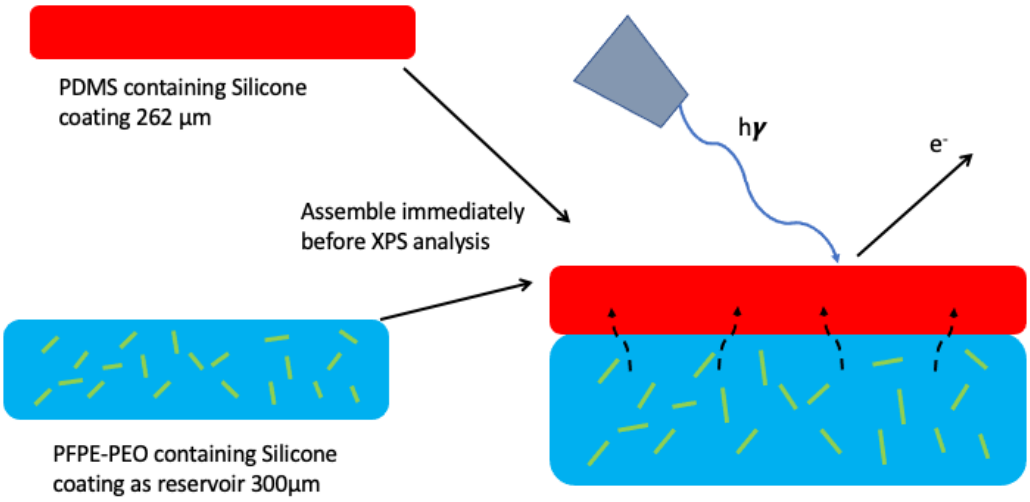

Figure 6.23: Assembly concept using PFPE-PEO containing silicone coating as a diffusion reservoir for PDMS membranes.

A fresh piece of PFPE-PEO FR coating was also subject to a small ion milling depth profile of 200 nm. This milling used the smooth underside of the coating as the top surface (as have all diffusion measurements using PFPE-PEO FR coatings as diffusion reservoirs). In each case atomic compositions were measured and determined across the measured depth range.

6.4.2 Results from XPS ion milling experiments

Figure 6.24 shows the XPS depth profile for the CYTOP-PDMS bilayer across the entire sample thickness with measurements taken every 60s ≈ 10nm etching.

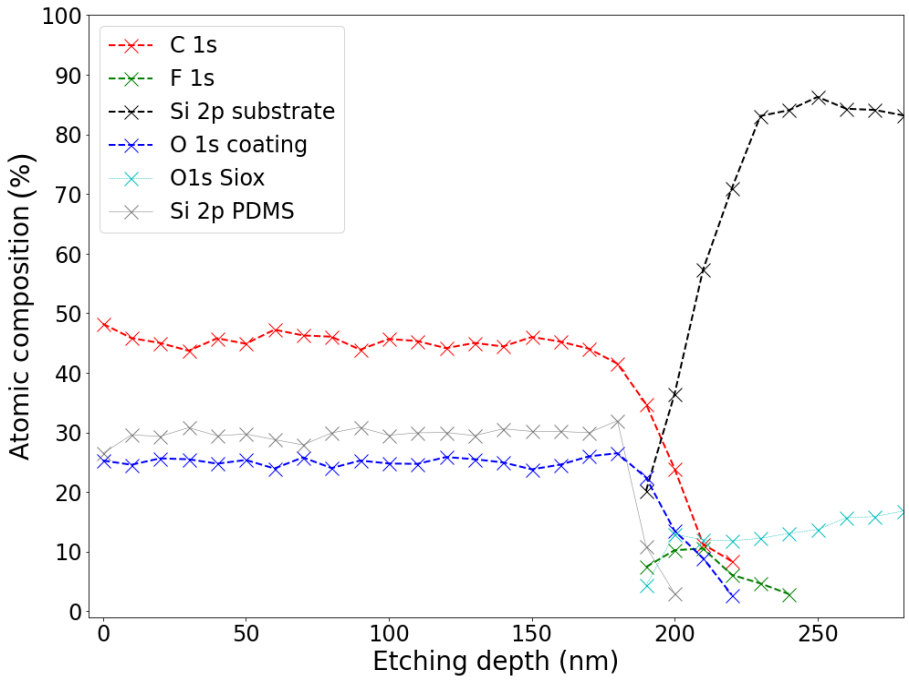

(a) Full Depth profile.

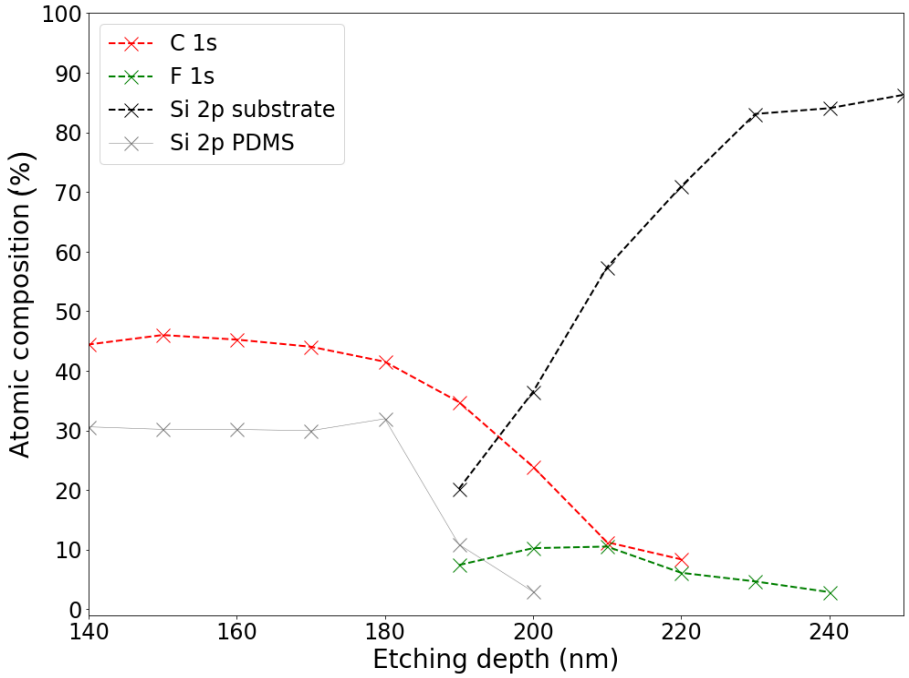

(b) Abridged profile for fluorinated region of CYTOP layer.

Figure 6.24: XPS depth profile of 220nm PDMS - 6nm CYTOP bilayer on silicon.

For XPS, the atomic signals for silicon Si 2p and oxygen O 1s in PDMS and in the oxide layer of the silicon wafer can be differentiated by the photoelectron energy spectra and the relative concentration of these two molecular states are presented in figure 6.24. After 1140 s or ≈ 190-200nm through the thickness of the coating, Si and O signals begin to fall significantly with substrate first signals becoming detectable. This is also when the CYTOP exclusive F1s signal first becomes detectable. By 1500 s (etch depth ≈ 250nm) the signal from coating specific elements has collapsed and only substrate associated signals are detectable confirming that the ion source has milled through the entire thickness of the sample. Fluorine signal peaks at 10.5% between 1200-1260 s and is present across 300 s of etching (≈50nm range).
Figure 6.25, the XPS depth profile from the thin PFPE-PEO-PDMS 1.5-2.2μm bilayer sample was obtained using an extended ion mill, with each XPS measurement taken every 600s. This yielded XPS data from the surface and from through the depth of the coating at ≈100nm intervals.

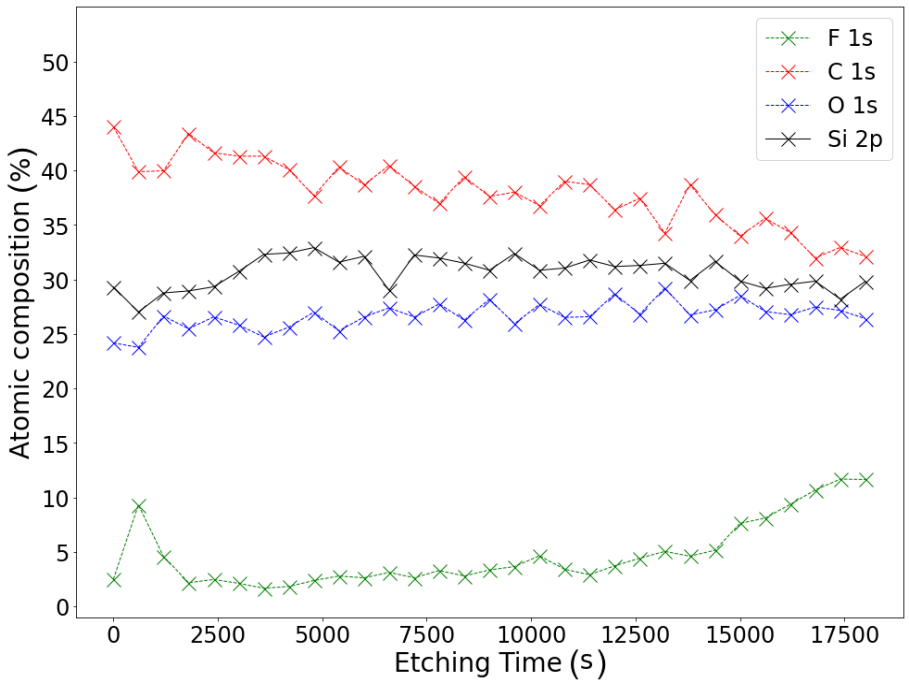

Figure 6.25: Elemental Atomic composition for a PDMS/PFPE-PEO bilayer as determined from depth profiling XPS.

For this sample we present only the elemental composition, the substrate Si 2p and O1s signals are never detected suggesting the entire thickness of the sample

≈3.5-4μm is not milled through. The milling time for this experiment was 18000 s or 5 hours based on determined etch rates this would be equivalent to 3μm of PDMS. The initial surface measurement at t=0 shows a small initial fluorine composition of 2.5% followed by a peak fluorine composition of 9.5% after the first ion mill. Further milling results in a fall in the fluorine composition to a fairly stable value averaging 3.2±1% for the next 13000 s of milling. It is clear from this that PFPE-PEO has diffused through the thickness of the film and is present throughout the thickness of the PDMS. In the final stage of milling the fluorine signal increases and saturates to 11.6% the rise in F1s after 13800 s is attributed to the initial etch through the entire PDMS thickness, with further etches exposing more of the PFPE-PEO reservoir underneath the film and increasing the measured fluorine composition of the surface.

We can calculate an approximate volume fraction for PFPE-PEO based on the stoichiometry for Fluorolink E10/6 discussed in section 1.5.4, in which we determine the non-hydrogen, molecular composition of fluorine as 36.0%. The initial surface composition of fluorine indicates a volume fraction of ϕ ≈0.0695, the peak fluorine composition after the initial 10nm etch of 9.5% implies a volume % ϕ ≈26.4. The bulk fluorine composition value of 3.2±1% suggests that the bulk volume % of PFPE-PEO is ϕ ≈8.9±0.9%.

Examining the using a thin PFPE-PEO reservoir of 1.5μm for a bulk membrane of 219μm yielded slightly different results, the sample was first probed 4 days after sample formation as shown in table 6.2. With both a surface scan and an depth etch attempted. When milling was attempted however, the reduction in scan size resulted in a reduction in signal to noise an initial surface composition of F1s of 0.2% was found for this smaller area but with depth profiling no fluorine could be detected above the noise limit [252].

Table 6.2: Atomic surface composition of 219μm PDMS membrane after 4 days exposure to PFPE-PEO.

Element	F	O	C	Si
Atomic Composition (%)	0.3	28.3	45	26.4

When milling was attempted however, the reduction in scan size resulted in a reduction in signal to noise an initial surface composition of F1s of 0.2% was

found for this smaller area but with depth profiling no fluorine could be detected above the noise limit [252].

A second measurement taken 14 days after the initial sample formation showed greater surface fluorine and yielded observable fluorine composition in depth profiling, as shown in figure 6.26.

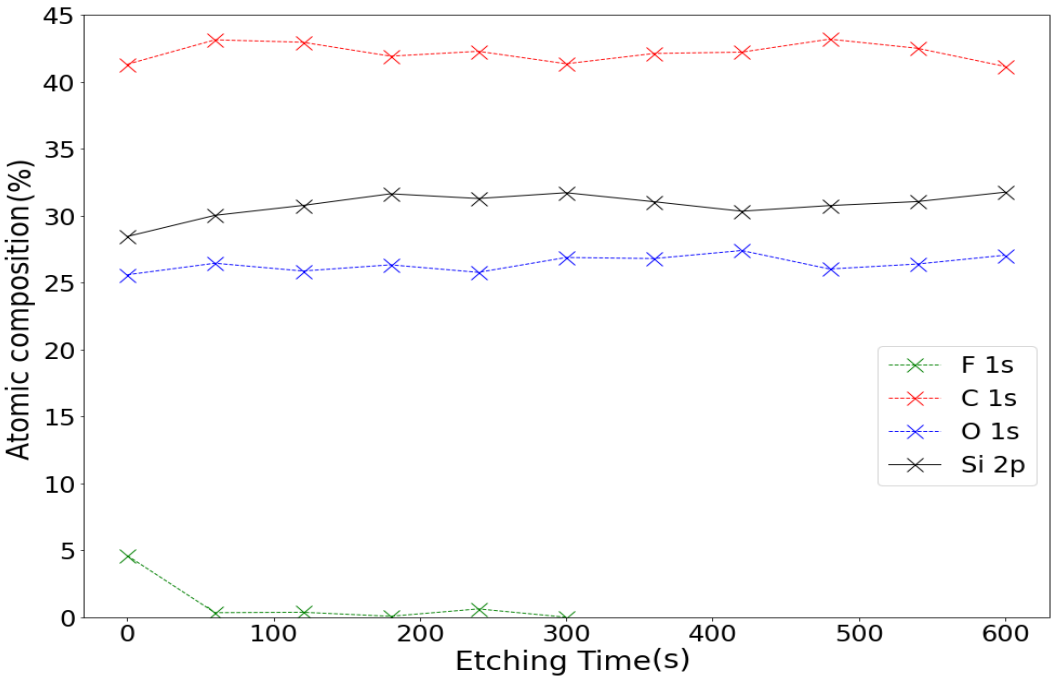

(a) Atomic composition of sample against ion milling time.

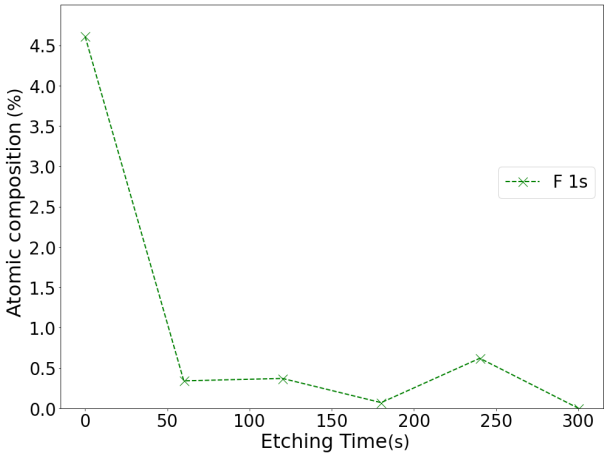

(b) Atomic composition of fluorine against milling time shown at a higher resolution.

Figure 6.26: Depth profile of 219μm PDMS membrane 14 days after exposure to penetrant (60s of ion milling equivalent to ≈10nm etch of PDMS).

In this later measurement a much higher initial surface fluorine concentration of 4.6% was observed. The approximate surface volume % of PFPE-PEO changes from ϕ_{4days} ≈0.8% to ϕ_{14days} ≈12.8%. Etches at 60 s intervals detected a much lower fluorine composition in the bulk a few 10s of nm beneath the surface before

the signal reached undetectable levels after 5 etches 50nm into the film.

An equivalent sample of 220μm exposed to a reservoir of 1.5μm PFPE-PEO was examined using water contact angle measurements 48 hours after initial exposure, figure 6.27 shows evidence of surface active PFPE-PEO hydrophilising the solid/liquid interface already within this timeframe.

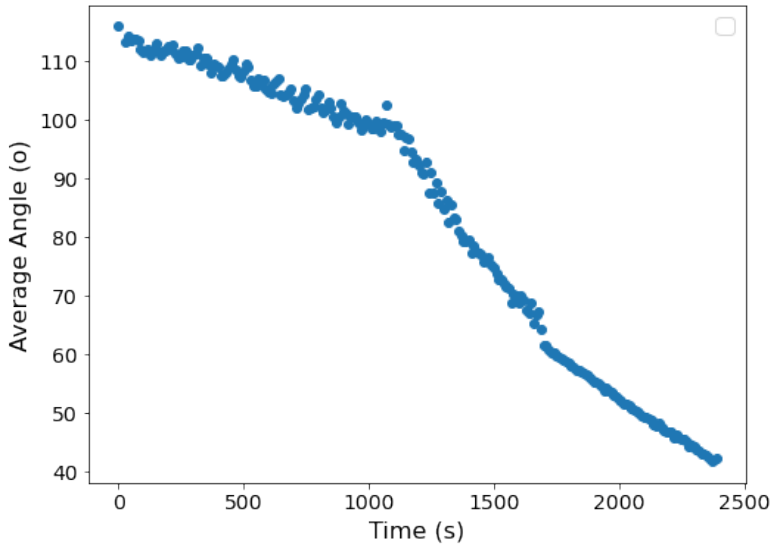

Figure 6.27: Time dependent contact angle for a 220μm thick PDMS membrane with a thin PFPE-PEO penetrant reservoir 48 hours after exposure.

6.4.2.1 XPS study using PFPE-PEO containing silicone foul release coating as a diffusive reservoir

The assembly sample of a 262μm PDMS membrane on PFPE-PEO initially showed no surface fluorine as expected, over the timeframe of analysis the atomic surface composition changed.

Table 6.3: Surface composition evolution over time for 262μm thick PDMS diffusion membrane in contact with PFPE-PEO FR coating.

Time Since Diffusion	Elemental Composition (%				) Volume of PFPE-PEO %
Hours	F	O	C	Si	
0.5	28.4	44.8	26.5	<0.1	n/a
2.7	28.5	44.9	26.5	<0.1	n/a
18	28.5±0.32	44.8±0.1	26.3±0.35	0.43±0.06	1.2±0.2
168(7 days)	28.1	44.5	26	1.5	4

As summarised in table 6.3, the initial measurement shows no indication of surface fluorine, demonstrating that prior to time lag there is no fluorinated species on the surface and the PFPE-PEO has not diffused through the membrane. After the second measurement over 2.5 hours after the assembly and post anticipated time lag there is agin no evidence of fluorine on the surface. However, at later measurements slightly later than 1 day later, taken as an average from 3 areas, we first detect evidence of fluorine on the surface at a concentration of 0.43%, note also at this time the silicon signal has declined slightly. In the final measurement 1 week after sample penetration the surface fluorine concentration has increased to 1.5%, with the composition of non fluorine atoms declining in turn, the largest proportional decline being for silicon, consistent with a model in which the volume fraction of silicon containing PDMS is falling and the concentration of fluorinated PFPE-PEO rises, given both polymers contain carbon and oxygen the silicon atomic composition should see the steepest decline as PFPE-PEO diffuses to the surface.

Consider also that the measured <0.1 F 1s atomic composition is not strictly evidence of the absence of PFPE-PEO at the interface but that any composition is below detectable limits for an XPS system. We therefore argue that the discrepancy between calculated time lag and the null result for surface fluorine after 2.7 hours may be the result of an undetectably small concentration of PFPE-PEO diffused to the interface at this time. In light of this, the water contact angle method whilst seemingly crude, may be more effective at detecting the presence of small initial concentrations of diffusing amphiphiles, as the presence of the solid/liquid interface will create an enthalpic incentive for surface functionalisation and high surface enrichment of the amphiphile even at very low overall concentrations.

Figure 6.28, shows the result of an ion milling XPS depth profile of the PFPE-PEO FR coating, which yielded an interesting fluorine concentration profile through the first 200nm of the coating.

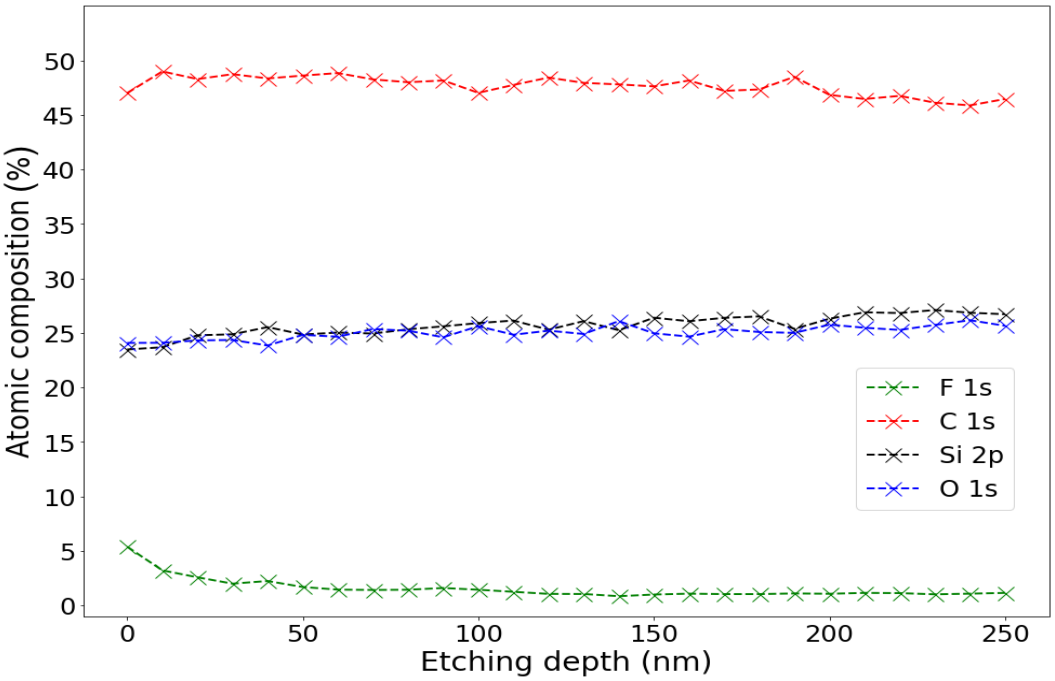

(a) Atomic composition of sample across depth.

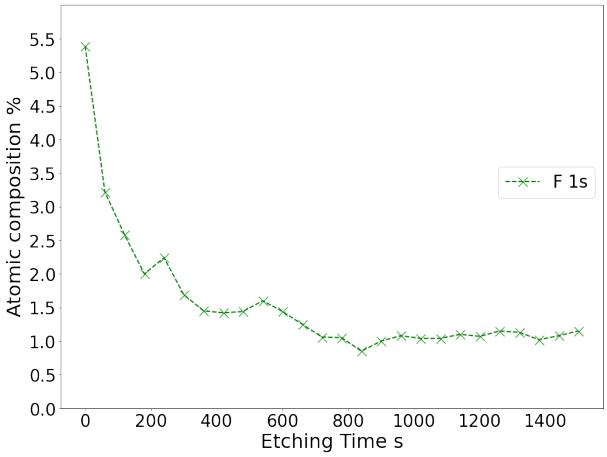

(b) Atomic composition of fluorine across depth shown at a higher resolution.

Figure 6.28: Depth Profile of 300μm PFPE-PEO containing PDMS silicone foul release coating PFPE-PEO FR (60s of ion milling equivalent to ≈10nm etch of PDMS).

At the surface of the smooth underside of the coating we see clearly there is an enrichment of the fluorine composition corresponding to an enrichment of PFPE-PEO at the surface even in air. Although as table 6.4 shows, a significantly

lower enrichment than seen in the rough topside of the coating where PFPE-PEO droplets can be observed on the surface.

Table 6.4: XPS surface composition of PFPE-PEO FR coating, smooth side and rough side (from preliminary SSAC report).

	Elemental Composition (%)			
	F	O	C	Si
Smooth underside	5.39	24.09	47.02	23.49
Rough top side	12.9	21.9	43.4	21.8

During the depth profile the fluorine composition falls over an etching time of 600s (equivalent to $\approx$ 100nm) before reaching a steady value as the etch continues for another further 100nm. We take this constant value to be that of the bulk concentration of fluorine in the foul release coating F %= 1.06$\pm$0.08%. Using the assumption that the non hydrogen fraction Fluorolink E10/6 is $\approx$ 36% fluorine as per the stoichiometry outlined in section 1.5.4, the % volume PFPE-PEO at the smooth surface of the PFPE-PEO FR coating is $\approx$ 15%. The interfacial enrichment of the PFPE-PEO additive extends for 10s of nm into the bulk of the coating before reaching the value of the bulk % volume which we find to be 2.94$\pm$0.02%.

6.4.3 Discussion of XPS measurements

These XPS experiments designed to probe evidence of diffusion and surface enrichment of PFPE-PEO amphiphiles in silicone support the conclusions of the contact angle diffusion studies showing that PFPE-PEO does diffuse through PDMS silicone albeit a slow rate, these results also indicate that PFPE-PEO is strongly surface active and will be present at an enriched concentration at the surface interface of PDSM coatings in air or water.
Figure 6.24 demonstrates the viability of full thickness ion milling experiments for sample <300nm. Although we would expect the CYTOP related fluorine signal to only be present in one measurement at an etch rate of 10nm per etch, the broadening of this peak is quite small with only 2 etches 10nm apart showing the peak fluorine composition which roughly approximates the 6nm thickness of the CYTOP layer. Considering the silicon and oxygen energy spectra, substrate associated energy spectra are already detectable as soon as fluorine is measurable in the sample. Given that the XPS already measures the substrate as the CYTOP under-layer is exposed by etching. this should be understood by considering the

nature of the ion mill beam; although the beam is projected across the diameter of 1.5mm , the intensity of this ion beam is not uniform and is most intense at the centre of beam. This means that over an extended time the etch into the sample becomes parabolic rather than a a uniform cylinder. We could interpret the simultaneous detection of substrate energy spectra with the early fluorine signal at etching time 1150s as the deepest etch at the centre of the region carving completely through the last 4-5nm of PDMS and the 6nm CYTOP layer to expose the substrate. It is this distorted milling crater that results in the fluorine peak being broader than the the deposited fluoropolymer film. Although the broader milling milling has resulting in a lack of strictly defined layers, with no fluorine detected through 90% of the PDMS etching, we find only limited evidence of diffusing fluorine fragments spreading the fluorine presence throughout the film as a result of ion milling.

The PDMS/PFPE-PEO bilayer probed in figure 6.25 yielded some important evidence of PFPE-PEO presence through the depth of a thin PDMS film but interpreting this milling plot also demonstrates the limitations and distortions of extended ion etching through thicknesses greater than a few. hundred nanometers. This thin bilayer sample was prepared well over a month prior to XPS ion milling depth profiling, this is also the sample with the highest ratio of reservoir to membrane thickness $\frac{1.5}{2.2} = 68\%$. If the entire reservoir of penetrant absorbed into the PDMS film it would represent a volume fraction of 40.5% and with PFPE-PEO's substantially higher density the mass fraction would be even higher at 54.7%. Based on the prior determined diffusion coefficient, the initial Fickian diffusive time lag for this membrane thickness would be <1 second. We therefore argue that the reservoir for this sample is sufficiently large to penetrate the PDMS membrane to a saturation concentration and the timeframe allotted for the sample was far greater than the timescales of diffusion such that full equilibrium of penetrant was achieved within the film.

Initially, little fluorine is detected on the top surface, this is due to an organic contaminant on the top surface on top of the sample surface proper. Following the first ion etch of $\approx$ 100nm there is a peak in the fluorine concentration, this is likely to be near or at the true surface of the sample suggesting that there is an interfacial enrichment of PFPE-PEO, although some caution should be given to this data point as this sample's extended lifetime and handling may contribute to surface contamination as with the initial surface measurement indicated. Observing similar surface enrichments of PFEP-PEO on other diffusion samples such as figure 6.26 and the PFPE-PEO FR coating figure 6.28 corroborates this observation and strengthens the argument for a real surface enrichment of PFPE-PEO. Further milling though the sample sees a decrease in the observed fluorine content as the

ion beam penetrates into the sample to a depth of 100s of nm which then reaches a constant value as reported of 3.2% which should represent the saturation value of PFPE-PEO in PDMS. The extended milling effect will have caused an even more exaggerated cratering effect over time the total milling time would equate to a mill of 3μm of PDMS which is considerably greater than the measured thickness of the prepared thin film even allowing for uncertainty. Despite this the silicon 2p signal never vanishes from the XPS elemental composition spectra as would be expected if the ion source milled a clear region through PDMS and into the PFPE-PEO reservoir underneath. Instead this signal is remains constant but there is a rise in the measured fluorine composition of the film after 14500s (2.4μm) which begins to saturate after several further milling intervals. At the approximated milling rate this would be consistent with having first milled through the full thickness of the PDMS membrane and so exposed the under layer of PFPE-PEO.

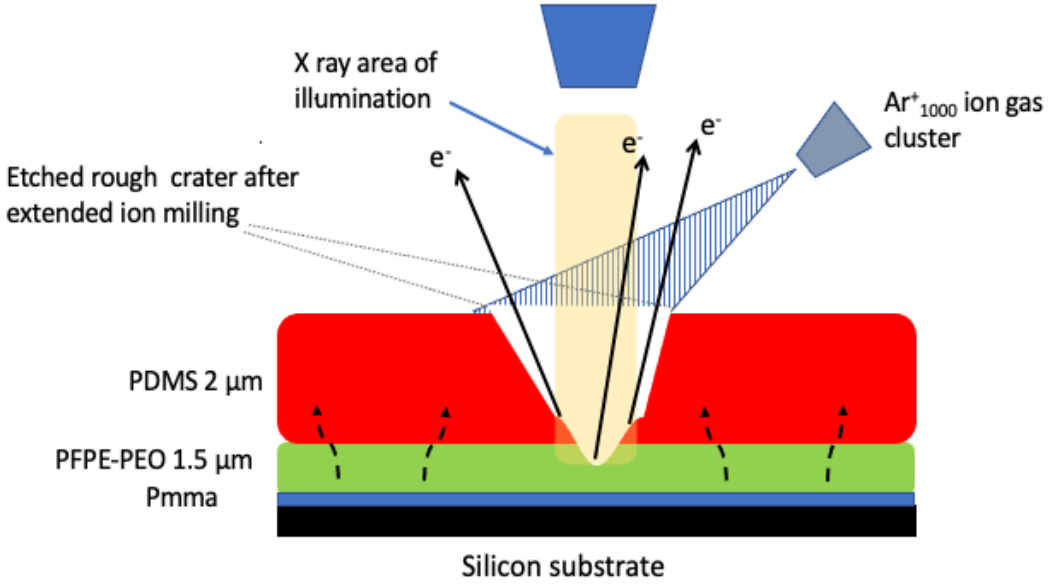

Figure 6.29: Diagram of proposed long term ion etching, as surface becomes too rough and the non uniform region encroaches on the XPS area of illumination.

The diagram in figure 6.29 offers a potential explanation for these observations; the silicon signature of PDMS does not change appreciably because at such long term excavations the non uniform milling beam results in an ever narrower crater, with the PDMS walls of the crater now encroaching on the XPS analysis area. At this stage in the profile, the examined depth is increasingly imprecise and

broad as the measurement is in effect observing a composite area of greater depth at the centre and lesser depth at the edges[253]. Previous studies have cautioned against ion etching more than 300nm for this reason; the interface becomes too rough, the real etch rate declines and consequently the depth resolution declines so one can no longer be certain of the etch depth at extended milling times[254]. Smith et al reported the etching of a 15μm multi-bilayer of alternating 300nm ayers Polystyrene and polyvinylpyrrolidone, they found that after 500s of etching (equivalent to 1μm of etching) the resolution of distinct layers had declined with atomic composition shifts across depth becoming smoother and within 2500s of ion gas exposure atomic composition of the system was constant with distinct layers no longer resolvable (depth resolution reaching $>$ 300nm)[255]. They attributed this to radiation damage in the probed area due to extended X-ray exposure and and impurities and defects seeding an offset in the depth profile [256]. They suggest rotating the sample around the milled region during XPS analysis in order to minimise x-ray damage by distributing the exposure across a larger area. Despite these limitations, this attempt at a full depth bilayer mill provides some evidence of surface segregation and definitively demonstrates the penetration and diffusion of PFPE-PEO in PDMS first suggested by contact angle experiments.

The 219μm bulk diffusion test further corroborates the diffusion behaviour and surface segregation of PFPE-PEO first suggested by figure 6.25. Unlike the thin bilayer sample this sample was completely pristine, requiring minimal handling to prepare before examination meaning a lack of surface contaminants so the presence of fluorine on the surface can be firmly attributed to the diffusion of PFPE-PEO through the membrane. The initial depth profile attempt did not yield observable fluorine signals above noise suggesting internal concentrations of 0.1% or less therefore after 4 days surface concentrations are small at 0.3% but already enriched relative to bulk. Comparing to the sister sample used for contact angle analysis shown in figure 6.27 we see that a similar sample already exhibits the signature surface wetting seen in previous tests (eg. figures 6.18,6.15), if the equivalent surface concentrations as implied by fluorine surface compositions are still rather low, barely above detection limits, it suggests surface functionalisation is possible with extremely low concentrations of the amphiphile and that ,whilst seemingly crude, the water contact angle is quite a sensitive detection method of surface active amphiphiles in a hydrophobic material and may be more able to detect initial no zero concentrations post time lag than XPS or Infra red spectroscopy.

The second round of measurements yielded a successful depth profile, see figure 6.26 showing a continued migration of the PFPE-PEO to the surface now present at much higher concentrations at the surface and near the surface but still

very strongly segregated to the surface with concentrations dying away quickly the further into the sample. This bulk material diffusion test uses a penetrant reservoir representing a volume fraction of <0.7% of the membrane to yield these results, demonstrating that even with very small quantities of the amphiphile a diffusion and surface enrichment of this additive can be achieved, producing the desired interfacial properties in water.

These same surface enrichments were further demonstrated by the bulk sample using PFPE-PEO FR coating, as demonstrated by table 6.3, which shows that diffusion of PFPE-PEO across these thick membranes continues over days. Although direct depth profile of this sample was not attempted it is reasonable to infer from the diffusion in the other samples that the surface concentrations detected at the surface of the 262μm membrane would be higher than those for the bulk. By demonstrating that the PFPE-PEO FR coating can act as a reservoir for the diffusion of PFPE-PEO, this measurement further validates the methodology employed to produce the time lag data shown in figure 6.18 and supports the diffusion coefficient value derived using the time lag method. This experiment also places an absolute lower limit on the diffusion coefficient showing that PFPE-PEO crosses a 260μm membrane within 18 hours (crude time lag would yield 1.77$\times$ 10^{-}13 m^{2}s^{-1}) and most likely occurs much sooner as no measurements were taken of the surface chemistry for 16 hours between the last null measurement and the 18 hour measurement showing a 0.4% fluorine composition at the surface. Comparing this result with the contact angle behaviour seen in figure 6.17 showing the wetting behaviour for a 310μm thick membrane using PFPE-PEO FR coating as a reservoir 2.5 hours after the time lag and 24 hours after the time lag. Here, we see behaviours that are consistent with the XPS observations with the wetting shift becoming larger and more rapid with extended diffusion time just as XPS measurements indicate that surface concentrations of PFPE-PEO would continue to increase over days. Further, the observed contact angle behaviour 24 hours after measured diffusive time lag is still much smaller than the highly hydrophilic wetting shifts shown for top surface PFPE-PEO FR coating (figure 6.14) and post time lag DBE type PDMS-PEG penetrants (figure 6.10), with confirmation from XPS that after such extended diffusion timeframes there is PFPE-PEO present at the surface the small but consistent contact angle wetting shifts we observed can be considered evidence of the presence of PFPE-PEO on surfaces at these lower concentrations. This XPS result has therefore validated both the method of using PFPE-PEO coatings as diffusion reservoirs and provided evidence that the wetting shift signal used to indicate PFPE-PEO diffusion to the surface are both valid and therefore further support the calculated diffusion coefficient of 3.55$\pm$0 0.24 $\times$ 10^{-12}m^{2}s^{-1}.

Considering the discrepancy between the bulk composition value for the thin bilayer sample shown in figure 6.25 and the PFPE-PEO FR coating shown in figure 6.28 is significant. As previously stated, the 1.5 μm layer of PFPE-PEO reservoir used in the bilayer should be sufficient to diffuse to saturation in the PDMS membrane which might support this higher value as the true peak concentration. However, this sample visibly contained defects with surface microscope images showing a number of small pinholes in the PDMS film, illumination of an area of the film containing these small effects would have directly probed the underlying PFPE-PEE layer as part of the XPS spectrum which would exaggerate the fluorine composition detected. Similarly, the opaque nature of the PFPE-PEO FR coating suggests that PFPE-PEO could present in the PDMS above miscible levels implying that this lower concentration may be at or above the saturation value for PFPE-PEO in PDMS. As this foul release coating was in better condition and much thicker we would treat the value derived from the depth profile of this coating as more reliable. A repeat of the bilayer experiment using a slightly larger reservoir and a thicker, less fragile, defect free membrane (eg. 4μm PFPE-PEO and 10μm PDMS) might clarify the true saturation concentration of PFPE-PEO.

6.5 Future work: Raman spectroscopy

One technique that would yield highly valuable analysis and further clarify the diffusion coefficient for PFPE-PEO in PDMS would be Raman spectroscopy. Raman spectroscopy is a light spectroscopy technique similar but distinct from IR absorbance spectroscopy in which the inelastic scattering of light by molecules can yield signature spectra for a particular element or compound just as the IR absorbance bands can be used to identify specific compounds and chemical groups. Monochromatic laser light is incident on a sample and interacts with the molecules exciting it to a virtual energy state equivalent to the energy of the photon. This photon is then remitted if the molecule returns to it's ground energy state this scattering is elastic (Rayleigh scattering). If after the scattering event the molecule is in a different vibrational energy state the scattering is inelastic, with the emitted photon having a different energy to the incident pre scattered photon. If the final energy state is higher and the emitted photon has a lower energy (photon gives energy to the molecule) this is known as Stokes Raman, if the final energy state of is lower than before the interaction and the emitted photon has a higher energy (photon gains energy from the molecule during scattering) this is known as anti-stokes Raman. The Raman shift for a given wavelength will be characteristic of the vibrational states of a given molecule.

Figure 6.30 shows the Raman spectra for PFPE-PEO and PDMS, which were acquired using a transmission Raman system.

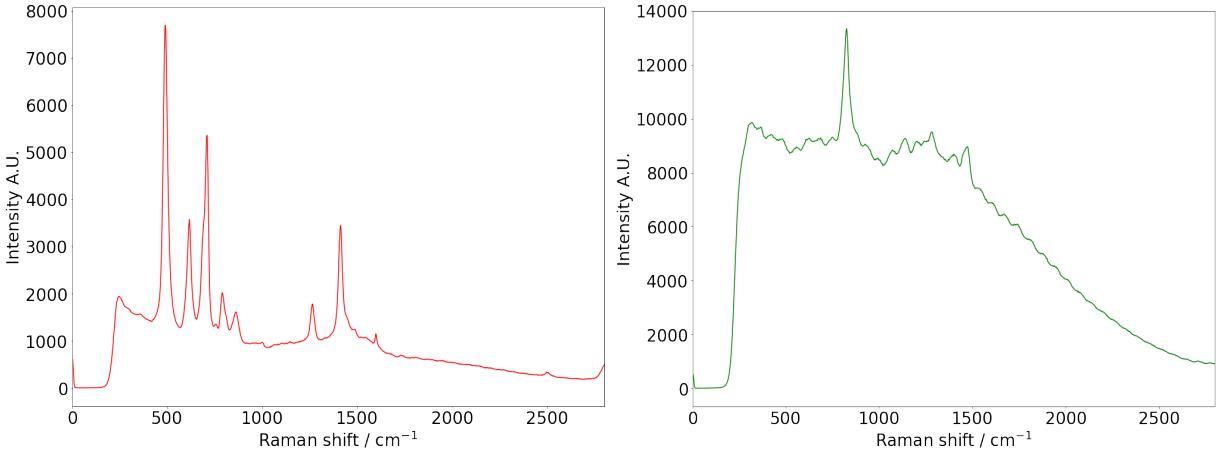

(a) Raman Shift for uncured Sylgard PDMS

(b) Raman Shift for liquid PFPE-PEO.

Figure 6.30: Depth Profile of 300μm PFPE-PEO containing PDMS silicone foul release coating (60s of ion milling equivalent to ≈10nm etch of PDMS).

We can see clearly that the Raman shift signals for both molecules are significantly distinct and could be used to identify the concentration of one species mixed into the other via their Raman fingerprint in a manner not dissimilar to FT-IR. Attempts were made to perform diffusion measurement utilising Raman by exposing a film of PDMS to a droplet of PFPE-PEO and using Raman confocal microscopy to measure the depth profile concentration of the PFPE-PEO signal through the film over time inspired by the methodology of Jonas et al [257]. However, initial trials never successfully detected the presence of PFPE-PEO in PDMS and this method was not pursued further and it was abandoned. Upon further research it has become clear that other Raman techniques utilising a simpler 1-Dimensional Raman Spectroscopy setup have been developed for the determination of diffusion coefficients and may have been more appropriate and practical for our experiment. In the reported setup utilised by Bardow et al [258] known volumes of two liquid molecules are inserted into a small diffusion cell such that the initial interface between the liquids is clearly identified at the onset of diffusion. Transmission Raman measurements. are then taken through small areas at successive heights across the length of the diffusion cell to detect the concentrations of both phases throughout the diffusion cell. In this way the 1-dimensonal time dependent interdiffusion can be measured and a diffusion coefficient determined[259]. With the

right experimental setup and sufficient volumes of PFPE-PEO and PDMS such an experiment should be feasible and with distinct Raman signals should lead a quantitative value for the diffusion coefficient which could be compared with that achieved from time lag diffusion experiments.

6.6 Conclusion

A series of methods were employed to find the diffusion coefficient of PFPE-PEO in PDMS membranes with the contact angle time lag method proving to be highly sensitive to very small concentrations of this amphiphilic molecule and yielding a credible value for the diffusion coefficient. A series of bilayer XPS depth profile experiments were conducted which demonstrate the diffusivity of PFPE-PEO in PDMS, found and corroborate the findings and of the contact time lag experiments, as well as demonstrating the interfacial enrichment of PFPE-PEO at the surface of silicone membranes in air as well as in water and providing valuable information about the effective bulk concentration of PFPE-PEO in FR silicone coatings. Our findings Show PFPE-PEO are capable of diffusing through PDMS membranes and functionalising silicone/water interfaces even at low concentrations.

Chapter 7

Conclusions and future work

7.1 Conclusions

In chapter 1 we provided a general introduction to biofouling, with a particular focus on the challenges posed by marine biofouling, outlining the historic approaches utilised to inhibit marine biofouling such as biocidal coatings. The concept of foul release coatings for marine applications was described as well as early research into surface bioadhesion such as the Baier curve which demonstrates the importance of surface energy and bulk mechanical properties to foul resistance. The importance of PDMS silicone as an elastic low surface energy foul release material was explored highlighting both it's advantages and limitations. The effectiveness of highly hydrophilic materials such as polyethylene glycol at resisting protein adhesion was explained, emphasising the values of PEG based molecules as modifiers for bulk foul release materials. Finally, we introduce ultra low surface energy amphiphilic perfluoropolyether polyethylene oxide triblock copolymers as promising foul release molecules and identify the key aims of the project which were to study the incorporation of PFPE-PEO Fluorolink E10/6 into PDMS silicones and determine how the inclusion of these amphiphilic molecules would affect the interfacial behaviour and foul release properties of PDMS.

In chapter 2 all major experimental techniques were discussed in detail, providing general technique theory and explaining the relevance of these techniques for the research of solid liquid interfaces .

In chapter 3 early experimental work attempting to make thin model films suitable for neutron reflectivity was discussed, highlighting a series of challenges preventing the formation of suitable thin film model coatings such as solution

aggregation in mixed PDMS/PFPE-PEO mixed solutions. The phenomenon of autophobic de-wetting of PFPE-PEO molecules on silicon substrates was identified using tof sims, neutron reflectivity, ellipsometry and water contact angles. PFPE-PEO was found to form a bonding monolayer of measured thickness 1.2nm, similar effects were also observed with hydroxy terminated PDMS molecules of various molecular weights that formed a bonded monolayer on silicon wafers causing large changes in hydrophobicity of the modified surface. A hazard free catalyst for the hydrolysis cure of PDMS was identified; amino propyl PDMS oligomers, these molecules proved to be effective initiators of the curing reaction and could inhibit autophobic detwetting effects in blended films by inducing rapid silicone cure.

In chapter 4 surface analysis of PFPE-PEO modified PDMS films was performed both in air and at the solid liquid interface, using neutron reflectivity and atomic force microscopy. Films formed via the spin coating of blended films were studied first, these showed evidence of some surface enrichment of PFPE-PEO from air AFM and surface XPS measurements, but when analysed with neutron reflectivity at the ISIS neutron source, these blends showed no apparent change in surface between air and water. Blend samples were then analysed with depth profiling XPS, which indicated very low concentrations of PFPE-PEO at the surface and undetectable quantities in the depth of the film suggesting much smaller PFPE-PEO volume fractions in these films than implied from solution fractions.

PDMS/PFPE-PEO topcoat samples formed by depositing PFPE-PEO on top of a PDMS film showed PFPE-PEO dewets into droplets on PDMS in air, AFM imaging of PFPE-PEO microdroplets on PDMS enabled the determination of the PFPE-PEO/PDMS interfacial tension from droplet contact angles as $8.28 \mathrm{mJm}^{-2}$. Neutron reflectivity measurements performed at the ILL neutron source confirmed no interfacial spreading layer of PFPE-PEO on PDMS in air. However, when PDMS/PFPE-PEO topcoat films were studied in liquid using 3 different water contrasts we found that the solid liquid interface reconstructs with a partial wetting monolayer of PFPE-PEO forming at the solid liquid interface, modelling found the monolayer was of consistent thickness across samples at $\approx$3nm. When thick (>100nm) layers of PFPE-PEO were deposited on the surface Bragg peak features were observed in the reflectivity spectra, indicating the possible formation of a lamella or ordered micelles near the solid surface. Qi imaging AFM was also performed on PFPE-PEO modified silicone films in liquid which corroborated findings from NR, showing largely flat surfaces in liquid but with lower measured peak adhesion and Young's modulus compared to PDMS, which is consistent with a monolayer covering the solid liquid interface.

Time dependent water contact angle measurements on these surfaces indicate

a rapid wetting spreading change in droplet contact to the surface. This indicates that the surface reconstruction is both rapid and results in a more hydrophilic surface. The evidence of surface reconstruction in liquid implies that the spreading monolayer is driven by a hydrophobic interaction between PDMS and the PFPE block of the amphiphile with the PEO end blocks solvated and presenting to the liquid interface. In this orientation, the interface is very hydrophilic implying a possible hydration layer at the solid liquid interface as the mechanism by which PFPE-PEO monolayers resist biofouling. We note that these topcoats are comparable to the top surface of industrially provided bulk PFPE-PEO modified silicone coatings with PFPE-PEO droplets on the top of a PDMS surface, we therefore argue that the same wetting monolayer of PFPE-PEO also occurs at the surface of bulk foul release coatings in water.

PB-PEO liquid block copolymers were sourced to assess whether similar wetting effects could be induced on PDMS surfaces using similar but non-fluorinated short chain amphiphilic polymers. However, the particular candidate molecule showed no evidence of surface reconstruction or reduced biofouling.

In chapter 5, Bio adsorption to the model PDMS/PFPE-PEO topcoats was tested using a series of proteins and a dextran polysaccharide. First bioadhesion was measured on a series of model surfaces in real time using QCM, films were prepared on QCM quartz crystals and experiments were performed using a stop flow process. For the globular protein BSA most adsorption was found on hydrophilic gold and silica surfaces, with a smaller mass adsorbed on PDMS. The mass adsorbed on PDMS/PFPE-PEO topcoats was reduced by 80% compared to PDMS. Ex situ AFM measurements of surfaces immersed in a BSA solution for 50 minutes also indicate substantial protein adsorption to PDMS surfaces but far less observable protein on PFPE-PEO modified PDMS films.

For lysozyme the same pattern was observed but adsorption on PDMS/PFPE-PEO topcoats was negligible (3.4 ng cm^{-2}), with adsorbed mass reduced by more than 95%. Measurements performed with the marine mussel foot protein mefp-1 also indicate minimum adsorption to PFPE-PEO/PDMS surfaces with adsorbed mass reduced by 85% compared to PDMS surfaces. These findings corroborate the established vulnerability of PDMS surfaces to protein fouling and show that when modified with PFPE-PEO, protein fouling to these surfaces is radically reduced.

The adsorption of the polysaccharide dextran was also monitored using QCM. The adsorption of polysaccharides on silica, PDMS and PDMS/PFPE-PEO surfaces was viscoelastic and was analysed with the Voigt model. In contrast to protein adsorption, PFPE-PEO/PDMS surfaces showed no enhanced resistance

to the bioadsorption of dextran; the wet mass adsorbed to PFPE-PEO PDMS surfaces was higher than on PDMS or silica surfaces, upon rinsing with buffer the adsorbed dextran layer was reduced by 90% but the PFPE-PEO/PDMS surface still retained a greater adsorbed mass than other surfaces after rinsing. This suggests that dextran bonds weakly to surfaces and can be easily removed, but nevertheless PFPE-PEO offers no resistance to it's adsorption.

Finally, the adsorption of BSA protein on PDMS and PFPE-PEO/PDMS films was measured using neutron reflectivity on the D17 Reflectometer at the ILL. After the protein solution was injected surfaces were monitored for 80 minutes with 1 minute reflectivity scans to observe the kinetic process of protein adsorption. On PDMS, this process occurs rapidly with changes in the reflectivity profile evident after 4 minutes and largely complete within 16 minutes, consistent with observations from QCM of the adsorption of protein on PDMS saturating within 20 minutes. When modelling the adsorbed layer, it was clear that BSA proteins had not maintain solution structure and had denatured consistent with the theory of protein adsorption to hydrophobic surfaces. The attached BSA was modelled as a bilayer fit with a thin highly dehydrated layer of $4\mathring{A}$ and a larger solvated outer layer of $33.5\mathring{A}$. There was no evident desorption of protein from the surface upon rinsing with buffer solution. In contrast when the PDSM PFPE-PEO surface was exposed to BSA protein solution there was minimal change in the reflectivity spectra implying negligible protein adsorption to this surface, thus validating the findings from QCM that PFPE-PEO greatly reduces protein adsorption to PDMS surfaces.

In chapter 6, the diffusion coefficient of PFPE-PEO molecules in PDMS silicone was determined using the diffusive time lag method. By monitoring the change in wetting of a water droplet on the surface of a silicone membrane it was possible to determine the time lag for amphiphiles to diffuse the full thickness of the membrane and determine diffusion coefficients. This method was used successfully to find the diffusion coefficient for two branched PDMS PEG amphiphiles DBE 411 and DBE 712 and for PFPE-PEO. The diffusion coefficient for PFPE-PEO in PDMS was found to be 3.55 x 10^{-12} m^2s-1. It was noted that when comparing to prior literature, this value was at the lower end of a range of diffusion coefficients previously found for amphiphiles in PDMS.

To further analyse the diffusion of PFPE-PEO in PDMS, XPS ion milling measurements were performed to find the depth profile of PFPE-PEO through the sample from fluorine elemental composition. These measurements demonstrated the process of PFPE-PEO through PDMS and revealed an enrichment of PFPE-PEO at the surface of PDMS compared to the bulk value driven by the lower surface energy of PFPE-PEO.

In summary, when incorporated into PDMS coatings PFPE-PEO will diffuse to the surface at an enriched concentration in air, driven by low surface tension but will not form a covering layer. When exposed to water, the surface of these coatings will reconstruct with a wetting monolayer of PFPE-PEO forming at the solid/liquid interface. This interface is highly hydrophilic and dramatically reduces the susceptibility of the surface to protein adsorption compared to unmodified PDMS. We hypothesise the mechanism of foul resistance may be the result of strong hydrogen bonds between PFPE-PEO and water molecules at the interface creating a hydration layer which represents an energy barrier to biomolecule adhesion.

7.2 Future work

This research project has done much to clarify this behaviour and the interaction between PEPE-PEO amphiphiles and PDMS however, there are also aspects of these coatings and the solid/liquid interface that would benefit from further research.

7.2.1 Further liquid AFM and surface adhesion studies

Firstly, we were only able to achieve a single set of Qi liquid AFM measurements, repeat analysis of comparable samples would further confirm our results and demonstrate the reliability of our findings that PFPE-PEO reduces the cantilever adhesion and measured elastic moduli at the solid liquid interface. Further, if we had the opportunity, these studies would have been extended beyond the thin model film samples of bulk coating thickness $\approx$100's μm, comparing PFPE-PEO based industrial FR coatings with blank silicone controls. We would hypothesise similar changes in peak adhesive force and measured elastic modulus (both reduced in PFPE-PEO containing coatings) for bulk coatings as seen in our model thin film systems. Performing these experiments with bulk coatings would demonstrate that the effects we have observed with the model films are indeed occurring at the interface of the industrial coating. Further, using coatings much thicker than the penetration depth of the cantilever we should be able to find more accurate values of the elastic modulus for silicone based coatings and so clarify the effect of the PFPE-PEO monolayer on the measured elastic modulus without the effect of the ridged substrate seen in the thin film models.

Mechanical characterisation via AFM could be extended even further, to compliment the research into diffusion and bio adhesion. When using contact angle

goniometry to observe diffusive time lag and surface functionalisation, we were observing the macro effect on water droplet surface wettability of amphiphilic molecules functionalising the solid/liquid interface. This same effect could be explored at the nanoscale via in situ liquid AFM. Recent studies by Hawkins et al [260] characterised the dynamic surface reorganisation of a silicone coating modified with an amphiphilic PEO-Silane molecule when in an aqueous environment. This was achieved using an off resonance tapping AFM mode which did not collect mechanical surface data but did provide valuable insight into the topographical changes during dynamic reorganisation, imaging the processes by which PEO rich domains develop and then dominate the interface. With Qi mode AFM, it is possible to collect topographical and mechanical surface data simultaneously with image collection speeds similar to standard topographical AFM. Using the JPK in Qi mode, it would be possible to obtain even more enlightening information about dynamic surface reorganisation with both topographical and mechanical data. Such measurements would be well suited to our studied systems; the measured diffusion coefficient of PFPE-PEO in PDMS being very low results in long diffusion times, so the surface functionalisation of PFPE-PEO at the silicone surface should be slow enough to be studied at the nanoscale with AFM. We predict the final stage of surface functionalisation to be a uniform PFPE-PEO rich surface in water comparable to the interface seen from our model thin film systems.

AFM could also be used to study the mechanics of bio adhesion onto our foul release coatings. The peak adhesive force data we have been able to acquire has been useful for demonstrating the change in surface properties between PDMS and PFPE-PEO modified PDMS but the force of adhesion between surfaces and an AFM cantilever tip is not of particular interest to foul release coating performance. Nevertheless, previous researchers have pioneered techniques using AFM probes to measure the mechanical force of adhesion between biomolecules and surfaces. In particular, the adhesion of protein to surfaces has been studied either by functionalising a silica probe with protein and measuring pull off forces on various surfaces [261] or by immobilising proteins on a surface and modifying a AFM probes with colloids coated surface materials of interest [262]. Both methods have advantages and disadvantages they have both been used successfully to compare the strength of adhesion between proteins and different material surfaces in water and would be highly complementary to our studies of protein adhesion and high protein resistance of PDMS and PFPE-PEO modified PDMS surfaces.

AFM probes have also been utilised to measure mechanical adhesion forces between surfaces and biofilms by cultivating biofilms onto tip-less AFM cantilevers [263]. This method has been able to investigate the relative strength of adhesion of biofilms on a number of material surfaces including foul resistant PEG surfaces.

This is a particularly interesting method of assessing bioadhesion as biofilms are a key component of early biofouling and this method allows the direct study of their adhesion to various surfaces. Biofilms are much more complex systems excreting various polysaccharides and proteins in their EPS, so their adhesion is more complex than the studies of single biomolecule adhesion performed on PFPE-PEO/PDMS surfaces thus far. Colleagues within our research department have developed the capability to perform this technique and we have had preliminary discussions about the possibility of performing such experiments.

7.2.2 Studying water structure at the interface of foul release coatings.

As established in chapter 4, a thin wetting monolayer of PFPE-PEO spreads across the solid liquid interface in water. This layer had a consistent thickness across all samples of ≈3nm. We attribute the foul release enhancement of PFPE-PEO modified films to this interfacial monolayer, contact angle measurements have suggested this layer is highly hydrophilic implying the PEO end blocks of the amphiphile present to the water interface. The precise mechanism of foul resistance of this surface is still in question, polyethylene glycol end tethered polymer brushes have long been recognised as an effective biofouling resistant surface with one hypothesised mechanism being that steric repulsion forces inhibit the adhesion of biological matter to the surface. However, this steric repulsion mechanism is more effective with increasing brush chain length, the PFPE-PEO molecule studied in this project contains a total of only 9 ethylene oxide moieties distributed between each end of the molecule. It is therefore unlikely that PFPE-PEO is forming a brush surface with a significant steric barrier to protein adhesion, the mechanism of biofouling resistance must be different[174].

Another mechanism for non-fouling has been proposed for many short chain hydrophilic materials in which biofouling is inhibited due to interactions between interfacial water molecules and the surface[264] [265]. This model of anti-fouling argues that strong hydrogen bonds form between water molecules and the surface, resulting in a physical and energetic barrier to the adsorption of biomolecules[266]. Evidence of strong hydrogen bonded water on foul resistant material surfaces has been found using a variety of techniques such as IR absorption microscopy, which has been used to identify water bond states within a hydrated polyelectrolyte brush [267]. It was found that water associated IR adsorption shifted from the bulk liquid value of 3400 cm^{-1} to 3200 cm^{-1} a value associated with strong hydrogen bonds. These bands have often been associated with water and ice respectively, as these IR adsorption bands were first associated with bulk water in the two states of matter.

Similar changes to water bonding structure have been observed for brushes using x ray absorption and emission spectra [268].

To confirm the non fouling mechanism of PFPE-PEO modified silicones the bond structure of interfacial water should be studied, the most suitable technique for this coating system would be in situ sum frequency generation vibrational spectroscopy. Sum Frequency Generation (SFG) is a non linear optics technique in which two laser beams of visible and infra red laser light are aligned to spatially and temporally overlap at the surface of the studied sample, this results in a signal output laser beam with a frequency that is the sum of the two input beams. This sum frequency output beam is collected and analysed, resulting in a spectra analogous to infra red absorption spectroscopy. The advantage of this technique is that an SFG signal can only be achieved where inversion symmetry is broken i.e at an interface. This highly interface sensitive quality of SFG makes the technique ideal for studying the structure and orientation of water at surfaces , with spectra being produced by a few layers of molecules at the interface SFG has been used to identify water bonding on both hydrophilic and hydrophobic surfaces [269]. SFG has shown strong hydrogen bonding of water molecules at the surfaces of peptide, Zwitterionic and PEG based foul release surfaces [270] [271].

In order to acquire SFG measurements, we have communicated with Dr Dowhj of Manchester University for assistance performing preliminary SFG measurements on PDMS and PFPE-PEO/PDMS films samples both air and water. The experimental setup has been reported in detail elsewhere [272]; when in liquid, IR and visible light beams travel through a small volume of water (for this system D2O is more commonly used), generate a sum beam at the interface, which reflects from the surface and is collected in a sapphire prism. The advantage of this setup is that samples can be prepared for SFG in the same way as the thin PFPE-PEO silicone films studied in chapters 4 and 5 . Previous studies have shown evidence of strongly hydrogen bonded water on both very hydrophobic surfaces such as PDMS and on highly hydrophilic surfaces [270]. As such, we would expect to see strongly hydrogen bonded water at the interface of both model surfaces. However, at hydrophobic interfaces 'dangling' OD resonances at 2745cm $^{-1}$ [273] are often detected due to the absence of hydrogen bonding between water and the hydrophobic interface[269], we therefore expect to see evidence of strongly H-bonded water at both interfaces but also dangling OD resonances for water at the interface of a pure PDMS film only and not at the surface of the PDMS/PFPE-PEO film. Confirming the presence of a strongly bound interfacial hydration layer on the PFPE-PEO wetting monolayer would clarify the mechanism of foul resistance which we anticipate SFG. studies will elucidate.

7.2.3 GISANS studies to investigate evidence of micelle formation near the interface of water PDMS/PFPE-PEO interfaces

As discussed in chapter 4 the neutron reflectivity spectra from PDMS/PFPE-PEO topcoat films can exhibit a Bragg peak feature in liquid if the layer of PFPE-PEO deposited is sufficiently thick. Fitting was attempted for these Bragg peak features using a large repeating lamella parallel to the plane of the sample surface. However, given the limited quality of these fits we have acknowledged the possibility of alternative structures forming near the solid liquid interface. Similar features have been observed in the reflectivity spectra of quartz crystals exposed to an aqueous solution of amphiphilic pluronic block copolymers [181]. It is known that at high concentrations these pluronics form micelles in water and the reflectivity data indicated that there was a degree of ordering consistent with micellular layering near the quartz liquid interface. Bragg peaks were particularly defined at high concentration which was attributed to the formation of a micellular crystal phase in solution. If similar effects are present for our system at high surface concentrations of PFPE-PEO more information needs to be collected in order to demonstrate the presence of micelles and their ordering in order to then fit the complex reflectivity profiles.

A valuable technique for studying micelles at liquid interface is grazing incidence small angle neutrons scattering (GISANS).Standard small angle neutron scattering (SANS) is a technique that uses neutrons to find structures and characteristic length scales in bulk materials. SANS has been used in numerous studies to find the size, structure and hydration of micelles in solution [274]. Grazing incidence SANS (GISANS) can be used to study solid liquid interfaces, neutrons penetrate the solid substrate at a small angle and are scattered at the solid liquid interface with the resulting neutron spectra collected by a 2 dimensional position sensitive detector [275] [276]. This enables SANS measurements at close proximity to the solid liquid interface, variable depth penetration into the bulk liquid can be achieved by varying the angle of the incident neutron beam. Extensive studies have been performed on pluronic micelle structures at liquid interfaces using GISANS, determining important structural qualities such as micellular crystal lattice shape, lattice parameter and lateral crystal domain size[277][278].

GISANS would be able to confirm the presence of micelles at the liquid interface of PDMS/PFPE-PEO films and provide useful structural information about any ordered micellular layer. Some reflectometers such as SuperAdam at the ILL are capable of preforming GISANS measurements and neutron reflectivity, using these reflectometers to study our films would be ideal as acquiring both GISANS

and reflectivity data on the same sample would yield complimentary information about the interface and aid the fitting of both data sets[279].

Bibliography

[1] Paula Watnick and Roberto Kolter. Biofilm, city of microbes. *Journal of bacteriology*, 182(10):2675–2679, 2000.

[2] Lina Xu, Peipei Ma, Bo Yuan, Qiang Chen, Sicong Lin, Xiao Chen, Zichun Hua, and Jian Shen. Anti-biofouling contact lenses bearing surface-immobilized layers of zwitterionic polymer by one-step modification. *RSC Adv.*, 4:15030–15035, 2014.

[3] Alex Wallace, Hassan Albadawi, Nikasha Patel, Ali Khademhosseini, Yu Shrike Zhang, Sailendra Naidu, Grace Knuttinen, and Rahmi Oklu. Anti-fouling strategies for central venous catheters. *Cardiovascular diagnosis and therapy*, 7(Suppl 3):S246–S257, 12 2017.

[4] D Pavithra and Mukesh Doble. Biofilm formation, bacterial adhesion and host response on polymeric implants—issues and prevention. *Biomedical Materials*, 3(3):034003, 2008.

[5] Matthew Wilkins, Luanne Hall-Stoodley, Raymond N Allan, and Saul N Faust. New approaches to the treatment of biofilm-related infections. *Journal of Infection*, 69:S47–S52, 2014.

[6] Niels Høiby, Thomas Bjarnsholt, Michael Givskov, Søren Molin, and Oana Ciofu. Antibiotic resistance of bacterial biofilms. *International journal of antimicrobial agents*, 35(4):322–332, 2010.

[7] Maneesha P Ginige, Jason Wylie, and Jason Plumb. Influence of biofilms on iron and manganese deposition in drinking water distribution systems. *Biofouling*, 27(2):151–163, 2011.

[8] Asif Matin, Tahar Laoui, Wail Falath, and Mohammed Farooque. Fouling control in reverse osmosis for water desalination & reuse: Current practices & emerging environment-friendly technologies. *Science of The Total Environment*, 765:142721, 2021.

[9] Katherine E Fish, Richard Collins, Nicola H Green, Rebecca L Sharpe, Isabel Douterelo, A Mark Osborn, and Joby B Boxall. Characterisation of the physical composition and microbial community structure of biofilms within a model full-scale drinking water distribution system. *PLoS One*, 10(2):e0115824, 2015.

[10] Gadi Borkow and Jeffrey Gabbay. Copper as a biocidal tool. *Current Medicinal Chemistry*, 12(18):2163–2175, aug 2005.

[11] Woods Hole Oceanographic Institution and United States. Navy Dept. Bureau of Ships. *Marine fouling and its prevention*. Number 580. United States Naval Institute, 1952.

[12] WF Higgins. Electrolytic corrosion of iron and copper. *Nature*, 173(4412):994, 1954.

[13] RL Townsin. The ship hull fouling penalty. *Biofouling*, 19(S1):9–15, 2003.

[14] MP Schultz, JA Bendick, ER Holm, and WM Hertel. Economic impact of biofouling on a naval surface ship. *Biofouling*, 27(1):87–98, 2011.

[15] Liesbeth Schrooten, Ina De Vlieger, Luc Int Panis, Cosimo Chiffi, and Enrico Pastori. Emissions of maritime transport: A european reference system. *Science of the Total Environment*, 408(2):318–323, 2009.

[16] Øyvind Buhaug, JJ Corbett, Ø Endresen, V Eyring, Jasper Faber, Shinichi Hanayama, David S Lee, Donchool Lee, Håkon Lindstad, Agnieszka Z Markowska, et al. *Second IMO ghg study 2009*. International Maritime Organization (IMO), 2009.

[17] Maureen E Callow and James A Callow. Marine biofouling: a sticky problem. *Biologist*, 49(1):1–5, 2002.

[18] George I. Loeb and Rex A. Neihof. *Marine Conditioning Films*, volume 145 of *Advances in Chemistry*, doi:10.1021/ba-1975-0145.ch016 16, pages 319–335. American Chemical Society (ACS), 2021/12/30 1975.

[19] Barbara Vu, Miao Chen, Russell J. Crawford, and Elena P. Ivanova. Bacterial extracellular polysaccharides involved in biofilm formation. *Molecules*, 14(7):2535–2554, 2009.

[20] Stefan Nehring. After the tbt era: Alternative anti-fouling paints and their ecological risks. *Senckenbergiana maritima*, 31(2):341, 2001.

[21] Michael A Champ. Economic and environmental impacts on ports and harbors from the convention to ban harmful marine anti-fouling systems. *Marine pollution bulletin*, 46(8):935–940, 2003.

[22] R.E Baier. The role of surface energy in thrombogenesis. *Bulletin of the New York Academy of Medicine*, 48:257–272, 1972.

[23] Robert F Brady Jr and Irwin L Singer. Mechanical factors favoring release from fouling release coatings. *Biofouling*, 15(1-3):73–81, 2000.

[24] Geoffrey W Swain and Michael P Schultz. The testing and evaluation of non-toxic antifouling coatings. *Biofouling*, 10(1-3):187–197, 1996.

[25] Michael Wade Keller, Scott R White, and Nancy R Sottos. A self-healing poly (dimethyl siloxane) elastomer. *Advanced Functional Materials*, 17(14):2399–2404, 2007.

[26] Irwin L Singer, James G Kohl, and Marc Patterson. Mechanical aspects of silicone coatings for hard foulant control. *Biofouling*, 16(2-4):301–309, 2000.

[27] S.K. Rath, J.G. Chavan, Savita Sasane, Jagannath, M. Patri, A.B. Samui, and B.C. Chakraborty. Two component silicone modified epoxy foul release coatings: Effect of modulus, surface energy and surface restructuring on pseudobarnacle and macrofouling behavior. *Applied Surface Science*, 256(8):2440–2446, 2010.

[28] Karin Y. Chumbimuni-Torres, Ramon E. Coronado, Adelphe M. Mfuh, Carlos Castro-Guerrero, Maria Fernanda Silva, George R. Negrete, Rena Bizios, and Carlos D. Garcia. Adsorption of proteins to thin-films of PDMS and its effect on the adhesion of human endothelial cells. *RSC Advances*, 1(4):706, 2011.

[29] Paul J Molino, Ewan Campbell, and Richard Wetherbee. Development of the initial diatom microfouling layer on antifouling and fouling-release surfaces in temperate and tropical australia. *Biofouling*, 25(8):685–694, 2009.

[30] John A Finlay, Maureen E Callow, Linnea K Ista, Gabriel P Lopez, and James A Callow. The influence of surface wettability on the adhesion strength of settled spores of the green alga enteromorpha and the diatom amphora. *Integrative and comparative biology*, 42(6):1116–1122, 2002.

[31] M E Callow, J A Callow, L K Ista, S E Coleman, A C Nolasco, and G P López. Use of self-assembled monolayers of different wettabilities to study surface selection and primary adhesion processes of green algal (enteromorpha) zoospores. *Appl Environ Microbiol*, 66(8):3249–3254, Aug 2000.

[32] Christopher R Deible, Patty Petrosko, Peter C Johnson, Eric J Beckman, Alan J Russell, and William R Wagner. Molecular barriers to biomaterial thrombosis by modification of surface proteins with polyethylene glycol. *Biomaterials*, 19(20):1885–1893, 1998.

[33] S. I Jeon, J. H Lee, J. D Andrade, and P. G De Gennes. Protein—surface interactions in the presence of polyethylene oxide: I. simplified theory. *Journal of Colloid and Interface Science*, 142(1):149–158, 1991.

[34] Willem Norde and Dick Gage. Interaction of bovine serum albumin and human blood plasma with PEO-tethered surfaces: influence of PEO chain length, grafting density, and temperature. *Langmuir*, 20(10):4162–4167, apr 2004.

[35] Warren Taylor, Stephen Ebbens, Maximillian WA Skoda, John RP Webster, and Richard AL Jones. Mode of lysozyme protein adsorption at end-tethered polyethylene oxide brushes on gold surfaces determined by neutron reflectivity. *The European Physical Journal E*, 38(3):14, 2015.

[36] Victoria M. Latza, Ignacio Rodriguez-Loureiro, Irena Kiesel, Avraham Halperin, Giovanna Fragneto, and Emanuel Schneck. Neutron reflectometry elucidates protein adsorption from human blood serum onto peg brushes. *Langmuir*, 33(44):12708–12718, 11 2017.

[37] Yan-qiang Wang, Ting Wang, Yan-lei Su, Fu-bing Peng, Hong Wu, and Zhong-yi Jiang. Remarkable reduction of irreversible fouling and improvement of the permeation properties of poly(ether sulfone) ultrafiltration membranes by blending with pluronic f127. *Langmuir*, 21(25):11856–11862, 12 2005.

[38] Yukari Oda, Manabu Inutsuka, Ryo Awane, Masayasu Totani, Norifumi L. Yamada, Masayuki Haraguchi, Masaaki Ozawa, Hisao Matsuno, and Keiji Tanaka. A dynamic interface based on segregation of an amphiphilic hyperbranched polymer containing fluoroalkyl and oligo(ethylene oxide) moieties. *Macromolecules*, 53(7):2380–2387, 04 2020.

[39] Wendy Van Zoelen, Ronald N Zuckermann, and Rachel A Segalman. Tunable surface properties from sequence-specific polypeptoid–polystyrene block copolymer thin films. *Macromolecules*, 45(17):7072–7082, 2012.

[40] Mahati Chintapalli, Ksenia Timachova, Kevin R Olson, Michał Banaszak, Jacob L Thelen, Sue J Mecham, Joseph M DeSimone, and Nitash P Balsara. Incipient microphase separation in short chain perfluoropolyether-block-poly (ethylene oxide) copolymers. *Soft matter*, 13(22):4047–4056, 2017.

[41] Elena Molena, Caterina Credi, Carmela De Marco, Marinella Levi, Stefano Turri, and Giovanni Simeone. Protein antifouling and fouling-release in perfluoropolyether surfaces. *Applied Surface Science*, 309:160–167, 2014.

[42] Yapei Wang, Louis M Pitet, John A Finlay, Lenora H Brewer, Gemma Cone, Douglas E Betts, Maureen E Callow, James A Callow, Dean E Wendt, Marc A Hillmyer, et al. Investigation of the role of hydrophilic chain length in amphiphilic perfluoropolyether/poly (ethylene glycol) networks: towards high-performance antifouling coatings. *Biofouling*, 27(10):1139–1150, 2011.

[43] Richard A. L. Jones and Randal W. Richards. *Polymers at surfaces and interfaces*. Cambridge University Press, 1999.

[44] Wei Chen and Thomas J McCarthy. Adsorption/migration of a perfluorohexylated fullerene from the bulk to the polymer/air interface. *Macromolecules*, 32(7):2342–2347, 1999.

[45] E Hecht. *Optics*, pages 114–115. Addision Wesley, San Francisco, 4th edition, 2002.

[46] G.E. Jellison. Ellipsometry. In John C. Lindon, editor, *Encyclopedia of Spectroscopy and Spectrometry*, pages 402–411. Elsevier, Oxford, 1999.

[47] S.O. Kasap, W.C. Tan, Jai Singh, and Asim K. Ray. *Fundamental Optical Properties of Materials I*, chapter 1, pages 1–36. John Wiley & Sons, Ltd, 2019.

[48] G. Beaucage, R. Composto, and R. S. Stein. Ellipsometric study of the glass transition and thermal expansion coefficients of thin polymer films. *Journal of Polymer Science Part B: Polymer Physics*, 31(3):319–326, 1993.

[49] J. L Keddie, R. A. L Jones, and R. A Cory. Size-dependent depression of the glass transition temperature in polymer films. *Europhysics Letters*, 27(1):59–64, jul 1994.

[50] Peiqing Ying, Yong Yu, Gang Jin, and Zulai Tao. Competitive protein adsorption studied with atomic force microscopy and imaging ellipsometry. *Colloids and Surfaces B: Biointerfaces*, 32(1):1–10, 2003.

[51] Michael P. Weir, Sasha Y. Heriot, Simon J. Martin, Andrew J. Parnell, Stephen A. Holt, John R. P. Webster, and Richard A. L. Jones. Voltage-induced swelling and deswelling of weak polybase brushes. *Langmuir*, 27(17):11000–11007, jul 2011.

[52] *Guide to Using WVASE 32: Spectroscopic Ellipsometry Data Acquisition and Analysis Software*. J. A. Woollam Company, Incorporated, 2008.

[53] John A. Woollam, Blaine D. Johs, Craig M. Herzinger, James N. Hilfiker, Ron A. Synowicki, and Corey L. Bungay. Overview of variable-angle spectroscopic ellipsometry (VASE): I. basic theory and typical applications. In *Optical Metrology: A Critical Review*, volume 10294. SPIE, jul 1999.

[54] Gerd Binnig and Heinrich Rohrer. Scanning tunneling microscopy. *IBM Journal of research and development*, 44(1/2):279, 2000.

[55] Yang Gan. Atomic and subnanometer resolution in ambient conditions by atomic force microscopy. *Surface Science Reports*, 64(3):99–121, 2009.

[56] Gerd Binnig, Calvin F Quate, and Ch Gerber. Atomic force microscope. *Physical review letters*, 56(9):930, 1986.

[57] Gerhard Meyer and Nabil M. Amer. Novel optical approach to atomic force microscopy. *Applied Physics Letters*, 53(12):1045–1047, sep 1988.

[58] Q. Zhong, D. Inniss, K. Kjoller, and V.B. Elings. Fractured polymer/silica fiber surface studied by tapping mode atomic force microscopy. *Surface Science*, 290(1):L688–L692, 1993.

[59] I. Schmitz, T. Prohaska, G. Friedbacher, M. Schreiner, and M. Grasserbauer. Investigation of corrosion processes on cleavage edges of potash-lime-silica glasses by atomic force microscopy. *Fresenius's Journal of Analytical Chemistry*, 353(5-8):666–669, 1995.

[60] E. Meyer, R. Overney, D. Brodbeck, L. Howald, R. Luthi, J. Frommer, and H.-J. Guntherodt. Friction and wear of langmuir-blodgett films observed by friction force microscopy. *Phys. Rev. Lett.*, 69(12):1777–1780, Sep 1992.

[61] I. Schmitz, M. Schreiner, G. Friedbacher, and M. Grasserbauer. Tapping-mode AFM in comparison to contact-mode AFM as a tool for in situ investigations of surface reactions with reference to glass corrosion. *Analytical Chemistry*, 69(6):1012–1018, mar 1997.

[62] 4PK Hansma, JP Cleveland, M Radmacher, DA Walters, PE Hillner, M Bezanilla, M Fritz, D Vie, HG Hansma, CB Prater, et al. Tapping mode atomic force microscopy in liquids. *Applied Physics Letters*, 64(13):1738–1740, 1994.

[63] L. Pasquina-Lemonche, J. Burns, R. D. Turner, S. Kumar, R. Tank, N. Mullin, J. S. Wilson, B. Chakrabarti, P. A. Bullough, S. J. Foster, and J. K. Hobbs. The architecture of the gram-positive bacterial cell wall. *Nature*, 582(7811):294–297, apr 2020.

[64] Andrew J. Parnell, Simon J. Martin, Richard A. L. Jones, C. Vasilev, Colin J. Crook, and Anthony J. Ryan. Direct visualization of the real time swelling and collapse of a poly(methacrylic acid) brush using atomic force microscopy. *Soft Matter*, 5(2):296–299, 2009.

[65] M. Radmacher, J.P. Cleveland, M. Fritz, H.G. Hansma, and P.K. Hansma. Mapping interaction forces with the atomic force microscope. *Biophysical Journal*, 66(6):2159–2165, 1994.

[66] L. Chopinet, C. Formosa, M.P. Rols, R.E. Duval, and E. Dague. Imaging living cells surface and quantifying its properties at high resolution using afm in qi^{TM} mode. *Micron*, 48:26–33, 2013.

[67] G. Smolyakov, C. Formosa-Dague, C. Severac, R.E. Duval, and E. Dague. High speed indentation measures by fv, qi and qnm introduce a new understanding of bionanomechanical experiments. *Micron*, 85:8–14, 2016.

[68] Lijiang Chen, Xiaohong Gu, Michael J. Fasolka, Jonathan W. Martin, and Tinh Nguyen. Effects of humidity and sample surface free energy on AFM probe-sample interactions and lateral force microscopy image contrast. *Langmuir*, 25(6):3494–3503, feb 2009.

[69] B. Cappella and G. Dietler. Force-distance curves by atomic force microscopy. *Surface Science Reports*, 34(1):1–104, 1999.

[70] Heinrich Hertz. Ueber die berührung fester elastischer körper. *Journal für die reine und angewandte Mathematik*, 1882(92):156–171, 1882.

[71] Ian N. Sneddon. The relation between load and penetration in the axisymmetric boussinesq problem for a punch of arbitrary profile. *International Journal of Engineering Science*, 3(1):47–57, 1965.

[72] Sidney R Cohen and Estelle Kalfon-Cohen. Dynamic nanoindentation by instrumented nanoindentation and force microscopy: a comparative review. *Bellstein Journal of Nanotechnology*, 4:815–833, nov 2013.

[73] Artur Zdunek and Andrzej Kurenda. Determination of the elastic properties of tomato fruit cells with an atomic force microscope. *Sensors*, 13(9):12175–12191, sep 2013.

[74] David Nečas and Petr Klapetek. Gwyddion: an open-source software for SPM data analysis. *Central European Journal of Physics*, 10(1):181–188, jan 2012.

[75] D.S. Sivia. *Elementary Scattering Theory*. Number 93. Oxford University Press, jan 2011.

[76] T.P. Russell. X-ray and neutron reflectivity for the investigation of polymers. *Materials Science Reports*, 5(4):171–271, 1990.

[77] Jeffrey Penfold and Robert K. Thomas. Neutron reflectivity and small angle neutron scattering: An introduction and perspective on recent progress. *Current Opinion in Colloid & Interface Science*, 19(3):198–206, 2014.

[78] Eric K. Lin, Darrin J. Pochan, Rainer Kolb, Wen-li Wu, and Sushil K. Satija. Neutron reflectometry for interfacial materials characterization. *AIP Conference Proceedings*, 449(1):879–882, 1998.

[79] T. Kanaya, T. Miyazaki, H. Watanabe, K. Nishida, H. Yamano, S. Tasaki, and D.B. Bucknall. Annealing effects on thickness of polystyrene thin films as studied by neutron reflectivity. *Polymer*, 44(14):3769–3773, 2003.

[80] Noboru Miyata and Tsukasa Miyazaki. Relatively thick (few micrometers) film structure estimated by back-incidence neutron reflectometry. *Physica B: Condensed Matter*, 551:449–451, 2018. The 11th International Conference on Neutron Scattering (ICNS 2017).

[81] R. A. L Jones, L. J Norton, E. J Kramer, R. J Composto, R. S Stein, T. P Russell, A Mansour, A Karim, G. P Felcher, M. H Rafailovich, J Sokolov, X Zhao, and S. A Schwarz. The form of the enriched surface layer in polymer blends. *EPL (Europhysics Letters)*, 12(1):41–46, may 1990.

[82] Andrew J. Parnell, Alan D. F. Dunbar, Andrew J. Pearson, Paul A. Staniec, Andrew J. C. Dennison, Hiroshi Hamamatsu, Maximilian W. A. Skoda, David G. Lidzey, and Richard. A. L. Jones. Depletion of pcbm at the cathode interface in p3ht/pcbm thin films as quantified via neutron reflectivity measurements. *Advanced Materials*, 22(22):2444–2447, 2010.

[83] G. BÜLDT, H. U. GALLY, A. SEELIG, J. SEELIG, and G. ZACCAI. Neutron diffraction studies on selectively deuterated phospholipid bilayers. *Nature*, 271(5641):182–184, jan 1978.

[84] JF Elman, BD Johs, TE Long, and JT Koberstein. A neutron reflectivity investigation of surface and interface segregation of polymer functional end groups. *Macromolecules*, 27(19):5341–5349, 1994.

[85] Giovanna Fragneto, Robert K. Thomas, Adrian R. Rennie, and Jeffrey Penfold. Neutron reflection from hexadecyltrimethylammonium bromide adsorbed on smooth and rough silicon surfaces. *Langmuir*, 12(25):6036–6043, 1996.

[86] Weinan Wang, Ezzeldin Metwalli, Jan Perlich, Kordelia Troll, Christine M. Papadakis, Robert Cubitt, and Peter Müller-Buschbaum. Water storage in thin films maintaining the total film thickness as probed with in situ neutron reflectivity. *Macromolecular Rapid Communications*, 30(2):114–119, 2009.

[87] J.J. Thomson. LXXXIII. rays of positive electricity. *The London, Edinburgh, and Dublin Philosophical Magazine and Journal of Science*, 20(118):752–767, oct 1910.

[88] Sarah Fearn. *An Introduction to Time-of-Flight Secondary Ion Mass Spectrometry (ToF-SIMS) and its Application to Materials Science*. 2053-2571. Morgan & Claypool Publishers, 2015.

[89] Ioannis V. Bletsos, David M. Hercules, Dieter. VanLeyen, and Alfred. Benninghoven. Time-of-flight secondary ion mass spectrometry of polymers in the mass range 500-10000. *Macromolecules*, 20(2):407–413, feb 1987.

[90] D. Briggs. Analysis of polymer surfaces by sims. 2—fingerprint spectra from simple polymer films. *Surface and Interface Analysis*, 4(4):151–155, 1982.

[91] Andrew L. Hook, Philip M. Williams, Morgan R. Alexander, and David J. Scurr. Multivariate ToF-SIMS image analysis of polymer microarrays and protein adsorption. *Biointerphases*, 10(1):019005, mar 2015.

[92] M. J. Bailey, M. Ismail, S. Bleay, N. Bright, M. Levin Elad, Y. Cohen, B. Geller, D. Everson, C. Costa, R. P. Webb, J. F. Watts, and M. de Puit. Enhanced imaging of developed fingerprints using mass spectrometry imaging. *The Analyst*, 138(21):6246, 2013.

[93] Tshaiya Devi Thandauthapani, Adam J. Reeve, Adam S. Long, Ian J. Turner, and James S. Sharp. Exposing latent fingermarks on problematic metal surfaces using time of flight secondary ion mass spectroscopy. *Science and Justice*, 58(6):405–414, 2018.

[94] James Bailey, Rasmus Havelund, Alexander G. Shard, Ian S. Gilmore, Morgan R. Alexander, James S. Sharp, and David J. Scurr. 3d ToF-SIMS imaging of polymer multilayer films using argon cluster sputter depth profiling. *ACS Applied Materials & Interfaces*, 7(4):2654–2659, jan 2015.

[95] A. Einstein. Über einen die erzeugung und verwandlung des lichtes betreffenden heuristischen gesichtspunkt. *Annalen der Physik*, 322(6):132–148, 1905.

[96] R. T. Beatty and Joseph John Thomson. The direct production of characteristic röntgen radiations by cathode particles. *Proceedings of the Royal*

Society of London. Series A, Containing Papers of a Mathematical and Physical Character, 87(598):511–518, 1912.

[97] S. Tougaard. Composition depth information from the inelastic background signal in xps. *Surface Science*, 162(1):875–885, 1985.

[98] Mark H. Engelhard, Donald R. Baer, Alberto Herrera-Gomez, and Peter M. A. Sherwood. Introductory guide to backgrounds in XPS spectra and their impact on determining peak intensities. *Journal of Vacuum Science & Technology A*, 38(6):063203, dec 2020.

[99] Gabriel P. López, David G. Castner, and Buddy D. Ratner. Xps o 1s binding energies for polymers containing hydroxyl, ether, ketone and ester groups. *Surface and Interface Analysis*, 17(5):267–272, 1991.

[100] Gianfranco Giorgianni, Chalachew Mebrahtu, Manfred Erwin Schuster, Alexander Ian Large, Georg Held, Pilar Ferrer, Federica Venturini, David Grinter, Regina Palkovits, Siglinda Perathoner, Gabriele Centi, Salvatore Abate, and Rosa Arrigo. Elucidating the mechanism of the CO2 methanation reaction over ni–fe hydrotalcite-derived catalysts via surface-sensitive in situ XPS and NEXAFS. *Physical Chemistry Chemical Physics*, 22(34):18788–18797, 2020.

[101] C. D. Wagner, L. E. Davis, M. V. Zeller, J. A. Taylor, R. H. Raymond, and L. H. Gale. Empirical atomic sensitivity factors for quantitative analysis by electron spectroscopy for chemical analysis. *Surface and Interface Analysis*, 3(5):211–225, 1981.

[102] Jacques Cazaux. About the charge compensation of insulating samples in xps. *Journal of Electron Spectroscopy and Related Phenomena*, 113(1):15–33, 2000.

[103] Donald R. Baer, Kateryna Artyushkova, Hagai Cohen, Christopher D. Easton, Mark Engelhard, Thomas R. Gengenbach, Grzegorz Greczynski, Paul Mack, David J. Morgan, and Adam Roberts. XPS guide: Charge neutralization and binding energy referencing for insulating samples. *Journal of Vacuum Science & Technology A*, 38(3):031204, may 2020.

[104] J.H. Scofield. Hartree-slater subshell photoionization cross-sections at 1254 and 1487 ev. *Journal of Electron Spectroscopy and Related Phenomena*, 8(2):129–137, 1976.

[105] Nenad Stojilovic. Why can't we see hydrogen in x-ray photoelectron spectroscopy? *Journal of Chemical Education*, 89(10):1331–1332, jul 2012.

[106] Jian-Qiang Zhong, Mengen Wang, William H. Hoffmann, Matthijs A. van Spronsen, Deyu Lu, and J. Anibal Boscoboinik. Synchrotron-based ambient pressure x-ray photoelectron spectroscopy of hydrogen and helium. *Appllied Physics Letters*, 112(9):091602, feb 2018.

[107] G Ketteler, P Ashby, B S Mun, I Ratera, H Bluhm, B Kasemo, and M Salmeron. In situ photoelectron spectroscopy study of water adsorption on model biomaterial surfaces. *Journal of Physics: Condensed Matter*, 20(18):184024, apr 2008.

[108] Pinar Aydogan Gokturk, Mikayla Barry, Rachel Segalman, and Ethan J. Crumlin. Directly probing polymer thin film chemistry and counterion influence on water sorption. *Applied Polymer Materials*, 2(11):4752–4761, sep 2020.

[109] Susan Trolier-McKinstry. *Crystal Chemistry of Piezoelectric Materials*, pages 39–56. Springer US, Boston, MA, 2008.

[110] F. R. Lack, G. W. Willard, and I. E. Fair. Some improvements in quartz crystal circuit elements. *The Bell System Technical Journal*, 13(3):453–463, 1934.

[111] Gunter Sauerbrey. Verwendung von schwingquarzen zur wagung dunner schichten und zur mikrowagung. *Zeitschrift fur Physik*, 155(2):206–222, apr 1959.

[112] Han Zhuang, Pin Lu, Siak Piang Lim, and Heow Pueh Lee. Frequency response of a quartz crystal microbalance loaded by liquid drops. *Langmuir*, 23(13):7392–7397, may 2007.

[113] W. H. King. Piezoelectric sorption detector. *Analytical Chemistry*, 36(9):1735–1739, aug 1964.

[114] K. Keiji. Kanazawa and Joseph G. Gordon. Frequency of a quartz microbalance in contact with liquid. *Analytical Chemistry*, 57(8):1770–1771, jul 1985.

[115] K Keiji Kanazawa and Joseph G Gordon. The oscillation frequency of a quartz resonator in contact with liquid. *Analytica Chimica Acta*, 175:99–105, 1985.

[116] Bryan D. Vogt, Eric K. Lin, Wen li Wu, and Christopher C. White. Effect of film thickness on the validity of the sauerbrey equation for hydrated polyelectrolyte films. *The Journal of Physical Chemsitry B*, 108(34):12685–12690, jul 2004.

[117] Christopher C. White and John L. Schrag. Theoretical predictions for the mechanical response of a model quartz crystal microbalance to two viscoelastic media: A thin sample layer and surrounding bath medium. *The Journal of Chemical Physics*, 111(24):11192–11206, dec 1999.

[118] Michael Rodahl, Fredrik Höök, Anatol Krozer, Peter Brzezinski, and Bengt Kasemo. Quartz crystal microbalance setup for frequency and q-factor measurements in gaseous and liquid environments. *Review of Scientific Instruments*, 66(7):3924–3930, jul 1995.

[119] Lloyd B. Eldred, William P. Baker, and Anthony N. Palazotto. Kelvin-voigt versus fractional derivative model as constitutive relations for viscoelastic materials. *AAIA Journal*, 33(3):547–550, mar 1995.

[120] M V Voinova, M Rodahl, M Jonson, and B Kasemo. Viscoelastic acoustic response of layered polymer films at fluid-solid interfaces: Continuum mechanics approach. *Physica Scripta*, 59(5):391–396, may 1999.

[121] Arno Domack, Oswald Prucker, Jürgen Rühe, and Diethelm Johannsmann. Swelling of a polymer brush probed with a quartz crystal resonator. *Phys. Rev. E*, 56:680–689, Jul 1997.

[122] Kazi Sadman, Clinton G. Wiener, R. A. Weiss, Christopher C. White, Kenneth R. Shull, and Bryan D. Vogt. Quantitative rheometry of thin soft materials using the quartz crystal microbalance with dissipation. *Analytical Chemistry*, 90(6):4079–4088, feb 2018.

[123] Garret C. DeNolf, Lauren F. Sturdy, and Kenneth R. Shull. High-frequency rheological characterization of homogeneous polymer films with the quartz crystal microbalance. *Langmuir*, 30(32):9731–9740, aug 2014.

[124] D. H. Bangham and R. I. Razouk. Adsorption and the wettability of solid surfaces. *From the journal: Transactions of the Faraday Society*, 33:1459, 1937.

[125] Thomas Young. Iii. an essay on the cohesion of fluids. *Philosophical Transactions of the Royal Society of London*, 95:65–87, 1805.

[126] Malcolm E Schrader. Young-dupre revisited. *Langmuir*, 11(9):3585–3589, 1995.

[127] Frederick M. Fowkes. ATTRACTIVE FORCES AT INTERFACES. *Industrial and Engineering Chemistry*, 56(12):40–52, dec 1964.

[128] D. K. Owens and R. C. Wendt. Estimation of the surface free energy of polymers. *Journal of Applied Polymer Science*, 13(8):1741–1747, 1969.

[129] D. H. Kaelble. Dispersion-polar surface tension properties of organic solids. *The Journal of Adhesion*, 2(2):66–81, apr 1970.

[130] Bronisław Jańczuk and Tomasz Białłopiotrowicz. Surface free-energy components of liquids and low energy solids and contact angles. *Journal of Colloid and Interface Science*, 127(1):189–204, 1989.

[131] Ivan J. Boyer. Toxicity of dibutyltin, tributyltin and other organotin compounds to humans and to experimental animals. *Toxicology*, 55(3):253–298, 1989.

[132] Shengxin Zhang, Lei Wang, Zhen Wang, Deling Fan, Lili Shi, and Jining Liu. Derivation of freshwater water quality criteria for dibutyltin dilaurate from measured data and data predicted using interspecies correlation estimate models. *Chemosphere*, 171:142–148, 2017.

[133] Li hui An, Yanqiang Zhang, Shuang shuang Song, Yue Liu, Zi cheng Li, Hao Chen, Xing ru Zhao, Kun Lei, Junmin Gao, and Bing hui Zheng. Imposex effects on the veined rapa whelk (rapana venosa) in bohai bay, china. *Ecotoxicology*, 22(3):538–547, feb 2013.

[134] G. Wagner, Ö.Kenessey. A new catalytic method for crosslinking of silicone polymers. *Journal of Applied Polymer Science*, 69(9):1705–1709, 1998.

[135] Azadeh Kaffashi, Ali Jannesari, and Zahra Ranjbar. Silicone fouling-release coatings: effects of the molecular weight of poly(dimethylsiloxane) and tetraethyl orthosilicate on the magnitude of pseudobarnacle adhesion strength. *Biofouling*, 28(7):729–741, 2012. PMID: 22793997.

[136] Vinodh Rajendra, Yang Chen, and Michael A. Brook. Structured hydrophilic domains on silicone elastomers. *Polym. Chem.*, 1:312–320, 2010.

[137] Adrian R. Rennie, Maja S. Hellsing, Eric Lindholm, and Anders Olsson. Note: Sample cells to investigate solid/liquid interfaces with neutrons. *Review of Scientific Instruments*, 86(1):016115, 2015.

[138] Doekele G. Stavenga. Thin film and multilayer optics cause structural colors of many insects and birds. *Materials Today: Proceedings*, 1:109–121, 2014. Living Light: Uniting biology and photonics – A memorial meeting in honour of Prof Jean-Pol Vigneron.

[139] G. Carcano, M. Ceriani, and F. Soglio. Spin coating with high viscosity photoresist on square substrates — applications in the thin film hybrid microwave integrated circuit field. *Microelectonics International*, 10(3):12–20, mar 1993.

[140] Lothar Weh. Hyperbolic spirals as surface structures in thin layers. *Journal of Colloid and Interface Science*, 235(2):210–217, 2001.

[141] Kenneth R. Shull. Wetting autophobicity of polymer melts. *Faraday Discuss.*, 98:203–217, 1994.

[142] E. F. Hare and W. A. Zisman. Autophobic liquids and the properties of their adsorbed films. *The Journal of Physical Chemistry*, 59(4):335–340, apr 1955.

[143] R. J. Waltman. Autophobic dewetting of z-tetraol perfluoropolyether lubricant films on the amorphous nitrogenated carbon surface. *Langmuir*, 20(8):3166–3172, mar 2004.

[144] B.V Derjaguin and N.V Churaev. Structural component of disjoining pressure. *Journal of Colloid and Interface Science*, 49(2):249–255, 1974.

[145] Günter Reiter and Rajesh Khanna. Real-time determination of the slippage length in autophobic polymer dewetting. *Phys. Rev. Lett.*, 85:2753–2756, Sep 2000.

[146] ByungG. Min, JeongW. Choi, HughR. Brown, DoY. Yoon, TeresaM. O'Connor, and MyungS. Jhon. Spreading characteristics of thin liquid films of perfluoropolyalkylethers on solid surfaces. effects of chain-end functionality and humidity. *Tribology Letters*, 1(2-3), nov 1995.

[147] Hyun I. Kim, C. Mathew Mate, Kelly A. Hannibal, and Scott S. Perry. How disjoining pressure drives the dewetting of a polymer film on a silicon surface. *Phys. Rev. Lett.*, 82:3496–3499, Apr 1999.

[148] R.J. Waltman. The stability of ultra-thin perfluoropolyether mixture films on the amorphous nitrogenated carbon surface. *Journal of Colloid and Interface Science*, 313(2):608–611, 2007.

[149] F. Heslot, A. M. Cazabat, and P. Levinson. Dynamics of wetting of tiny drops: Ellipsometric study of the late stages of spreading. *Phys. Rev. Lett.*, 62:1286–1289, Mar 1989.

[150] F. Heslot, N. Fraysse, and A. M. Cazabat. Molecular layering in the spreading of wetting liquid drops. *Nature*, 338(6217):640–642, 1989.

[151] M. P. Valignat, N. Fraysse, A. M. Cazabat, and F. Heslot. Molecular networks in the spreading of microdroplets. *Langmuir*, 9(2):601–603, feb 1993.

[152] N. Fraysse, M.P. Valignat, A.M. Cazabat, F. Heslot, and P. Levinson. The spreading of layered microdroplets. *Journal of Colloid and Interface Science*, 158(1):27–32, 1993.

[153] Michael F. Toney, C. Mathew Mate, and K. Amanda Leach. Roughness of molecularly thin perfluoropolyether polymer films. *Applied Physics Letters*, 77(20):3296–3298, 2000.

[154] Li Yang, Naoto Shirahata, Gaurav Saini, Feng Zhang, Lei Pei, Matthew C. Asplund, Dirk G. Kurth, Katsuhiko Ariga, Ken Sautter, Takashi Nakanishi, Vincent Smentkowski, and Matthew R. Linford. Effect of surface free energy on PDMS transfer in microcontact printing and its application to ToF-SIMS to probe surface energies. *Langmuir*, 25(10):5674–5683, apr 2009.

[155] B Shogrin, WR Jones JR, and P Herrera-Fierro. Spontaneous dewetting of a perfluoropolyether. *Lubrication engineering*, 52(9):712–717, 1996.

[156] Alain Lapp, Claude Picot, and Henri Benoit. Determination of the flory interaction parameters in miscible polymer blends by measurement of the apparent radius of gyration. *Macromolecules*, 18(12):2437–2441, 1985.

[157] V. Arrighi, S. Gagliardi, A. C. Dagger, J. A. Semlyen, J. S. Higgins, and M. J. Shenton. Conformation of cyclics and linear chain polymers in bulk by sans. *Macromolecules*, 37(21):8057–8065, 10 2004.

[158] Guennadi Evmenenko, Haiding Mo, Sumit Kewalramani, and Pulak Dutta. Conformational rearrangements in interfacial region of polydimethylsiloxane melt films. *Polymer*, 47(3):878–882, 2006.

[159] N. Herbots, Qian Xing, M. Hart, J.D. Bradley, D.A. Sell, R.J. Culbertson, and Barry J. Wilkens. Ibmm of oh adsorbates and interphases on si-based materials. *Nuclear Instruments and Methods in Physics Research Section B: Beam Interactions with Materials and Atoms*, 272:330–333, 2012. Proceedings of the 17th International Conference on Ion Beam Modification of Materials (IBMM 2010).

[160] Chunyan Chen, Jie Wang, and Zhan Chen. Surface restructuring behavior of various types of poly(dimethylsiloxane) in water detected by sfg. *Langmuir*, 20(23):10186–10193, 11 2004.

[161] Yuwei Liu, Chuan Leng, Bret Chisholm, Shane Stafslien, Partha Majumdar, and Zhan Chen. Surface structures of pdms incorporated with quaternary ammonium salts designed for antibiofouling and fouling release applications. *Langmuir*, 29(9):2897–2905, 03 2013.

[162] Manabu Inutsuka, Norifumi L. Yamada, Kohzo Ito, and Hideaki Yokoyama. High density polymer brush spontaneously formed by the segregation of amphiphilic diblock copolymers to the polymer/water interface. *ACS Macro Letters*, 2(3):265–268, mar 2013.

[163] Harihara S. Sundaram, Youngjin Cho, Michael D. Dimitriou, Craig J. Weinman, John A. Finlay, Gemma Cone, Maureen E. Callow, James A. Callow, Edward J. Kramer, and Christopher K. Ober. Fluorine-free mixed amphiphilic polymers based on pdms and peg side chains for fouling release applications. *Biofouling*, 27(6):589–602, 2011. PMID: 21985292.

[164] Robert T Foister. Dynamic surface properties due to amine migration and chemical reaction in primary amine/epoxide systems. *Journal of Colloid and Interface Science*, 99(2):568–585, 1984.

[165] Chwan-Hwa Chiang, Hatsuo Ishida, and Jack L Koenig. The structure of γ-aminopropyltriethoxysilane on glass surfaces. *Journal of Colloid and Interface Science*, 74(2):396–404, 1980.

[166] Viktoriia Drebezghova, Hubert Gojzewski, Ahmed Allal, Mark A. Hempenius, Corinne Nardin, and G. Julius Vancso. Network mesh nanostructures in cross-linked poly(dimethylsiloxane) visualized by afm. *Macromolecular Chemistry and Physics*, 221(17):2000170, 2020.

[167] Nora Graf, Eda Yegen, Thomas Gross, Andreas Lippitz, Wilfried Weigel, Simone Krakert, Andreas Terfort, and Wolfgang E.S. Unger. Xps and nexafs studies of aliphatic and aromatic amine species on functionalized surfaces. *Surface Science*, 603(18):2849–2860, 2009.

[168] David S. Jensen, Supriya S. Kanyal, Nitesh Madaan, Michael A. Vail, Andrew E. Dadson, Mark H. Engelhard, and Matthew R. Linford. Silicon (100)/sio2 by xps. *Surface Science Spectra*, 20(1):36–42, 2013.

[169] Pierre Louette, Frederic Bodino, and Jean-Jacques Pireaux. Poly(dimethyl siloxane) (pdms) xps reference core level and energy loss spectra. *Surface Science Spectra*, 12(1):38–43, 2005.

[170] Zhixin Wang, Alex A. Volinsky, and Nathan D. Gallant. Crosslinking effect on polydimethylsiloxane elastic modulus measured by custom-built compression instrument. *Journal of Applied Polymer Science*, 131(22), 2014.

[171] Koji Miyake, Noriaki Satomi, and Shinya Sasaki. Elastic modulus of polystyrene film from near surface to bulk measured by nanoindentation using atomic force microscopy. *Applied Physics Letters*, 89(3):031925, jul 2006.

[172] CGPH Schroen, MA Cohen Stuart, K Van der Voort Maarschalk, A Van der Padt, and K Van't Riet. Influence of preadsorbed block copolymers on protein adsorption: surface properties, layer thickness, and surface coverage. *Langmuir*, 11(8):3068–3074, 1995.

[173] M. Reza Nejadnik, Adam L. J. Olsson, Prashant K. Sharma, Henny C. van der Mei, Willem Norde, and Henk J. Busscher. Adsorption of pluronic f-127 on surfaces with different hydrophobicities probed by quartz crystal microbalance with dissipation. *Langmuir*, 25(11):6245–6249, apr 2009.

[174] Kevin L. Prime and George M. Whitesides. Adsorption of proteins onto surfaces containing end-attached oligo(ethylene oxide): a model system using self-assembled monolayers. *Journal of the American Chemical Society*, 115(23):10714–10721, nov 1993.

[175] Yi He, Yung Chang, Jason C. Hower, Jie Zheng, Shengfu Chen, and Shaoyi Jiang. Origin of repulsive force and structure/dynamics of interfacial water in OEG–protein interactions: a molecular simulation study. *Physical Chemistry Chemical Physics*, 10(36):5539, 2008.

[176] Tomohiro Hayashi, Yusaku Tanaka, Yuki Koide, Masaru Tanaka, and Masahiko Hara. Mechanism underlying bioinertness of self-assembled monolayers of oligo(ethyleneglycol)-terminated alkanethiols on gold: protein adsorption, platelet adhesion, and surface forces. *Phys. Chem. Chem. Phys.*, 14:10196–10206, 2012.

[177] Daniel J. Müller, Dimitrios Fotiadis, Simon Scheuring, Shirley A. Müller, and Andreas Engel. Electrostatically balanced subnanometer imaging of biological specimens by atomic force microscope. *Biophysical Journal*, 76(2):1101–1111, 1999.

[178] Yohei Kamata, Andrew J. Parnell, Philipp Gutfreund, Maximilian W. A. Skoda, Andrew J. C. Dennison, Robert Barker, Shaomin Mai, Jonathan R. Howse, Anthony J. Ryan, Naoya Torikai, Masami Kawaguchi, and Richard A. L. Jones. Hydration and ordering of lamellar block copolymer films under controlled water vapor. *Macromolecules*, 47(24):8682–8690, dec 2014.

[179] Aljoša Hafner, Philipp Gutfreund, Boris P Toperverg, Mark Geoghegan, and Michele Sferrazza. 2d reflectometry for the investigation of polymer interfaces: off-specular neutron scattering. *Journal of Physics: Condensed Matter*, 33(36):364002, jul 2021.

[180] Aljoša Hafner, Philipp Gutfreund, Boris P. Toperverg, Andrew O. F. Jones, Johann P. de Silva, Andrew Wildes, Henry E. Fischer, Mark Geoghegan,

and Michele Sferrazza. Combined specular and off-specular reflectometry: elucidating the complex structure of soft buried interfaces. *Journal of Applied Crystallography*, 54(3):924–948, Jun 2021.

[181] M. C. Gerstenberg, J. S. Pedersen, J. Majewski, and G. S. Smith. Surface induced ordering of triblock copolymer micelles at the solid-liquid interface. 1. experimental results. *Langmuir*, 18(12):4933–4943, may 2002.

[182] Marc A. Rufin, Mikayla E. Barry, Paige A. Adair, Melissa L. Hawkins, Jeffery E. Raymond, and Melissa A. Grunlan. Protein resistance efficacy of peo-silane amphiphiles: Dependence on peo-segment length and concentration. *Acta Biomaterialia*, 41:247–252, 2016.

[183] Bryan Khai D. Ngo, Kendrick K. Lim, Shane J. Stafslien, and Melissa A. Grunlan. Stability of silicones modified with peo-silane amphiphiles: Impact of structure and concentration. *Polymer Degradation and Stability*, 163:136–142, 2019.

[184] Zhangwang Xie, Nagaveena Nagaraja, Lucy Skillman, Dan Li, and Goen Ho. Comparison of polysaccharide fouling in forward osmosis and reverse osmosis separations. *Desalination*, 402:174–184, 2017.

[185] Veena Nagaraj, Lucy Skillman, Dan Li, and Goen Ho. Review – bacteria and their extracellular polymeric substances causing biofouling on seawater reverse osmosis desalination membranes. *Journal of Environmental Management*, 223:586–599, 2018.

[186] Shawn Lewenza. Extracellular dna-induced antimicrobial peptide resistance mechanisms in pseudomonas aeruginosa. *Frontiers in Microbiology*, 4:21, 2013.

[187] Satoshi Tsuneda, Hirotoshi Aikawa, Hiroshi Hayashi, Atsushi Yuasa, and Akira Hirata. Extracellular polymeric substances responsible for bacterial adhesion onto solid surface. *FEMS microbiology letters*, 223(2):287–292, 2003.

[188] Moshe Herzberg, Seoktae Kang, and Menachem Elimelech. Role of extracellular polymeric substances (EPS) in biofouling of reverse osmosis membranes. *Environmental Science and Technology*, 43(12):4393–4398, may 2009.

[189] Vladimir Hlady and Jos Buijs. Protein adsorption on solid surfaces. *Current Opinion in Biotechnology*, 7(1):72–77, 1996.

[190] Singhvi Rahul, Kumar Amit, Lopez Gabriel P., Stephanopoulos Gregory N., Wang Daniel I. C., Whitesides George M., and Ingber Donald E. Engineering cell shape and function. *Science*, 264(5159):696–698, 2021/11/15 1994.

[191] Robert H. Staat, Thomas H. Gawronski, and Charles F. Schachtele. Detection and preliminary studies on dextranase-producing microorganisms from human dental plaque. *Infecion and Immunity*, 8(6):1009–1016, dec 1973.

[192] World Health Organization. World health organization model list of essential medicines: 21st list 2019. Technical documents, World Health Organization, 2019.

[193] S. Badel, C. Laroche, C. Gardarin, T. Bernardi, and P. Michaud. New method showing the influence of matrix components in leuconostoc mesenteroides biofilm formation. *Applied Biochemistry and Biotechnology*, 151(2-3):364–370, apr 2008.

[194] Weilan Li, Hongyan Liu, and Qiong Xu. Extracellular dextran and dna affect the formation of enterococcus faecalis biofilms and their susceptibility to 2% chlorhexidine. *Journal of Endodontics*, 38(7):894–898, 2012.

[195] Paul J. Molino, Michael J. Higgins, Peter C. Innis, Robert. M. I. Kapsa, and Gordon G. Wallace. Fibronectin and bovine serum albumin adsorption and conformational dynamics on inherently conducting polymers: A QCM-d study. *Langmuir*, 28(22):8433–8445, may 2012.

[196] Hanh T. M. Phan, Shannon Bartelt-Hunt, Keith B. Rodenhausen, Mathias Schubert, and Jason C. Bartz. Investigation of bovine serum albumin (bsa) attachment onto self-assembled monolayers (sams) using combinatorial quartz crystal microbalance with dissipation (qcm-d) and spectroscopic ellipsometry (se). *PLOS ONE*, 10(10):1–20, 10 2015.

[197] Theodore Peters Jr. *All about albumin: biochemistry, genetics, and medical applications*. Academic press, 1995.

[198] Marie Wahlgren, Thomas Arnebrant, and Ingemar Lundström. The adsorption of lysozyme to hydrophilic silicon oxide surfaces: Comparison between experimental data and models for adsorption kinetics. *Journal of colloid and interface science*, 175(2):506–514, 1995.

[199] L. M. Rzepecki, K. M. Hansen, and J. H. Waite. Characterization of a cystine-rich polyphenolic protein family from the blue mussel mytilus edulis l. *The Biological Bulletin*, 183(1):123–137, 1992. PMID: 29304577.

[200] Miaoer Yu and Timothy J. Deming. Synthetic polypeptide mimics of marine adhesives. *Macromolecules*, 31(15):4739–4745, 07 1998.

[201] Sander Haemers, Ger J. M. Koper, and Gert Frens. Effect of oxidation rate on cross-linking of mussel adhesive proteins. *Macromolecules*, 4(3):632–640, mar 2003.

[202] Matt P. Deacon, Stanley S. Davis, J. Herbert Waite, and Stephen E. Harding. Structure and mucoadhesion of mussel glue protein in dilute solution. *Biochemistry*, 37(40):14108–14112, 10 1998.

[203] Warren Taylor and Richard A. L. Jones. Protein adsorption on well-characterized polyethylene oxide brushes on gold: Dependence on molecular weight and grafting density. *Langmuir*, 29(20):6116–6122, 05 2013.

[204] Kamatchi Sankaranarayanan, A Dhathathreyan, and Reinhard Miller. Assembling fibrinogen at air/water and solid/liquid interfaces using langmuir and langmuir- blodgett films. *The Journal of Physical Chemistry B*, 114(24):8067–8075, 2010.

[205] Kim S. Siow, Leanne Britcher, Sunil Kumar, and Hans J. Griesser. Qcm-d and xps study of protein adsorption on plasma polymers with sulfonate and phosphonate surface groups. *Colloids and Surfaces B: Biointerfaces*, 173:447–453, 2019.

[206] Fan Zhang, Guoxin Xie, and Jinshan Pan. Tunable adsorption and film formation of mussel adhesive protein by potential control. *Langmuir*, 33(35):8749–8756, jan 2017.

[207] Fredrik Höök, Bengt Kasemo, Tommy Nylander, Camilla Fant, Kristin Sott, and Hans Elwing. Variations in coupled water, viscoelastic properties, and film thickness of a mefp-1 protein film during adsorption and cross-linking: a quartz crystal microbalance with dissipation monitoring, ellipsometry, and surface plasmon resonance study. *Analytical chemistry*, 73(24):5796–5804, 2001.

[208] Kideok D. Kwon, Hans Green, Patrik Bjöörn, and James D. Kubicki. Model bacterial extracellular polysaccharide adsorption onto silica and alumina: quartz crystal microbalance with dissipation monitoring of dextran adsorption. *Environmental Science and Technology*, 40(24):7739–7744, nov 2006.

[209] W. A. Porter and Stephen W. Anderson. The effects of temperature on the accuracy of crystal oscillator thickness monitors. *Journal of Vacuum Science and Technology*, 9(6):1472–1474, nov 1972.

[210] Theresa M. McIntire and David A. Brant. Observations of the (1→3)-β-d-glucan linear triple helix to macrocycle interconversion using noncontact atomic force microscopy. *Journal of the American Chemical Society*, 120(28):6909–6919, 07 1998.

[211] Theresa M. McIntire and David A. Brant. Imaging of individual biopolymers and supramolecular assemblies using noncontact atomic force microscopy. *Biopolymers*, 42(2):133–146, 1997.

[212] Yonggang Liu, Reinhard Lipowsky, and Rumiana Dimova. Concentration dependence of the interfacial tension for aqueous two-phase polymer solutions of dextran and polyethylene glycol. *Langmuir*, 28(8):3831–3839, 02 2012.

[213] Tsueu Ju Su, Jian Ren Lu, Robert K. Thomas, Zhan Feng Cui, and Jeffrey Penfold. The adsorption of lysozyme at the silica–water interface: A neutron reflection study. *Journal of Colloid and Interface Science*, 203(2):419–429, 1998.

[214] T. J. Su, Lu, R. K. Thomas, Z. F. Cui, and J. Penfold. The conformational structure of bovine serum albumin layers adsorbed at the silica-water interface. *The Journal of Physical Chemistry B*, 102(41):8100–8108, sep 1998.

[215] J.R. Lu, T.J. Su, P.N. Thirtle, R.K. Thomas, A.R. Rennie, and R. Cubitt. The denaturation of lysozyme layers adsorbed at the hydrophobic solid/liquid surface studied by neutron reflection. *Journal of Colloid and Interface Science*, 206(1):212–223, 1998.

[216] H. Hillborg, J.F. Ankner, U.W. Gedde, G.D. Smith, H.K. Yasuda, and K. Wikström. Crosslinked polydimethylsiloxane exposed to oxygen plasma studied by neutron reflectometry and other surface specific techniques. *Polymer*, 41(18):6851–6863, 2000.

[217] Aase Hvidt and Sigurd O. Nielsen. Hydrogen exchange in proteins. volume 21 of *Advances in Protein Chemistry*, pages 287–386. Academic Press, 1966.

[218] Ywu-Jang Fu, Hsuan zhi Qui, Kuo-Sung Liao, Shingjiang Jessie Lue, Chien-Chieh Hu, Kueir-Rarn Lee, and Juin-Yih Lai. Effect of UV-ozone treatment on poly(dimethylsiloxane) membranes: Surface characterization and gas separation performance. *Langmuir*, 26(6):4392–4399, dec 2009.

[219] F Höök, J Vörös, M Rodahl, R Kurrat, P Böni, J.J Ramsden, M Textor, N.D Spencer, P Tengvall, J Gold, and B Kasemo. A comparative study of protein adsorption on titanium oxide surfaces using in situ ellipsometry, optical waveguide lightmode spectroscopy, and quartz crystal microbal-

ance/dissipation. *Colloids and Surfaces B: Biointerfaces*, 24(2):155–170, 2002.

[220] Tatsuro Goda and Yuji Miyahara. Interpretation of protein adsorption through its intrinsic electric charges: A comparative study using a field-effect transistor, surface plasmon resonance, and quartz crystal microbalance. *Langmuir*, 28(41):14730–14738, oct 2012.

[221] J. Talbot, G. Tarjus, P.R. Van Tassel, and P. Viot. From car parking to protein adsorption: an overview of sequential adsorption processes. *Colloids and Surfaces A: Physicochemical and Engineering Aspects*, 165(1):287–324, 2000.

[222] Einar L. Hinrichsen, Jens Feder, and Torstein Jossang. Geometry of random sequential adsorption. *Journal of Statistical Physics*, 44(5-6):793–827, sep 1986.

[223] Akihiko Kondo, Shinya Oku, and Ko Higashitani. Structural changes in protein molecules adsorbed on ultrafine silica particles. *Journal of Colloid and Interface Science*, 143(1):214–221, 1991.

[224] Christian F. Wertz and Maria M. Santore. Effect of surface hydrophobicity on adsorption and relaxation kinetics of albumin and fibrinogen: single-species and competitive behavior. *Langmuir*, 17(10):3006–3016, apr 2001.

[225] R. J. Green, I. Hopkinson, and R. A. L. Jones. Unfolding and intermolecular association in globular proteins adsorbed at interfaces. *Langmuir*, 15(15):5102–5110, jun 1999.

[226] Yasuhiro Yokoyama, Ryo Ishiguro, Hirotaka Maeda, Mayumi Mukaiyama, Keiichi Kameyama, and Koichi Hiramatsu. Quantitative analysis of protein adsorption on a planar surface by fourier transform infrared spectroscopy: lysozyme adsorbed on hydrophobic silicon-containing polymer. *Journal of Colloid and Interface Science*, 268(1):23–32, 2003.

[227] Nicolas Brouette, Giovanna Fragneto, Fabrice Cousin, Martine Moulin, Michael Haertlein, and Michele Sferrazza. A neutron reflection study of adsorbed deuterated myoglobin layers on hydrophobic surfaces. *Journal of Colloid and Interface Science*, 390(1):114–120, 2013.

[228] B.A. Jucker, H. Harms, S.J. Hug, and A.J.B. Zehnder. Adsorption of bacterial surface polysaccharides on mineral oxides is mediated by hydrogen bonds. *Colloids and Surfaces B: Biointerfaces*, 9(6):331–343, 1997.

[229] Benjamin T. Käsdorf, Florian Weber, Georgia Petrou, Vaibhav Srivastava, Thomas Crouzier, and Oliver Lieleg. Mucin-inspired lubrication on hydrophobic surfaces. *Biomacromolecules*, 18(8):2454–2462, jul 2017.

[230] Adolf Fick. Ueber diffusion. *Annalen der Physik*, 170(1):59–86, 1855.

[231] J. Crank. *The Mathematics of Diffusion*, page 4. Oxford science publications. Clarendon Press, 1975.

[232] G.T. Fieldson and T.A. Barbari. The use of fti.r.-a.t.r. spectroscopy to characterize penetrant diffusion in polymers. *Polymer*, 34(6):1146–1153, 1993.

[233] Kathleen Cogan Farinas, Lisa Doh, Subbu Venkatraman, and Russell O Potts. Characterization of solute diffusion in a polymer using atr-ftir spectroscopy and bulk transport techniques. *Macromolecules*, 27(18):5220–5222, 1994.

[234] Jack W. London and Alexis T. Bell. Infrared spectra of carbon monoxide, carbon dioxide, nitric oxide, nitrogen dioxide, nitrous oxide, and nitrogen adsorbed on copper oxide. *Journal of Catalysis*, 31(1):32–40, 1973.

[235] A. Camós Noguer, S.M. Olsen, S. Hvilsted, and S. Kiil. Diffusion of surface-active amphiphiles in silicone-based fouling-release coatings. *Progress in Organic Coatings*, 106:77–86, 2017.

[236] Amilcar Pillay Narrainen, Lian R. Hutchings, Imtiyaz Ansari, Richard L. Thompson, and Nigel Clarke. Multi-end-functionalized polymers: Additives to modify polymer properties at surfaces and interfaces. *Macromolecules*, 40(6):1969–1980, 03 2007.

[237] Hojun Lee and Lynden A Archer. Functionalizing polymer surfaces by surface migration of copolymer additives: role of additive molecular weight. *Polymer*, 43(9):2721–2728, 2002.

[238] Alex CM Kuo. Poly (dimethylsiloxane). *Polymer data handbook*, pages 411–435, 1999.

[239] H. A. Daynes and Samuel Walter Johnson Smith. The process of diffusion through a rubber membrane. *Proceedings of the Royal Society of London. Series A, Containing Papers of a Mathematical and Physical Character*, 97(685):286–307, 1920.

[240] R. M. Barrer and Eric K. Rideal. Permeation, diffusion and solution of gases in organic polymers. *Trans. Faraday Soc.*, 35:628–643, 1939.

[241] Francis J. Norton. Permeation of gaseous oxygen through vitreous silica. *Nature*, 191:701–701, 1961.

[242] Artur J. M. Valente, Alexandre Ya. Polishchuk, Victor M. M. Lobo, and Hugh D. Burrows. Transport properties of concentrated aqueous sodium dodecyl sulfate solutions in polymer membranes derived from cellulose esters. *Langmuir*, 16(16):6475–6479, 08 2000.

[243] Aslıhan Gøkaltun, Young Bok (Abraham) Kang, Martin L. Yarmush, O. Berk Usta, and Ayse Asatekin. Simple surface modification of poly(dimethylsiloxane) via surface segregating smart polymers for biomicrofluidics. *Scientific Reports*, 9(1):7377, 2019.

[244] Jun Kwon Park, Jeongeun Ryu, Bonchull C. Koo, Sanghyun Lee, and Kwan Hyoung Kang. How the change of contact angle occurs for an evaporating droplet: effect of impurity and attached water films. *Soft Matter*, 8:11889–11896, 2012.

[245] Tobias E. Balmer, Heinz Schmid, Richard Stutz, Emmanuel Delamarche, Bruno Michel, Nicholas D. Spencer, and Heiko Wolf. Diffusion of alkanethiols in pdms and its implications on microcontact printing (μcp). *Langmuir*, 21(2):622–632, 01 2005.

[246] A. N. Gent and R. H. Tobias. Diffusion and equilibrium swelling of macromolecular networks by their linear homologs. *Journal of Polymer Science: Polymer Physics Edition*, 20(12):2317–2327, 1982.

[247] L Masaro and X.X Zhu. Physical models of diffusion for polymer solutions, gels and solids. *Progress in Polymer Science*, 24(5):731–775, 1999.

[248] Leoncio Garrido, James E. Mark, Jerome L. Ackerman, and Robert A. Kinsey. Studies of self-diffusion of poly(dimethylsiloxane) chains in pdms model networks by pulsed field gradient nmr. *Journal of Polymer Science Part B: Polymer Physics*, 26(11):2367–2377, 1988.

[249] Vikash Sharma, Marshal Dhayal, Govind Gupta, Sonnada Shivaprasad, and S.C. Jain. Surface characterization of plasma-treated and peg-grafted pdms for micro fluidic applications. *Vacuum*, 81:1094–1100, 05 2007.

[250] Yalei Qiu, Shu Yang, and Kuang Sheng. Photolithographic patterning of cytop with limited contact angle degradation. *Micromachines*, 9(10), 2018.

[251] M. P. Walser, W. L. Kalb, T. Mathis, T. J. Brenner, and B. Batlogg. Stable complementary inverters with organic field-effect transistors on cytop fluoropolymer gate dielectric. *Applied Physics Letters*, 94(5):053303, 2009.

[252] Alexander G. Shard. Detection limits in xps for more than 6000 binary systems using al and mg kα x-rays. *Surface and Interface Analysis*, 46(3):175–185, 2014.

[253] J. L. S. Lee, S. Ninomiya, J. Matsuo, I. S. Gilmore, M. P. Seah, and A. G. Shard. Organic depth profiling of a nanostructured delta layer reference material using large argon cluster ions. *Analytical Chemistry*, 82(1):98–105, 01 2010.

[254] Nunzio Tuccitto, Alessandra Bombace, Alberto Torrisi, and Antonino Licciardello. Effect of sputtering yield changes on the depth resolution in cluster beam depth-profiling of polymers. *Journal of Vacuum Science & Technology B*, 36(3):03F124, 2018.

[255] Emily F. Smith, Jonathan D. P. Counsell, James Bailey, James S. Sharp, Morgan R. Alexander, Alexander G. Shard, and David J. Scurr. Sample rotation improves gas cluster sputter depth profiling of polymers. *Surface and Interface Analysis*, 49(10):953–959, 2017.

[256] James Bailey, Rasmus Havelund, Alexander G. Shard, Ian S. Gilmore, Morgan R. Alexander, James S. Sharp, and David J. Scurr. 3d tof-sims imaging of polymer multilayer films using argon cluster sputter depth profiling. *ACS Applied Materials & Interfaces*, 7(4):2654–2659, 02 2015.

[257] A. Jonáš, A. C. De Luca, G. Pesce, G. Rusciano, A. Sasso, S. Caserta, S. Guido, and G. Marrucci. Diffusive mixing of polymers investigated by raman microspectroscopy and microrheology. *Langmuir*, 26(17):14223–14230, 09 2010.

[258] André Bardow, Wolfgang Marquardt, Volker Göke, Hans-Jürgen Koss, and Klaus Lucas. Model-based measurement of diffusion using raman spectroscopy. *AIChE Journal*, 49(2):323–334, 2003.

[259] Christine Blesinger, Peter Beumers, Frederic Buttler, Christoph Pauls, and André Bardow. Temperature-dependent diffusion coefficients from 1d raman spectroscopy. *Journal of Solution Chemistry*, 43(1):144–157, 2014.

[260] Melissa L. Hawkins, Marc A. Rufin, Jeffery E. Raymond, and Melissa A. Grunlan. Direct observation of the nanocomplex surface reorganization of antifouling silicones containing a highly mobile PEO-silane amphiphile. *J. Mater. Chem. B*, 2(34):5689–5697, 2014.

[261] G. Sagvolden, I. Giaever, and J. Feder. Characteristic protein adhesion forces on glass and polystyrene substrates by atomic force microscopy. *Langmuir*, 14(21):5984–5987, 10 1998.

[262] Ananthakrishnan Sethuraman, Mina Han, Ravi S. Kane, and Georges Belfort. Effect of surface wettability on the adhesion of proteins. *Langmuir*, 20(18):7779–7788, 08 2004.

[263] He Xu, Anne E Murdaugh, Wei Chen, Katherine E Aidala, Megan A Ferguson, Eileen M Spain, and Megan E Núñez. Characterizing pilus-mediated adhesion of biofilm-forming *E*.coli to chemically diverse surfaces using atomic force microscopy. *Langmuir*, 29(9):3000–3011, 2013.

[264] R. L. C. Wang, H. J. Kreuzer, and M. Grunze. Molecular conformation and solvation of oligo(ethylene glycol)-terminated self-assembled monolayers and their resistance to protein adsorption. *The Journal of Physical Chemistry B*, 101(47):9767–9773, 11 1997.

[265] P. Harder, M. Grunze, R. Dahint, G. M. Whitesides, and P. E. Laibinis. Molecular conformation in oligo(ethylene glycol)-terminated self-assembled monolayers on gold and silver surfaces determines their ability to resist protein adsorption. *The Journal of Physical Chemistry B*, 102(2):426–436, 01 1998.

[266] Soeren Schilp, Alexander Kueller, Axel Rosenhahn, Michael Grunze, Michala E. Pettitt, Maureen E. Callow, and James A. Callow. Settlement and adhesion of algal cells to hexa(ethylene glycol)-containing self-assembled monolayers with systematically changed wetting properties. *Biointerphases*, 2(4):143–150, dec 2007.

[267] Daiki Murakami, Motoyasu Kobayashi, Taro Moriwaki, Yuka Ikemoto, Hiroshi Jinnai, and Atsushi Takahara. Spreading and structuring of water on superhydrophilic polyelectrolyte brush surfaces. *Langmuir*, 29(4):1148–1151, jan 2013.

[268] Kosuke Yamazoe, Yuji Higaki, Yoshihiro Inutsuka, Jun Miyawaki, Yi-Tao Cui, Atsushi Takahara, and Yoshihisa Harada. Enhancement of the hydrogen-bonding network of water confined in a polyelectrolyte brush. *Langmuir*, 33(16):3954–3959, apr 2017.

[269] Quan Du, Eric Freysz, and Y. Ron Shen. Surface vibrational spectroscopic studies of hydrogen bonding and hydrophobicity. *Science*, 264(5160):826–828, 1994.

[270] Mikayla E. Barry, Emily C. Davidson, Chengcheng Zhang, Anastasia L. Patterson, Beihang Yu, Amanda K. Leonardi, Nilay Duzen, Ketaki Malaviya, Jessica L. Clarke, John A. Finlay, Anthony S. Clare, Zhan Chen, Christopher K. Ober, and Rachel A. Segalman. The role of hydrogen bonding

in peptoid-based marine antifouling coatings. *Macromolecules*, 52(3):1287–1295, jan 2019.

[271] Chuan Leng, Hsiang-Chieh Hung, Shuwen Sun, Dayang Wang, Yuting Li, Shaoyi Jiang, and Zhan Chen. Probing the surface hydration of nonfouling zwitterionic and peg materials in contact with proteins. *ACS Applied Materials & Interfaces*, 7(30):16881–16888, 08 2015.

[272] Michael Dowhyj. *Exploring inhibited interfaces using Vibrational Sum-Frequency Spectroscopy*. PhD thesis, University of Manchester, 2020.

[273] P. B. Miranda, Lei Xu, Y. R. Shen, and Miquel Salmeron. Icelike water monolayer adsorbed on mica at room temperature. *Phys. Rev. Lett.*, 81:5876–5879, Dec 1998.

[274] Yingchun Liu, Sow-Hsin Chen, and John S Huang. Small-angle neutron scattering analysis of the structure and interaction of triblock copolymer micelles in aqueous solution. *Macromolecules*, 31(7):2236–2244, 1998.

[275] M. Wolff, J. Herbel, F. Adlmann, A. J. C. Dennison, G. Liesche, P. Gutfreund, and S. Rogers. Depth-resolved grazing-incidence time-of-flight neutron scattering from a solid-liquid interface. *Journal of applied crystallography*, 47(1):130–135, 2014.

[276] Max Wolff, Roland Steitz, Philipp Gutfreund, Nicole Voss, Stefan Gerth, Marco Walz, Andreas Magerl, and Hartmut Zabel. Shear induced relaxation of polymer micelles at the solid-liquid interface. *Langmuir*, 24(20):11331–11333, 10 2008.

[277] Max Wolff, Andreas Magerl, and Hartmut Zabel. Crystallization of soft crystals. *Langmuir*, 25(1):64–66, nov 2008.

[278] M. Wolff, A. Magerl, and H. Zabel. Structure of polymer micelles close to the solid interface. *The European Physical Journal E*, 16(2):141–145, feb 2005.

[279] Max Wolff, Uwe Scholz, Rainer Hock, Andreas Magerl, Vincent Leiner, and Hartmut Zabel. Crystallization of micelles at chemically terminated interfaces. *Phys. Rev. Lett.*, 92:255501, Jun 2004.